Scanning

Characterization of the Corroding Interface using Scanning Techniques 2021

Lead Guest Editor: J. Chen
Guest Editors: Y. X. Qiao, F. J. Meng, Y. Yang, and T. C. Dan

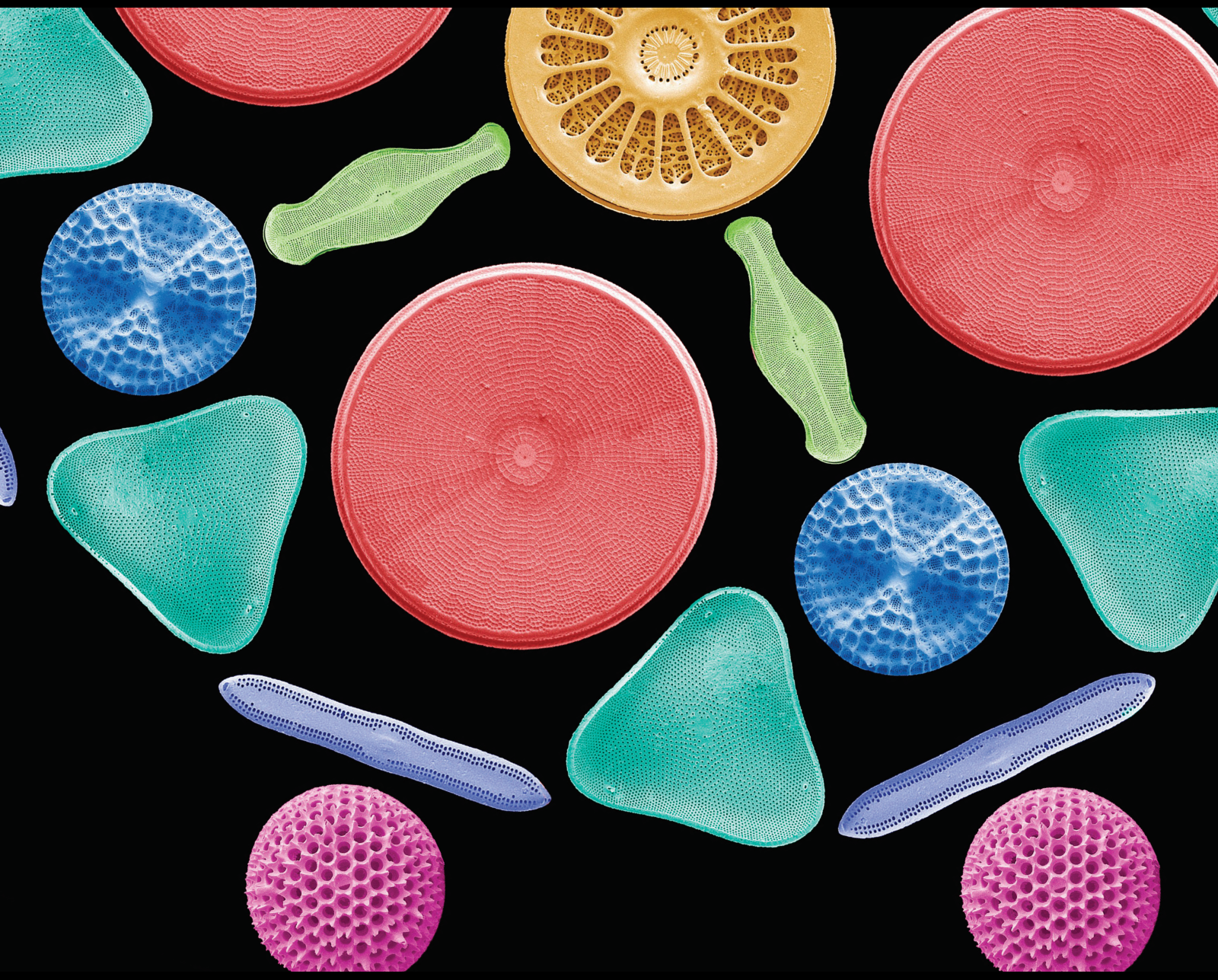

Characterization of the Corroding Interface using Scanning Techniques 2021

Scanning

Characterization of the Corroding Interface using Scanning Techniques 2021

Lead Guest Editor: J. Chen
Guest Editors: Y. X. Qiao, F. J. Meng, Y. Yang, and T. C. Dan

Contents

Hindawi
Scanning
Volume 2022, Article ID 8503314, 9 pages
https://doi.org/10.1155/2022/8503314

Review Article

Effects of Electron Microscope Parameters and Sample Thickness on High Angle Annular Dark Field Imaging

Pucheng Yang, Zheng Li, Yi Yang, Rui Li, Lufei Qin, and Yunhao Zou

School of Materials Science and Engineering, Xiangtan University, Xiangtan, Hunan 411105, China

Correspondence should be addressed to Yi Yang; yangyi@xtu.edu.cn

Received 14 October 2021; Accepted 7 March 2022; Published 20 March 2022

Academic Editor: Ovidiu Cretu

Scanning transmission electron microscopy (STEM) developed into a very important characterization tool for atomic analysis of crystalline specimens. High-angle annular dark field (HAADF) scanning transmission electron microscopy (STEM) has become one of the most powerful tools to visualize material structures at atomic resolution. However, the parameter of electron microscope and sample thickness is the important influence factors on HAADF-STEM imaging. The effect of convergence angle, spherical aberration, and defocus to HAADF imaging process has been analyzed through simulation. The applicability of two HAADF simulation software has been compared, and suggestions for their usage have been given.

1. Introduction

In recent years, dynamical diffraction is the major limitation to structure determination by electron methods, scanning transmission electron microscopy (STEM) which can effectively overcome this limitation by providing an incoherent image with electrons [1]. It has become a very popular and widespread technique and has been developed with different imaging modes (i.e., bright field (BF), annular bright field (ABF), and annular dark field (ADF)). High-resolution STEM using higher-angle scattered electrons (high-angle annular dark field, HAADF-STEM), where scattered electrons at higher angles are collected by an annular detector for STEM imaging, now attracts material scientists and semiconductor researchers [2] and becomes a powerful tool in characterizing nanoparticles [3, 4]), lithium ion batteries [5], quasicrystal [6–8], and alloy [9, 10]. HAADF has high resolution up to 40.5 pm [11, 12], image intuitive with the sensitive to chemical composition [13], and less damage to the sample, etc. It has become an important approach of material analysis at the atomic level due to the fact that its contrast depends highly on atomic number Z in a form of Z^n $(n = 1.6 - 1.9)$ [14, 15].

There are two steps in STEM imaging: first, the parallel electron wave is emitted by the electron gun and converged by the lens to form the convergent electron wave; second, the convergent electron wave scans the surface of sample point by point, and each sample point will get an exit wave. The effect of imaging process in these steps should be considered: the influence of lens on image including the convergence angle [16], spherical aberration and defocus [17], and detector angle [18] and the influence of sample including the sample thickness and the atomic number [15, 19]. In STEM imaging mode, there are two theories that have been proposed to reveal the image formation process, such as multislice method [20, 21] and Bloch wave method [1, 22]. The Bloch wave method has the advantage of high calculation accuracy, but it can only suit for perfect crystal [23] and has a long calculation time [24, 25]. Compared to the Bloch wave method, the multislice method has the advantages of fast calculation speed and wide applicability [26]. However, the images calculated by the multislice method are greatly influenced by the thickness of slice [27]. Thus, it is important to choose an appropriate theory according to the requirement. In recent years, there are several approximation theories applied in simulated calculation for speeding up the STEM imaging, such as the frozen phonon model [28] and the absorptive potential approximation [29]. The frozen phonon model divides the wave function into an average and a fluctuating part, which is suitable for carrying

out the incoherent averages [28]. And the absorptive potential approximation was proposed based on the fast Fourier transform (FFT) multislice approach [29].

In general, HAADF provides incoherent images without any phase problem and can be directly inverted to object without additional image simulations [30, 31]. However, in a series of HAADF investigations [31–34] under STEM imaging condition, crystal tilt, probe convergence angle unavoidable factor (e.g., specimen thickness [35, 36], and collection angles of the detector [36], etc.) will impact on the quality of high resolution images. For example, sample bending and deviating slightly from the zone axis will result in remarkable contrast reduction and could cause atoms to be considerably displaced in HAADF image. Intensities of atomic-resolution HAADF images of zone-axis-oriented specimens change with defocus at rates that depend on lattice spacing, thickness, and strain which also effect on the intensities [27].

In this paper, the effect of electron microscope parameters and sample thickness on high angle annular dark field imaging was discussed in detail by simulation. In addition, simulation software QSTEM and Dr. Probe have been chosen for comparing their convenience in different simulation conditions.

2. The Frozen Phonon Model

In HAADF-STEM imaging, most of the signals received by annular detector come from phonon scattering [18].While frozen phonon model provides a simple method that the crystal potential is time-dependent under the assumption of independent atomic motion, under this assumption, the intensity of image $I_D(Z)$ can be described as [37]

$$I_D(z) = \int_0^z \left\langle W^2\left(z', t\right)\right\rangle \left|\left\langle \psi\left(z'\right)\right\rangle\right|^2 dz'. \tag{1}$$

The $\langle W^2(z', t)\rangle$ is related to the scattering factors, and the $|\langle\psi(z')\rangle|^2$ is the elastic intensity. The image intensity is essentially obtained from the signal received by the detector. Under the screening of big angle annular detector in HAADF-STEM imaging mode, the final signal $g(x_p)$ from the probe position x_p should be

$$g\left(x_p\right) = \int \left|\psi_t\left(k, x_p\right)\right|^2 D(k) d^2k, \tag{2}$$

where the $\psi_t(k, x_p)$ is the wave function diffracted onto the detector plane, and $D(k)$ is the detector function [38].

$$D(k) = \begin{matrix} 1 & \text{for } k_{D_{\min}} \le k \le k_{D_{\max}} \\ 0 & \text{otherwise} \end{matrix}. \tag{3}$$

The inner and outer angles of detector are the product of wavelength λ and the maximum and the minimum of the wave vector k. Therefore, $k_{D_{\max}}$ and $k_{D_{\min}}$ are determined by the angle of detector. Thus, the key to analyze the intensity of HAADF image at the same detector angle is the exit wave function. While the exit wave function is the product of the incident wave function and sample transfer function which are determined by electron microscope and sample parameters, therefore, in the subsequent sections, we will analyze the effect of these parameters on HAADF image.

3. Exit Wave

When the parameters of the incident electron beam and the sample are known, the equation of the exit wave can be obtained.

It started from the stationary Schrödinger equation:

$$-\frac{\hbar^2}{2\mu}\nabla^2\psi + U\psi = E\psi, \tag{4}$$

where the ψ is the wave function, which presents the electron trajectory, $\hbar$ is the reduced Planck constant, U is the potential field function, E is the energy of the electron, and μ is the electron mass under relativistic correction. Due to the equation of wave-particle duality, $\lambda = h/p$, we know that $K^2 = 2\text{meE}/h^2$. Therefore, the Schrödinger equation can be written as

$$\nabla^2\psi(r) + 4\pi^2K^2\psi(r) + 4\pi^2U(r)\psi(r) = 0. \tag{5}$$

While under the condition of high energy approximate, the electron wave function can be written as the form of modulation wave:

$$\psi(r) = \phi(r)\ \exp\ (2\pi ik \cdot r). \tag{6}$$

Substituting it into the Schrödinger equation, then

$$\begin{aligned}\Delta_{xy}\phi(r) + \frac{\partial^2}{\partial z^2}\phi(r) + 4\pi ik_{xy}\nabla_{xy}\phi(r) + 4\pi ik_z\frac{d\phi(r)}{dz} \\ + 4\pi^2U(r)\phi(r) = 0.\end{aligned} \tag{7}$$

Under the condition of high energy approximate, $(\partial^2/\partial z^2)\varphi(r)$ can be ignored, and we can obtain

$$\phi(r, z) = \exp\left\{\frac{iz}{4\pi k_z}\left[\Delta_{xy} + 4\pi ik_{xy}\nabla_{xy} + 4\pi^2U\right]\right\}\phi(r, 0). \tag{8}$$

Equation (8) shows that the relationship of the incident wave and the exit wave is determined by following factors: z is the sample thickness, k_z is the reciprocal of wavelength λ, Δ_{xy} is the direction of the scattering, and U is the crystal potential. These factors, effect on imaging process, will be analyzed in subsequent sections.

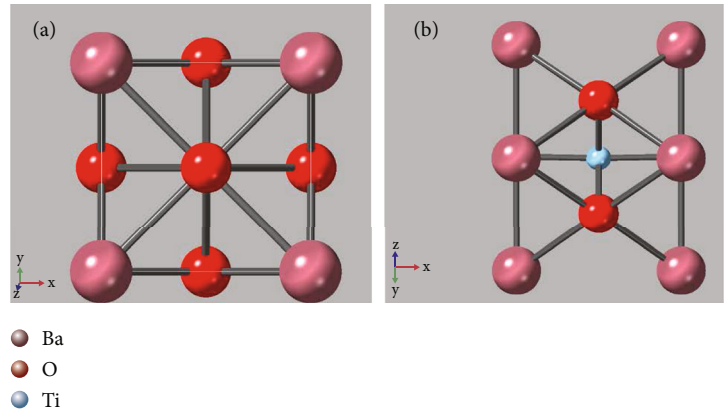

Figure 1: Projection structure model of $BaTiO_3$: (a) at [001] direction and (b) at [011] direction.

4. The Effect of Electron Microscope Parameters on HAADF

In STEM imaging mode, the parallel electron waves from the electron gun pass through electron microscope before they are incident to the sample and become convergent electron waves. The incident waves will be affected by convergence angle, spherical aberration, and defocus. In order to illustrate the effects, $BaTiO_3$ was taken as an example for simulation, and its structure model is shown in Figure 1. The simulation parameters are as follows: accelerating voltage is 300 kV (wavelength is 1.97 pm); the sample thickness is 82.7 Å, the tilt angle is 0, the convergence angle is 25 mrad, the spherical aberration and defocus are 0, and the detector angle is 50-250 mrad. The simulation software is QSTEM [39] which uses the frozen phonon model based on the multislice method [40].

4.1. Convergence Angle. When convergent electron waves are incident on the position x_p of the sample surface, the equation of incident wave function [38] is

$$\psi_p(x, x_p) = A_p \int_0^{k_{\max}} \exp\left[-i\chi(k) - 2\pi i k \cdot (x - x_p)\right] d^2k. \quad (9)$$

The $\chi(k)$ is the aberration function, A_p is the factor which comments $\int |\psi_p(x, x_p)|^2 d^2x = 1$, the influence of convergence angle on the incident wave function is the upper limit of integral $k_{\max} = \alpha/\lambda$, and α is the convergence semiangle.

As shown in Figure 2(a), when the convergence angle increases, the contrast of center atom Ti will decrease. It is more obviously in thick sample (i.e., Figure 2(b)). Besides, the spots of Ba atom are larger at small convergence angle, but smaller at large convergence angle. The same situations are obtained in reference [34] which analyzed the intensity profiles of 195 nm $Si_{0.8}Ge_{0.2}$ in different convergence angles. In the HAADF-STEM model, the electron probe with small convergence angle is more sensitive to crystal potential, the atomic brightness is larger, and the spot of atom is larger in small convergence angle.

4.2. Spherical Aberration and Defocus. In fact, the spherical aberration of a real STEM is not 0. The convergence angle, spherical aberration, and defocus should be consider to choose the best condition for imaging [41, 42]. In Equation (9), $\chi(k) = \pi\lambda k^2(0.5C_s\lambda^2k^2 - \Delta f)$, it can be found that spherical aberration has a great influence on the incident convergent electron wave. In order to correct the influence of spherical aberration on the imaging process, the Scherzer focus condition [43] had been proposed. When the convergence angle is 10 mrad and spherical aberration is less than 0.1 mm, Figure 3(a) with the Scherzer focus condition has little changes as the spherical aberration increases. As shown in Figure 3(b), when defocus is 0, the simulated HAADF image becomes more and more anamorphose as the spherical aberration increases. When the convergence angle is 25 mrad, as shown in Figure 4, the anamorphose of the simulated HAADF images becomes worse as the spherical aberration is larger than 0.1 mm. It can be concluded that small convergence angle has good HAADF image at small spherical aberration conditions.

In HAADF-STEM mode, the Scherzer focus condition ($\Delta f = -1.15(C_s\lambda)^{0.5}$) makes the transfer function have a wide flat area which leads to simulation images that have less abnormal structure information [17]. Therefore, it is obvious that the anamorphose deformation of the simulated HAADF images with the Scherzer condition is less than those who do not satisfy with it. And when the Scherzer focus condition is satisfied, the best convergence semiangle is

$$\alpha_0 = 1.41\left(\frac{\lambda}{C_s}\right)^{0.25}. \quad (10)$$

Combined with the limit point resolution in STEM mode, $d_0 = 0.61\lambda/\alpha_0$, it can be concluded that

$$d_0 = 0.43C_s^{0.25}\lambda^{0.75}. \quad (11)$$

So, appropriate defocus and convergence angle should be chosen according to its spherical aberration. At present, the resolution of STEM image with spherical aberration correction has reached 40.5 pm [11]. Therefore, for an electron

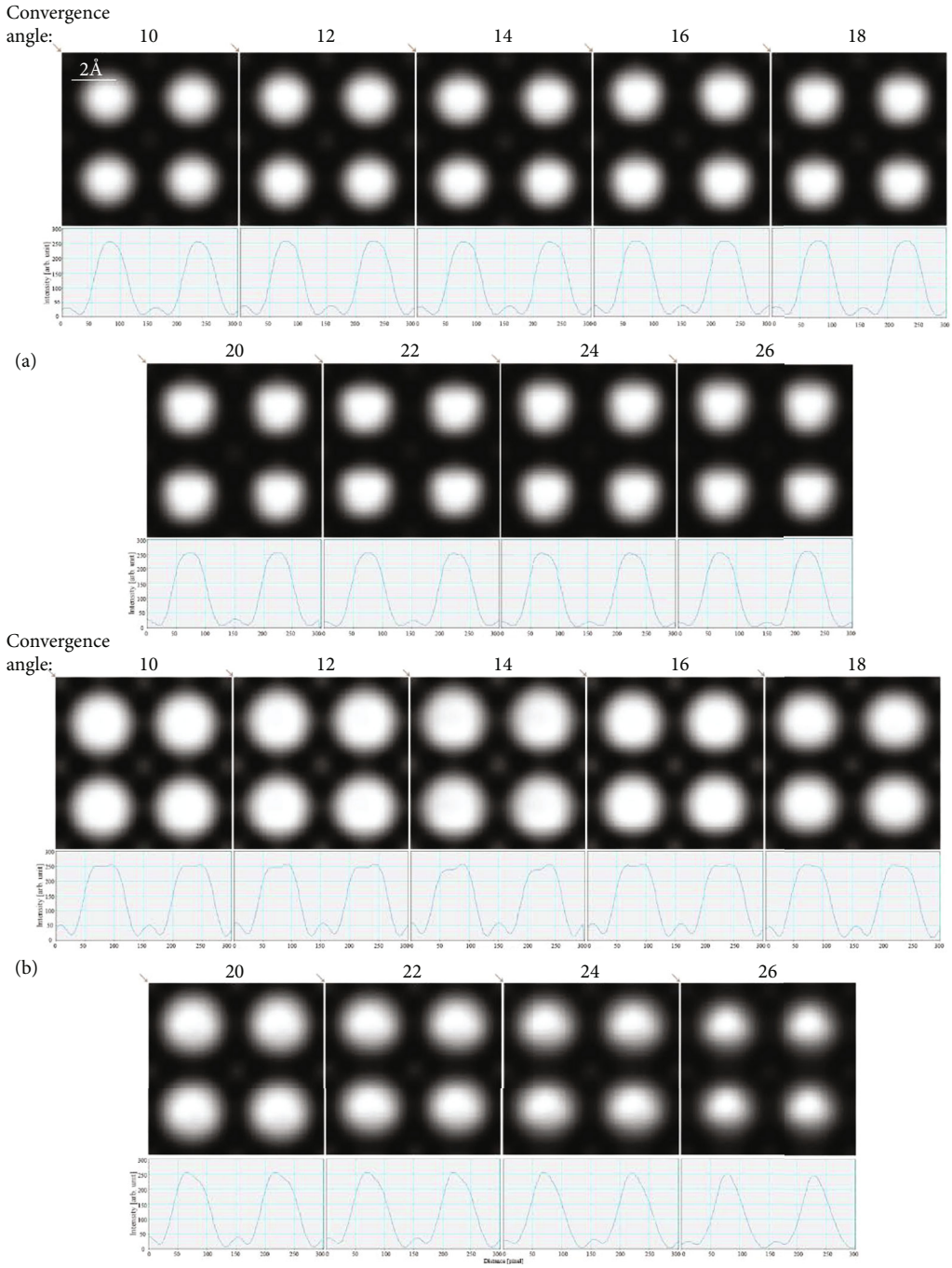

FIGURE 2: Simulated HAADF image (the source size = 0.8 Å, detector angle = 50 mrad ~ 250 mrad, defocus = 0, spherical aberration = 0) and its intensity profile along the diagonal as the arrow shown of $BaTiO_3$ at [001] axis zones with different convergence angles: (a) 42.3 Å thickness and (b) 82.7 Å thickness.

microscope with a certain spherical aberration, the key to high-quality STEM image is the appropriate defocus and convergence angle.

4.3. Detector Angle. In HAADF-STEM mode, the annular detector mainly receives high angle scattered electrons. Its scattering intensity can be expressed as the internal of inner angle θ_1 to outer angle θ_2 [18]:

$$\sigma_{\theta_1,\theta 2} = \left(\frac{m}{m_0}\right)\frac{Z^2\lambda^4}{4\pi^3 {a_0}^2}\left(\frac{1}{{\theta_1}^2+{\theta_0}^2}-\frac{1}{{\theta_2}^2+{\theta_0}^2}\right). \quad (12)$$

In equation (12), m is the mass of high-velocity electrons, m_0 is the static mass of electron, Z is the atomic number, λ is the wavelength, α_0 is the Bohr radius, and θ_0 is the Born characteristic scattering angle.

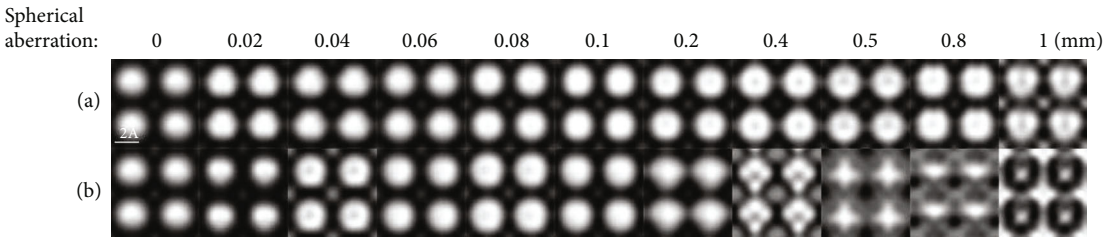

Figure 3: Simulated HAADF images (sample thickness = 82.7 Å, source size = 0.8 Å, detector angle = 50 mrad ~ 250 mrad, convergence angle = 10 mrad) with different spherical aberrations and defocus: (a) Scherzer focus condition and (b) defocus is 0.

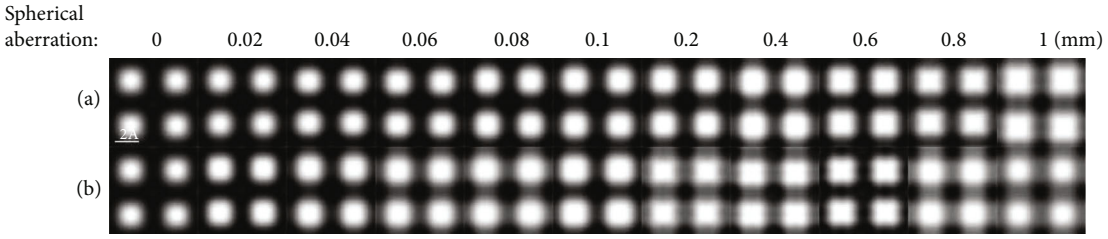

Figure 4: Simulated HAADF images (sample thickness = 82.7 Å, source size = 0.8 Å, detector angle = 50 mrad ~ 250 mrad, convergence angle = 25 mrad) with different spherical aberrations and defocus: (a) Scherzer focus condition and (b) defocus is 0.

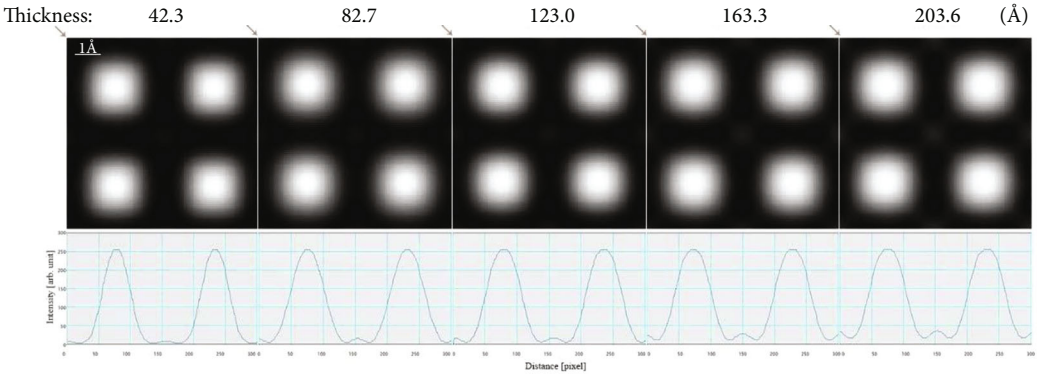

Figure 5: Simulated HAADF-STEM image (source size = 0.8 Å, detector angle = 50 mrad ~ 250 mrad, convergence angle = 25 mrad, defocus = 0, spherical aberration = 0) of $BaTiO_3$ sample at different thicknesses and its intensity profile along the diagonal as the arrow shown.

When the thickness of a sample is t, the intensity of exit electron wave is I, the number of atoms per unit volume is N, and the scattering intensity can be expressed as equation (13):

$$I_s = \sigma_{\theta_1,\theta_2} \cdot NtI. \tag{13}$$

Equation (12) can be transformed into equation (14):

$$\sigma_{\theta_1,\theta 2} = \left(\frac{m}{m_0}\right) \frac{Z^2\lambda^4}{4\pi^3 {a_0}^2} \left(\frac{{\theta_2}^2 - {\theta_1}^2}{\left({\theta_1}^2 + {\theta_0}^2\right)\left({\theta_2}^2 + {\theta_0}^2\right)}\right). \tag{14}$$

It obvious in Equation (14) that the larger inner angle θ_1, the weaker the image intensity. The partial derivative of outer angle θ_2 can be obtained:

$$\frac{\partial \sigma_{\theta_1,\theta 2}}{\partial \theta_2} = \left(\frac{m}{m_0}\right) \frac{Z^2\lambda^4}{4\pi^3 {a_0}^2} \left(\frac{2\theta_2}{\left({\theta_2}^2 + {\theta_0}^2\right)^2}\right). \tag{15}$$

Table 1: The simulation parameters of QSTEM and Dr. Probe.

Parameters	QSTEM and Dr. Probe
Accelerating voltage	300 kV
Sources size	0.8 Å
Convergence angle	25 mrad
C_c	1 mm
C_s	0 mm
HADDF detector angle	50-250 mrad

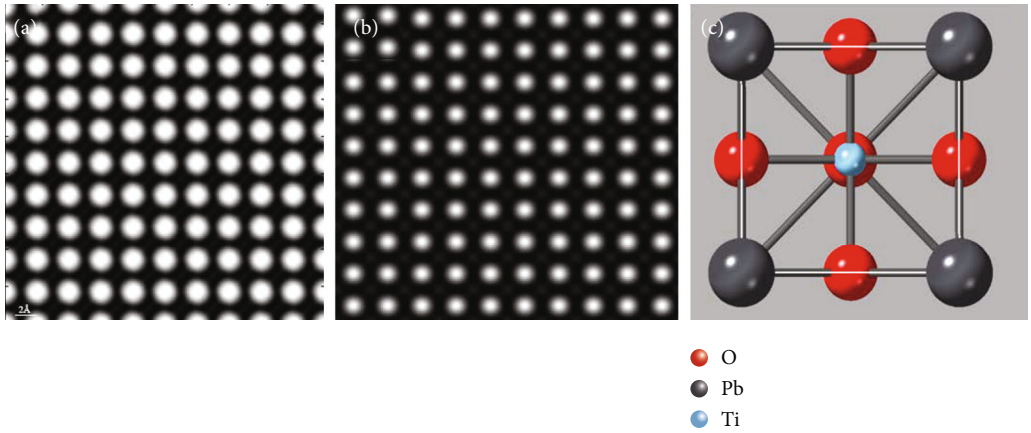

Figure 6: Simulated HAADF-STEM images (sample thickness = 83.0 Å, source size = 0.8 Å, detector angle = 50 mrad ~ 250 mrad, convergence angle = 25 mrad, defocus = 0, spherical aberration = 0) along $PbTiO_3$ [001]: (a) QSTEM, (b) Dr. Probe, and (c) structure model projection of $PbTiO_3$ at the [001] zone axis.

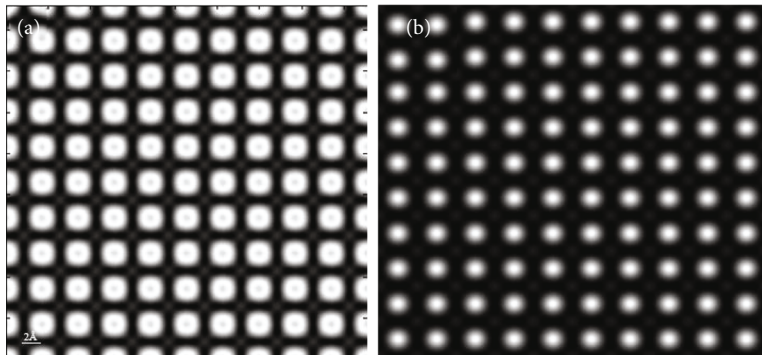

Figure 7: Simulated HAADF-STEM images (sample thickness = 166.0 Å, source size = 0.8 Å, detector angle = 50 mrad ~ 250 mrad, convergence angle = 25 mrad, defocus = 0, spherical aberration = 0) along $PbTiO_3$ [001]: (a) QSTEM and (b) Dr. Probe.

The overall intensity of the image will be stronger with the increase of the outer angle. This also reflects that a larger detector angle range can obtain a stronger intensity image. However, the small inner angle may cause other signals to be detected (e.g., the diffraction contrast caused by Bragg reflection). Larger inner angle will also affect the relationship between the contrast of the atomic column and the atomic number Z in the final image which will be analyzed in the following sections. The intensity of the image atomic column is not simply linear with the sample thickness and the range of the detector angle [1]. Therefore, it is necessary to consider both the detector angle and image interpretation.

4.4. The Effect of Sample Thickness on HAADF. In imaging process, the incident wave is converged by the electron microscope and the surface of the sample is scanned point by point. There is no doubt that, sample parameters are also important influence on HAADF image. This section will discuss the influence of sample thickness on imaging process which is based on the simulation calculation of the multislice method.

It can be found in Figure 5 that the contrast of center atoms (Ti) is stronger in thick sample. This phenomenon has been explained in [15]. Equation (12) shows that the intensity of atomic column is proportional to the square of the atomic number Z, while it should not consider the scattering intensity of one atomic array only in HAADF-STEM. For thin sample, if convergence semiangle α_0 and the inner angle θ_1 of the detector have the relationship:

$$\theta_1 \geq 3\alpha_0, \tag{16}$$

then the coherent effect between different atomic arrays of thin samples can be ignored. The approximation of the image intensity to the n-th power of the atomic number Z is very accurate. The range of n is 1.6-1.9 which is related to the inner and outer angle of detector.

5. Comparison HAADF Simulation Software

There is several software for HAADF simulation, and Dr. Probe and QSTEM are two free software which has wide used for researchers. In Dr. Probe software, the frozen-lattice approach [44] was used to simulate thermal-diffuse

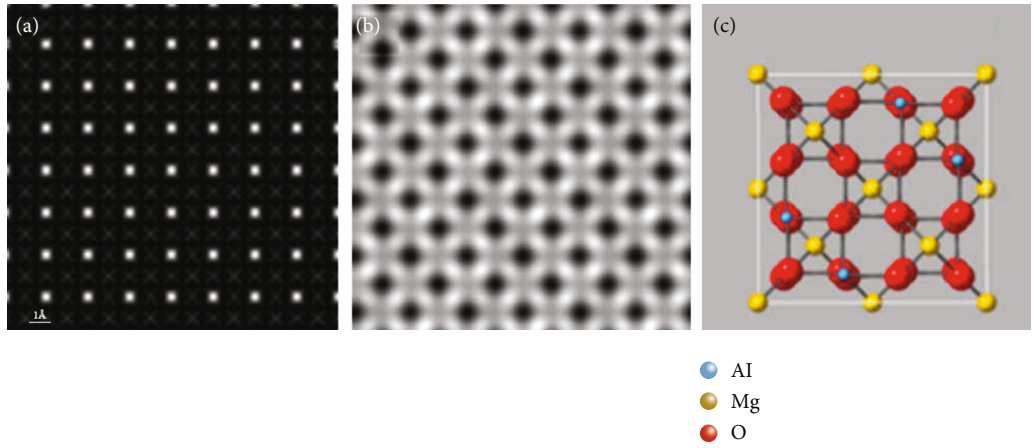

Figure 8: Simulated HAADF-STEM images (sample thickness = 80.9 Å, source size = 0.8 Å, detector angle = 50 mrad ~ 250 mrad, convergence angle = 25 mrad, defocus = 0, spherical aberration = 0) along $MgAlO_4$ [001]: (a) QSTEM, (b) Dr. Probe, and (c) structure model projection of $MgAlO_4$ at the [001] zone axis.

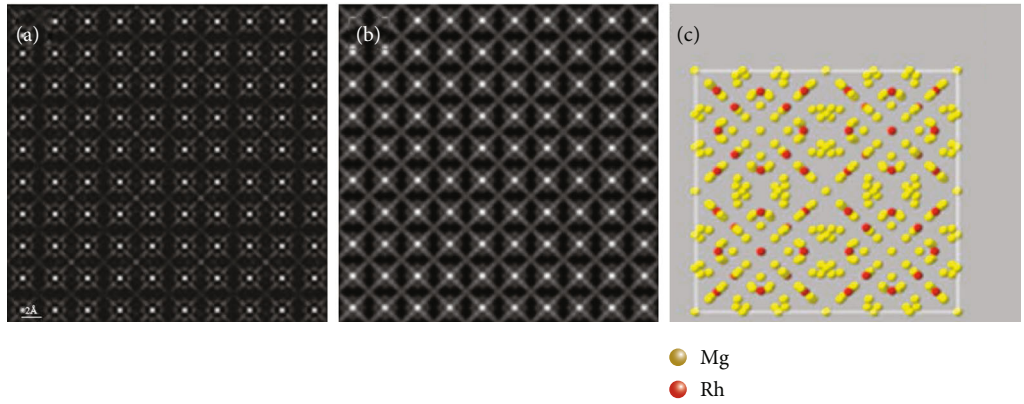

Figure 9: Simulated HAADF-STEM images (sample thickness = 201.5 Å, s, detector angle = 50 mrad ~ 250 mrad, convergence angle = 25 mrad, defocus = 0, spherical aberration = 0) along $Mg_{44}Rh_7$ [001]: (a) QSTEM, (b) Dr. Probe, and (c) structure model projection of $Mg_{44}Rh_7$ at the [001] zone axis.

scattering (TDS). In this section, a horizontal comparison has been made between the two software to provide some reference for researchers. The simulation parameters of the two software are shown in Table 1.

5.1. Unit Cell with Small Size. $PbTiO_3$ was chosen as the simulated material whose lattice constants are $a = 3.90$ Å, $b = 3.90$ Å, and $C = 4.15$ Å. As shown in Figure 6, the white highlights are Pb ($Z = 82$) atoms, and the gray and white ones are Ti atoms. The atomic number of O is too small which does not show in the image. Figure 6(c) is the structure projection of $PbTiO_3$ at the [001] zone axis. The simulation results of the two software for small crystal cell have good quality, and both correctly reflect the crystal structure and atomic phase arrangement, while the contrast of Figure 6(b) is better. The contrast of Ti atoms in QSTEM is very fuzzy and difficult to distinguish. Moreover, the difference of the contrast and image point size of Pb atoms and Ti atoms in Figure 6(a) are too large. The image quality of Figure 6(a) is unnatural and unreal compared with Figure 6(b).

Figure 7 shows the simulated HAADF image of $PbTiO_3$ along [001] at thicknesses with 40 unit cells. As shown in Figure 7(a), there are black dots in the center of the white bright spots representing Pb, but the contrast of Ti atom is improved obviously as compared with Figure 6(a). However, Figure 7(b) has problems in showing the contrast of Ti atoms, and it was difficult to observe the distribution of Ti atoms.

5.2. Unit Cells with Moderate Size. $MgAlO_4$ ($a = b = c = 8.0858$ Å) was chosen as the simulated material with moderate unit cell size whose lattice parameters are between $PbTiO_3$ and $Mg_{44}Rh_7$. The thickness is 10 unit cells. The simulation results are shown in Figure 8. Compared with Figure 8(c), the white spots in Figure 8(a) and 8(b) represent Mg ($Z = 12$) atom. In Figure 8(a), the brightest atom is Mg atom, and the surrounding gray atom is Al atom. Due to the Mg atoms which are too close to the Al atoms in the projection of [001], the simulated image cannot

Table 2: Simulate time of QSTEM and Dr. probe.

Crystal	QSTEM	Dr. Probe
$PbTiO_3$	4641 s	934 s
$MgAlO_4$	34443 s	13045 s
$Mg_{44}Rh_7$	204573 s	37861 s

distinguish them. Obviously, when unit cell has moderate size, QSTEM does better.

5.3. Unit Cell with Big Size. $Mg_{44}Rh_7$ ($a = b = c = 20.148$ Å) was chosen as the simulated material. The simulation results are shown in Figure 9. As shown in Figures 9(a) and 9(b), the white bright spots represent Rh ($Z = 45$) atoms, and the gray bright spots around the white bright spots represent Mg ($Z = 12$) atoms. Figure 9(c) is the projection structure model of $Mg_{44}Rh_7$ at the [001] zone axis. By comparing Figure 9(c), the simulated results of the two software are consistent with the projection crystal structure. However, there are differences in Mg atoms. Figure 9(b) can well display the contrast of Mg atoms, but Figure 8(a) is not obvious in showing the contrast of Mg atoms, and the contrast of Mg atoms among the four Rh atoms is insufficient.

5.4. Calculate Speed. In order to control variables, Dr. Probe and QSTEM were kept consistent during calculation, and single-core calculation was performed. QSTEM and Dr. Probe are used on the same PC. According to the simulation time records, the calculate time of the two software is shown in Table 2. QSTEM generally takes much longer time than Dr. Probe. In the simulation of small cell $PbTiO_3$, the time of QSTEM was about 397% longer than that of Dr. Probe; in the simulation of medium cell $MgAlO_4$, the time of QSTEM was about 164% longer than that of Dr. Probe; in the simulation of large cell $Mg_{44}Rh_7$, the time of QSTEM was about 440% longer than that of Dr. Probe. Therefore, Dr. Probe has higher computational efficiency than that of QSTEM.

6. Conclusion

With the development of scanning transmission electron microscopy, image interpretation in HAADF-STEM mode has become particularly important. In the imaging process, the influence of the electron microscope parameters and sample parameters must be considered. In this paper, the effect of electron microscope parameters and sample thickness on high angle annular dark field imaging were discussed in detail by simulation and experiment. In addition, simulation software QSTEM and Dr. Probe have been chosen for comparing their convenience in different simulation conditions. The conclusion is as follows:

(1) Appropriate convergence angle is one of the key parameters for getting a good HAADF image. Small convergence angle has better image quality

(2) Appropriate defocus and convergence angle should be chosen according to its spherical aberration

(3) Under the condition of thin sample, sample thickness has little effect on HAADF image

(4) QSTEM and Dr. Probe both are excellent like simulation software. Dr. Probe has higher computational efficiency than that of QSTEM

Conflicts of Interest

The authors declare that they have no known competing financial interests or personal relationships that could have appeared to influence the work reported in this paper.

Acknowledgments

This work has been funded by the National Science Foundation of the China (No. 11904307, No. 52001268), the Scientific Research Fund of Hunan Provincial Educational Department (No. 18C0111 and No. 20C1797), and the Natural Science Foundation of Hunan Province (Grant No. 2019JJ50576 and No. 2021JJ40539).

References

[1] K. Watanabe, T. Yamazaki, I. Hashimoto, and M. Shiojiri, "Atomic-resolution annular dark-field STEM image calculations," *Physical Review B Condensed Matter*, vol. 64, no. 11, article 115432, 2001.

[2] H. Sawada, "Aberration correction in STEM(book chapter)," in *Scanning Transmission Electron Microscopy of Nanomaterials*, N. Tanaka, Ed., pp. 283–305, Imperial College Press, London, 2014.

[3] Y. Chen, Y. Chen, C. Qiu, C. Chen, and Z. Wang, "HAADF STEM observation of the Au/CeO_2 nanostructures," *Materials Letters*, vol. 141, pp. 31–34, 2015.

[4] A. S. Van, K. J. Batenburg, M. D. Rossell, R. Erni, and G. Van Tendeloo, "Three-dimensional atomic imaging of crystalline nanoparticles," *Nature*, vol. 470, no. 7334, pp. 374–377, 2011.

[5] Y. X. Tong, Q. H. Zhang, and L. Gu, "Scanning transmission electron microscopy: a review of high angle annular dark field and annular bright field imaging and applications in lithium-ion batteries," *Chinese Physics B*, vol. 27, no. 6, article 066107, 2018.

[6] Z. Yang, L. Zhang, M. F. Chisholm, X. Zhou, H. Ye, and S. J. Pennycook, "Precipitation of binary quasicrystals along dislocations," *Nature Communications*, vol. 9, no. 1, p. 809, 2018.

[7] A. J. P. M. Yasuhara, "The structure of an Al–Rh–Cu decagonal quasicrystal studied by spherical aberration (Cs)-corrected scanning transmission electron microscopy," *Philosophical Magazine*, vol. 95, no. 14, pp. 1524–1535, 2015.

[8] K. Yubuta, K. Yamamoto, A. Yasuhara, and K. Hiraga, "Structure of an Al–Cu–Co decagonal quasicrystal studied by *Cs*-corrected STEM," *Materials Transactions*, vol. 55, no. 6, pp. 866–870, 2014.

[9] L. Duschek, P. Kükelhan, A. Beyer et al., "Composition determination of semiconductor alloys towards atomic accuracy by HAADF-STEM," *Ultramicroscopy*, vol. 200, pp. 84–96, 2019.

[10] N. Liu, Z. Zhang, L. Peng, and W. Ding, "Microstructure evolution and mechanical properties of Mg-Gd-Sm-Zr alloys," *Materials Science and Engineering: A*, vol. 627, pp. 223–229, 2015.

[11] S. Morishita, R. Ishikawa, Y. Kohno, H. Sawada, N. Shibata, and Y. Ikuhara, "Resolution achievement of 40.5 pm in scanning transmission electron microscopy using 300 kV microscope with delta corrector," *Microscopy and Microanalysis*, vol. 24, no. S1, pp. 120-121, 2018.

[12] A. S. Van, A. J. Dekker, A. Bos, and D. D. Van, "High-resolution electron microscopy: from imaging toward measuring," *IEEE Transactions on Instrumentation and Measurement*, vol. 51, no. 4, pp. 611–615, 2002.

[13] A. Yasuhara, K. Saito, M. Nishijima, and K. Hiraga, "Characterization of Guinier-Preston zones in Mg-Gd-Zn alloys by using transmission electron microscopy," *Microscopy and Microanalysis*, vol. 17, no. S2, pp. 1878-1879, 2011.

[14] S. C. Anderson, C. R. Birkeland, G. R. Anstis, and D. Cockayne, "An approach to quantitative compositional profiling at near-atomic resolution using high-angle annular dark field imaging," *Ultramicroscopy*, vol. 69, no. 2, pp. 83–103, 1997.

[15] P. Hartel, H. Rose, and C. Dinges, "Conditions and reasons for incoherent imaging in STEM," *Ultramicroscopy*, vol. 63, no. 2, pp. 93–114, 1996.

[16] M. D. Weyland and D. A. Muller, "Tuning the convergence angle for optimum STEM performance," *NanoSolutions*, vol. 1, no. 1, pp. 24–35, 2005.

[17] C. Mory, C. Colliex, and J. M. Cowley, "Optimum defocus for STEM imaging and microanalysis," *Ultramicroscopy*, vol. 21, no. 2, pp. 171–177, 1987.

[18] S. J. Pennycook, S. D. Berger, and R. J. Culbertson, "Elemental mapping with elastically scattered electrons," *Journal of Microscopy*, vol. 144, no. 3, pp. 229–249, 1986.

[19] Y. Liu, Y. L. Zhu, Y. L. Tang, and X. L. Ma, "An effect of crystal tilt on the determination of ions displacements in perovskite oxides under BF/HAADF-STEM imaging mode," *Journal of Materials Research*, vol. 32, no. 5, pp. 947–956, 2017.

[20] C. Dwyer, "Simulation of scanning transmission electron microscope images on desktop computers," *Ultramicroscopy*, vol. 110, no. 3, pp. 195–198, 2010.

[21] V. Grillo and F. Rossi, "STEM_CELL: a software tool for electron microscopy. Part 2 analysis of crystalline materials," *Ultramicroscopy*, vol. 125, no. 1, pp. 112–129, 2013.

[22] T. Yamazaki, K. Watanabe, K. Kuramochi, and I. Hashimoto, "Extended dynamical HAADF STEM image simulation using the Bloch-wave method," *Acta Crystallographica*, vol. 62, no. 4, pp. 233–236, 2006.

[23] S. J. Pennycook and D. E. Jesson, "High-resolution incoherent imaging of crystals," *Physical Review Letters*, vol. 64, no. 8, pp. 938–941, 1991.

[24] Y. Yang, C. Y. Cai, and Q. B. Yang, "Comparison of two simulation methods in electron crystallography: BW method and a modified direct product method of scattering matrix," *Journal of Material Science & Technology*, vol. 33, no. 2, pp. 210–214, 2017.

[25] Y. Yang, Q. B. Yang, J. Y. Huang, C. Y. Cai, and J. G. Lin, "Quantitative comparison between real space and Bloch wave methods in image simulation," *Micron*, vol. 100, pp. 73–78, 2017.

[26] P. D. Nellist and S. J. Pennycook, "The principles and interpretation of annular dark-field Z-contrast imaging," *Advances in imaging and electron physics*, vol. 113, pp. 147–203, 2000.

[27] S. Hillyard and J. Silcox, "Detector geometry, thermal diffuse scattering and strain effects in ADF STEM imaging," *Ultramicroscopy*, vol. 58, no. 1, pp. 6–17, 1995.

[28] C. Fanidis, D. V. Dyck, and J. V. Landuyt, "Inelastic scattering of high-energy electrons in a crystal in thermal equilibrium with the environment I. Theoretical framework," *Ultramicroscopy*, vol. 41, no. 1-3, pp. 55–64, 1992.

[29] K. Ishizuka, "A practical approach for STEM image simulation based on the FFT multislice method," *Ultramicroscopy*, vol. 90, no. 2-3, pp. 71–83, 2001.

[30] S. J. Pennycook and P. D. Nellist, "Z-contrast scanning transmission electron microscopy," in *Impact of electron and scanning probe microscopy on materials research*, D. G. Rickerby, G. Valdrè, and U. Valdrè, Eds., pp. 161–207, Springer Netherlands, Dordrecht, 1999.

[31] T. Yamazaki, M. Kawasaki, K. Watanabe, I. Hashimoto, and M. Shiojiri, "Effect of small crystal tilt on atomic-resolution high-angle annular dark field STEM imaging," *Ultramicroscopy*, vol. 92, no. 3-4, pp. 181–189, 2002.

[32] J. Cui, Y. Yao, Y. G. Wang, X. Shen, and R. C. Yu, "Origin of atomic displacement in HAADF image of the tilted specimen," *Ultramicroscopy*, vol. 182, pp. 156–162, 2017.

[33] M. Kawasaki, T. Yamazaki, S. Sato, K. Watanabe, and M. Shiojiri, "Atomic-scale quantitative elemental analysis of boundary layers in a SrTiO3ceramic condenser by high-angle annular dark-field electron microscopy," *Philosophical Magazine A*, vol. 81, no. 1, pp. 245–260, 2001.

[34] X. Wu, M. D. Robertson, M. Kawasaki, and J. M. Baribeau, "Effects of small specimen tilt and probe convergence angle on ADF-STEM image contrast of $Si_{0.8}Ge_{0.2}$ epitaxial strained layers on (100) Si," *Ultramicroscopy*, vol. 114, pp. 46–55, 2012.

[35] S. E. Maccagnano-Zacher, K. A. Mkhoyan, E. J. Kirkland, and J. Silcox, "Effects of tilt on high-resolution ADF-STEM imaging," *Ultramicroscopy*, vol. 108, no. 8, pp. 718–726, 2008.

[36] Y. So and K. Kimoto, "Effect of specimen misalignment on local structure analysis using annular dark-field imaging," *Microscopy*, vol. 61, no. 4, pp. 207–215, 2012.

[37] D. D. Van, "Is the frozen phonon model adequate to describe inelastic phonon scattering?," *Ultramicroscopy*, vol. 109, no. 6, pp. 677–682, 2009.

[38] E. J. Kirkland, *Advanced Computinging Electron Microscopy*, Springer, 2010.

[39] C. Koch, *Determination of Core Structure Periodicity and Point Defect Density along Dislocations*, Arizona State University, 2002.

[40] J. M. Cowley and A. F. Moodie, "The scattering of electrons by atoms and crystals. I. a new theoretical approach," *Acta Crystallographica*, vol. 10, no. 10, pp. 609–619, 1957.

[41] L. Hayani, *Optimizing Precision of High-Angle Annular Dark Field Images in Scanning Transmission Electron Microscopy*, Cornell University, 2018.

[42] E. J. Kirkland, "On the optimum probe in aberration corrected ADF-STEM," *Ultramicroscopy*, vol. 111, no. 11, pp. 1523–1530, 2011.

[43] O. Scherzer, "The theoretical resolution limit of the electron microscope," *Journal of Applied Physics*, vol. 20, no. 1, pp. 20–29, 1949.

[44] J. Barthel, "Dr. Probe: a software for high-resolution STEM image simulation," *Ultramicroscopy*, vol. 193, pp. 1–11, 2018.

Hindawi
Scanning
Volume 2022, Article ID 1704544, 11 pages
https://doi.org/10.1155/2022/1704544

Research Article

Bearing Strength of Concrete-Filled Steel Tube Reinforced with Internal Transverse Stiffened Bars under Axial Compression

Nan Li,[1] **Yajun Xi**,[2] **He Li**,[1] **Guangxi Zhang**,[1] **Tao Ren**,[1] **and Xinhao Mu**[1]

[1]*College of Resources, Shandong University of Science & Technology, Taian 271019, China*
[2]*Tai'an Engineering Construction Standard Cost Office, Taian 271000, China*

Correspondence should be addressed to Nan Li; lnsdust@163.com

Received 9 September 2021; Accepted 30 December 2021; Published 21 February 2022

Academic Editor: Qiao Yanxin

A new type of square concrete-filled steel tubular (SCFST) column is proposed, which is characterized by transverse stiffened bars inside the steel tube to improve the effective constraint performance of the concrete core. The experiment of this kind of composite material under axial compression was carried out. The results showed that the bearing capacity of the SCFST column reinforced by internal transverse stiffened bars increased by 4.5%-15% than that of the ordinary SCFST column. The transverse strain is smaller than the SCFST column. As the diameter of the reinforcement increases and decreases the spacing of bars, the axial load bearing capacity increased. The transverse strain of the member decreased obviously. It is noted that the confinement performance of the concrete core of this type was improved to some extent. At the same time, based on the unified theory, the simplified calculation formula of axial compression bearing capacity is derived.

1. Introduction

The outer steel tube of the concrete-filled steel tube structure can effectively improve the restraint internal concrete, and the concrete under the transverse restraint of the steel tube is better in the three-dimensional compression state, so that the concrete can better exert its compressive performance [1–5]. As a kind of steel-concrete composite system, the SCFST column has been widely used in the structure because of its convenient connection, high flexural bearing capacity, and beautiful appearance. Based on the above characteristics, square steel tube concrete in civil engineering theoretical research and engineering applications has become more widespread in recent years [6–12]. Kong and Moon [13] studied the carrying capacity and energy dissipation of SCFST columns under long-term axial load. Uy [14] studied the mechanical properties of the short columns under the combined action of axial compression and bending moment. Susantha et al. [15] proposed an approximate formula for the axial compression-strain of confined concrete in concrete-filled steel tubular columns with different cross-sections. Liu et al. [16] studied axial compression bearing capacity of rectangular steel tube high-strength concrete short column. The load capacity obtained by the experiment was compared with the calculated values of EC4, AISC, and ACI. Liang et al. [17] proposed a method of nonlinear analysis of fibrous elements to predict the ultimate strength and ductility of thin-walled steel columns made of concrete subject to local buckling. Normal stress redistribution in the steel sheet appears after the local buckling. It is also proposed that the ductility and section performance of reinforced concrete square columns can also be described by two performance indexes. Dundu [18] carried out axial compression tests on 29 square concrete-filled steel tubes, obtained the axial compressive strength, and proposed a two-stage equation to simulate the calculation formula of short columns and medium to slender columns. Dai and Lam [19] studied the structural fire behavior of a series of concrete-filled steel tubular (CFST) short columns with four typical column cross-sections under standard fire conditions. The experimental results show that the circular section of CFST columns has the best structural fire behavior. Based on this, the design simplified formula of the concrete column under high temperature is put forward. Evirgen et al.

[20] conducted axial compression tests on 48 concrete-filled steel tubular columns with different variables and studied and analyzed the influences of width-thickness ratio, compressive strength of concrete, and column geometric parameters on axial bearing capacity, ductility, and buckling performance of concrete columns. Ellobody and Young [21] proposed a way for calculating the bearing capacity of square stainless steel reinforced concrete tubular columns. Raed et al. [22] proposed a method for calculating the axial load capacity of concrete-filled steel tubes through the experimental results of the axial compression performance of square stainless steel pipes. Many experts and scholars have put forward various measures and structures to enhance the restraint effect of square steel tubes on core concrete in the SCFST structure. Alfarabi et al. [23] studied the axial carrying capacity of the stainless steel short column without or filled with concrete. It is improved by welding carbon steel reinforcement on the inner surface of the circular hollow stainless steel pipe and the stainless steel pipe concrete short column. The change of adding stiffeners in square section concrete-filled steel tubular members is studied by Fang [24], and the eccentric compression test of members is carried out. It is found that the stability and ultimate strength of columns are improved. The reinforced concrete column with external restraint reinforcement ring and internal reinforcement is studied by Alrebeh [25]. The experiment shows that compared with the member with external reinforcement ring or internal reinforcement, the combined use is more effective to improve the structural performance of short column members. To further improve the performance, the spacing of internal reinforcement can be reduced and the number of internal reinforcement can be increased. Li et al. [26] proposed a new composite member with I-shaped carbon fiber reinforced polymer wrapped inside to strengthen square steel tube short columns and carried out a bidirectional bending test on it. The results show that the new short column has good bearing capacity and ductility in the biaxial bending test. Alatshan et al. [27] reviewed the existing literature on stiffened concrete-filled steel tubular and proposed a method to systematically review the relevant knowledge of stiffened concrete-filled steel tubular in the existing literature. Zhu et al. [28] proposed the connection method of the outer diaphragm using perfobond ribs (PBL) to strengthen concrete-filled square steel tubes (CFSST). The test shows that this innovative connection method improves the load transfer and deformation of the joint.

From the above studies, it is not difficult to find that the outer steel tube is less constrained to the internal concrete core of the SCFST column. Therefore, in order to better promote restraint of foreign steel tubes to concrete, more effective restraint measures should be developed and researched.

In this paper, a new type of SCFST column is presented. The main structural feature of the column is that some transverse reinforcing bars are welded on the inner wall of the square steel tube to strengthen the restraint of the core concrete of the square steel tube; at the same time, the local stability of square steel tube walls is strengthened, and the ultimate bearing capacity and deformation capacity of the SCFST column under axial pressure are effectively enhanced. Axial load capacity and ductility are analyzed; from the perspective of unified theory, a formula for a theoretical evaluation of load bearing capacity of SCFST with internal transverse stiffened bars is proposed.

2. Experimental Programme

2.1. Specimen Fabrication. A total of 10 specimens were tested under compression, including one square concrete steel tubular stub column and nine SCFST with internal transverse stiffened bars. Before the experiment, in order to facilitate the observation of the deformation of the specimen, a square was drawn with chalk on the test block in advance. All specimens were made of 6 mm thick steel plates with a height of 600 mm and a side length of 200 mm. The stiffener diameters are 4 mm, 6 mm, and 8 mm, respectively, and the stiffener length is 180 mm. Internal transverse reinforcement spacing is 50 mm, 75 mm, and 100 mm, respectively. The steel plate material is Q235B, and the transverse bar is HPB335. The typical section is shown in Figure 1, and all specimens are given in Table 1.

2.2. Material Properties. All the samples were made of a 6 mm thick steel plate. A part of steel was cut directly from the steel plate of the square steel pipe, and the standard tensile test strip of steel was made for the material property test. Tables 2 and 3 describe the mechanical properties of steel and reinforcement, respectively. Meanwhile, concrete-filled square steel tube specimens were poured; 3 pieces of concrete cube specimens with side length of 150 mm were made for the material performance test. The average compressive strength of concrete cube specimens with curing age of 28 days is 31.6 MPa.

2.3. Experiment Setup. This test uses the YAW-3000A electrohydraulic Servo pressure testing machine as shown in the figure. The load is carried out by the way of hierarchical axial loading [29]. Place the sample in the center of the tester. A steel block is fixed at the upper and lower ends of the specimen to prevent local failure near the load surface. At the same time, ensure that the centroids of the base, sample, and steel block are on the same vertical line. The experimental loading equipment used in the study is shown in Figure 2.

The main measurement content includes the longitudinal and transverse strain of the specimen, the axial pressure of the specimen, and the value of axial compression deformation. The longitudinal strain of the column is attached to the 4 outer surfaces of the steel pipe column, 3 on each surface, and the positions are located at 1/4, 1/2, and 3/4 of the height of the specimen. The transverse strain is measured by the horizontally attached strain gauges. Paste 3 on the 4 outer surfaces of the steel pipe column. The positions are located at the middle height of the test piece and distributed at 1/4, 1/2, and 3/4 of the cross-sectional width. The outer surface of the test piece is longitudinal and transverse. The position of the strain gauge is shown in Figure 3.

In the elastic phase, the value of the control load at each step is about 10% of the value of the limit load. Each loading step takes 3-5 minutes. When the value of the load increases to 85% of the calculated limit load, the loading speed is

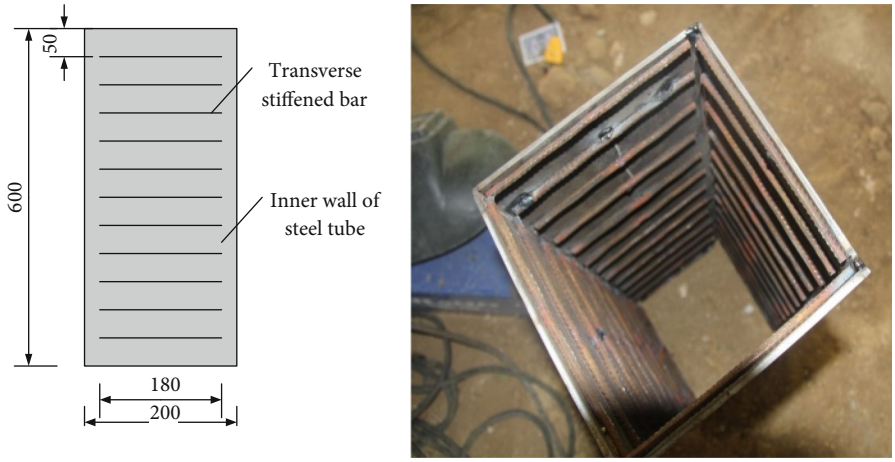

(a) Configuration of steel tube (b) Square steel tubes

Figure 1: The specimen.

Table 1: The dimension of specimens.

Specimen	Width (mm)	Height (mm)	t (mm)	Diameter (mm)	Length (mm)	Spacing (mm)
B0	200 * 200	600	6	None	None	None
B1	200 * 200	600	6	4	180	100
B2	200 * 200	600	6	4	180	75
B3	200 * 200	600	6	4	180	50
B4	200 * 200	600	6	6	180	100
B5	200 * 200	600	6	6	180	75
B6	200 * 200	600	6	6	180	50
B7	200 * 200	600	6	8	180	100
B8	200 * 200	600	6	8	180	75
B9	200 * 200	600	6	8	180	50

Table 2: Mechanical properties of steel.

Plate thickness (mm)	Yield strength (MPa)	Tensile strength (MPa)
6	228	310

Table 3: Mechanical properties of steel bar.

Diameter of steel bar (mm)	Yield strength (MPa)	Tensile strength (MPa)
4	353	460
6	345	430
8	332	420

reduced until failure. The test loading time for each specimen is about 2 hours.

3. Experimental Results

3.1. Failure Mode. The failure mode of specimens is shown in Figure 4. Both samples showed local buckling of the steel pipe. For the specimens of B0, local buckling of steel pipes is in the height direction, but for specimens of B1-B9, the local buckling is a little or not obvious. The failure mode of SCFST specimens is mainly the outward bulging and buckling of steel tubes at the top and middle, and the outer bulging area and size are large. The failure of SCFST with internal transverse stiffened bars columns mainly occurs at the top. At the same time, there is a slight bulging and buckling at the middle and upper parts of SCFST, but it is not particularly obvious. The size is 5~10 mm. In the same group of specimens, with the decrease of the spacing of transverse stiffeners, the degree of external bulging tends to decrease, indicating that the increase of transverse reinforcement on the pipe wall can effectively delay the buckling of the steel plate.

3.2. Comparison of Load Bearing Capacity. According to the experimental observation and the load-displacement curves of specimens, as shown in Figure 5, these compression specimens usually have three stages from the beginning of loading to the failure of the specimen.

In the first stage, at the beginning of loading, the specimens are in an elastic phase as seen from the load-strain curves. There are no obvious changes in the steel tube.

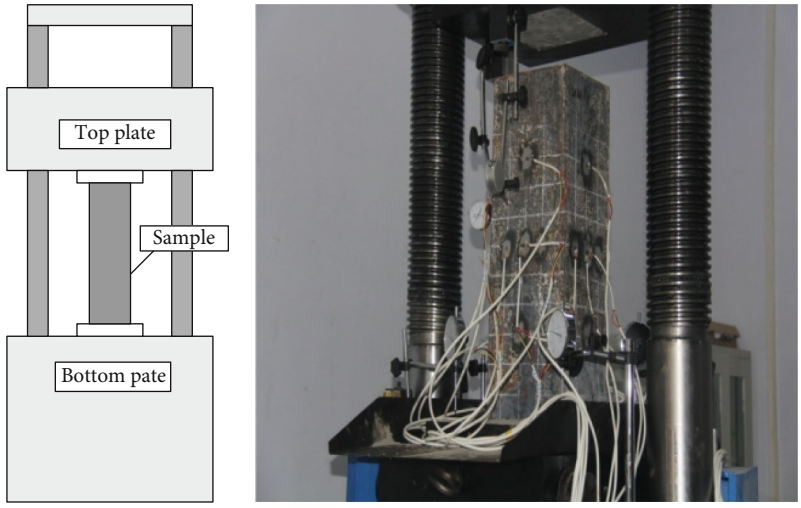

(a) Schematic diagram (b) Loading equipment

Figure 2: Test device.

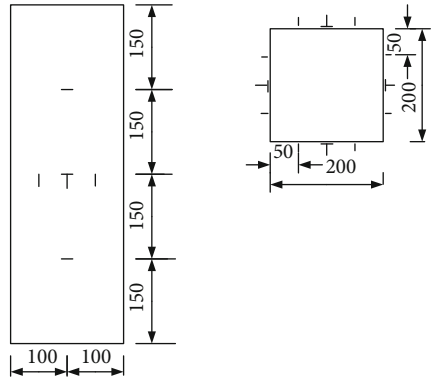

(a) Placement of strain gauge (b) Cross-section

Figure 3: Layout of measuring points.

In the second stage, when the load is up to 85% of the ultimate capacity, the surface deformation of the square steel tube appears in some parts and the specimens show elastic-plastic behavior. At this stage, the local buckling of the steel tube appears at first near the upper end of the specimen, then develops to the middle of the specimen, and the phenomenon of local buckling is gradually obvious. When the load reaches the limit load, the local buckling deformation of the steel pipe wall is obvious.

At the last stage, when the load reaches the ultimate load, the internal concrete is destroyed, the load-carrying capacity of the specimen decreases rapidly, and the displacement increases continuously.

As seen from Figure 5, the load summit of the ordinary SCFST column specimen (B0) is much smaller than that of the other 9 specimens (SCFST with internal transverse stiffened bars column). It is indicated that the transverse stiffened bars can play an active role in SCFST. With the different configurations of transverse stiffened bars, the increase in the axial load bearing capacity is different.

From Figures 5(a)–5(c), it can be seen that when the diameter of the transverse steel bars is constant, reducing the spacing of the transverse steel bars will increase the axial load bearing capacity, but the magnitude of the increase varies. Traditional SCFST specimens have a small peak point displacement; SCFST with internal transverse stiffened bars column has better ductility due to the stiffened steel bars. The peak point displacement is large, and the final displacement can reach 10-15 mm. When the spacing of the transverse stiffening ribs remains unchanged at $S = 100$ mm and the diameter changes, the bearing capacity only increases by 0.8% to 1.8%; when the spacing of transverse stiffeners is $S = 75$ mm, the ultimate bearing capacity is only increased by 1.6%~3.3%; when the spacing of transverse stiffeners is $S = 50$ mm, the change of diameter increases the bearing capacity by 1.7%~4.9%.

According to the above analysis, for the SCFST with internal transverse stiffened bars column, the effect of improving the bearing capacity of SCFST with internal transverse stiffened bars column through the change of reinforcement diameter is not obvious; the change of the spacing of transverse stiffeners is conducive to improve the bearing capacity of SCFST with internal transverse stiffened bars column. Decreasing the spacing of transverse stiffeners is more

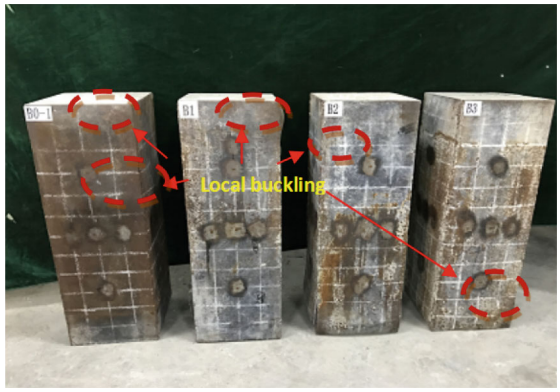

(a) Comparison of B0, B1, B2, and B3

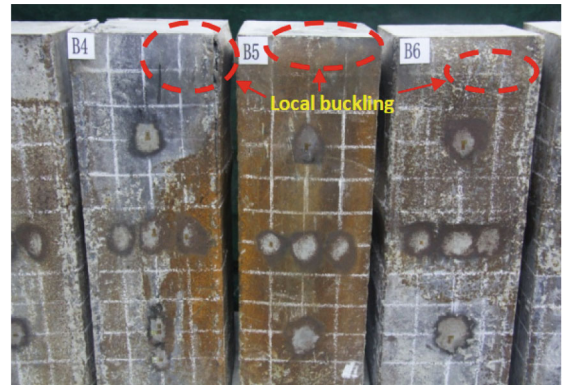

(b) Comparison of B4, B5, and B6

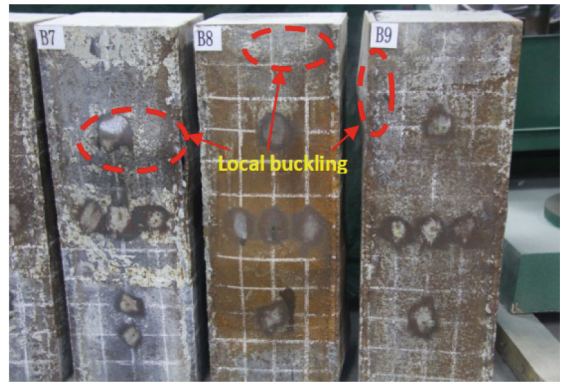

(c) Comparison of B7, B8, and B9

Figure 4: Failure mode of specimens.

effective than increasing the diameter of stiffeners. With the larger diameter of bars and the smaller spacing of transverse bars, the increase of axial supporting capacity is more obvious. The axial supporting capacity of all specimens is shown in Table 4.

As seen from Table 4, the load bearing capacity of the SCFST column with transverse stiffened bars is better than that of SCFST columns. In all specimens, the maximum increase amplitude is 15%; the smallest increase reached 4.5%; this is mainly due to the weak confinement of the square steel tube on the core concrete. When transverse stiffened bars are welded on the inside steel tube, it can strengthen the restraint effect of the square steel tube on concrete, make the concrete in the core area get better compression from three directions, and improve the bearing capacity of concrete. It is noted that the transverse stiffened bars inside the steel tube can play an important role in promoting the load bearing capacity of SCFST columns.

3.3. The Amount of Steel in Concrete-Filled Steel Tube. The amount of steel of specimens is shown in Table 5.

3.3.1. The Effect of the Variation on the Bar Diameter. According to the data in Table 5, we can know that the steel consumption of the square steel reinforced concrete column is 2.3%, 3%, 4%, 5.1%, 6.6%, 9.5%, 9.1%, 11.7%, and 16.8%, respectively. And the corresponding increase in bearing capacity is 3%, 5%, 7%, 4%, 9%, 12%, 6%, 12%, and 15%, respectively. Remaining the spacing of 100 mm unchanged, when the diameter of the transverse stiffened bars changed from 4 mm, 6 mm, and 8 mm, the corresponding increase in the amount of steel was from 2.3%, 5.1%, and 9.1%, while the corresponding increase in the bearing capacity changed from 4.5%, 5.3%, and 7.1%; remaining the spacing of 75 mm unchanged, when the diameter of the transverse stiffened bars changed from 4 mm, 6 mm, and 8 mm, the corresponding increase in the amount of steel was from 3%, 6.6%, and 11.7%, while the corresponding increase in the bearing capacity changed from 6.7%, 9.9%, and 11.5%; remaining the spacing of 50 mm unchanged, when the diameter of the transverse stiffened bars changed from 4 mm, 6 mm, and 8 mm, the corresponding increase in the amount of steel was from 4%, 9.5%, and 16.8%, while the corresponding increase in the bearing capacity changed from 8.4%, 13.3%, and 15%.

3.3.2. The Effect of the Variation on the Bar Spacing. Remaining 4 mm of the diameter of bars unchanged, when the cross bar spacing is reduced from 100 mm to 75 mm and from 75 mm to 50 mm, the corresponding increase in the amount of steel is 2.3% and 4%, respectively. The increase of the bearing capacity is 4.5% and 8.4%, respectively. Remaining 6 mm of the diameter of bars unchanged, when the cross bar spacing is reduced from 100 mm to 75 mm and from 75 mm to 50 mm, the corresponding increase in the amount of steel is 5.1% and 9.5%, respectively. The increase of the bearing capacity is 5.3% and 13.3%, respectively. Remaining

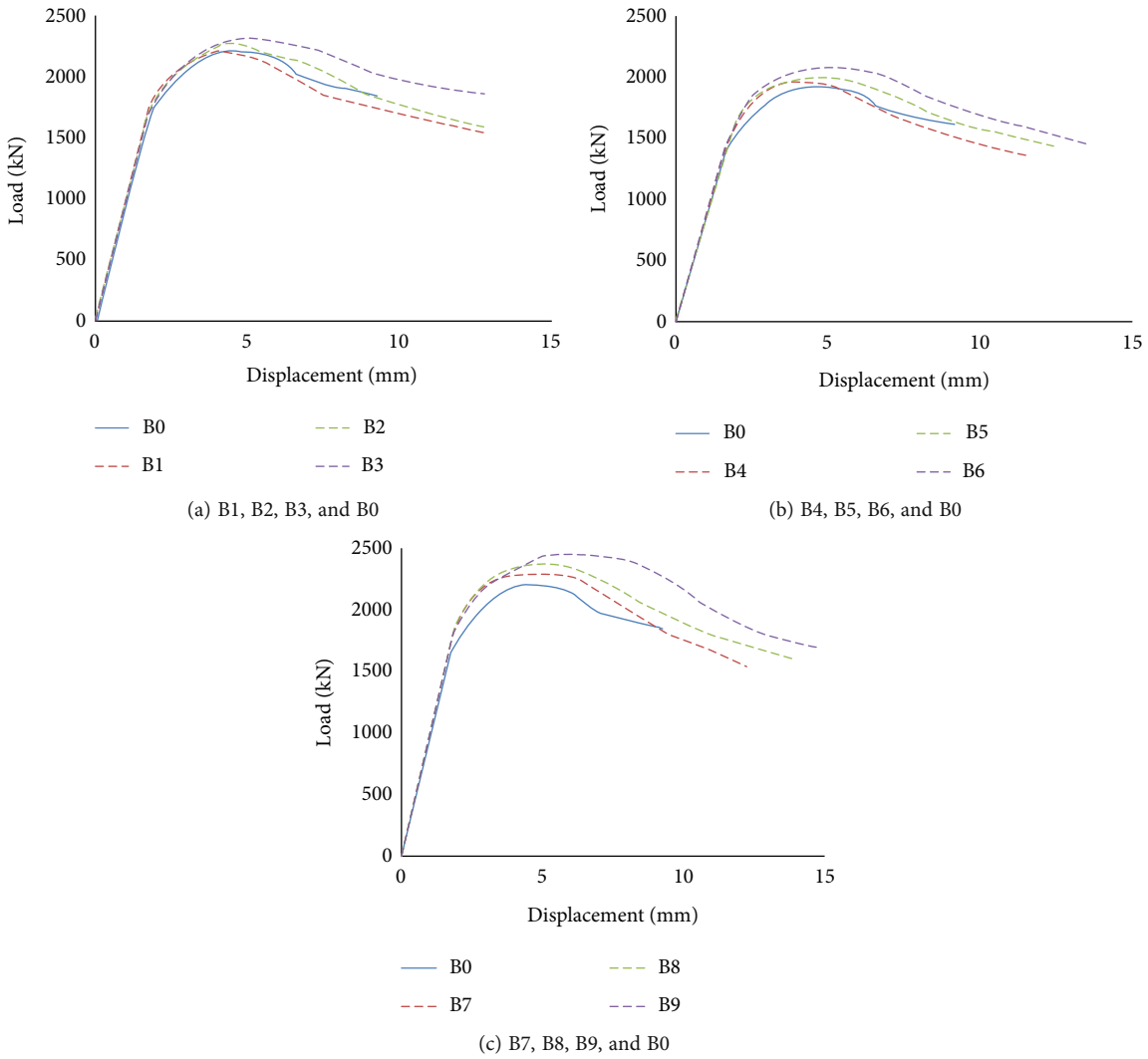

Figure 5: Comparison of load-displacement curve.

Table 4: Bearing capacity of specimens.

Specimens	Bearing capacity (kN)	Increasing amplitude (%)
B0	2112	—
B1	2177	4.5
B2	2230	6.7
B3	2270	8.4
B4	2197	5.3
B5	2310	9.9
B6	2400	13.3
B7	2240	7.1
B8	2350	11.5
B9	2440	15

Table 5: Comparison of steel consumption.

Specimen number	Weight of steel tube (kg)	Weight of steel bars (kg)	Total amount of steel (kg)	Steel ratio
B0	21.9	0	21.9	1
B1	21.9	0.50	22.4	1.023
B2	21.9	0.64	22.54	1.033
B3	21.9	0.92	22.82	1.043
B4	21.9	1.12	23.02	1.051
B5	21.9	1.44	23.98	1.066
B6	21.9	2.08	23.89	1.081
B7	21.9	1.99	23.89	1.095
B8	21.9	2.56	24.46	1.117
B9	21.9	3.69	25.59	1.168

8 mm of the diameter of bars is unchanged, when the cross bar spacing is reduced from 100 mm to 75 mm and from 75 mm to 50 mm, the corresponding increase in the amount of steel is 9.1% and 16.8%, respectively. The increase of the bearing capacity is 7.1% and 15%, respectively. Under the condition of constant reinforcement diameter, when the transverse reinforcement spacing is reduced from 100 mm to 50 mm, the bearing capacity of the transverse reinforced concrete column is about 4% higher than that of the concrete-filled steel tubular column.

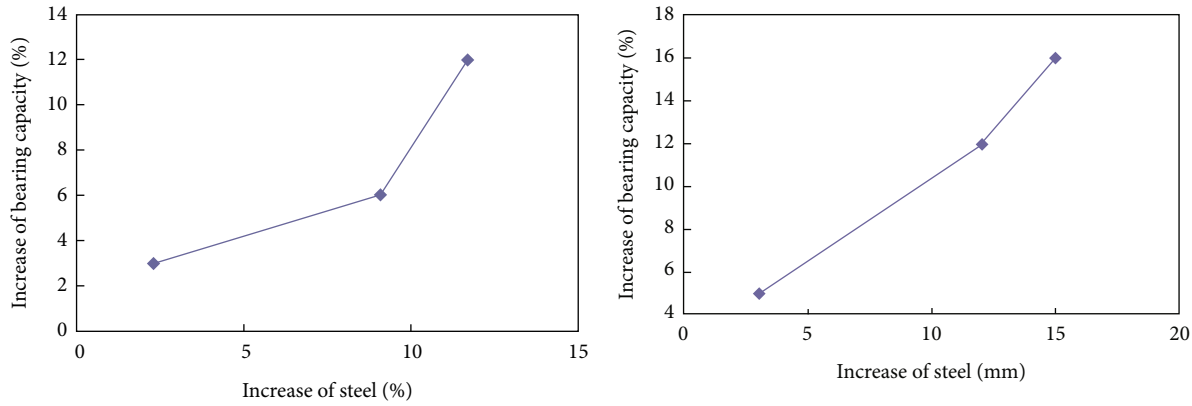

(a) Spacing from 100 mm to 75 mm

(b) Spacing from 75 mm to 50 mm

FIGURE 6: The influence between the change of steel and load bearing capacity.

It can be seen from Figure 6 that the influence of the increase of bearing capacity by the decrease in the bar spacing is more obvious than the increase of the bar diameter in the SCFST with the internal transverse stiffened bars column. In Figure 5(b), the changes of load capacity are more obvious when spacing from 75 to 50 mm. Therefore, in the practical application, the ultimate bearing capacity of SCFST columns can be improved by reducing the internal transverse bar spacing firstly when the same amount of steel is used.

3.4. Comparative Analysis of Transverse Strain. The transverse strain of three sections on all specimens is shown in Figure 7.

As seen from Figure 7, due to the confinement effect of transverse stiffened bars, transverse strain is smaller than that of the SCFST column; meanwhile, with the decrease of spacing of stiffened bars, transverse strain becomes smaller. The change of transverse strain affected by the diameter of the stiffened bar is not obvious, stiffened bars are confined to the core concrete in the steel tube, and the confinement effect of SCFST with internal transverse stiffened bars column is strengthened. The change trend of transverse strain on each section of the column is basically the same.

3.5. Comparison of Concrete Failure Forms inside the Square Steel Tube. In order to observe the failure of the steel pipe wall and the concrete, the outer steel plate was cut off after the test. It was found that the main form of failure of the concrete near the square steel pipe wall in the specimen was crushing (Figure 8). For the specimens without transverse stiffeners, the concrete collapse is serious. The concrete is crushed obviously at the outer drum of the outer steel plate; the cracks have extended to the inside of the core concrete, indicating that the specimens are damaged. But the concrete collapse in the square steel tube with transverse stiffeners is not obvious. Only a small number of concrete fragments are found falling off at the location of the transverse reinforcement. After removing the concrete on the outer surface, the size of the cracked area became smaller, indicating that the steel pipe and the concrete are reliably combined through the transverse steel bars. The restraining effect is obvious, and its bearing capacity has a certain degree of improvement.

4. Simplified Calculation Method

In order to facilitate the calculation and be easy to apply in practical engineering, the form of the formula should be simplified as far as possible. In the simplified formula proposed in this paper, the bearing capacity of concrete under the restraint of internal transverse reinforcing steel bar and square steel tube is taken as the basic calculation part, and the confinement factor of the transverse reinforcing steel bar and SCFST has been considered. A large number of studies show that the restraint effect of SCFST on the core area is an important factor to improve the bearing capacity of SCFST, so the confinement effect coefficient ξ is introduced. This coefficient is related to the strength of steel, the cross-sectional area of the steel tube, the strength of concrete, the cross-sectional area of core concrete, and so on. The calculation formula of ξ is shown in (4). With the unified theory based on the concrete-filled steel tube, Zhong [8] put forward a composite compressive strength design formula:

$$N_0 = \left(1.212 + B\xi + C\xi^2\right) f_{ck} A_{sc}, \tag{1}$$

where

$$B = 0.1759 \frac{f_{yk}}{235} + 0.974, \tag{2}$$

$$C = -0.1038 \frac{f_{yk}}{20} + 0.0309, \tag{3}$$

$$\xi = \frac{A_S / A_C}{f_y / f_c}, \tag{4}$$

$$A_{SC} = A_S + A_C. \tag{5}$$

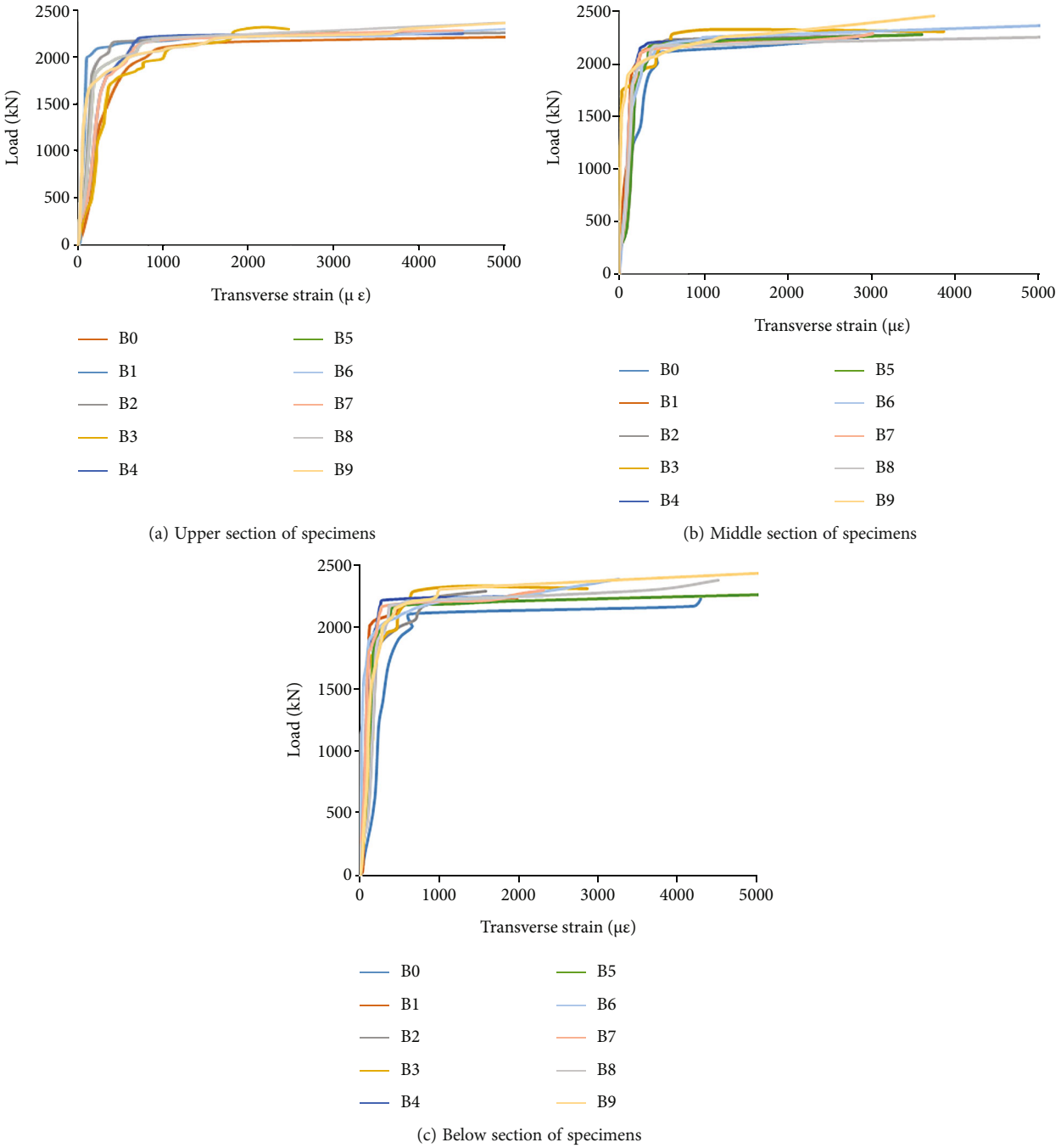

(a) Upper section of specimens

(b) Middle section of specimens

(c) Below section of specimens

Figure 7: Comparison of transverse strain of columns.

In this paper, according to the calculation model of the above formula, the axial bearing capacity of the SCFST column with internal transverse stiffened steel bars is calculated as follows:

$$N_0 = \left(A_1 + B_1\xi + C_1\xi^2\right) f_c A_{sc}. \tag{6}$$

Based on (6), the bearing capacity of the SCFST column with internal transverse stiffened steel bars can be calculated, as shown in Table 6, and the value of the test results and the test values of the bearing capacity of the test are calculated by the method of the two regressions:

$$\frac{N_0}{f_c A_{SC}} = A_1 + B_1\xi + C_1\xi^2. \tag{7}$$

The regression coefficient, $A_1 = 0.25$, $B_1 = 2.185$, $C_1 = -0.1987$, $R^2 = 0.96$.

(a) Damage of concrete in B0 (b) Damage of concrete in B4

Figure 8: Damage of concrete in square steel tubes B0 and B4.

Table 6: Comparison of bearing capacity between theory and test.

Specimen	ξ	Value of test N_1 (kN)	Value of calculation N_0 (kN)	N_0/N_1
B1	2.020	2177	2204	1.01
B2	2.040	2230	2220	1.00
B3	2.061	2270	2236	0.99
B4	2.071	2197	2244	1.02
B5	2.127	2310	2287	0.99
B6	2.170	2400	2320	0.97
B7	2.150	2240	2305	1.03
B8	2.245	2350	2376	1.01
B9	2.317	2440	2429	1.00

Substituting Formula (7),

$$N_0 = \left(0.25 + 2.185\xi - 0.1987\xi^2\right) f_c A_{sc}. \quad (8)$$

It should be noted that this paper analyzed the parameters of the range as follows.

Width thickness ratio $B/t = 33.3\text{-}50$, yield strength of steel $f_y = 235$ MPa, and compressive strength of concrete $f_c = 14.3$ MPa (concrete strength grade C30). By $\xi = A_s f_y/(A_c f_c) \approx 4t' f_y/(b f_c)$, the coefficient range is approximate to $\xi = 1.3 - 2.3$.

The bearing capacity of the specimens calculated by Formula (8) and the test piece pressure bearing capacity obtained from the experiment are recorded in Table 6.

From Table 6, the average value of N_0/N_1 is 1.0, the standard deviation of N_0/N_1 is 0.015, and the coefficient of variation of N_0/N_1 is 0.015. The test results are basically consistent with the calculation results, which can be used in engineering practice.

5. Conclusion

In this paper, the variation law of axial compression capacity of the SCFST column with internal transverse stiffened steel bars is studied. Through the comparison of test results, the correlation between column bearing capacity and steel quantity is analyzed, and the following conclusions are drawn:

(1) By adding transverse reinforcement, the constraint effect of steel tube wall on concrete is improved, and the local buckling of steel tube wall outward is effectively delayed, and the interaction between steel tube and core concrete is strengthened

(2) The existence of transverse reinforcement enhances the hoop sleeve effect and increases the bearing capacity of the SCFST column with internal transverse stiffened steel bars by 4.5~15%. At the same time, the strain of each cross-section of the SCFST column with internal transverse stiffened steel bars decreases and distributes more evenly along the height direction

(3) When the amount of steel used is the same, the bearing capacity of the new structure column can be improved more effectively by decreasing the spacing of transverse stiffeners than by increasing the diameter of reinforcement

(4) When the diameter of the steel bars is the same, the bearing capacity of the SCFST column with internal transverse stiffened steel bars increases significantly with the decrease of the spacing of the transverse steel bars; when the spacing of the transverse steel bars is the same, the bearing capacity of the SCFST column with internal transverse stiffened steel bars slightly increases with the increase of the diameter

(5) Based on the unified theory of SCFST, the simplified formula for calculating the pressure bearing capacity of the SCFST column with internal transverse stiffened steel bars is proposed

Data Availability

The data supporting the results of this study are available in the article.

Conflicts of Interest

The authors declare that there is no conflict of interest.

Authors' Contributions

Project administration was performed by Nan Li; methodology was performed by Nan Li and Yajun Xi; the test was performed by He Li and Guangxi Zhang; formal analysis was performed by Tao Ren and Xinhao Mu; investigation was performed by Nan Li; writing (original draft preparation) was performed by Nan Li; writing (review and editing) was performed by Nan Li. All authors have read and agreed to the published version of the manuscript.

Acknowledgments

This work was supported by the Technology Project of Shandong Province Construction Department of Urban and Rural Housing of China (grant numbers 2016KY028, 2018-K1-09, and 2018-R3-10) and the Scientific Research and Innovation Team Support Plan of Tai'an Campus of SDUST, China (grant number 2019TD01).

References

[1] L. H. Han and Y. F. Yang, *Modern concrete-filled steel tube technology*, China Construction Industry Press, 2004.

[2] S. T. Zhong, *High-Rise Concrete-Filled Steel Tube Structure*, Heilongjiang Science and Technology Press, Harbin, 1997.

[3] X. Li, H. Yang, J. Zhang, G. Qian, H. Yu, and J. Cai, "Time-domain analysis of tamper displacement during dynamic compaction based on automatic control," *Coatings*, vol. 11, no. 9, p. 1092, 2021.

[4] D. Xu, Q. Liu, Y. Qin, and B. Chen, "Analytical approach for crack identification of glass fiber reinforced polymer–sea sand concrete composite structures based on strain dissipations," *Structural Health Monitoring-An International Journal*, p. 147592172097429, 2020.

[5] N. Lu, H. Wang, K. Wang, and Y. Liu, "Maximum probabilistic and dynamic traffic load effects on short-to-medium span bridges," *Cmes-Computer Modeling in Engineering & Sciences*, vol. 127, no. 1, pp. 345–360, 2021.

[6] S. H. Cai, *Modern Concrete-Filled Steel Tube (First Edition)*, People's Communications Press, 2003.

[7] L. H. Han, *Steel Pipe Concrete Theory and Practice (2nd Edition)*, Science Press, Beijing, 2007.

[8] S. T. Zhong, *Steel Pipe Concrete (Third Edition)*, Tsinghua University Press, Beijing, 2003.

[9] Y. Luo, H. Zheng, H. Zhang, and Y. Liu, "Fatigue reliability evaluation of aging prestressed concrete bridge accounting for stochastic traffic loading and resistance degradation," *Advances in Structural Engineering*, vol. 24, no. 13, pp. 3021–3029, 2021.

[10] H. Huang, M. Huang, W. Zhang, M. Guo, and S. Pospisil, "Seismic performance of predamaged RC columns strengthened with HPFL and BSP under combined loadings," *Structure and Infrastructure Engineering*, vol. 203, p. 109871, 2020.

[11] W. Zhang and Z. Tang, "Numerical modeling of response of CFRP–concrete interfaces subjected to fatigue loading," *Journal of Composites for Construction*, vol. 25, no. 5, p. 04021043, 2021.

[12] C. Zhang, H. Kordestani, S. F. Masri, J. Wang, and L. Sun, "Data-driven system parameter change detection for a chain-like uncertainties embedded structure," *Structural Control & Health Monitoring*, vol. 28, no. 11, 2021.

[13] C. H. Kong and T. S. Moon, "Behavior of concrete-filled steel tubular beam-column under combined axial and lateral forces," in *Proceedings of the Fifth Pacific Structural Steel Conference*, pp. 961–966, Seoul, Korea, 1998.

[14] B. Uy, "Strength of concrete filled steel box columns incorporating local buckling," *Journal of Structural Engineering*, vol. 126, no. 3, pp. 341–352, 2000.

[15] K. A. S. Susantha, H. Ge, and T. Usami, "Uniaxial stress-strain relationship of concrete confined by various shaped steel tubes," *Engineering Structures*, vol. 23, no. 10, pp. 1331–1347, 2001.

[16] D. L. Liu, W. M. Gho, and J. Yuan, "Ultimate capacity of high-strength rectangular concrete-filled steel hollow section stub columns," *Journal of Constructional Steel Research*, vol. 59, no. 12, pp. 1499–1515, 2003.

[17] Q. Q. Liang, B. Uy, and J. Y. R. Liew, "Nonlinear analysis of concrete-filled thin-walled steel box columns with local buckling effects," *Journal of Constructional Steel Research*, vol. 62, no. 6, pp. 581–591, 2006.

[18] M. Dundu, "Column buckling tests of hot-rolled concrete filled square hollow sections of mild to high strength steel," *Engineering Structures*, vol. 127, pp. 73–85, 2016.

[19] X. H. Dai and D. Lam, "Shape effect on the behaviour of axially loaded concrete filled steel tubular stub columns at elevated temperature," *Journal of Constructional Steel Research*, vol. 73, pp. 117–127, 2012.

[20] B. Evirgen, A. Tuncan, and K. Taskin, "Structural behavior of concrete filled steel tubular sections (CFT/CFSt) under axial compression," *Thin-Walled Structures*, vol. 80, pp. 46–56, 2014.

[21] E. Ellobody and B. Young, "Design and behaviour of concrete-filled cold-formed stainless steel tube columns," *Engineering Structures*, vol. 28, no. 5, pp. 716–728, 2006.

[22] A. Raed, H. S. Ahmad, and Y. M. Hunaiti, "Experimental studies on the behavior of concrete-filled steel tubes incorporating crumb rubber," *Journal of Constructional Steel Research*, vol. 122, pp. 251–260, 2016.

[23] M. S. Alfarabi, M. A. M. Galal, and A. A. O. Mohammed, "Behavior of circular stainless steel stub columns internally strengthened by longitudinal carbon steel bars," *Engineering Structures*, vol. 199, p. 109617, 2019.

[24] Y. Fang, "Effect of stiffeners on the eccentric compression behaviour of square concrete-filled steel tubular columns," *Thin-Walled Structures*, vol. 135, pp. 196–209, 2019.

[25] S. K. Alrebeh, "Structural performance of short concrete-filled steel tube columns with external and internal stiffening under axial compression," *Structure*, vol. 20, pp. 702–716, 2019.

[26] G. C. Li, Z. C. Zhan, Z. J. Yang, C. Fang, and Y. Yang, "Behavior of concrete-filled square steel tubular stub columns stiffened with encased I-section CFRP profile under biaxial bending," *Journal of Constructional Steel Research*, vol. 169, p. 106065, 2020.

[27] F. Alatshan, S. A. Osman, R. Hamid, and F. Mashiri, "Stiffened concrete-filled steel tubes: a systematic review," *Thin-Walled Structures*, vol. 148, p. 106590, 2020.

[28] W. Q. Zhu, Z. P. Mo, Y. J. Liu, and Y. Cui, "Tensile behavior and load transfer mechanism of concrete-filled square steel tube exterior-diaphragm connections stiffened with PBL," *Engineering Structures*, vol. 231, p. 111780, 2021.

[29] N. Li, L. Wang, Y. Xi et al., "The experimental research on axial compression performance of concrete-filled steel square tube strengthened by internal transverse stiffened bars," *Functional Materials*, vol. 24, no. 3, pp. 005–433, 2017.

Hindawi
Scanning
Volume 2022, Article ID 4188727, 12 pages
https://doi.org/10.1155/2022/4188727

Research Article

Study on the Phase Equilibria of the Fe-Al-Ni-O System at 750°C

Meng Du,[1] Haifeng Mei,[2,3] and Ya Liu [2,3]

[1]*College of Vehicle Engineering, Changzhou Vocational Institute of Mechatronic Technology, Changzhou 213164, China*
[2]*School of Materials Science and Engineering, Changzhou University, Changzhou 213164, China*
[3]*Jiangsu Key Laboratory of Materials Surface Science and Technology, Changzhou University, Changzhou 213164, China*

Correspondence should be addressed to Ya Liu; yliu@cczu.edu.cn

Received 15 October 2021; Accepted 14 December 2021; Published 15 January 2022

Academic Editor: Jian Chen

Phase equilibria of the Fe-Al-Ni-O system at 750°C were determined by scanning electron microscopy coupled with energy-dispersive X-ray spectrometer and X-ray power diffraction. 54 alloys were prepared with weighted metal and Ni_2O_3 powder and were annealed at 750°C for 45 days. Two four-phase equilibrium regions and three three-phase equilibrium regions were confirmed, and the boundary between spinel and corundum was obtained. Comparing with the Fe-Al-Ni-O oxidation diagram at 750°C calculated with FSstel and FToxid databases, the phase boundary of the spinel and corundum oxides from experiments was inclined to the Ni-Al side. The determined relationship between primary oxides and alloy composition in this work can be used as a reference for the preparation of the oxide film by selective oxidation.

1. Introduction

Corrosion is one of the major problems hindering the development and industrial application of steel. Anticorrosion surface protective layer has been prepared not only by dipping, infiltrating, or injecting more than one kind of anticorrosion element or compound on the surface of metal material but also by high-temperature preoxidation treatment [1–6]. If enough Cr, Al, Si, and Ti are added into the alloy, oxide film such as Cr_2O_3, Al_2O_3, SiO_2, and spinel will be formed. These oxides have less defects, compactness, good adhesion, and high temperature stability, which can effectively prevent corrosion and protect the alloy [1, 4, 5, 7].

Under the condition of high temperature and low oxygen pressure, the main elements (Fe, Ni, and Co) of the alloy will not be oxidized, but the elements (Cr, Al, Si, and Ti) with high affinity to oxygen in the alloy are easy to be oxidized according to the Ellingham diagram [8]. Selective oxidation promotes the enrichment of alloy elements to the surface, and only a small amount of alloy elements can form a complete and dense oxide film [3–7], so the addition of alloy elements is greatly reduced, which makes the design of materials more flexible.

Alloy composition has a great influence on oxidation. There are many studies on the oxidation and wettability of Fe-Ni-based alloys and the oxidation behavior of other alloys in air in the literature [9–11]. However, there are few systematic studies on the influence of alloy composition change on the oxidation process at low oxygen pressure based on the development of anticorrosion oxide film. The relationship between primary oxide and alloy composition is called primary oxidation phase diagram, which is an important basis for understanding the effect of alloy composition change on oxidation process. Our research group has carried out some work in this area [12, 13].

Rhamdhani et al. [14] had researched the subsolidus phase equilibrium of Fe-Al-Ni-O system in air. Raghavan [15] had also discussed equilibria of oxide phases at high temperature in the atmosphere. However, there are relatively few researches on the phase equilibrium of the Fe-Al-Ni-O system under the circumstance of low oxygen content. In this paper, the phase relationship of the Fe-Al-Ni-O system at 750°C was determined by thermodynamic calculation and experiments, which would be helpful to explain the selective oxidation of iron-based or nickel-based alloys with Al addition.

Table 1: Crystal structure data for the matrix phases and oxides in the Fe-Al-Ni-O system.

Phase	Pearson symbol	Space group	Lattice parameters (nm)			PDF no.
			a	*b*	*c*	
α-Fe	*cI2*	*Im3m*	2.866	2.866	2.866	06-0696
γ-(Fe,Ni)	*cI2*	*Im3m*	2.868	2.868	2.868	37-0474
γ-(Fe,Ni)	*cF4*	*Fm3m*	3.598	3.598	3.598	47-1417
β-FeAl	*cP2*	*Pm3m*	2.881	2.881	2.881	33-0020
β-NiAl	*cP2*	*Pm3m*	2.910	2.910	2.910	65-5171
β-$AlFe_{0.23}Ni_{0.77}$	*cP2*	*Pm3m*	2.885	2.885	2.885	47-1126
γ'-Ni_3Al	*cP4*	*Pm3m*	3.572	3.572	3.572	65-6613
$NiAl_3$	*oP16*	*Parma*	6.598	7.352	4.802	02-0416
Ni_2Al_3	*hP5*	*P3m1*	4.036	4.036	4.900	65-3454
Fe_4Al_{13}	*mC102*	*C2/m*	15.492	8.078	12.471	50-0797
Fe_2Al_5	*oC14*	*Cmcm*	7.649	6.413	4.216	47-1435
$FeAl_2$	*aP18*	*P1*	4.878	6.461	8.748	33-0019
$FeAl_9Ni$	*mp22*	$P2_1/c$	8.598	6.271	6.207	[16]
$Fe_3Al_{10}Ni$	*hP28*	$P6_3/mmc$	_	_	_	[16]
Al_2O_3 (corundum structure)	*hR10*	*R3C*	4.758	4.758	12.991	10-0173
Fe_2O_3 (corundum structure)	*hR10*	*R3C*	5.036	5.036	13.749	33-0664
Ni_2O_3 (corundum structure)	*hp10*	*P*	4.610	4.610	5.610	14-0481
$FeAlO_3$ (corundum structure)	*oP40*	*Pc21n*(33)	8.566	9.249	4.989	30-0024
$FeAl_2O_4$ (spinel structure)	*cF56*	*Fd3m*	8.153	8.153	8.153	34-0192
$NiAl_2O_4$ (spinel structure)	*cF56*	*Fd3m*	8.048	8.048	8.048	10-0339
Fe_3O_4 (spinel structure)	*cF56*	*Fd3m*	8.090	8.090	8.090	65-3107
$NiFe_2O_4$ (spinel structure)	*cF56*	*Fd3m*	8.337	8.337	8.337	54-0964
FeO (NaCl structure)	*cF8*	*Fm3m*	4.293	4.293	4.293	46-1312
NiO (NaCl structure)	*cF8*	*Fm3m*	4.177	4.177	4.177	47-1049

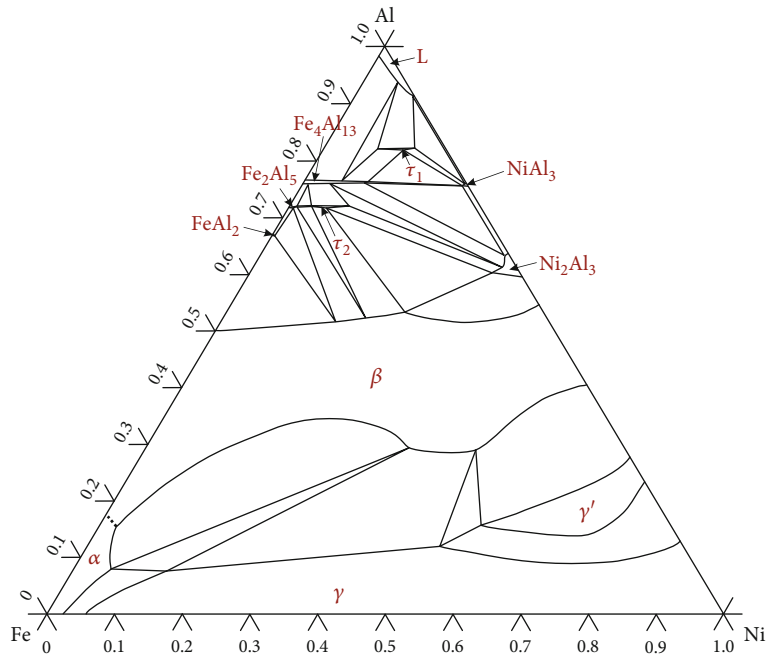

Figure 1: The calculated 750°C isothermal section of the Fe-Al-Ni ternary system.

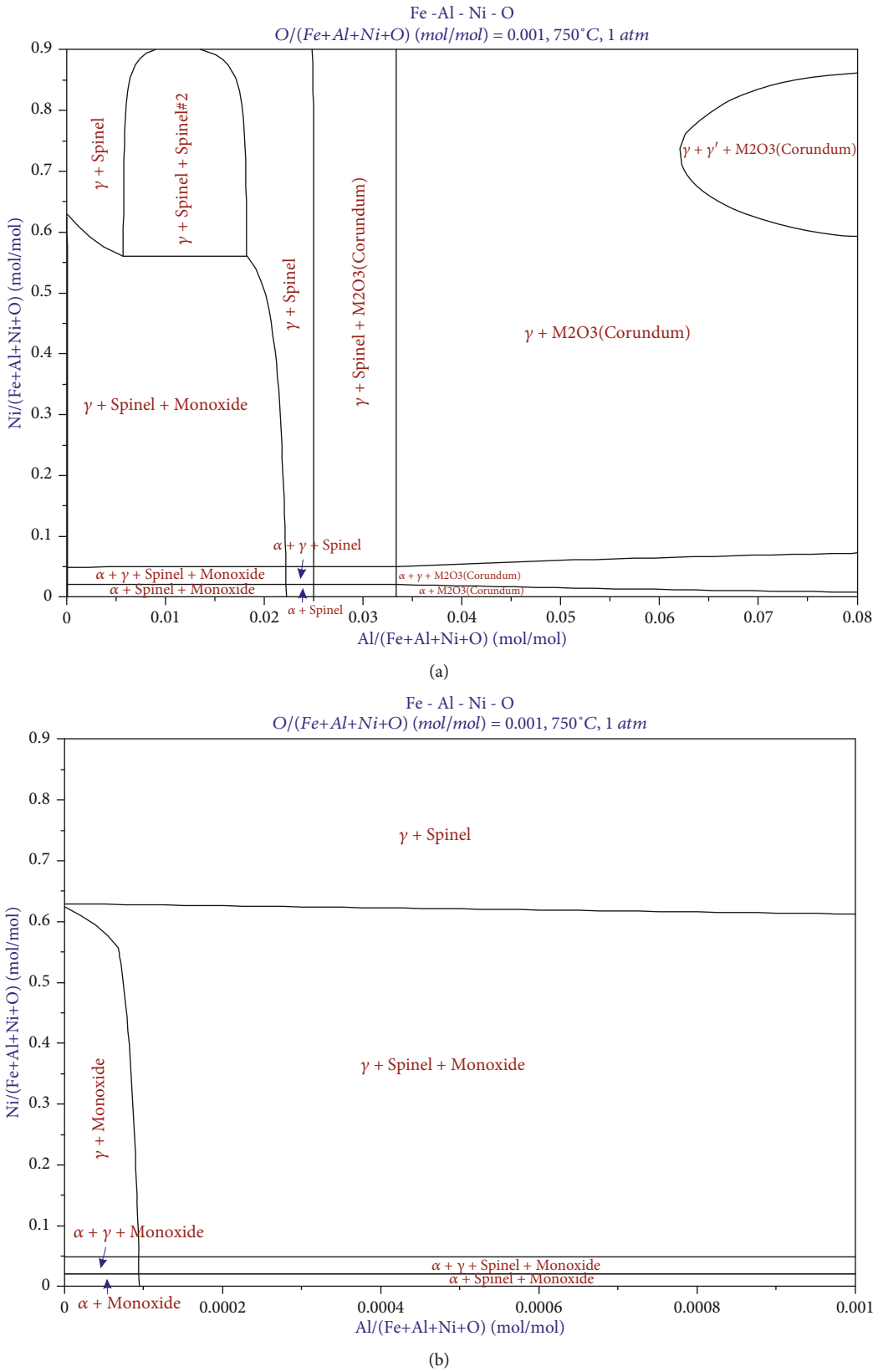

Figure 2: The calculated isothermal section of Fe-Al-Ni-O system at 750°C: (a) Al content ranges from 0 to 8 at.%; (b) Al content ranges from 0 to 0.1 at.%.

2. Literature Data

The four constituting ternaries of the Fe-Al-Ni-O quaternary are the Fe-Al-Ni, Fe-Al-O, Fe-Ni-O, and Al-Ni-O systems. Crystal structure data for the matrix phases and oxides in the Fe-Al-Ni-O system is summarized in Table 1.

2.1. The Fe-Al-Ni Ternary System. The Fe-Al-Ni ternary system has been studied experimentally, evaluated thermodynamically, reviewed, and updated many times. The most recent review was published by Raghavan [17] in 2010, in which the work from Zhang and Du [18] was presented. The isothermal section of the Fe-Al-Ni ternary system at 750°C shown in Figure 1 was redrawn based on thermodynamic description from Zhang and Du [18]. There are four solid solution phases (namely, α, β, γ, and γ'), five binary intermetallic compounds ($FeAl_2$, Fe_2Al_5, Fe_4Al_{13}, $NiAl_3$, and Ni_2Al_3), and two ternary intermetallic compounds (τ_1 and τ_2) included in this isothermal section.

2.2. The Fe-Al-O System. Raghavan reviewed the Fe-Al-O system twice. The recent article in 2010 presented the Al-Fe-O pseudobinary section in air along the Fe_2O_3-Al_2O_3 join [19]. Since then, Lindwall et al. [20] and Shishin et al. [21] assessed this system thermodynamically in 2015 and 2016, respectively. The following oxidation phases, corundum (Al_2O_3 and Fe_2O_3), wustite (FeO), magnetite (Fe_3O_4), and spinel ($FeAl_2O_4$), were included in the Al-Fe-O system.

2.3. The Fe-Ni-O System. Raghavan [22] reviewed the research results on the Fe-Ni-O system. In addition to the calculated Fe-Ni-O isothermal section at 1540°C by Luoma [23], this review had also presented Fe-Ni-O pseudobinary section along the Fe_2O_3-NiO join in air and the Fe-Ni-O isothermal phase diagram at low oxygen partial pressure between 1000°C and 1200°C [24]. $NiFe_2O_4$, NiO, FeO, Fe_2O_3, and Fe_3O_4 oxidation phases were evidenced in these isothermal sections.

2.4. The Al-Ni-O System. As early as 1981, Elrefaie and Smeltzer [25] determined the equilibrium oxygen pressure of Ni-NiO-$NiAl_2O_4$ and Ni-$NiAl_{2.54}O_{4.81}$-Al_2O_3 systems between 850°C and 1050°C by EMF method; Saltykov et al. [26] thermodynamically evaluated the Ni-Al-O system. Al_2O_3, $NiAl_2O_4$, NiO, Ni_2O_3, and Ni_3O_4 were stable in the 940°C isothermal section of the Al-Ni-O system. However, there are few reports on the phase equilibrium of the Ni-Al-O system since then, probably due to the low oxygen partial pressure.

2.5. The Fe-Al-Ni-O System. Information on the phase equilibrium of the Fe-Al-Ni-O system is scary, except for the results reported by Rhamdhani et al. [14] and Kjellqvist et al. [27]. Three three-phase equilibria of spinel+corundum+hematite, spinel+corundum+$Fe_2Al_2O_6$, and spinel+hematite+$Fe_2Al_2O_6$ were found in the system between 1200°C and 1400°C.

Table 2: Nominal compositions (at.%) of typical specimens in this study.

No.	Al	Fe	Ni	No.	Al	Fe	Ni
A1	12	86	2	B1	10	88	2
A2	11	84	5	B2	9	86	5
A3	10	75	15	B3	8	77	15
A4	9	66	25	B4	7	68	25
A5	8	57	35	B5	6	59	35
A6	6	49	45	B6	4	51	45
A7	5	35	60	B7	3	37	60
A8	4	16	80	B8	3	17	80

Table 3: Constitution of the corundum and matrix phases coexisting in the Fe-Al-Ni-O system at 750°C.

No.	Substrate				Oxides				
	Al	Fe	Ni	Matrix phases	O	Al	Fe	Ni	Oxide phases
A1	10.8	86.9	2.3	α	58.4	36.5	1.4	3.7	Corundum
A2	10.7	85.2	4.1	α	59.9	36.2	1.5	2.4	Corundum
	37.8	41.0	21.2	β					
A3	8.9	85.2	5.9	α	60.6	35.8	1.7	1.9	Corundum
	32.3	30.2	37.5	β					
	8.6	76.1	15.3	γ					
A4	31.3	30.8	37.9	β	56.7	36.9	2.3	4.1	Corundum
	8.4	66.4	25.2	γ					
A5	7.6	54.9	37.5	γ	57.9	36.4	2.2	3.5	Corundum
A6	5.7	49.5	44.8	γ	59.5	37.1	0.3	3.1	Corundum
A7	4.1	35.1	60.8	γ	56.2	37.0	1.4	5.4	Corundum
A8	3.7	17.4	78.9	γ	61.2	35.0	0.3	3.5	Corundum

3. Thermodynamic Calculation

In order to have a preliminary understanding of the Fe-Al-Ni-O system and provide a basis for the composition design of the experimental alloys, phase relationship of this system was calculated by using FactSage thermochemical software coupled with FSstel and FToxid databases. In the thermochemical calculation, considering that the oxygen partial pressure of the alloy was extremely low, oxygen content was set extremely low (0.1 at.%), and then, phase relationships of oxidation phase with Al and Ni content were simulated. The results are shown in Figure 2. The oxide coexisting with the matrix alloy phases (γ, α+γ, or α) varies with the Al content. Single oxide, monoxide, spinel, and corundum, is in equilibrium with the alloy phases when Al content lies in the ranges of 0~0.01 at.%, 2.2%~2.5 at.%, and more than 3.3 at.%, respectively. Two oxides, spinel and corundum, coexist with the alloy phases when the Al content varies between 2.5 at.% and 3.3 at.%. And monoxide and spinel are in equilibrium with the alloy phases when the Al content is between 0.01 and 2.2 at.%.

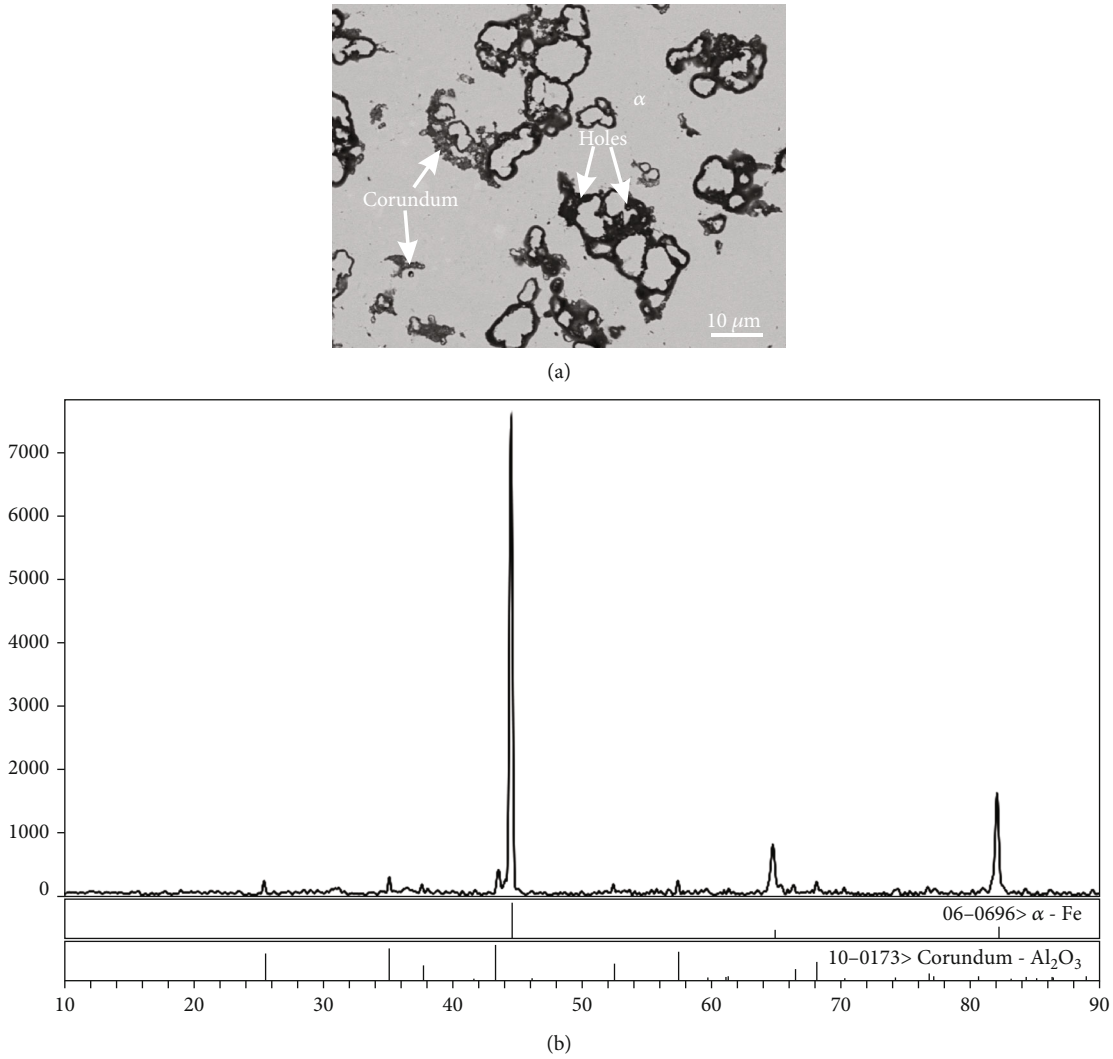

Figure 3: (a) BSE image and (b) XRD pattern of alloy A1 showing the coexistence of the α and corundum phases.

4. Experimental Procedure

According to the calculated the Fe-Al-Ni-O phase diagram, a series of alloys with Al content less than 5 at.% were prepared to study the oxide boundary; some alloys were added according to the experimental results. 54 Fe-Al-Ni-O specimens in all with the aggregate of 1 g in each were prepared from the Fe powders, Al powders, Ni powders, and Ni_2O_3 powders (>99.99%, mass fraction). In this work, the oxygen partial pressure was provided by adding Ni_2O_3 (0.02 g) to the sample. Agate mortar was used to mix and grind raw materials evenly to ensure their direct contact. Then, the raw materials were pressed into pieces by a tablet press. After that, the sample was sealed in a corundum crucible and stored in a silicon tube. Then, the silica tube was evacuated and flushed with Ar several times and finally sealed under vacuum. All samples were annealed at 750°C and kept for 45 days. During the annealing process, the Ni_2O_3 powders reacted with metal powders to reach the equilibrium between alloy and oxides. In fact, the equilibrium oxygen partial pressure of each sample was different, and the time required for the alloy-oxide system to reach equilibrium was determined by many attempts. It was found that annealing for 45 days could make the sample reach equilibrium. Finally, the samples were rapidly quenched into cold water.

A JSM-6510 scanning electron microscope (SEM) equipped with an Oxford INCA energy-dispersive X-ray spectroscope (EDS) was used to carry out detailed metallographic examination and composition analyses of the unetched samples. The compositions reported here were the average of at least five measurements. In addition, X-ray diffraction analysis of some critical alloys was carried out by using a D/max 2500 PC X-ray diffractometer with Cu K radiation and a step increase of 0.02° in the 2θ angle. Si powders were used as external calibrated standard. The XRD patterns were indexed and calculated by Jade software package.

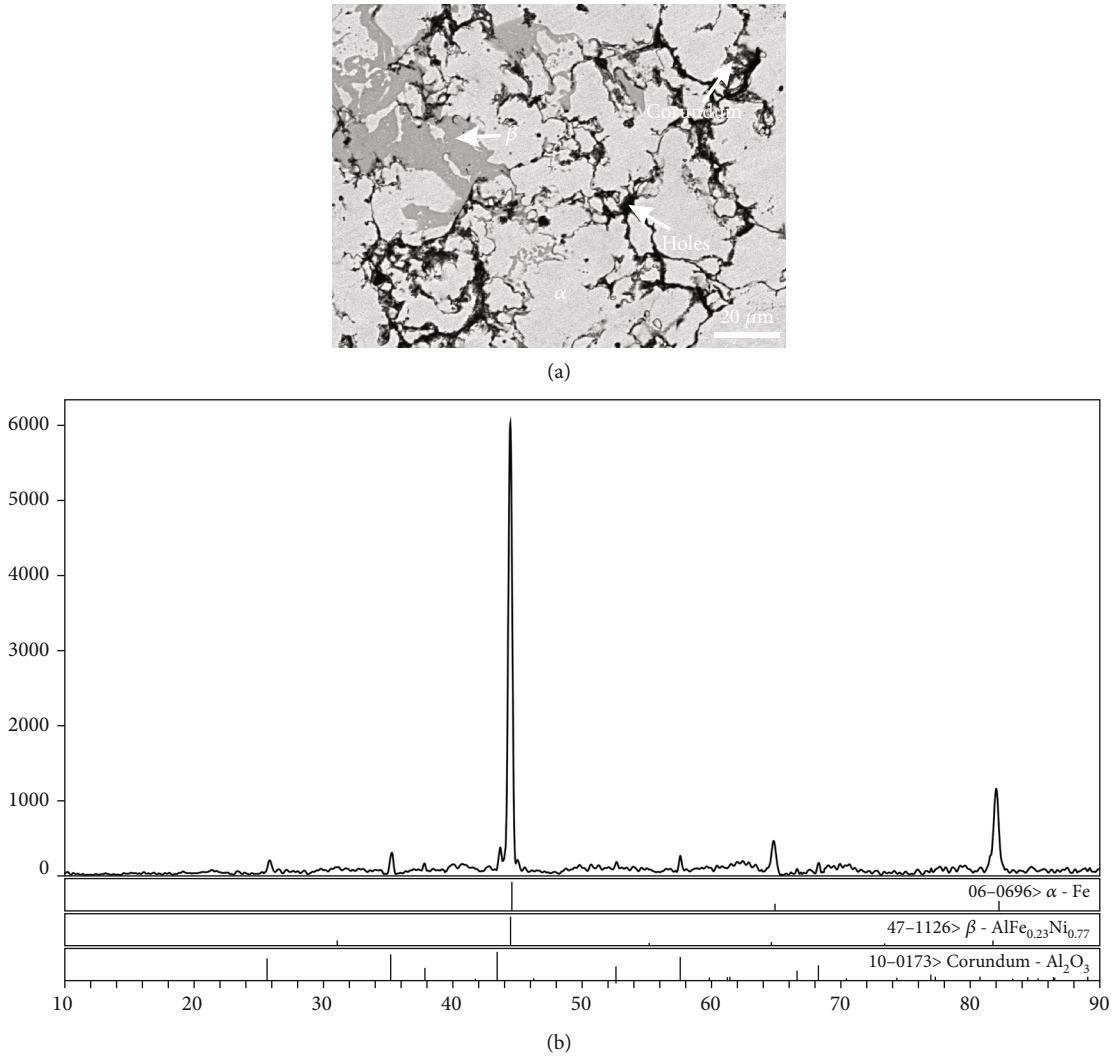

Figure 4: The α, β, and corundum phases coexisting in alloy A2: (a) BSE image and (b) XRD pattern.

5. Result and Discussion

After annealing at 750°C for 45 days, all oxides and corresponding matrix alloy phases observed in the specimens were analyzed. Sixteen key alloys (A1-A8, B1-B8) close to the boundary of corundum and spinel in the 750°C isothermal section of the Fe-Al-Ni-O system were selected. Nominal compositions of these selected specimens are listed in Table 2. According to the oxide phases summarized in Table 1, the corundum oxide phase can be Al_2O_3, Fe_2O_3, and other oxides, and the spinel oxide phase can be Fe_3O_4, $FeAl_2O_4$, $NiAl_2O_4$, and $NiFe_2O_4$. Therefore, spinel can be represented by chemical formula (Fe, Ni) $(Al, Fe)_2O_4$.

5.1. Corundum. The corundum and corresponding matrix phases in alloys A1-A8 identified by a combination of XRD and SEM-EDS are summarized in Table 3. As shown in Figure 3(a), the back-scattered electron (BSE) image of the alloy A1 proved that corundum can be in equilibrium with α matrix. The solubility of Fe and Ni in corundum was 1.4 and 3.7 at.%, respectively. The corresponding XRD patterns of the alloy A1 are shown in Figure 3(b). According to SEM and EDS analyses, the black areas in Figure 3(a) were confirmed as holes.

Figure 4(a) shows the BSE image of alloy A2. The light-grey area represents the α phase, the dark-grey area stands for the β phase, and the less dense area entrapped round holes are the corundum phase. The XRD pattern is shown in Figure 4(b), in which the characteristic peaks of α, β, and corundum phases are obvious.

Alloy A3 is in the region of four phases, α, β, γ, and corundum, as shown in Figure 5(a), in which the dark grey phase containing 32.3 at.% Al, 30.2 at.% Fe, and 37.5 at.% Ni is the β phase. Although the Al content in the α phase (8.9 at.% Al, 85.2 at.% Fe, and 5.9 at.% Ni) gets close to that in the γ phase (8.6 at.% Al, 76.1 at.% Fe, and 15.3 at.% Ni), the α and γ phases can be distinguished by changing contrast and brightness. As shown in Figure 5(b), characteristic

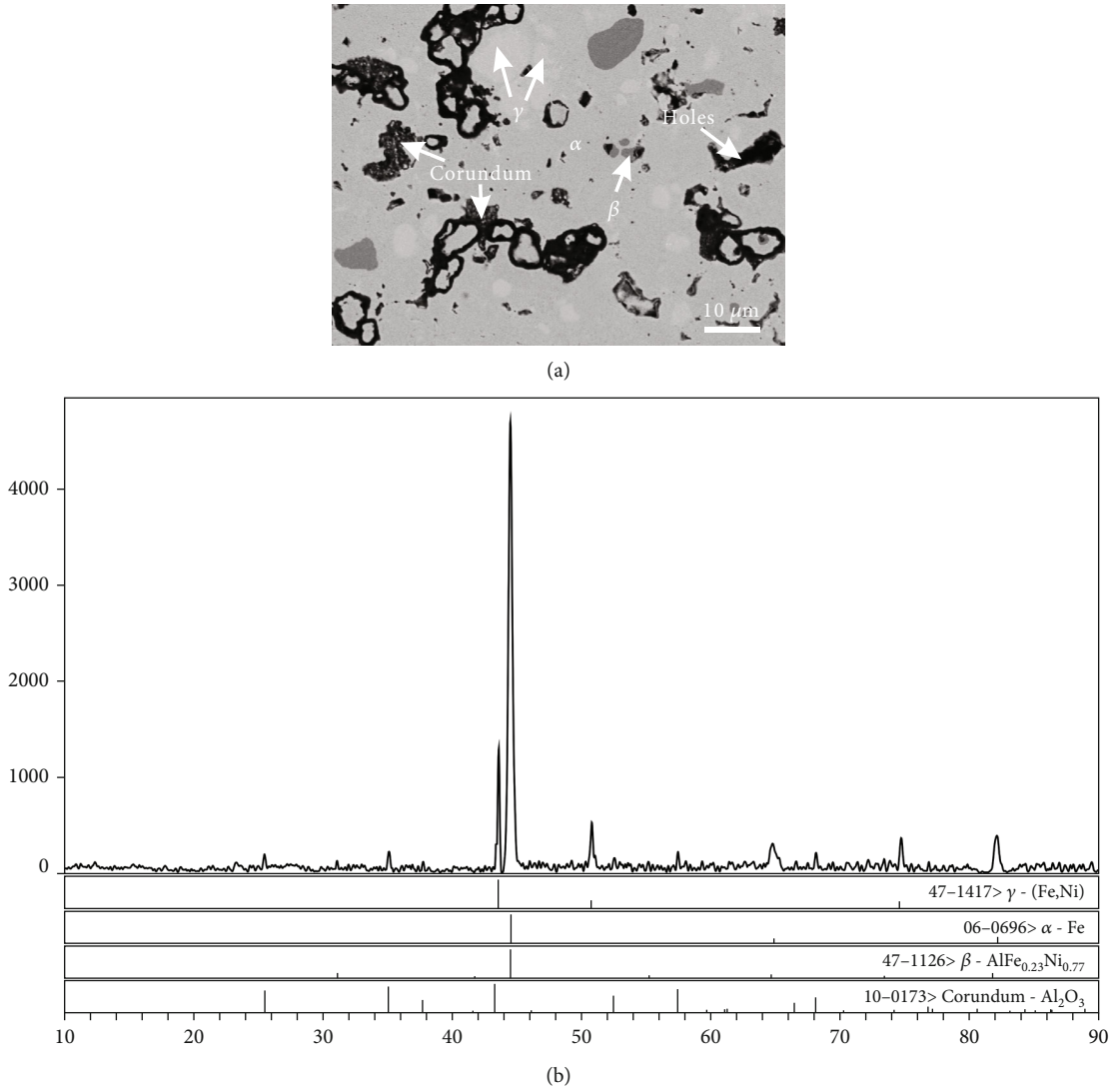

Figure 5: The α, β, γ, and corundum phases coexisting in alloy A3: (a) BSE image and (b) XRD pattern.

peaks of both α and γ are evidenced in the XRD patterns of alloy A3.

As seen from Figure 6(a), three-phase equilibrium between β, γ, and corundum was found in alloy A4. As the average atomic weight of the γ phase (Al: 8.4 at.%; Fe: 66.4 at.%; Ni: 25.2 at.%) is more than that of the β phase (Al: 31.3 at.%; Fe: 30.8 at.%; Ni: 37.9 at.%), the light grey phase is γ and the dark grey phase is β based on the image contrast. And the porous corundum phase is situated around the boundary of holes. Three-phase equilibrium of the above three phases in alloy A4 was confirmed by XRD patterns in Figure 6(b). It is worth mentioning that although the crystal structure types of the β phase in alloys A2, A3, and A4 are the same, the selected PDFs are different due to the varied solubility of elements and the change of lattice constants. The same is true for the γ phase in alloys A3 and A4.

The phase equilibrium between γ and corundum has been evidenced in alloys A5 to A8. As shown in Figure 7(a), in which the grey matrix phase is the γ phase, the dark grey phase located around the boundary of holes is the corundum phase according to the EDS analysis. The XRD patterns are shown in Figure 7(b), in which the characteristic peaks of the above two phases are proved. Based on the analyses of EDS and XRD patterns, corundum is mainly Al_2O_3.

In the Fe-Al-Ni system, Al has a stronger affinity for oxygen than Fe and Ni, and Al_2O_3 has the largest negative value for Gibbs free energy of formation than FeO and $FeAl_2O_4$, so Al_2O_3 is the most stable oxide in the Fe-Al-Ni-O system at low oxygen pressure. According to selective oxidation theory of Wagner [28, 29], when the Al concentration is lower than a critical value for the transformation from internal oxidation to external oxidation, Al_2O_3 will be formed in the subsurface layer of the specimen. Meanwhile, the Pilling-Bedworth ratio of Al_2O_3 is 1.29 [30], indicating a higher volume of the oxide than the volume of the metal, so there will be large stress produced during oxide's formation.

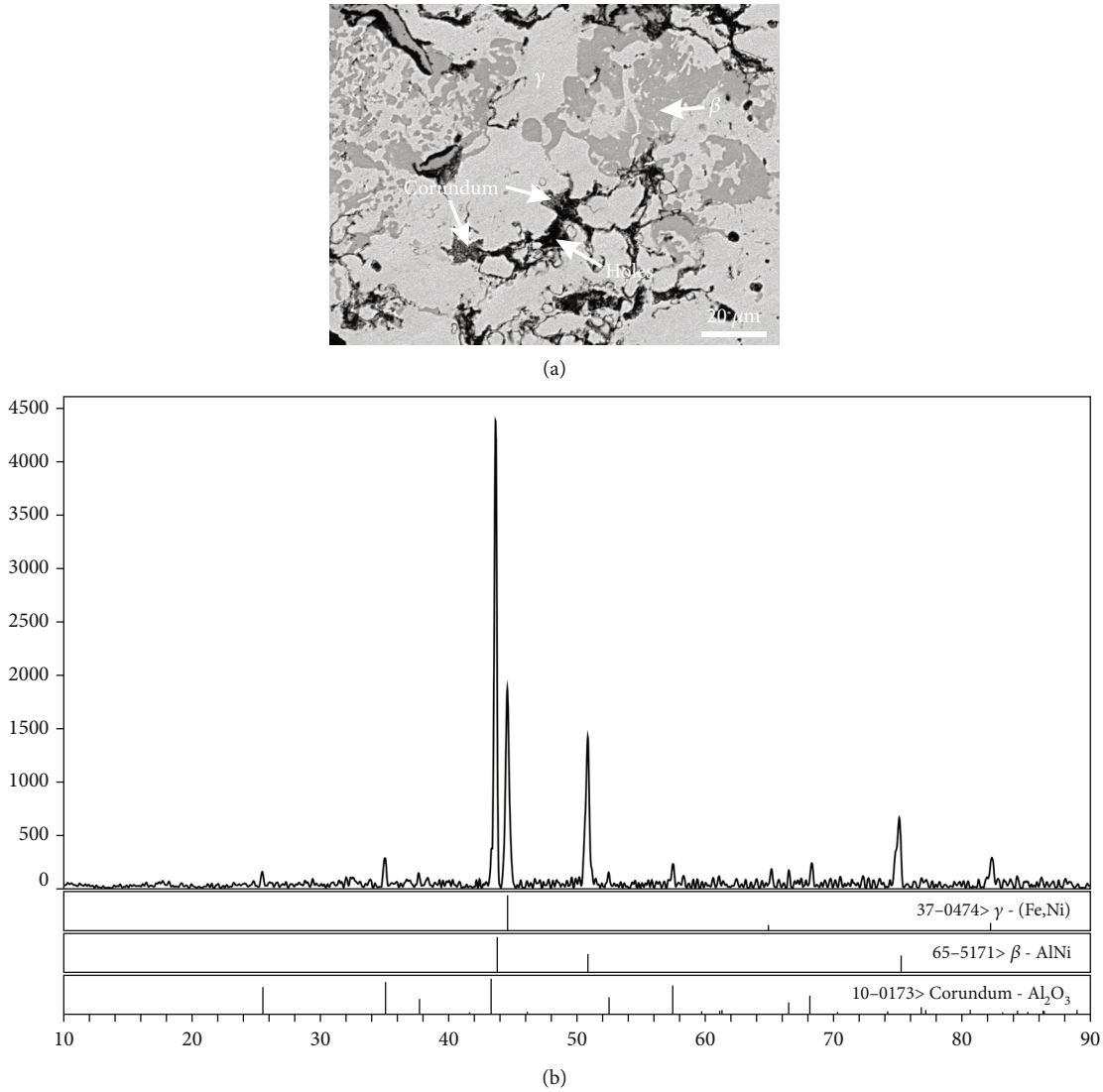

Figure 6: (a) BSE image and (b) XRD pattern of alloy A4 revealing that the β, γ, and corundum phases were in equilibrium.

That is account for why the corundum phase always locates around the boundary of holes.

5.2. Spinel. Table 4 shows the oxide phase spinel and the corresponding matrix phases detected in alloys B1-B8. Figure 8(a) is the BSE micrographs of the alloy B1. The matrix phase α is the same as above in Figure 3(a), and there are fine oxide particles around the grain boundary of the α phase. As the amount of these fine particles is low, it is difficult to identify them by XRD. However, the EDS pattern shown in Figure 8(b) suggests that it is the spinel phase. As being shown in Figure 9(a), the alloy B2 is located in the region of three phases, α, β, and spinel. BSE image shown in Figure 9(b) illustrates that the alloy B3 lies in the four-phase region, α, β, γ, and spinel. As same as that in the alloy B1, the spinel phase in B2-B3 was also determined based on EDS patterns. SEM-EDS analysis indicates that the alloys B4-B8 locate in the same two-phase region: γ and spinel. Typical micrograph of the alloy B6 is shown in Figure 10(a), and EDS patterns of the spinel phase are shown in Figure 10(b). By comparing Figure 10(b) with Figure 8(b), it can be found that the characteristic peaks of Ni in Figure 10(b) are much more obvious, indicating Ni content in the spinel phase in the alloy B6 is higher than that in the alloy B1.

5.3. Discussion. According to the experimental results analyzed above, the 750°C isothermal section of the Fe-Al-Ni-O system is constructed in a combination of the calculated Fe-Al-Ni phase diagram and experimentally detected oxide boundary between corundum and spinel. This isothermal section, also named primary oxide phase diagram of the Fe-Al-Ni-O system at 750°C, is shown in Figure 11. The following 9 regions are confirmed: (1) α+corundum, (2) α+β+corundum, (3) α+β+γ+corundum, (4) β+γ+corundum, (5) γ+corundum, (6) α+spinel, (7) α+β+spinel, (8)

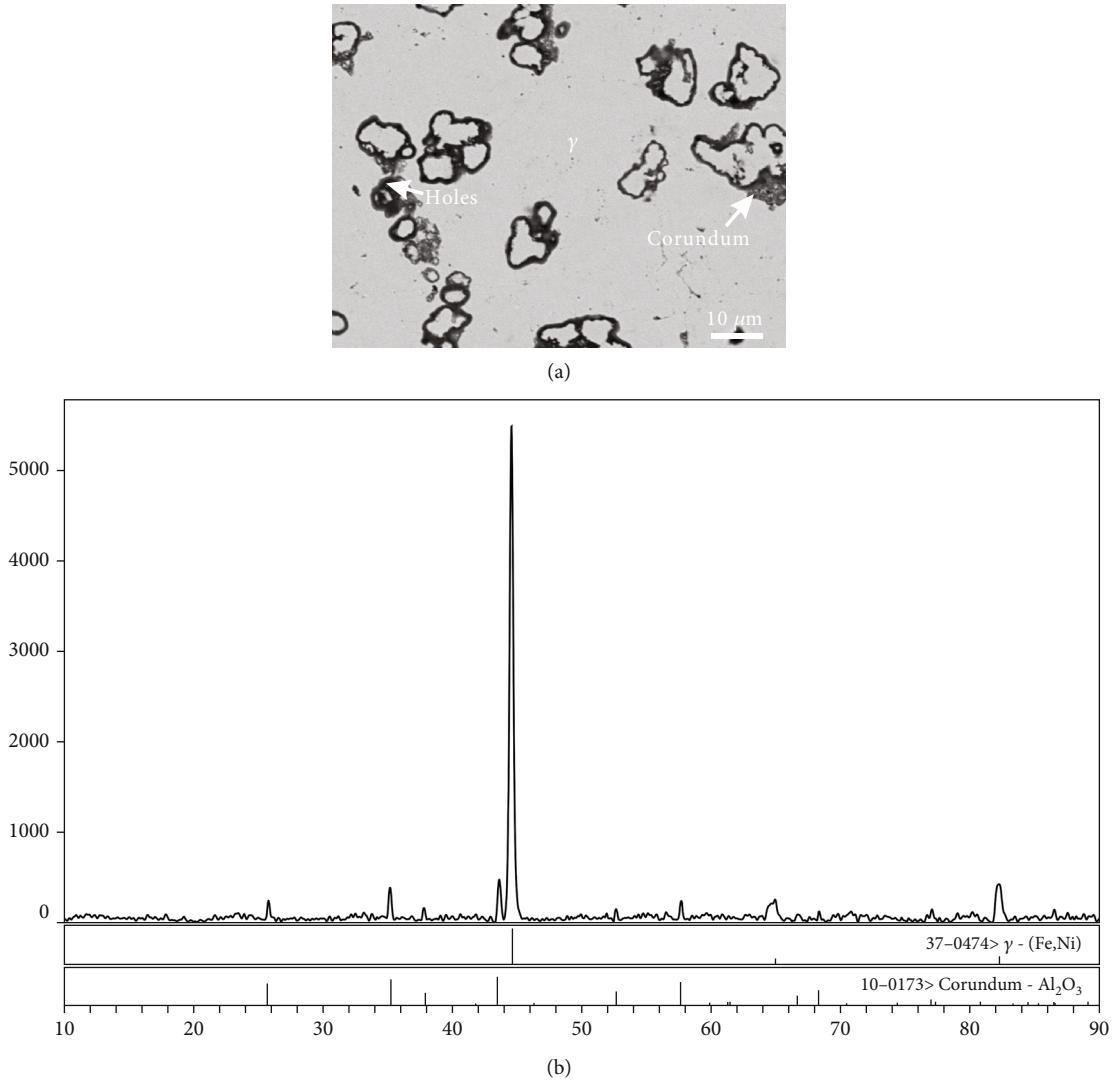

Figure 7: The γ and corundum phases were in equilibrium in alloy A5: (a) BSE image and (b) XRD pattern.

Table 4: Constitution of the spinel and matrix phases coexisting in the Fe-Al-Ni-O system at 750°C.

No.	Substrate				Oxides				
	Al	Fe	Ni	Matrix phases	O	Al	Fe	Ni	Oxide phases
B1	9.8	88.1	2.1	α	57.3	29.4	12.7	0.6	Spinel
B2	8.8	86.6	4.6	α	58.3	27.8	12.1	1.8	Spinel
	36.9	39.8	23.3	β					
B3	7.5	86.4	6.1	α	57.0	27.8	11.1	4.1	Spinel
	31.2	31.1	37.7	β					
	8.2	76.1	15.7	γ					
B4	6.8	68.6	24.6	γ	56.0	26.9	10.9	6.2	Spinel
B5	5.5	58.9	35.6	γ	56.5	25.6	10.7	7.2	Spinel
B6	3.7	52.1	44.2	γ	54.9	26.1	10.0	9.0	Spinel
B7	2.8	38.3	58.9	γ	54.7	27.1	10.1	8.1	Spinel
B8	2.7	19.5	77.8	γ	56.8	24.9	9.8	8.5	Spinel

α+β+γ+spinel, and (9) γ+spinel. The boundary between corundum and spinel measured by experiment is represented by a red line, and the calculated boundary is represented by a purple line. Red-dot lines are tie lines of the matrix alloy phases coexisting with corundum, and blue-dot lines are tie lines of the matrix alloy phases coexisting with spinel. It is worth mentioning that there should be a region where corundum and spinel coexist with the matrix alloy phase, for example, γ+corundum+spinel three-phase region in Figure 2(a). However, because the amount of oxide is too small to be analyzed by XRD, and the composition range for this region is limited; only the boundary between corundum and spinel is indicated in this study. Compared with the calculated results, the oxide phase boundary obtained in this experiment obviously moves to the Ni-Al side. When the Fe content is high, the experimental boundary offsets to the Al side. With the increase of Ni content, the boundary will gradually approach the calculated boundary and eventually almost overlap.

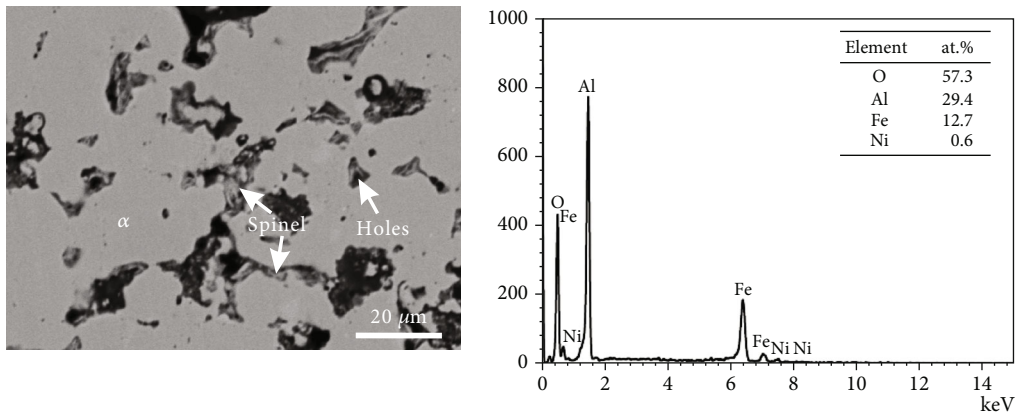

Figure 8: (a) BSE image and (b) the EDS patterns of the spinel phase in alloy B1.

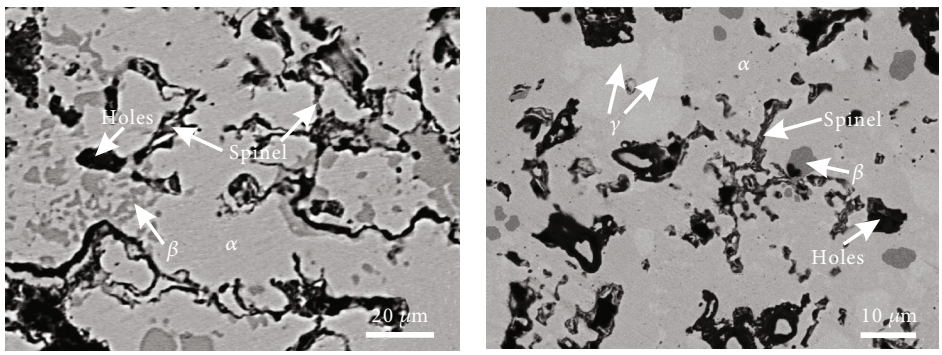

Figure 9: BSE images of (a) alloy B2 and (b) alloy B3.

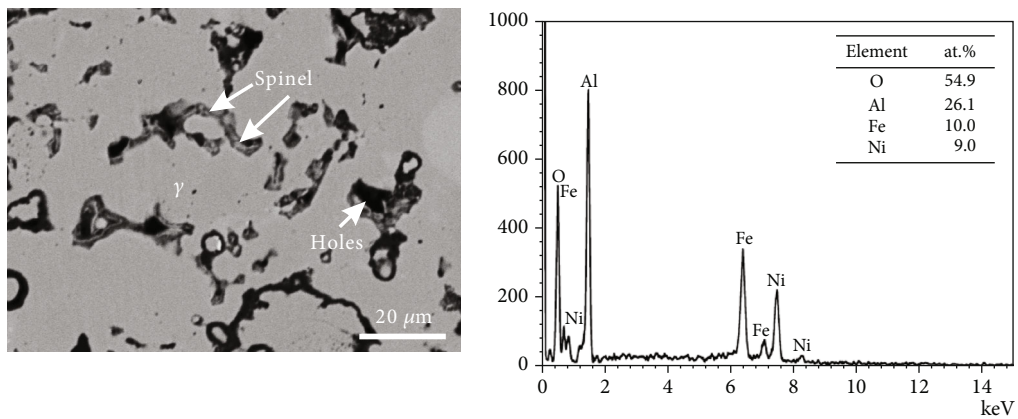

Figure 10: (a) BSE image and (b) the EDS patterns of the spinel phase in alloy B6.

From the experimental phase diagram, the spinel oxide can be formed only when the composition points of the original alloy fall in the region of phase equilibrium between spinel and matrix. Meanwhile, due to the low Gibbs free energy of alumina and the low equilibrium oxygen pressure required for the formation of the spinel phase, internal

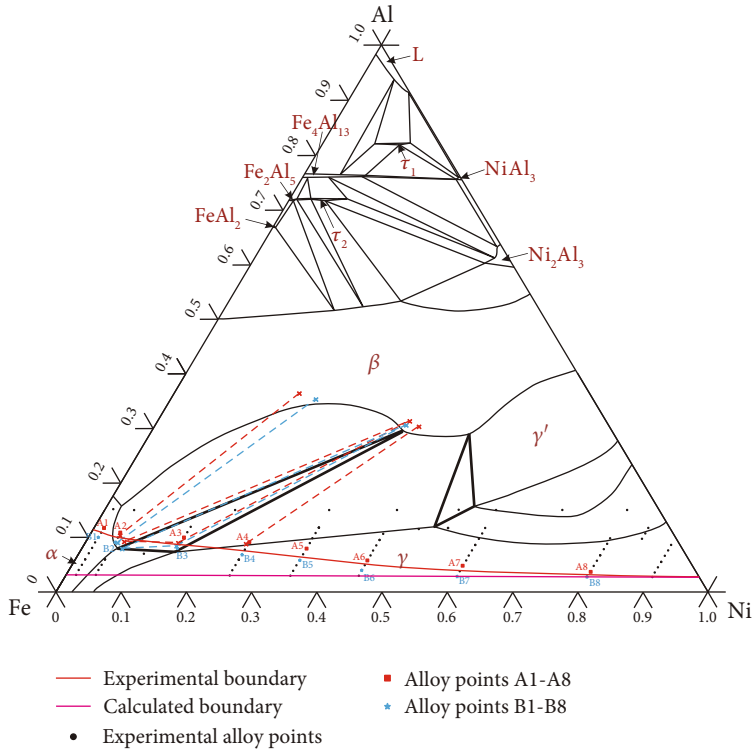

Figure 11: Phase boundary between corundum and spinel oxides in the 750°C isothermal section of the Fe-Al-Ni-O system.

oxidation is easy to occur when the Al content is low. According to Wagner's oxidation theory [28], the transition of spinel phase from internal oxidation to external oxidation to form a continuous spinel film requires the Al content to reach a critical value. Therefore, when designing the alloy composition in aim of forming anticorrosion spinel, both the phase equilibrium and the critical Al content under different oxygen pressure should be considered.

6. Conclusion

Phase equilibria of the Fe-Al-Ni-O system at 750°C were determined using the equilibration and quenching techniques, followed by characterization of alloys by means of SEM-EDS and XRD. Corundum can equilibrate with alloys close to the Al-rich region. Spinel is in equilibrium with matrix alloy phases close to the Fe-Ni side. Compared with the calculated results, the phase boundary of oxides moves to the Ni-Al side partially. Two four-phase equilibrium regions, α+β+γ+corundum and α+β+γ+spinel, and three three-phase equilibrium regions, α+β+corundum, β+γ+corundum, and α+β+spinel, were confirmed. This primary oxide phase diagram can be used as a guide for the preparation of the oxide film by selective oxidation.

Data Availability

The authors confirm that the data supporting the findings of this study are available within the article.

Conflicts of Interest

The authors declare that they have no conflicts of interest.

Acknowledgments

Financial supports from the National Science Foundation of China (Grant Nos. 51871030 and 51771035) and a project funded by the Priority Academic Program Development of Jiangsu Higher Education Institutions are greatly acknowledged.

References

[1] N. Israelsson, J. Engkvist, K. Hellstrom, M. Halvarsson, J.-E. Svensson, and L.-G. Johansson, "KCl-induced corrosion of a FeCrAl alloy at 600 °C in O_2+ H_2O environment: the effect of pre-oxidation," *Oxidation of Metals*, vol. 83, no. 1-2, pp. 29–53, 2015.

[2] X. W. Fang, Y. Wang, Y. Zhang et al., "Improving the corrosion resistance of Fe-21Cr-9Mn alloy in liquid zinc by heat treatment," *Corrosion Science*, vol. 111, pp. 362–369, 2016.

[3] B. Gorr, S. Burk, V. B. Trindade, and H.-J. Christ, "The effect of pre-oxidation treatment on the high temperature oxidation of Co–Re–Cr model alloys at laboratory air," *Oxidation of Metals*, vol. 74, pp. 239–253, 2010.

[4] F. J. Abe, H. Kutsumi, H. Haruyama, and H. Okubo, "Improvement of oxidation resistance of 9 mass% chromium steel for advanced-ultra supercritical power plant boilers by pre-oxidation treatment," *Corrosion Science*, vol. 114, pp. 1–9, 2017.

[5] L. C. Chen, C. Zhang, and Z. G. Yang, "Effect of pre-oxidation on the hot corrosion of CoNiCrAlYRe alloy," *Corrosion Science*, vol. 53, no. 1, pp. 374–380, 2011.

[6] E. Airiskallio, E. Nurmi, M. H. Heinonen et al., "High temperature oxidation of Fe-Al and Fe-Cr-Al alloys: the role of Cr as a chemically active element," *Corrosion Science*, vol. 52, no. 10, pp. 3394–3404, 2010.

[7] J. Shen, S. Liu, X. H. Guo, and Y. Niu, "Simultaneous oxidation and carburization of a Fe-9Cr alloy under different oxygen pressures at 800 ˚C," *Corrosion Science*, vol. 129, pp. 1–15, 2017.

[8] M. Hasegawa, "Ellingham Diagram," *Treatise on Process Metallurgy*, vol. 1, pp. 507–516, 2014.

[9] V. Torabinejad, M. Aliofkhazraei, and S. Assareh, "Electrodeposition of Ni-Fe alloys, composites, and nano coatings-a review," *Journal of Alloys and Compounds*, vol. 691, pp. 841–859, 2017.

[10] B. Wang, S. Wang, B. Liu, Q. Zhu, and X. Y. Li, "Oxide film prepared by selective oxidation of stainless steel and anti-coking behavior during n-hexane thermal cracking," *Surface and Coating Technology*, vol. 378, pp. 49–52, 2019.

[11] J. K. Yu, Q. Y. Li, X. C. Zhao, Q. Qiao, S. Zhai, and J. Zhao, "Correlation between microstructure and high-temperature oxidation resistance of jet-electrodeposited Ni-based alloy coatings," *Journal of Materials Engineering and Performance*, vol. 29, no. 5, pp. 3264–3276, 2020.

[12] X. P. Su, J. Zhou, J. H. Wang et al., "Thermodynamic analysis and experimental study on the oxidation of the Zn-Al-Mg coating baths," *Applied Surface Science*, vol. 396, pp. 154–160, 2017.

[13] Y. W. Ding, Y. Liu, Y. T. Yan, and X. P. Su, "Thermodynamic analysis and experimental study on the phase equilibria in Fe-Mn-Cr-O system," *Journal of Alloys and Compounds*, vol. 741, pp. 1080–1090, 2018.

[14] M. A. Rhamdhani, T. Hidayat, P. C. Hayes, and E. Jak, "Subsolidus phase equilibria of Fe-Ni-X-O (X= Mg, Al) systems in air," *Metallurgical and Materials Transactions B: Process Metallurgy and Materials Processing Science*, vol. 40, no. 1, pp. 25–38, 2009.

[15] V. Raghavan, "Al-Fe-Ni-O (aluminum-iron-nickel-oxygen)," *Journal of Phase Equilibria*, vol. 31, pp. 377-378, 2010.

[16] M. Khaidar, C. H. Allibert, and J. Driole, "Phase Eaquilibria of the Fe-Ni-Al system for Al content above 50 at.% and crystal structures of some ternary phases," *Zeitschrift fuer MetaIlkunde*, vol. 73, no. 7, pp. 433–438, 1982.

[17] V. Raghavan, "Al-Fe-Ni (aluminum-iron-nickel)," *Journal of Phase Equilibria*, vol. 31, no. 5, pp. 455–458, 2010.

[18] L. J. Zhang and Y. Du, "Thermodynamic description of the Al–Fe–Ni system over the whole composition and temperature ranges: modeling coupled with key experiment," *Calphad*, vol. 31, no. 4, pp. 529–540, 2007.

[19] V. Raghavan, "Al-Fe-O (aluminum-iron-oxygen)," *Journal of Phase Equilibria*, vol. 31, no. 4, pp. 367–367, 2010.

[20] G. Lindwall, X. L. Liu, A. Ross, and H. Z. Fang, "Thermodynamic modeling of the aluminum-iron-oxygen system," *Calphad*, vol. 51, pp. 178–192, 2015.

[21] D. Shishin, V. Prostakova, E. Jak, and S. A. Decterov, "Critical assessment and thermodynamic modeling of the Al-Fe-O system," *Metallurgical and Materials Transactions B*, vol. 47, no. 1, pp. 397–424, 2016.

[22] V. Raghavan, "Fe-Ni-O (iron-nickel-oxygen)," *Journal of Phase Equilibria*, vol. 31, no. 4, pp. 369–371, 2010.

[23] R. Luoma, "A thermodynamic analysis of the system Fe-Ni-O," *Calphad*, vol. 19, no. 3, pp. 279–295, 1995.

[24] M. A. Rhamdhani, P. C. Hayes, and E. Jak, "Subsolidus phase equilibria of the Fe-Ni-O system," *Metallurgical and Materials Transactions B: Process Metallurgy and Materials Processing Science*, vol. 39, no. 5, pp. 690–701, 2008.

[25] F. A. Elrefaie and W. W. Smeltzer, "Thermodynamics of nickel-aluminum-oxygen system between 900 and 1400 K," *Journal of the Electrochemical Society*, vol. 128, no. 10, pp. 2237–2242, 1981.

[26] P. Saltykov, O. Fabrichnaya, J. Golczewski, and F. Aldinger, "Thermodynamic modeling of oxidation of Al-Cr-Ni alloys," *Journal of Alloys and Compounds*, vol. 381, pp. 99–113, 2004.

[27] L. Kjellqvist, M. Selleby, and B. Sundman, "Thermodynamic modelling of the Cr-Fe-Ni-O system," *Calphad*, vol. 32, pp. 577–592, 2008.

[28] C. Wagner, "Theoretical analysis of the diffusion processes determining the oxidation rate of alloys," *Journal of the Electrochemical Society*, vol. 99, no. 10, pp. 369–379, 1952.

[29] G. Wang, B. Gleeson, and D. L. Douglass, "An extension of Wagner's analysis of competing scale formation," *Oxidation of Metals*, vol. 35, no. 3-4, pp. 317–332, 1991.

[30] C. H. Xu and W. Gao, "Pilling-Bedworth ratio for oxidation of alloys," *Materials Research Innovations*, vol. 3, no. 4, pp. 231–235, 2000.

Hindawi
Scanning
Volume 2021, Article ID 2717921, 7 pages
https://doi.org/10.1155/2021/2717921

Research Article

Preparation of TiO_2 Nanotube Array on the Pure Titanium Surface by Anodization Method and Its Hydrophilicity

Jianguo Lin,[1] Wenhao Cai,[1] Qing Peng,[1] Fanbin Meng,[2] and Dechuang Zhang[1]

[1]*School of Materials Science and Engineering, Xiangtan University, Xiangtan, 411105 Hunan, China*
[2]*Key Laboratory of Advanced Technologies of Materials (Ministry of Education), School of Materials Science and Engineering, Southwest Jiaotong University, Chengdu 610031, China*

Correspondence should be addressed to Dechuang Zhang; dczhang@xtu.edu.cn

Received 14 October 2021; Accepted 18 November 2021; Published 26 December 2021

Academic Editor: Jian Chen

In this work, a highly ordered TiO_2 nanotube array on pure titanium (Ti) was prepared by anodization. The effects of the applied voltage and anodization time on the microstructure of the TiO_2 nanotube arrays were investigated, and their hydrophilicity was evaluated by the water contact angle measurement. It was found that a highly ordered array of TiO_2 nanotubes can be formed on the surface of pure Ti by anodized under the applied voltage of 20 V and the anodization time in the range of 6-12 h, and the nanotube diameter and length can be regulated by anodization time. The as-prepared TiO_2 nanotubes were in an amorphous structure. After annealing at 550°C for 3 h, the amorphous TiO_2 can be transformed to the anatase TiO_2 through crystallization. The anatase TiO_2 array exhibited a greatly improved hydrophilicity, depending on the order degree of the array and the diameter of the nanotubes. The sample anodized at 20 V for 12 h and then annealed at 550°C for 3 h exhibited a superhydrophilicity due to its highly ordered anatase TiO_2 nanotube array with a tube diameter of 103.5 nm.

1. Introduction

Titanium (Ti) and its alloys have a broad application prospect as implant materials due to their high specific strength, low elastic modulus, excellent corrosion behaviour, and biocompatibility [1–5]. However, the surface of the Ti alloys will be coated with a cystic fiber membrane if they are directly implanted into the human body due to their bioinert, and thus, it is hard for the bioinert alloys to quickly form firm binding to the surrounding tissue, resulting in loosening or even shedding of the implants [6–8]. Therefore, many efforts have been done to devote to the improvement of bioactivity of Ti alloys through the surface modification of Ti alloys in the past decades [9]. In 2001, Sulka et al. [10] first successfully prepared an array of TiO_2 nanotubes on the surface of Ti by anodized oxidation in an electrolyte containing hydrofluoric acid. The array is highly ordered with a uniform tube diameter, which can effectively promote the specific surface area and adsorption capacity of the Ti alloy. The surface with the special structure has received great attention, and much work has been done on the impact of the nanotube TiO_2 array on the biocompatibility of Ti alloys. It has been found that the nanotube TiO_2 layer can enhance the osseointegration through the improvement of the adhesion of the hydroxyapatite (HAP) coating deposited onto TiO_2 [11]. Oh et al. [12] also indicated that the cell adhesion could be improved by up to 400% due to the mechanical interlocking between the HAP coating and the nanotube TiO_2 layer. Moreover, Park et al. [13] reported that the orderly array of TiO_2 nanotubes on a Ti alloy surface could promote its corrosion resistance in simulated body fluids. So, nanotubes fabricated on implant material surfaces provide great potential in promoting cell adhesion, proliferation, and differentiation. Moreover, nanotubes also offer the possibility of bacterial infection control by loading the tubes with antibacterial agents [14]. However, to establish the optimum nanotopography of nanotubes for favorable cell response, further studies are needed to find the optimum length and diameter of nanotubes for recognition and adherence by the sensing element of a bone cell.

It is well documented that the hydrophily of an implanting material plays an important role in the improvement of

osseointegration through inducing the enrichment of calcium and phosphorus ions in the body fluid, accelerating the binding with bone tissue and wound healing [15]. However, the hydrophilic of the TiO_2 nanotube array and its relationship with the topography of the TiO_2 nanotube has not been reported yet. Therefore, in the present work, highly ordered TiO_2 nanotube arrays were fabricated by electrochemically anodized in a mixed solution of glycerol and NH_4F aqueous electrolyte, and the effects of the applied voltage and time on the topography of the TiO_2 nanotube array were investigated. Moreover, the hydrophilicity of the TiO_2 nanopore array was evaluated.

2. Materials and Methods

2.1. Preparation of TiO_2 Nanotube Array. Ti plate (99.9% pure) with 1.0 mm thickness was used as a substrate to grow oxide nanotube arrays. Prior to the anodization, the surface was polished using silicon carbide papers (400, 600, 1000, 1500, and 2000 grits). The samples were ultrasonically cleaned in ethanol and acetone for 20 min successively and then dried in a nitrogen stream. After degreasing, the samples were eroded in a solution of 25 vol.% HF+25 vol.% HNO_3 for 30 s. Finally, the sample was cleaned in deionized water and dried in air. The samples were anodized in an electrolyte of 50 vol.% glycerol solution containing 0.3 mol/L ammonium fluoride (NH_4F). The anodization voltages were selected to be 10 V, 15 V, and 20 V, and the anodization time was 3 h, 6 h, 12 h, and 18 h, respectively. After anodizing, the samples were carefully cleaned with the deionized water and dried in air, and then, the as-prepared samples were annealed at 450°C, 550°C, and 650°C for 3 h in air with a heating rate of $10°C \cdot min^{-1}$.

2.2. Microstructure and Hydrophilic Property Characterization. The microstructure of the TiO_2 nanotube array was characterized at 20 kV by an XL30 S-FEG scanning electron microscope (SEM) equipped with energy dispersive X-ray analysis (EDS). The phase constitutions of the nanotubes were identified by using an X-ray diffractometer (Rigaku D/Max-2500VL/PC) employing Cu-Kα radiation ($\lambda = 1.54178 \times 10^{-9}$ nm). The hydrophilic properties of the TiO_2 nanotube array were evaluated via the measurement of the contact angle of a water droplet on its surface by a Contact Angle Goniometer (p/n 250-F1, USA).

3. Results

3.1. Microstructure Characterization. Figure 1 shows SEM topographies of TiO2 nanotube arrays on the Ti sample anodized under different voltages for 6 h. It is clear that a lot of grooves appeared on the sample surface without the formation of nanotubes after anodized at 10 V (Figure 1(a)). As the voltage increased to 15 V, the regular nanotube array can be observed on the sample surface, and the diameter of the nanotubes was about 40.3 nm (Figure 1(b)). With the voltage further increasing to 20 V, the nanotube array on the sample surface became more regular and ordered, and the average nanotube diameter also was increased to 71.2 nm. However, as the anodization voltage was increased to 40 V, the nanotubes collapsed due to the corrosion of the electrolyte, leading to the order breakdown of the nanotube array.

To study the effects of the anodization time on the microstructure of the nanotube array, the samples were anodized at 20 V for different times (3 h, 6 h, 12 h, and 18 h) under the constant temperature of 30°C. Figure 2 are the SEM images showing the surface topographies of the samples after anodized at 20 V for different times. It can be seen that, after being anodized at 20 V for 3 h, the nanotube arrays were formed at some area on the sample surface, but the entire surface of the sample was not completely covered by the nanotube arrays. The average nanotube diameter was about 44.5 nm. With the anodization time extending to 6 h, the regular and ordered nanotube array was formed on the entire surface of the sample, and the average diameter of the nanotubes was increased to about 71.2 nm (Figure 2(b)). With the anodization time further increasing to 12 h, the highly ordered nanotube array with the average nanotube diameter of about 103.5 nm was formed on the entire surface of the sample. However, as the anodization time extended to 18 h, the nanotube in the array began to collapse due to its increased length, resulting in a decrease in array order. Therefore, to obtain a highly ordered array of nanotubes on the surface of pure Ti through anodization in the electrolyte of the present work, the anodization voltage should be selected at 20 V with anodization time ranging from 3 h to 12 h, and the nanotube diameter and length can be regulated in the range of 44.5 nm to 103.5 nm by anodization time.

To determine the phase structure of the nanotubes, XRD diffraction analysis was performed on the nanotubes array on the surface of the sample anodized at 20 V for 12 h, and the result is shown in Figure 3. It can be seen that the as-prepared nanotubes were in an amorphous structure. To obtain the crystal nanotubes, the sample was annealed at 450°C, 550°C, and 650°C for 3 h, respectively. The XRD patterns of the samples after annealed at different temperatures were also illustrated in Figure 2. It can be seen that the diffraction peaks of the anatase TiO_2 appeared on the XRD pattern of the sample after annealing at 450°C for 3 h, implying the occurrence of the crystallization from the amorphous nanotubes to the anatase TiO_2. With the annealing temperature increasing to 550°C, the diffraction peaks of the anatase TiO_2 became sharper and more intense, indicating that the crystallinity of the nanotubes on the surface of the sample was greatly promoted. As the annealing temperature further increased to 650°C, the diffraction peaks of the rutile TiO_2 can be observed on the XRD pattern, implying that part of the anatase TiO_2 transformed into the rutile TiO_2 during the annealing treatment at 650°C of the nanotube arrays.

3.2. Hydrophilicity Property. The hydrophilicity of the surface of the anodized samples (anodized at 20 V for 12 h) before and after annealed at different temperatures were investigated by contact angle measurement. Figure 4 is the images of a water droplet on the surfaces of the samples anodized at different conditions, from which the contact

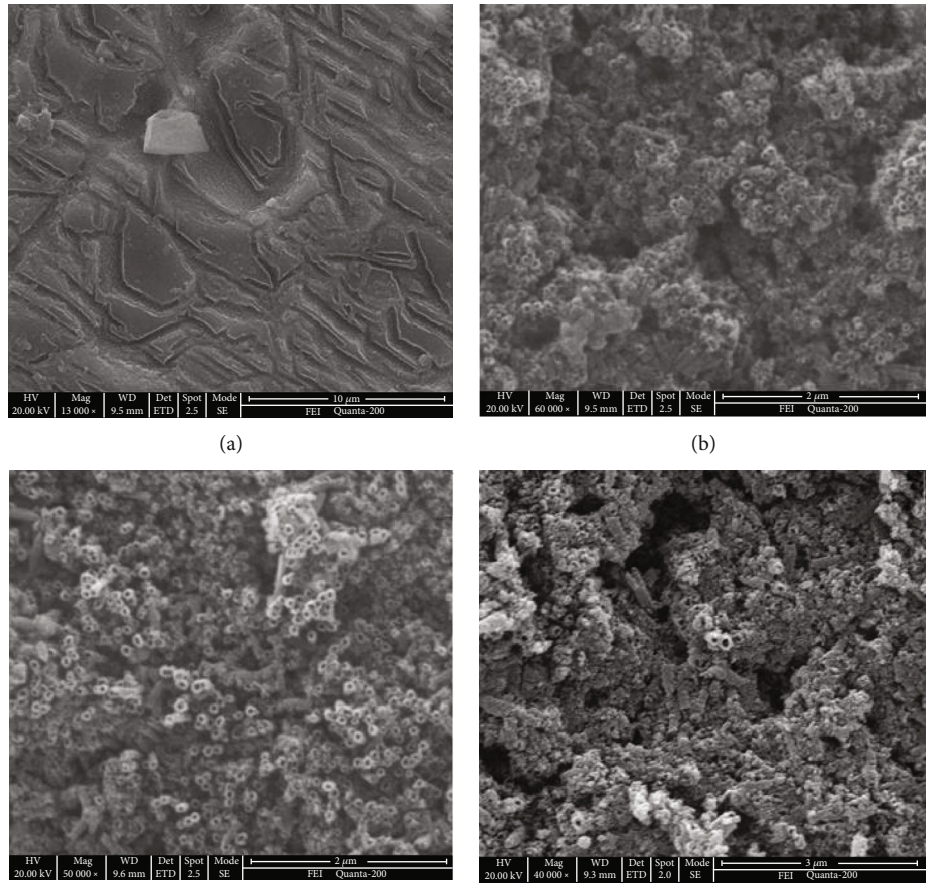

Figure 1: SEM topographies of the TiO_2 nanotube obtained by different applied voltages: (a) 10 V, (b) 15 V, (c) 20 V, and (d) 40 V.

angles of the water droplet with the sample surface can be measured, and the results were illustrated in Figure 3(b). It can be seen that the contact angle of the water droplet with the amorphous TiO_2 nanotube array surface of the sample anodized at 20 V for 12 h is 23.3°. In contrast, the anodized sample after annealing at 450°C exhibited an improved hydrophilicity due to the formation of the anatase TiO_2 by partial crystallization of the amorphous nanotubes on its surface, and the contact angle of the water droplet with its surface was decreased to 15.1°. With the annealing temperature increasing to 550°C, the nanotubes were fully crystallized to form the anatase TiO_2 nanotube array on the sample surface, leading to the further enhancement of its hydrophilicity, and the contact angle of the water droplet with the surface of the sample annealed at 550°C was about 5.0°. However, with the annealing temperature further increasing to 650°C, the rutile TiO_2 was formed in the nanotube array though the transformation of partial anatase TiO_2 to rutile TiO_2, and the hydrophilicity of the surface of the sample annealed at 650°C was decreased slightly and the contact angle of the water droplet with its surface was increased to 9.8°. As a result, the anatase TiO_2 nanotube array exhibited an excellent hydrophilicity.

Furthermore, the effects of the nanotube diameter on the hydrophilicity of the anatase TiO_2 nanotube array were investigated in the present work. To obtain the anatase TiO_2 nanotube array with different nanotube diameters, the pure Ti samples were firstly anodized at 20 V for 3 h, 6 h, 12 h, and 18 h and then were annealed at 550°C for 3 h, and after that, the anatase TiO_2 nanotube array with the diameters of 44.5 nm, 71.2 nm, 103.5 nm, and 136.8 nm were obtained, respectively. Figure 5 showed the contact angles with the surface of with different nanotube diameters. It can be seen that the contact angle on the surface of the anatase TiO_2 nanotube array on a nanotube diameter of 44.5 nm was about 30.1°, implying its low hydrophilicity. With the increase of the nanotube diameter, the hydrophilicity of the anatase TiO_2 nanotube array surface increased. As the nanotube diameter increased to 103.5 nm, the anatase TiO_2 nanotube array surface exhibited superhydrophilicity, and the water contact angle with the surface was close to 0°. However, with the nanotube diameter further increased to 136.8 nm, the hydrophilicity of the TiO_2 nanotube array decreased due to the collapse of the nanotubes.

4. Discussions

It has been documented that the formation of the TiO_2 nanotube array by electrochemical anodization is the result of the combination of the formation and chemical dissolution of the TiO_2 barrier layer on the Ti surface under the electric field. At the beginning of the anodization process, a

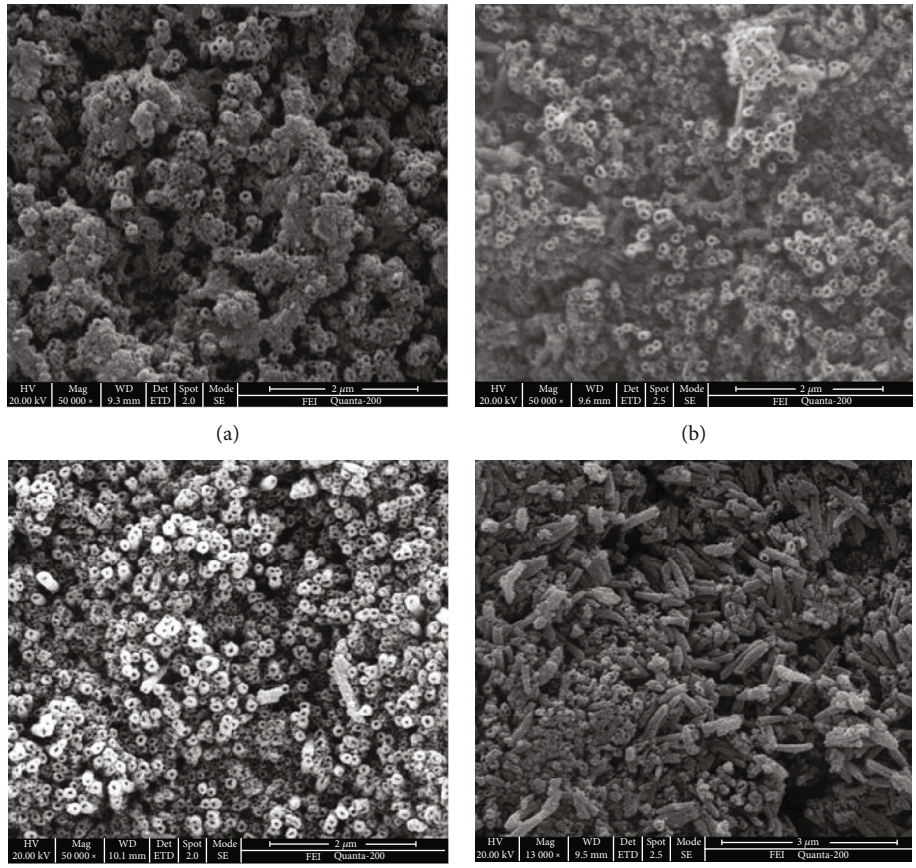

Figure 2: SEM images of the nanotube arrays anodized at 20 V for different times: (a) 3 h, (b) 6 h, (c) 12 h, and (d) 18 h.

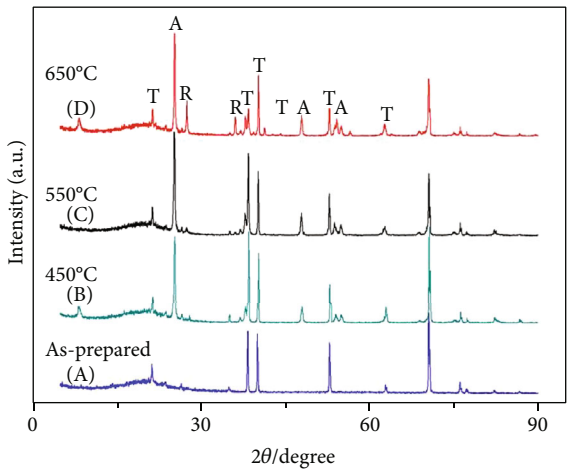

Figure 3: XRD patterns of the nanotube array obtained by anodization at 20 V for 6 h after with annealed at different temperatures: (a) as-prepared, (b) 450°C, (c) 550°C, and (d) 650°C.

thin TiO_2 layer (the barrier layer), is quickly formed on the surface of the Ti substrate in the electrolyte. Under the applied electric field, the ions of F^- in the electrolyte directly impact the surface of the Ti substrate anode and react with Ti, leading to the formation of a lot of small pits on the Ti surface. In this process, the following reactions are involved in the barrier layer:

$$Ti + 2H_2O - 4e \longrightarrow TiO_2 + 4H^+ \quad (1)$$

$$Ti^{4+} + 6F^- \longrightarrow [TiF_6]^{2-} \quad (2)$$

$$TiO_2 + 6F^- + 4H^+ \longrightarrow TiF_6{}^{2-} + 2H_2O \quad (3)$$

Under the electric field, the pits formed by the ions' impact on the Ti substrate surface gradually enlarge and deepen, and the number of the pits per unit area on the barrier layer surface also gradually increases and evenly cover over the surface of the barrier layer to form the original nanopores.

The barrier layer originally formed on the Ti surface is a thin TiO_2 film with a uniform thickness, and it has the same filed intensity throughout its surface in the applied electric field. However, as the pits are formed on the surface of the barrier layer, the electric field intensity at the bottom of the pit increases, and thus, the Ti-O bond at the pit bottom is weakened under the polarization of the applied electric field, leading to the dissolution of TiO_2 at this position. In the meaning time, the ions of O^{2-} in the electrolyte move to

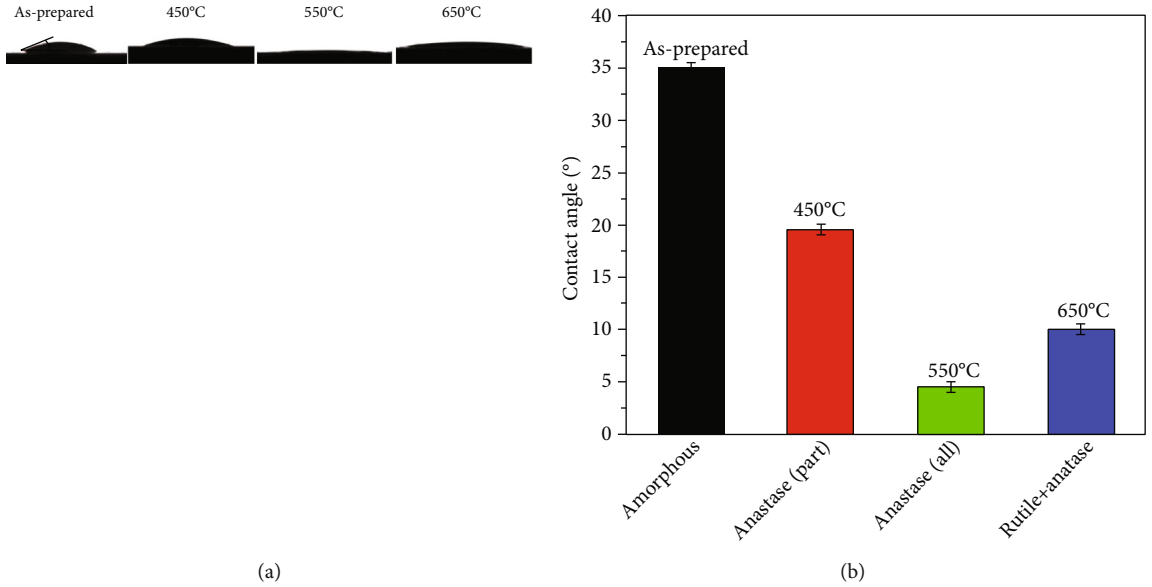

FIGURE 4: Topographies and contact angles of a water droplet on the surfaces of the TiO_2 arrays after annealed at different temperatures: (a) topographies and (b) contact angles.

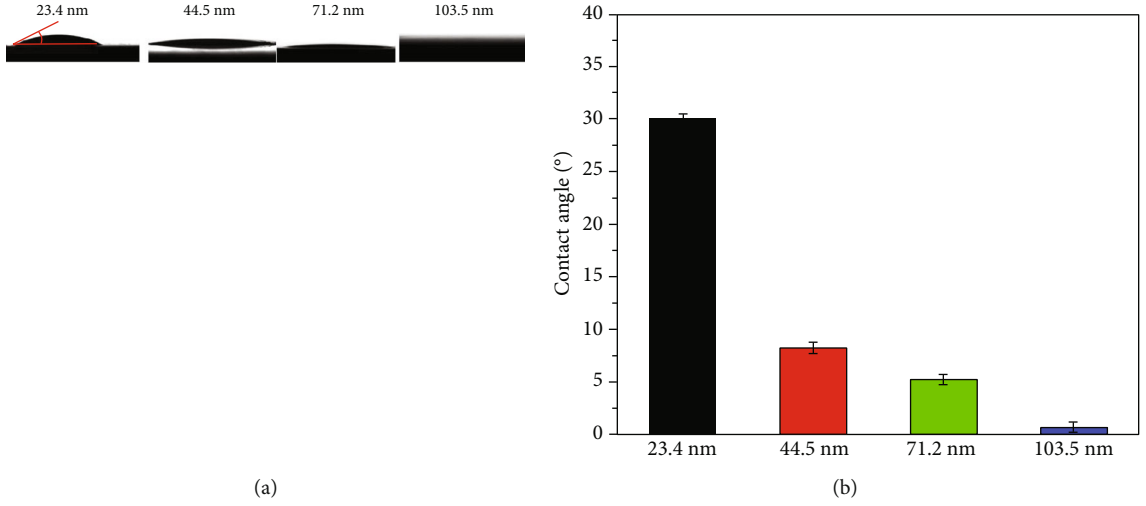

FIGURE 5: Topographies and contact angles of a water droplet on the surfaces of the TiO_2 arrays with different tube diameters: (a) topographies and (b) contact angles.

the Ti substrate/barrier layer interface and react with the Ti matrix to form a new barrier layer at the pit bottom. As a result, the pits in the barrier layer are continuously deepened to form a TiO_2 nanotube array on the Ti surface.

Therefore, the applied voltage and anodization time have an important impact on the size of TiO_2 nanotubes and the order degree of the nanotube array. When the applied voltage is too high in the anodization process, a large number of fluorine ions in the electrolyte can obtain greater impact kinetic energy, leading to the formation of a large number of pits with large size high density. These pits overlap each other so that an ordered nanotube array can not form. On the other hand, under the appropriate applied voltage, the anodization time determines the diameter and length of the nanotubes. With the oxidation time increasing, the diameter and length of the nanotubes are due to the corrosion of the electrolyte, but their tube wall is also thinning. So, too long anodization time will make the nanotube walls become too thin, which may cause the nanotubes to collapse. In the case of the present work, a highly ordered array of TiO_2 nanotubes can be obtained on the Ti surface by the anodization method under the conditions of the applied voltage of 20 V and the anodization time ranging from 3 h to 12 h, and the nanotube diameter can be regulated in the range of 23.4 nm to 103.5 nm by anodization time.

As regards the hydrophilicity of the TiO_2 nanotube array, it depends on the crystal structure of the TiO_2, the order degree of the nanotube array, and the tube diameter of the TiO_2 nanotubes. It was found that the anatase TiO_2 exhibits the best hydrophilicity in comparison with the

amorphous TiO_2 and the rutile TiO_2. Thus, after annealing at 550°C for 3 h, the sample with an amorphous TiO_2 array on its surface exhibited an excellent hydrophilicity due to the transformation of amorphous TiO_2 to the anatase TiO_2 through the full crystallization. The results in the present work indicated that the formation of a nanotube array on the Ti surface could significantly improve its hydrophilicity. This is because the nanotube array with a large number of pores can greatly enhance the specific surface area of the Ti surface, where the water droplet can enter the nanotube and the gaps between them, facilitating the smooth paving of the water droplet on the Ti surface.

5. Conclusions

In this paper, a highly ordered TiO_2 nanotube array on pure Ti was prepared by anodization, and their hydrophilicity was evaluated by contact angle of water droplet measurement. The main conclusions are as follows:

(1) A highly orderly TiO_2 nanotube array was successfully prepared on a pure Ti surface by the anodization oxidation method. The applied voltage and anodization time have an important effect on the microstructure of the nanotube array. Under the conditions of the applied voltage of 20 V and the anodization time in the range of 3-12 h, a highly ordered array of TiO_2 nanotubes can be obtained on the surface of pure Ti, and the nanotube diameter and length can be regulated by anodization time

(2) The TiO_2 nanotubes of the array prepared by anodization were an amorphous structure. After annealing at 550°C for 3 h, the amorphous TiO_2 array completely transformed to the anatase TiO_2 array through crystallization. As the annealing temperature increased to 650°C, the partial anatase TiO_2 nanotubes transformed into rutile TiO_2 nanotubes

(3) The formation of the TiO_2 nanotubes array on the Ti surface greatly improved its hydrophilicity, which depended on the crystal structure, order degree, and tube diameter of the nanotube array. The sample anodized at 20 V for 12 h and then annealed at 550°C for 3 h exhibited the superhydrophilicity due to its highly ordered anatase TiO_2 nanotube array with an appropriate nanotube diameter

Data Availability

The raw/processed data required to reproduce these findings cannot be shared at this time as the data also forms part of an ongoing study.

Conflicts of Interest

The authors declare that they have no conflicts of interest.

Acknowledgments

The authors would like to thanks the financial supports of the National Natural Science Foundation of China (Grant Nos. 51971190 and 11872053), Hunan Provincial Science and Technology Department (No. 2019JJ60006), and Key Laboratory of Advanced Technologies of Materials, Ministry of Education (No. A0920502052101-15).

References

[1] B. D. Boyan, "Role of material surfaces in regulating bone and cartilage cell response," *Biomaterials*, vol. 17, no. 2, pp. 137–146, 1996.

[2] J. Quinn, R. McFadden, C.-W. Chan, and L. Carson, "Titanium for Orthopedic Applications: An Overview of Surface Modification to Improve Biocompatibility and Prevent Bacterial Biofilm Formation," *Iscience*, vol. 23, no. 11, p. 101745, 2020.

[3] R. N. Salaie, A. Besinis, H. Le, C. Tredwin, and R. D. Handy, "The biocompatibility of silver and nanohydroxyapatite coatings on titanium dental implants with human primary osteoblast cells," *Materials Science and Engineering: C*, vol. 107, pp. 110210–110210, 2020.

[4] D. Lakstein, W. Kopelovitch, Z. Barkay, M. Bahaa, D. Hendel, and N. Eliaz, "Enhanced osseointegration of grit-blasted, NaOH-treated and electrochemically hydroxyapatite-coated Ti-6Al-4V implants in rabbits," *Acta Biomaterialia*, vol. 5, no. 6, pp. 2258–2269, 2009.

[5] H. Luo, Y. Wu, X. Diao et al., "Mechanical properties and biocompatibility of titanium with a high oxygen concentration for dental implants," *Materials Science and Engineering: C*, vol. 117, p. 111306, 2020.

[6] X. Liu, P. K. Chu, and C. Ding, "Surface modification of titanium, titanium alloys, and related materials for biomedical applications," *Materials Science and Engineering: R: Reports*, vol. 47, no. 3-4, pp. 49–121, 2004.

[7] T. Albrektsson, P.-I. Brånemark, H.-A. Hansson et al., "The interface zone of inorganic implantsIn vivo: titanium implants in bone," *Annals of Biomedical Engineering*, vol. 11, no. 1, pp. 1–27, 1983.

[8] P. I. Branemark, "Osseointegration and its experimental background," *The Journal of Prosthetic Dentistry*, vol. 50, no. 3, pp. 399–410, 1983.

[9] R. Narayanan, S. K. Seshadri, T. Y. Kwon, and K. H. Kim, "Calcium phosphate-based coatings on titanium and its alloys," *Journal of Biomedical Materials Research Part B: Applied Biomaterials*, vol. 85B, no. 1, pp. 279–299, 2008.

[10] G. D. Sulka, J. Kapusta-Kołodziej, A. Brzózka, and M. Jaskuła, "Anodic growth of TiO_2 nanopore arrays at various temperatures," *Electrochimica Acta*, vol. 104, pp. 526–535, 2013.

[11] F. S. Utku, E. Seckin, G. Goller, C. Tamerler, and M. Urgen, "Carbonated hydroxyapatite deposition at physiological temperature on ordered titanium oxide nanotubes using pulsed electrochemistry," *Ceramics International*, vol. 40, no. 10, pp. 15479–15487, 2014.

[12] S. OH, R. FINONES, C. DARAIO, L. CHEN, and S. JIN, "Growth of nano-scale hydroxyapatite using chemically treated titanium oxide nanotubes," *Biomaterials*, vol. 26, no. 24, pp. 4938–4943, 2005.

[13] J. Park, S. Bauer, K. von der Mark, and P. Schmuki, "Nanosize and Vitality: TiO2 Nanotube Diameter Directs Cell Fate," *Nano Letters*, vol. 7, no. 6, pp. 1686–1691, 2007.

[14] J. Zhou, M. A. Frank, Y. Yang, A. R. Boccaccini, and S. Virtanen, "A novel local drug delivery system: superhydrophobic titanium oxide nanotube arrays serve as the drug reservoir and ultrasonication functions as the drug release trigger," *Materials Science and Engineering: C*, vol. 82, pp. 277–283, 2018.

[15] C. Liu, A. Tian, H. Yang, Q. Xu, and X. Xue, "Electrodeposited hydroxyapatite coatings on the TiO_2 nanotube in static magnetic field," *Applied Surface Science*, vol. 287, pp. 218–222, 2013.

Hindawi
Scanning
Volume 2021, Article ID 5394782, 15 pages
https://doi.org/10.1155/2021/5394782

Research Article

Assessment of Cavitation Erosion in a Water-Jet Pump Based on the Erosive Power Method

Ning Qiu[1], **Han Zhu**[1], **Yun Long**[1], **Jinqing Zhong**[1], **Rongsheng Zhu**[1], **and Suhuan Wu**[2]

[1]*National Research Center of Pumps, Jiangsu University, Zhenjiang, 212013 Jiangsu, China*
[2]*Shanghai Bondpoly Engineering Material & Technology Co. Ltd., Shanghai 201601, China*

Correspondence should be addressed to Yun Long; longyun@ujs.edu.cn

Received 15 October 2021; Accepted 24 November 2021; Published 16 December 2021

Academic Editor: Qiao Yanxin

Cavitation affects the performance of water-jet pumps. Cavitation erosion will appear on the surface of the blade under long-duration cavitation conditions. The cavitation evolution under specific working conditions was simulated and analyzed. The erosive power method based on the theory of macroscopic cavitation was used to predict cavitation erosion. The result shows that the head of the water-jet pump calculated using the DCM-SST turbulence model is 12.48 m. The simulation error of the rated head is 3.8%. The cavitation structure of tip leakage vortex was better captured. With the decrease of the net positive suction head, the position where the severe cavitation appears in the impeller domain gradually moves from the tip to the root. The erosion region obtained by the cavitation simulation based on the erosive power method is similar to the practical erosion profile in engineering. As the net positive suction head decreases, the erodible area becomes larger, and the erosion intensity increases.

1. Introduction

Compared with traditional propellers, water-jet pumps have the advantages of high propulsion efficiency, good manoeuvrability, and low vibration. It is widely used in the propulsion of high-speed ships. But the performance of the water-jet pump will be affected by the cavitation problem [1–5]. The cavitation plays an important role in the design and operation of hydraulic machinery, and it causes degradation, noise, vibration, and erosion [6, 7]. Cavitation erosion will appear on the surface of the blades when the pump is operated under cavitation conditions for a long time. It will not only affect the reliability of the overall system but also cause high maintenance costs [8–11].

Many scholars have studied the cavitation structure in water-jet pumps and try to explain the effect of cavitation on the performance of water-jet pumps through experiments and simulations. Park et al. [1] conducted experimental research based on PIV technology. The results show that the flow separation phenomenon is easy to occur at the lips of the flow channel when the inflow velocity decreases. Tan et al. [12] observed the formation of perpendicular cavitation vortex (PCV) in the impeller of the water-jet pump by experimental method. The shedding of PCV can cause the head to drop sharply. Motley et al. [13] used high-speed photography to observe the evolution of cavitation on the impeller of a water-jet pump. Cavitation first appeared in the tip clearance of the impeller. Long et al. [14, 15] captured the cavitation structure on the impeller of the water-jet pump at inception cavitation. Wu et al. [16] used the particle image velocity measurement method to study the turbulence structure of the tip leakage vortex of an axial water-jet pump.

Lindau et al. [17] simulated cavitation in the water-jet pump and found that cavitation would cause a sudden drop in thrust and torque. Katz's research shows that the axial shear vortex structure has an impact on the development of cavitation in the separation zone [18]. The numerical result of Guo et al. [19] showed that the pressure pulsation amplitude of the monitors near the tip increases with the

extent of cavitation. Huang et al. [20–23] analyzed the cavitation and vortex structures in water-jet pumps. The results show that the evolution of cavitation has aggravated the generation of vortex and flow instability in pumps. When cavitation occurs, the vortex expansion and baroclinic torque appear as violent fluctuation. Xu et al. [24] found that the viscous dissipation term has a larger magnitude at the tip clearance of water-jet pumps.

Cavitation erosion is a hot research currently [25]. Traditionally, cavitation erosion risk is assessed by experimental methods [26–30]. High-speed videos are used to assess the visual collapsing cavities. And it is complemented by paint test or erosive material test. But these methods are expensive. With the development of computational fluid dynamics (CFD), numerical methods become an attractive alternative. Ochiai et al. [31] used a Lagrangian method to assess the risk of cavitation erosion based on acoustic pressure emitted from bubbles. Peter et al. [32, 33] proposed a new method considering the microjet mechanism and applied the method to predict cavitation erosion around a hydrofoil. Pereira et al. [25, 34–36] used a macroscopic cavitation theory to assess the cavitation erosion risk in experiment and simulation. Usta et al. [37] compared the applicability of intensity function method, Gary level method, and erosive power method and predicted the erosible areas on a ship propeller.

The cavitation mechanism in the water-jet pumps was analyzed based on the RANS method and the DCM-SST turbulence model, and the cavitation erosion was predicted based on the macroscopic cavitation theory in this paper.

2. Experimental Setup

2.1. Pump Parameters. The main parameters of the water-jet pump are shown in Table 1.

2.2. Experimental Method [38]. The cavitation in the water-jet propulsion pump will destroy the energy exchange between the impeller and the liquid, which results in the decline of the external characteristics. The experiment in this paper was completed on the closed test bench of the water-jet pump of the 708th Research Institute of China State Shipbuilding Corporation by Long et al. [38]. $NPSH_a$ is gradually reduced until the pump head drops by 3% through reducing the pressure at the pump's inlet. High-speed photography technology was used to observe the cavitation structure during cavitation evolution through the plexiglass window in the impeller shell.

2.3. High-Speed Photography Acquisition System [38]. The high-speed photography visualization system is shown in Figure 1. The middle section of the impeller is perpendicular to the camera's longitudinal axis. The distance from the camera lens to the Plexiglas is about 0.5 m, and the size of the shooting area is about 90 mm × 180 mm. The high-speed camera PCOS achieves fast frame rates at high photosensitivity and high dynamic range, reaching 4467 fps with a full resolution of 1008 × 1008 pixels which can guarantee good image quality.

Table 1: Design parameters of the test pump.

Design parameter	Design value
Flow rate Q (m^3/s)	0.46
Head H (m)	13
Rotating speed n (r/min)	1450
Power N (kW)	70
Specific speed n_s	524.3
Impeller inlet diameter D_j (mm)	270

To capture the cavitation flow of the pump, the shooting frequency is determined as follows. If the rotating speed of the pump is n and the impeller is required to acquire an image once it rotates a certain degree α, the shooting frequency f is

$$f = \frac{n \times 360/60}{\alpha}, \tag{1}$$

where n is the impeller rotating speed (r/min) and α is the impeller rotation angle (°).

In this paper, the camera is set as shooting one image for each 2° of the impeller rotation.

3. Numerical Simulation Methods

3.1. Continuity Equation and Momentum Equation. In the simulation, the vapor-liquid two-phase flow is generally assumed to be homogeneous. The Navier-Stokes equation based on the Newtonian fluid is used in this simulation [39, 40]. The equation is formulated in the Cartesian coordinate system as [23]

$$\begin{aligned}
&\frac{\partial \rho_m}{\partial t} + \frac{\partial \left(\rho_m u_j\right)}{\partial x_j} = 0,\\
&\frac{\partial (\rho_m u_i)}{\partial t} + \frac{\partial \left(\rho_m u_i u_j\right)}{\partial x_j} = -\frac{\partial p}{\partial x_i} + \frac{\partial}{\partial x_j} \times \left[(\mu_m + \mu_T) \cdot \left(\frac{\partial u_i}{\partial x_j} + \frac{\partial u_j}{\partial x_i} - \frac{2}{3}\frac{\partial u_i}{\partial xj}\delta_{ij} \right) \right],\\
&\frac{\partial \rho_l \alpha_l}{\partial t} + \frac{\partial \left(\rho_l \alpha_l u_j\right)}{\partial x_j} = m^+ + m^-,\\
&\rho_m = \rho_l \alpha_l + \rho_v \alpha_v,\\
&\mu_m = \mu_l \alpha_l + \mu_v \alpha_v,
\end{aligned} \tag{2}$$

where the subscript i, j indicates the coordinate direction, u indicates the velocity, p indicates the pressure, ρ_l indicates the liquid density, ρ_v indicates the vapor density, α_v indicates the vapor volume fraction, α_l indicates the liquid

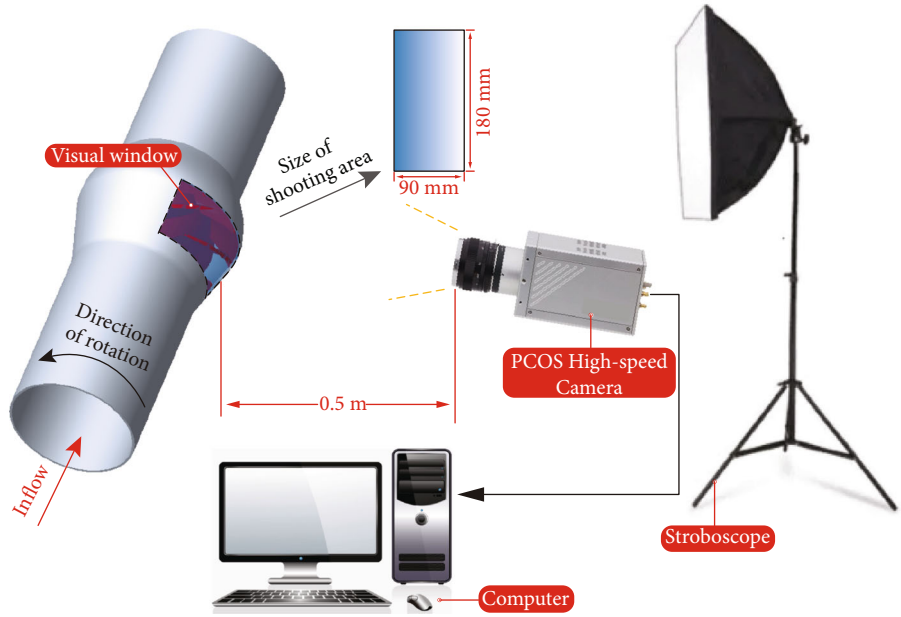

Figure 1: High-speed photography visualization system.

volume fraction, μ_l indicates the liquid laminar viscosity, μ_v indicates the vapor laminar viscosity, μ_T indicates the turbulent viscosity, m^+ indicates the vapor condensation rate, and m^- indicates the vapor evaporation rate. ρ_m indicates vapor-liquid mixed-phase density, and μ_m indicates vapor-liquid mixed-phase laminar viscosity.

3.2. Cavitation Model. The ZGB model [41, 42] is a cavitation model based on the mass transport equation, which describes the cavitation phase change process mainly by establishing the transport relationship between the vapor and liquid phases. Its evaporation rate and condensation rate are defined as follows:

$$m^+ = C_{\text{dest}} \frac{3\alpha_{\text{nuc}}(1-\alpha_v)\rho_v}{R_B}\left(\frac{2}{3}\frac{p_v - p}{\rho_l}\right)^{1/2}, \quad p < p_v,$$
$$m^- = -C_{\text{prod}} \frac{3\alpha_v \rho_v}{R_B}\left(\frac{2}{3}\frac{p - p_v}{\rho_l}\right)^{1/2}, \quad p > p_v, \tag{3}$$

where R_B is the bubble radius, α_{nuc} is the volume fraction of gas nuclei, p_v is the saturated vapor pressure, C_{prod} is the rates of steam condensation when the local static pressure is greater than the saturation vapor pressure, and C_{dest} is the rate of steam evaporation when the local static pressure is lower than the saturation vapor pressure. The values of the coefficients in the model are [43] $R_B = 1 \times 10^{-6} m$, $C_{\text{prod}} = 0.01$, $C_{\text{dest}} = 50$, and $\alpha_{\text{nuc}} = 1 \times 10^{-4}$.

3.3. Turbulence Model. This simulation is based on the *SST* $k-\omega$ turbulence model [50]. To more accurately simulate the development of cavitation in the centrifugal pump, the compressibility of the mixing of the vapor and liquid phases is considered, and the mixing density is corrected using the *DCM* method. Turbulent viscosity is defined as follows:

$$f_{\text{DCM}} = \rho_v + \left(\frac{\rho_m - \rho_v}{\rho_l - \rho_v}\right)^N \cdot (\rho_l - \rho_v),$$
$$\mu_{\text{T-DCM}} = \frac{C_\mu k^2}{\varepsilon} f_{\text{DCM}}, \tag{4}$$

where N is taken as 10 according to literature recommendations [43, 44].

Table 2: Calculation parameters.

Parameter	Value
Temperature (°C)	25
Saturated vapor pressure (Pa)	3169.93
Density of water (kg/m^3)	997.003
Dynamic viscosity of liquid phase (Pa·s)	8.9e – 04
Density of vapor (kg/m^3)	2.3e – 02
Dynamic viscosity of vapor phase (Pa·s)	9.87e – 06

3.4. Boundary Conditions and Grid Setup. The calculation parameters are shown in Table 2. Figure 2 shows the calculation domain and boundary conditions. The inlet of the calculation domain was set as the pressure inlet, and the outlet condition was mass flow rate. The domain of impeller was rotating with a speed of 1450 rpm, and other domains were static domains. Inlet and outlet extension pipes were added to avoid the large difference between experiment and simulation caused by backflow. The wall condition was set as *nonslip wall*. The residual was set to be 1e – 04. Total

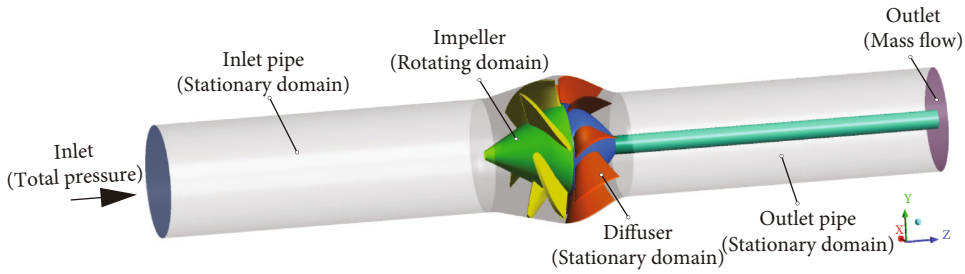

Figure 2: Calculation domain and boundary conditions.

calculation time was set as 0.12 s, and timestep was set to be $2.73e-05$ s.

After completing the 3D modeling, the inlet pipe and the outlet pipe were divided into structural grids by software *ICEM*. Impeller and diffuser grids were structured using software *TurboGrid*. The leading and trailing edges of the blades are elliptical. The spline curve is used to fit the contour of each layer of the grids. The tip clearance of the grid was set to 0.3 mm. The grid of tip clearance region was divided into 10 layers to obtain a better flow field. Regarding the grid-independent inspection, the water-jet propulsion pump studied in this paper is similar to the calculation model of Huang et al. [20–23] in terms of geometrical dimensions and operating conditions. In Huang's research, the mesh-independence check was made for the impeller, and it was pointed out that the mesh of the impeller is larger than 1.06 million to ensure the calculation accuracy. Considering the requirements of the turbulence model for the boundary layer, the $y+$ of near-wall surface shown in Figure 3 was adjusted below 40. The number of grids used in this paper is shown in Table 3, and the details of the grids are shown in Figure 4.

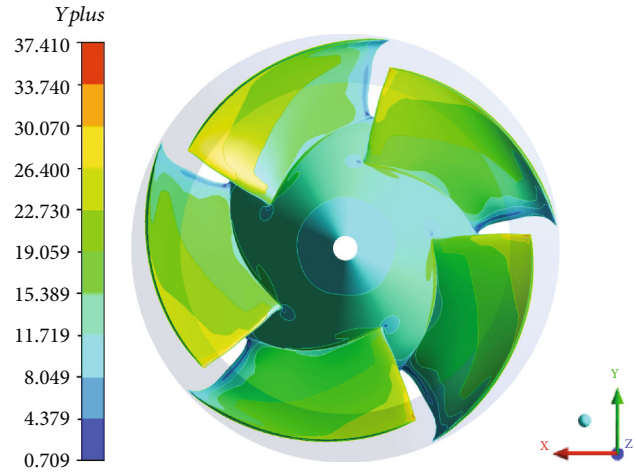

Figure 3: Distribution of *Yplus*.

Table 3: Mesh number of calculation domain.

Calculation domain	Mesh number
Impeller	1729170
Diffuser	1579710
Inlet pipe	626640
Outlet pipe	590236
Total mesh number	4525756

4. Analysis of Results

4.1. Cavitation Performance and Analysis. The net positive suction head and corresponding head under the design flow rate are obtained. The cavitation characteristic curve was obtained by reducing the inlet pressure gradually. The experimental and simulation results are shown in Figure 5. This water-jet propulsion pump's rated head is 13 m, and the simulated result is 12.5 m. The relative error is 3.8%, and this error can prove that the simulation is reliable. When the simulated head drops by 3%, $NPSH_a$ is 7.15 m, while $NPSH_a$ is 7.58 m in the experiment for the same situation. This difference may be because noncondensable gases, thermodynamic effects, and other factors were ignored. The existence of this difference does not affect capturing the flow characteristics in the pump by simulation. The cavitation image captured in the experiment is shown in Figure 6. Figures 5 and 6 are compared and analyzed. As can be seen in Figure 6(a), in the initial stage of cavitation, the head of point A basically does not change. It is generally believed that there is little cavitation in the blade channel at this operating condition, but the cavitation in the tip clearance can be seen from the image. As the inlet pressure decreases, the head curve begins to change. During the evolution of cavitation, point B on the cavitation performance curve was selected, as the initial cavitation. As the net positive suction head decreases, the tip leakage vortex (TLV) area becomes larger, and at the same time, the cavity grows on the suction surface, as shown in Figure 6(b). When the head drops by 3%, the point C on the cavitation performance curve is called the critical cavitation point. a~c on the simulated cavitation performance curve were selected to mark the cavitation situations corresponding to A~C on the experimental cavitation curve. The corresponding $NPSH_a$ of point A is 9.90 m, point b is 8.16 m, and point c is 7.15 m.

Figure 7 shows the cavitation structures under different net positive suction heads captured by the simulation, which were represented by gray isosurface with vapor volume fraction of 10%. Observed from the side view, the simulated

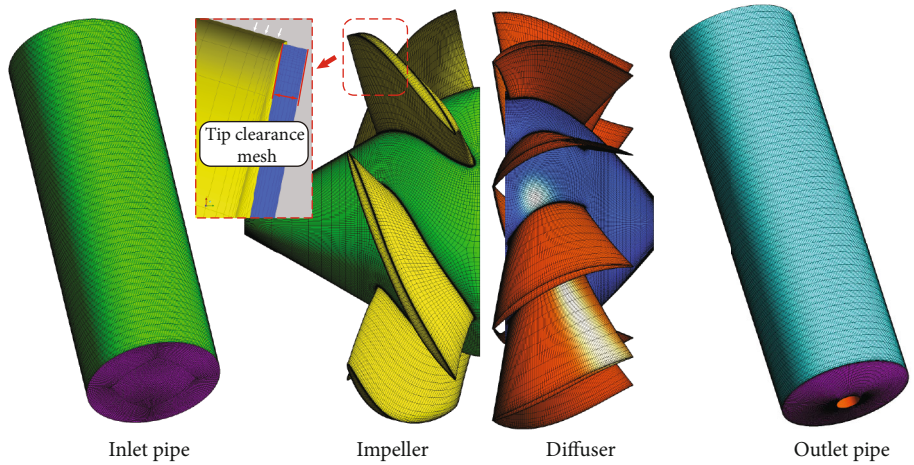

Figure 4: The detail of grid.

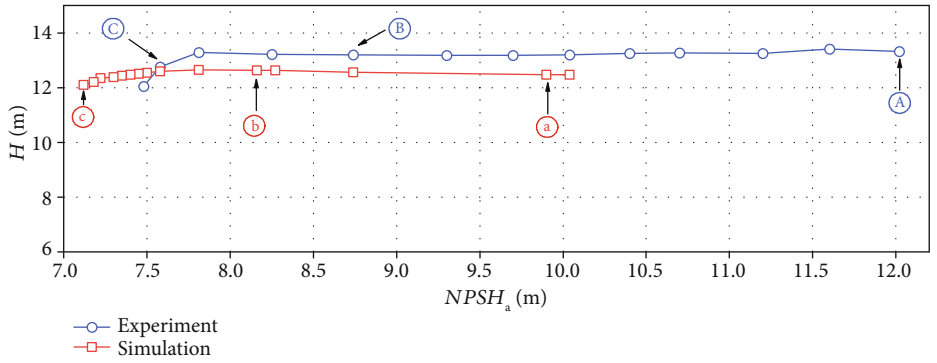

Figure 5: Comparison between simulated and experimental cavitation performance curves.

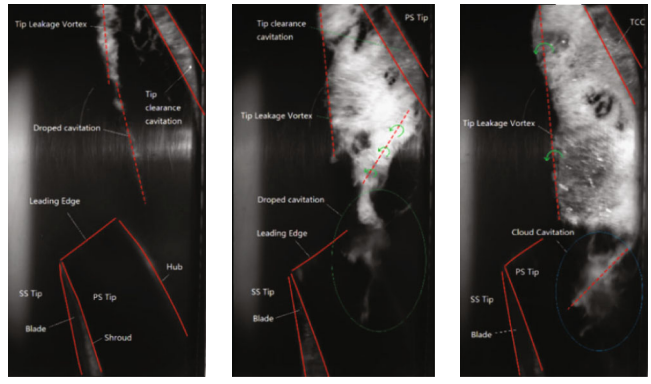

(a) Point A (b) Point B (c) Point C

Figure 6: The cavity flow structures at different cavitation conditions [15].

cavity structure is basically consistent with the experimental results. When $NPSH_a$ is 9.90 m, tiny cavitation appears near the tip on the suction surface of the blades, as shown in region 1 of the figure. At the same time, the cavitation in the tip clearance was also captured, as shown in region 2 of the figure. At this situation, the appearance of cavitation has no effect on performance. As the net positive suction head drops to 8.16 m, the cavity develops from the tip to the root of the blades. In the flow direction, it covers most of the blade surface. It can be observed that there is "gap" in the cavitation isosurface near the leading edge of blades. As the net positive suction head continues to drop, it can

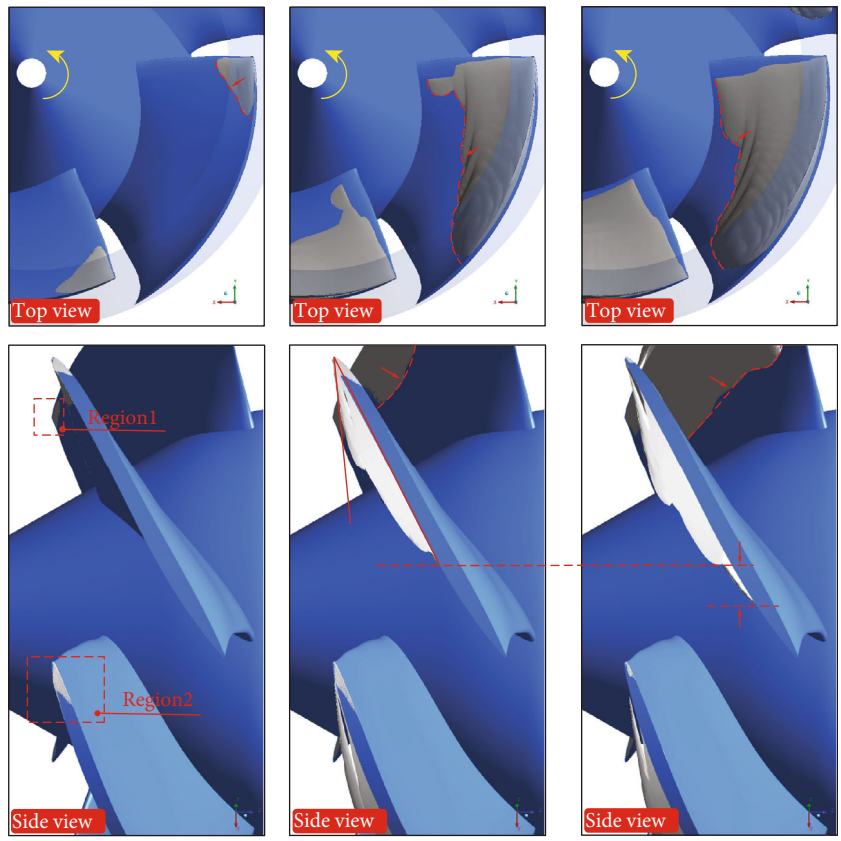

(a) $NPSH_\alpha = 9.90$ m (b) $NPSH_\alpha = 8.16$ m (c) $NPSH_\alpha = 7.15$ m

Figure 7: Simulated cavitation structures at different $NPSH_a$.

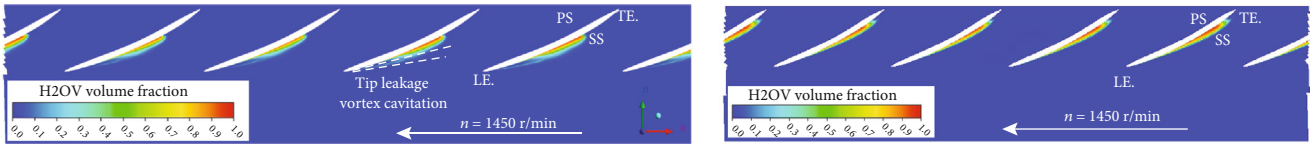

(a) $r/R = 99.5\%$ (b) $r/R = 80.0\%$

Figure 8: Contours of vapor volume fraction at $NPSH_a = 7.15$ m.

be observed that the "gap" is more obvious, and the cavitation appears to be stratified. Compared with Figure 6, it can be considered that this delamination may be caused by the tip leakage vortex (TLV) (this will be analyzed in Figures 8–10). The existence of leakage flow causes tip leakage vortex cavitation (TLVC). The local pressure near the blades is lower than the saturated vapor pressure, and cavitation appears on the suction surface. The different cavitation structures gathered together, resulting in a decrease in pump performance. Figure 11 shows the change of the cavitation area at different circumferential positions in the blade channel under design conditions. It can be seen from the figure that as r/R increases, the cavitation area first increases and then decreases. When $NPSH_a = 9.90$ m, the maximum cavitation area of $0.186\,cm^2$ appears at $r/R = 0.95$; when $NPSH_a = 8.16$ m, the maximum value of $8.20\,cm^2$ appears at $r/R = 0.85$; when $NPSH_a = 7.15$ m, the maximum cavitation area of $22.8\,cm^2$ appears at $r/R = 0.75$. This phenomenon verifies that the cavitation in the water-jet propulsion pump mainly occurs in the area near the tip of the blades. The cavitation coverage area expands from the tip to the root as the net positive suction head drops. The maximum cavitation area in the impeller domain moves from the tip to the root of the blades.

The evolution of cavitation is closely related to the flow field structure. There are many ways to identify the vortex structure [45]. To better analyze the structure of the flow field, the Q-criterion is introduced to describe the vortex:

$$Q = \frac{1}{2}\left(\|\Omega\|^2 - \|S\|^2\right) = \frac{1}{2}\left(\Omega_{ij}\Omega_{ji} - S_{ij}S_{ji}\right), \quad (5)$$

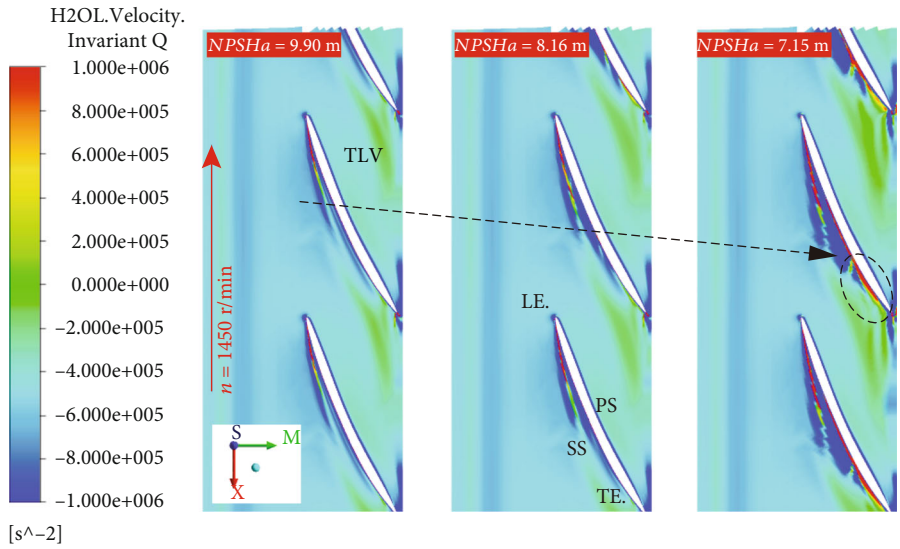

Figure 9: Distribution of vortex core by Q *invariant* method ($r/R = 99.5\%$).

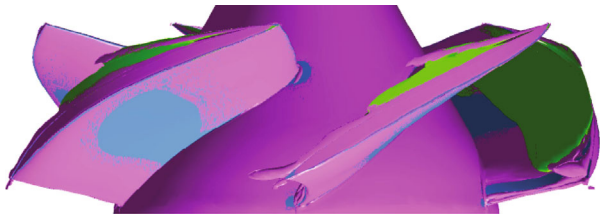

Figure 10: Cavitation vortex structure at $\mathrm{NPSH}_a = 7.15$ m. (The vortex center region is shown as pink isosurface of $Q = 5e + 05\ \mathrm{s}^{-2}$, and the green areas represent cavitation structures.)

where Q represents the second-order invariant of the velocity gradient tensor under Galileo transformation. Ω represents the vorticity tensor and S represents the deformation rate tensor, which are, respectively, defined as

$$S_{ij} = \frac{1}{2}\left(\frac{\partial u_i}{\partial x_j} + \frac{\partial u_j}{\partial x_i}\right),$$
$$\Omega_{ij} = \frac{1}{2}\left(\frac{\partial u_i}{\partial x_j} - \frac{\partial u_j}{\partial x_i}\right), \quad (6)$$

where i and j, respectively, represent different directions. It can be seen from the equation that Q is equal to the value of vorticity tensor subtracting the deformation rate tensor. When $Q > 0$, it means that the tendency of rotation is greater than the tendency of axial deformation. At this time, it can be considered that the flow in this area is dominated by eddy flow.

Figure 8 shows the cavity distribution on different r/R spanwise sections. When $r/R = 99.5\%$, the cavity in the impeller is divided into two parts: the attached cavity on the suction surface of the blades and the elongated vortex cavitation appearing at the leading edge of blades. When $r/R = 80\%$, only attached cavity exists on the blades. When r/R is 80%, the cavity length is greater than that when r/R is 99.5%. Figure 9 shows the distribution of Q in the spanwise section at different r/R locations. In the far-field region, the Q values are negative. The results show that the trend of axial deformation dominates the distribution of the Q value, due to the rotation of the impeller. Also, it can be seen from the figure that the method can accurately identify the core of the tip leakage vortex (TLV) with a higher positive value on the blades' suction side (SS). The TLV region gradually becomes longer with the decreases of NPSH_a. The Q value near the initial position of the TLV is the highest. As the TLV moves away from the leading edge, the Q value gradually decreases. But its value is still positive, and the flow is still dominated by the rotational effect. There is an area with extremely low value of Q around the TLV structure, which reflects the restriction of the rotation effect and the deformation effect. At the position corresponding to the TLV structure in Figure 8(a), there is a slender cavitation on the SS of the blades, and the shapes are basically similar. This cavitation is caused by tip leakage. As shown in Figure 10, the TLV structure seems a "boundary" that defines the cavitation on the leading edge of the blades. The cavitation only develops in this boundary. This is consistent with the results observed through experimental results in Figure 6. Three planes were set to analyze the relationship between tip leakage vortex and cavity structure as shown in Figure 12. The area of tip leakage vortex is small on plane A. The cavitation structure is located at the vortex core. And the value of Q beyond the phase boundary is also high. The development of tip leakage vortex will be affected by the rotation of the impeller. From plane A to plane C, the TLV region gradually became bigger and the max value of Q reduced. The position of the phase boundary moves away from the vortex core area.

4.2. Prediction of Cavitation Erosion. Cavitation will cause damage to the pump blades, and the erosion profile in

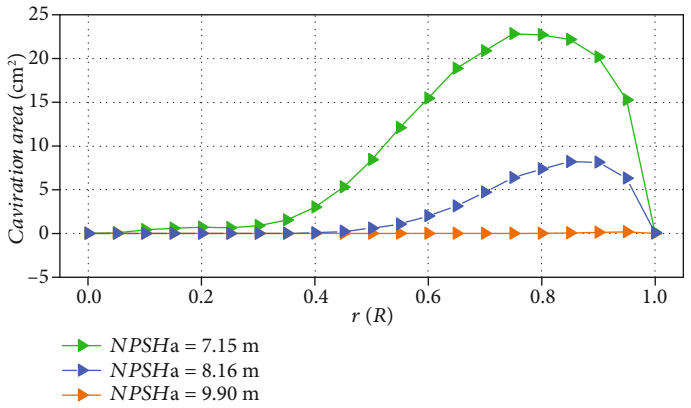

Figure 11: Cavity area at different $NPSH_a$.

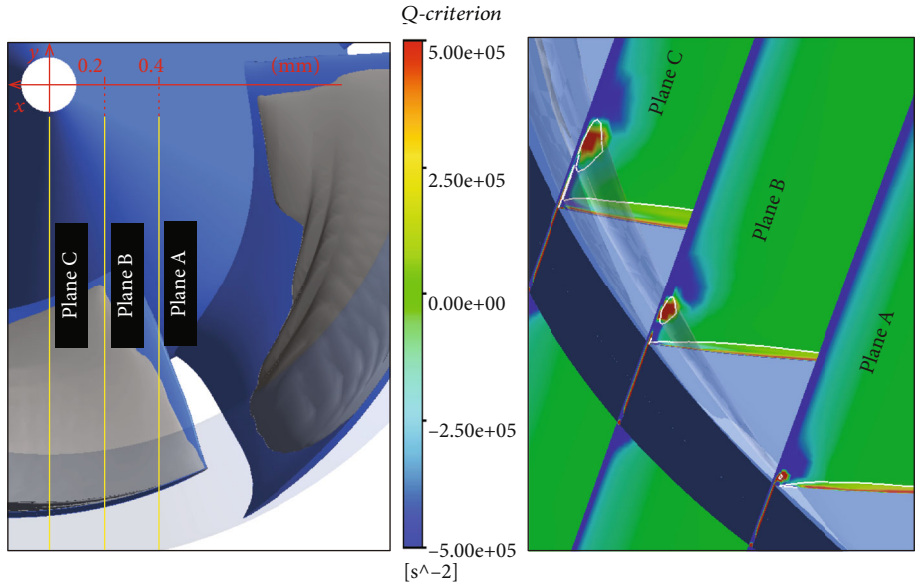

Figure 12: The relationship between cavitation and vortex structure. (The white line represents the boundary of vapor-liquid phase.)

(a) (b)

Figure 13: Distribution of cavitation erosion on pumps.

practical engineering is shown in Figure 13. Cavitation erosion is a microscopic and transient process, but it is also affected by macroscopic flow conditions. From the energy point of view, the collapse of the cavitation bubble will produce a pressure wave. This pressure wave is one of the factors that cause cavitation damage. Based on the hypothesis of Pereira et al. [25, 34], the potential energy of the cavity structure is defined as

$$E_{\text{pot}} = \Delta p \times V_{\text{vap}},$$
$$\Delta p = (p - p_{\text{sat}}). \tag{7}$$

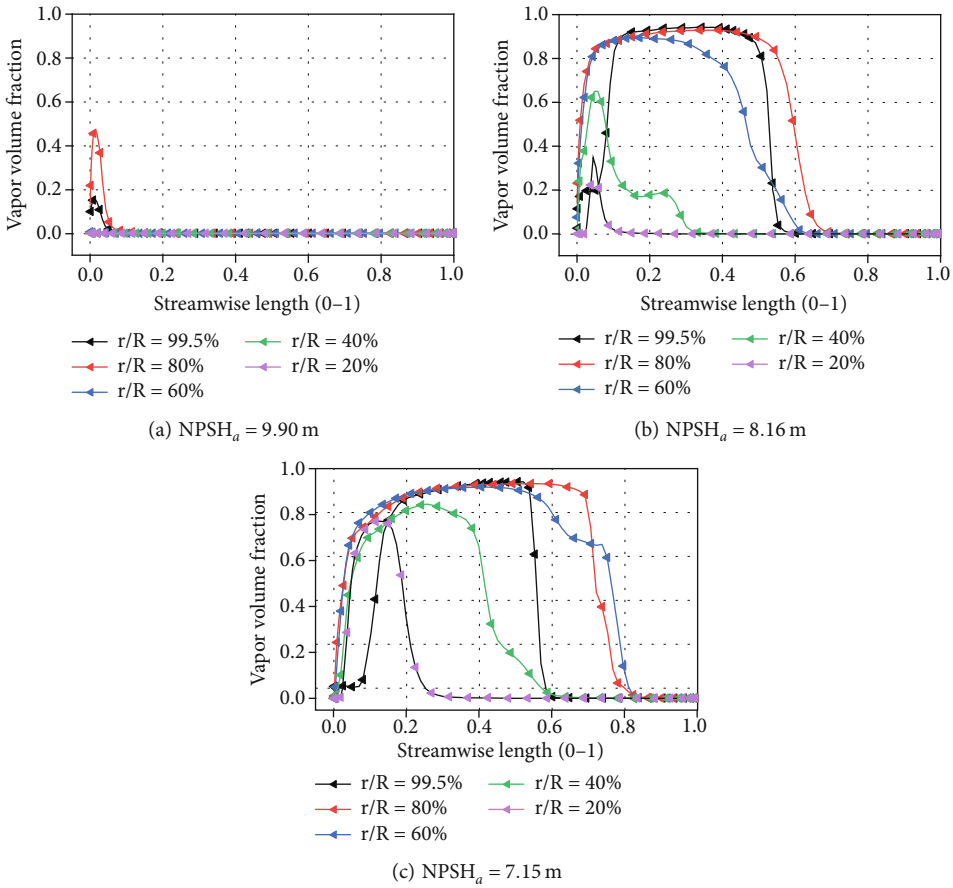

(a) $NPSH_a = 9.90$ m

(b) $NPSH_a = 8.16$ m

(c) $NPSH_a = 7.15$ m

Figure 14: Vapor volume fraction at different spans.

The cavitation volume is reduced when cavity collapses, and the pressure wave is released. The erosive power function p_{pot} can be defined as [25, 27–30, 33, 35, 36, 40, 46]

$$p_{pot} = \frac{\partial E_{pot}}{\partial t} = \Delta p \times \frac{\partial V_{vap}}{\partial t} + V_{vap} \times \frac{\partial \Delta p}{\partial t} = (p - p_{sat}) \times V_{cell} \times \frac{\partial \alpha}{\partial t} + V_{cell} \times \alpha \times \frac{\partial p}{\partial t}, \quad \text{if } p_{pot} \geq \varepsilon, \tag{8}$$

$$\alpha = \frac{V_{vap}}{V_{cell}} = \frac{\rho - \rho_l}{\rho_v - \rho_l}, \tag{9}$$

where p is the pressure surrounding the vapor (Pa), p_{sat} is the saturated vapor pressure (Pa), V_{vap} is the vapor volume (m^3), V_{cell} is the volume of the grid (m^3), α is the vapor volume fraction, and ε is the threshold.

There are 5 key parameters in equation (8), which are p, α, $\partial p/\partial t$, and $\partial \alpha/\partial t$. In order to better analyze the distribution of related parameters and their influence on cavitation erosion prediction, the distribution information of related parameters at different spans was extracted and drawn in Figures 14–16. Figure 14 shows the cavitation volume fraction distribution under rated flow rate. When $NPSH_a = 9.90$ m, there is a tiny cavity near the tip at $r/R = 80\%$ and 99.5%. At the position of $r/R = 80\%$, the cavity coverage length is longer than that at $r/R = 99.5\%$. But near the root at $r/R = 20\%$, 40%, and 60%, no cavity exists. When the net positive suction head decreases to 8.16 m, the cavity volume at $r/R = 80\%$ and 99.5% near the tip increased rapidly. In the flow direction, the length of the cavity coverage becomes longer, but the length of the cavity at the position of $r/R = 80\%$ is still greater than that at $r/R = 99.5\%$. Cavitation also exists at $r/R = 20\%$, 40%, and 60%. With a change of r/R from tip to the root, both the vapor content and the coverage length decreased. When $NPSH_a = 7.15$ m, the coverage length of cavity at different r/R positions becomes longer. The position with the longest cavity is at $r/R = 60\%$. The maximum vapor content at the positions of $r/R = 20\%$, 40%, and 60% all becomes larger. Comparing the vapor volume fraction distribution under different $NPSH_a$, it can also be observed that the leading edge of the blade at $r/R = 99.5\%$ has lower vapor content. The cavitation volumes at the leading edge (LE) of the blade at $r/R = 80\%$ position rise rapidly along the flow direction. The cause of this change may be due to the existence of the tip leakage vortex.

The pressure distribution on the blade surface will directly affect the performance of blades [51]. Figure 15 shows the absolute pressure distribution on the suction

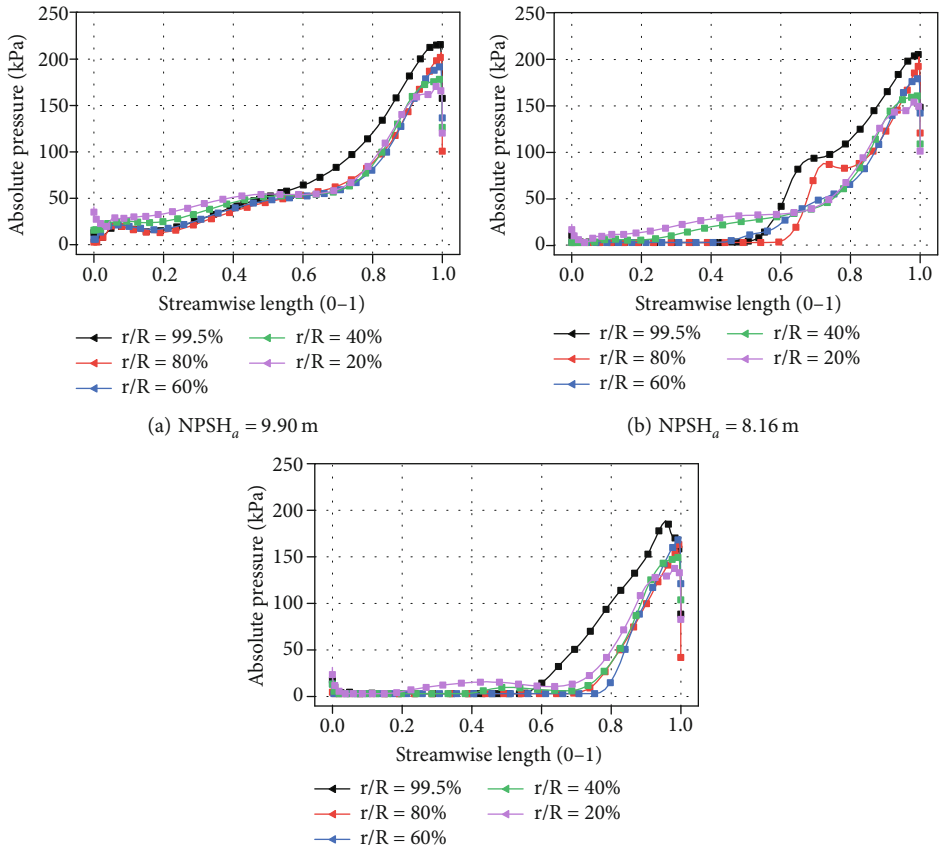

Figure 15: Absolute pressure at different spans.

surface of the blade under rated flow rate. The pressure gradually increases along with the flow direction. The absolute pressure near the root position when streamwise length ranges from 0 to 0.5 is greater than that near the tip position. But when streamwise length ranges from 0.5 to 1.0, the result is opposite. As the inlet pressure drops, the maximum pressure value on the blade gradually decreases. Due to the coverage of the cavity, the area where the absolute pressure is less than 50 kPa gradually becomes larger.

dp/dt can be used as an indicator for cavitation prediction [47]. Figure 16 shows the distribution of dp/dt under the rated flow rate. When NPSH$_a$ = 9.90 m, the variation of dp/dt mainly appears at the leading edge and trailing edge of the blades. The maximum value of $|dp/dt|$ appearing on the leading edge is greater than that appearing on the tailing edge. As the net positive suction head decreases to 8.16 m, the maximum value of $|dp/dt|$ still appears at the leading edge of the blade. But the fluctuation area of dp/dt near the trailing edge of the blade begins to become larger. When NPSH$_a$ decreases to 7.15 m, the area with large fluctuations of dp/dt on the suction surface of the blade expanded, and the maximum value of $|dp/dt|$ on the blade also increased from $0.87e+06$ to $1.34e+06$. This phenomenon shows that as the net positive suction head drops, the pressure fluctuations gradually become larger.

Figure 17 shows the distribution of $d\alpha/dt$ under the rated flow rate. The distribution of $d\alpha/dt$ is related to the location of the cavity. When NPSH$_a$ = 9.90 m, the sudden change of $d\alpha/dt$ mainly appears on the leading edge of the blade, and when NPSH$_a$ = 8.16 m, the sudden change of $d\alpha/dt$ appears when streamwise length ranges from 0 to 0.7. The sudden change of $d\alpha/dt$ appears when streamwise length ranges from 0 to 0.8 if NPSH$_a$ is 7.15 m. This distribution is consistent with the results in Figure 7. It can also be seen that as the net positive suction head decreases, the maximum value of $|d\alpha/dt|$ also increases from 11.5 to 29.6. This phenomenon shows that as the net positive suction head decreases, the fluctuation of the vapor content gradually increases.

The unsteady simulation captured the transient contours of vapor volume fraction, dp/dt, $d\alpha/dt$, and p_{pot}. The erosion caused by cavitation is the result of a long-duration accumulation. To better predict the erodible region, the *Matlab* code was used to process the images into time-averaged results. For ease of description, the abbreviated form is expressed as follows: TAV (time-averaged vapor volume fraction), TAA (time-averaged $d\alpha/dt$), TAP (time-averaged dp/dt), and TAPP (time-averaged p_{pot}).

72 snapshots were set during one rotation. The image processing method refers to the singular value decomposition (SVD) [48]. An image can be interpreted as a matrix

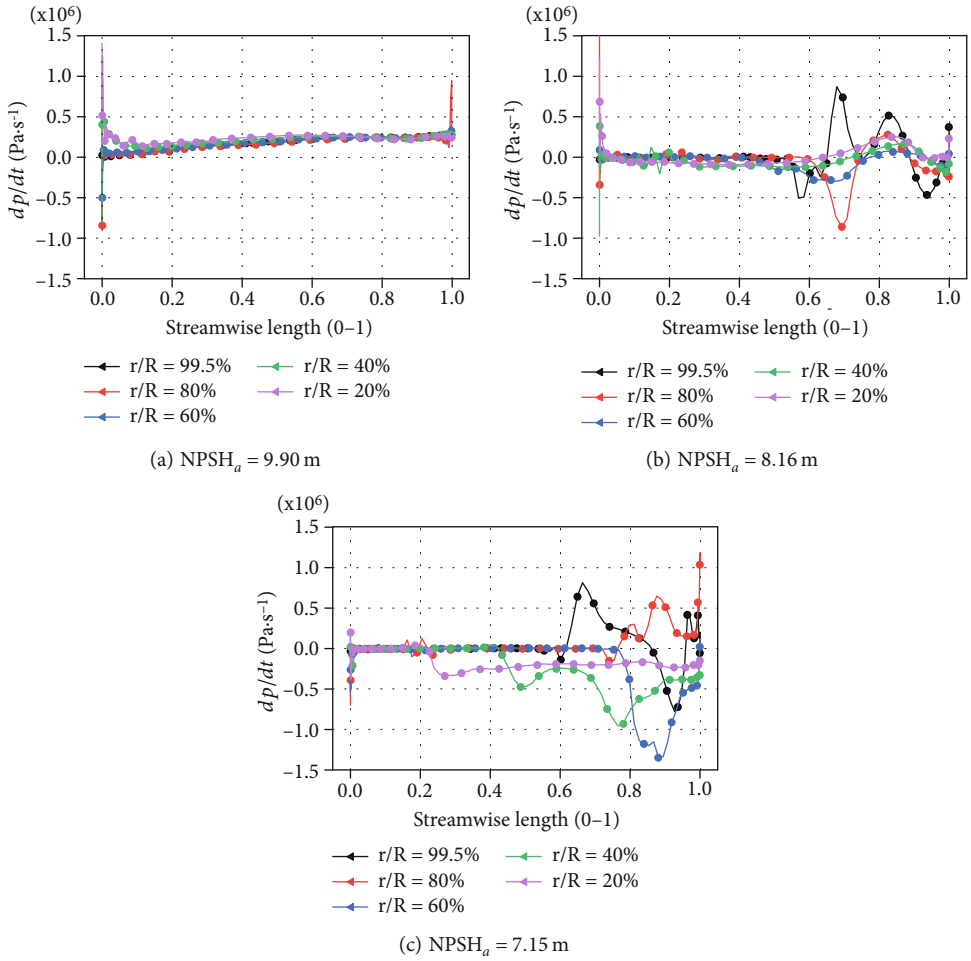

(a) $NPSH_a = 9.90$ m

(b) $NPSH_a = 8.16$ m

(c) $NPSH_a = 7.15$ m

Figure 16: dp/dt at different spans.

by linear transformation, described by eigenvalues and eigenvectors. If the flow variables $U(t, x)$ (pressure, velocity, etc.) during a period of time t are known (where x is the space vector of the flow field), the time information of M moments is stored in the form of row vectors and the spatial information of N nodes is stored in the form of column vectors. The matrix can be expressed as

$$U(t_i, x_j) = \begin{bmatrix} u(t_1, x_1) & u(t_1, x_2) & u(t_1, x_3) & .. & u(t_1, x_N) \\ u(t_2, x_1) & u(t_2, x_2) & u(t_2, x_3) & .. & u(t_2, x_N) \\ . & . & . & . & . \\ . & . & . & . & . \\ u(t_M, x_1) & u(t_M, x_2) & u(t_M, x_3) & .. & u(t_M, x_N) \end{bmatrix}. \tag{10}$$

The time average of the transient variables at each node can be expressed as

$$\bar{U}(x_j) = \frac{1}{M} \sum_{i=1}^{M} U(t_i, x_j). \tag{11}$$

Figure 18 shows the TAA distribution after one rotation at rated flow rate. Based on the hypothesis of macroscopic cavitation, pressure waves will be generated when the vapor content decreases. The threshold of the $d\alpha/dt$ parameter was set to $(-20, 0)$. When $NPSH_a$ is 9.90 m, the large value of | TAA | appears near the leading edge of the blade near the root. Compared with the other two $NPSH_a$, the maximum value of |TAA | is smaller and the distribution area is not obvious. As the net positive suction head decreases, the TAA distribution area gradually becomes larger, expanding from the leading edge to the tailing edge along the flow direction and from the tip to the root along the span direction. The maximum value of |TAA | on the suction surface of the blade gradually becomes larger. Compared to Figure 17, it can be seen that the distribution of TAA matches with the shape of the cavity coverage line.

A pressure pulse with positive amplitude is an important indicator of cavitation erosion [47]. The threshold of the dp/dt parameter was set to $(0, 1.0e + 06)$. Figure 19 shows the TAP distribution after one rotation at rated flow rate. It can be seen from the figure that there is a higher value on the leading edge of the blade after the time-averaged treatment. The occurrence of this area is related to the impact of the incoming flow on the blades. At the rear part

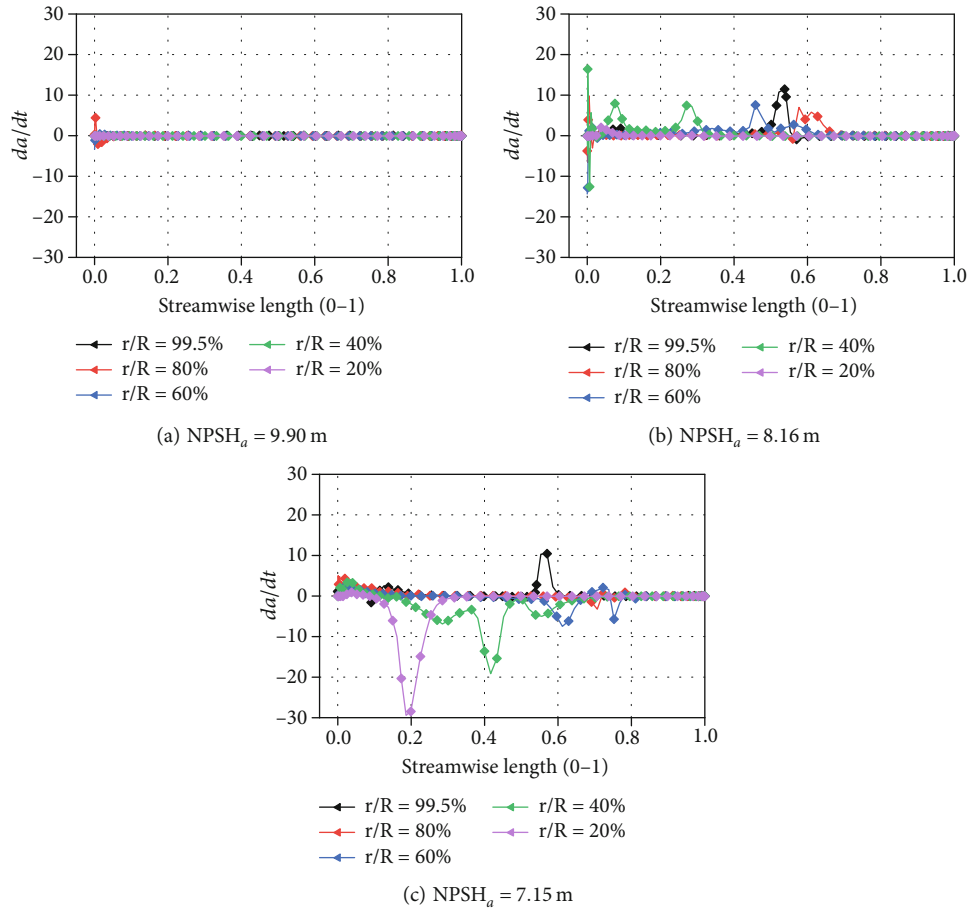

(a) $NPSH_a = 9.90$ m

(b) $NPSH_a = 8.16$ m

(c) $NPSH_a = 7.15$ m

Figure 17: $d\alpha/dt$ at different spans.

(a) $NPSH_a = 9.90$ m

(b) $NPSH_a = 8.16$ m

(c) $NPSH_a = 7.15$ m

Figure 18: Time-averaged $d\alpha/dt$.

of the blade, the distribution of TAP is related to the distribution of cavities. The high TAP in the midstream without cavitation is concentrated and is also close to the root of the blade, as shown in Figure 19(c). As the net positive suction head decreases, the maximum value of TAP gradually increases, and it gradually moves to the trailing edge.

Based on the distribution of TAA and TAP, the time-averaged distribution of erosion power after one rotation is obtained based on equation (8), as shown in Figure 20. The shape of the erosion region in the figure matches with the cavitation coverage area in Figure 21. This is consistent with the conclusions obtained by other scholars [49]. The result of cavitation prediction is also consistent with the phenomenon in Figure 13. The light-colored areas on the blades represent cavitation erosion in the figure. Cavitation erosion first appeared near the tip of the blade and developed to the trailing edge of

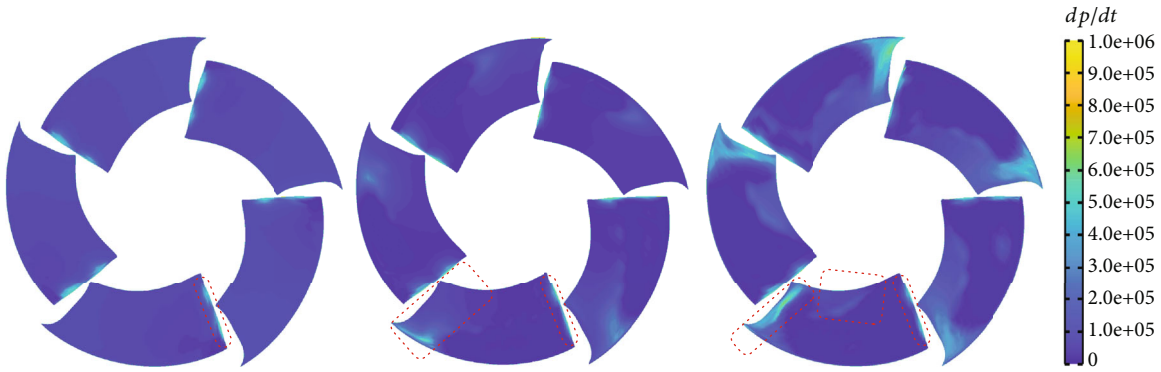

(a) $NPSH_a$ = 9.90 m (b) $NPSH_a$ = 8.16 m (c) $NPSH_a$ = 7.15 m

Figure 19: Time-averaged dp/dt.

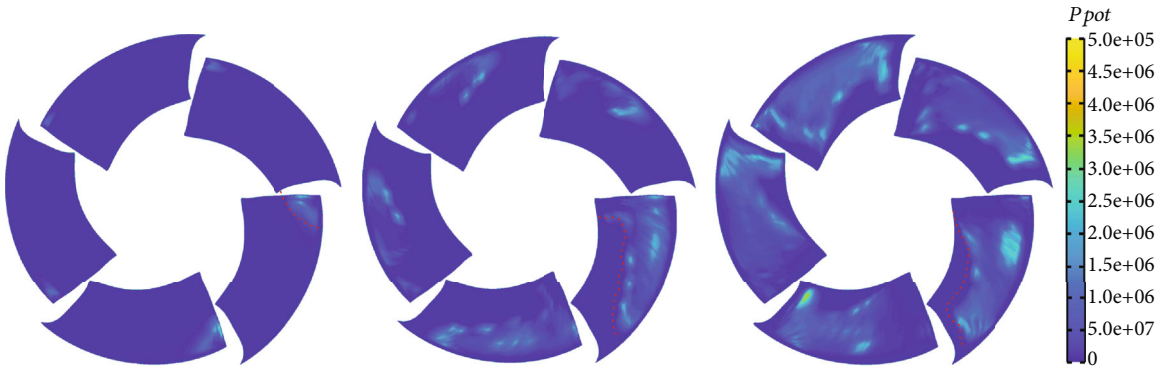

(a) $NPSH_a$ = 9.90 m (b) $NPSH_a$ = 8.16 m (c) $NPSH_a$ = 7.15 m

Figure 20: Time-averaged p_{pot}.

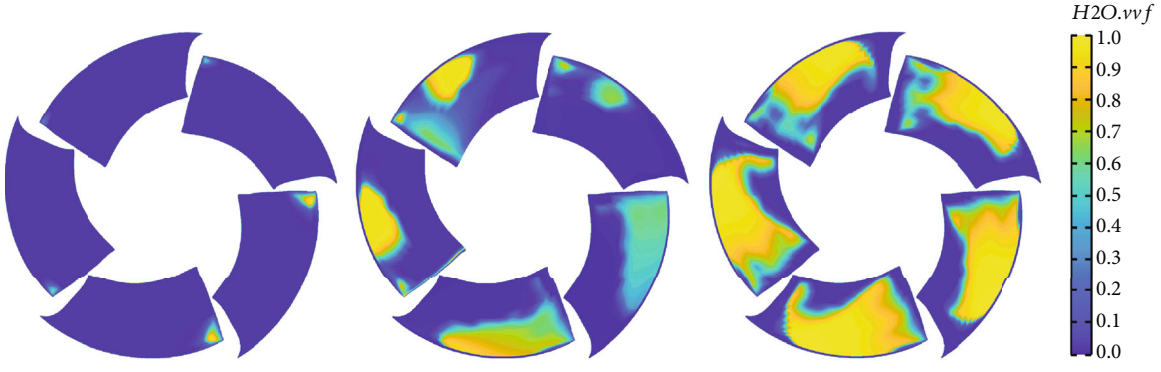

(a) $NPSH_a$ = 9.90 m (b) $NPSH_a$ = 8.16 m (c) $NPSH_a$ = 7.15 m

Figure 21: Time-averaged vapor volume fraction.

the blade along the flow direction. There is more cavitation erosion near the tip of the blades. And cavitation erosion basically does not exist on the blade roots. The simulation results showed the same trend. When $NPSH_a$ is 9.90 m, the region of cavitation erosion appears at the leading edge near the tip with a near-triangular shape. The erosion area expanded when $NPSH_a$ is 8.16 m and mainly distributed near the tip. The high value distribution of TAPP is basically located near the cavity closure. As the net positive suction head continues to decrease, the erosion area expands toward the trailing edge of the blade along the flow direction and expands toward the root of the blade along the span direction. It can be observed from

Figure 20 that as $NPSH_a$ decreases, the maximum value of TAPP gradually increases, and the risk of erosion becomes more serious.

5. Conclusion

Simulated and experimental methods were used to study the unsteady flow mechanism and cavitation erosion in a water-jet pump, and the following conclusions are obtained:

(1) The head of the water-jet pump calculated by using the DCM-SST turbulence model is 12.48 m. The calculation error at the rated head is 3.8%

(2) With the decrease of the net positive suction head, the position where the severe cavitation appears in the impeller domain gradually moves from the tip to the root

(3) The erosion region obtained by the erosion power method is similar to the cavity profile. As the net positive suction head decreases, the erodible area and the erosion intensity become larger

Data Availability

The data that support the findings of this study are available from the corresponding author upon reasonable request.

Conflicts of Interest

The authors declare that they have no conflicts of interest.

Acknowledgments

This study is supported by the National Natural Science Foundation of China (No. 51806082, No. 51906085, and No. U20A20292), National Key Research and Development Program of China (No. 2020YFC1512403), China Postdoctoral Science Foundation (No. 2020M671363, No. 2021T140282, and No. 2019M651734), Postdoctoral Science Foundation of Jiangsu Province (2020Z298), and Innovative and Entrepreneurial Doctor Program of Jiangsu Province (18SCBS016).

References

[1] W. Park, J. H. Jang, H. H. Chun, and M. C. Kim, "Numerical flow and performance analysis of waterjet propulsion system," *Ocean Engineering*, vol. 32, no. 14-15, pp. 1740–1761, 2005.

[2] Y. Wang, E. Hao, X. Zhao, Y. Xue, Y. An, and H. Zhou, "Effect of microstructure evolution of Ti6Al4V alloy on its cavitation erosion and corrosion resistance in artificial seawater," *Journal of Materials Science & Technology*, vol. 100, pp. 169–181, 2022.

[3] Z. Chen, H. Hu, X. Guo, and Y. Zheng, "Effect of groove depth on the slurry erosion of V-shaped grooved surfaces," *Wear*, vol. 488-489, 2022.

[4] L. M. Zhang, Z. X. Li, J. X. Hu et al., "Understanding the roles of deformation-induced martensite of 304 stainless steel in different stages of cavitation erosion," *Tribology International*, vol. 155, 2021.

[5] Q. N. Song, Y. Tong, H. L. Li et al., "Corrosion and cavitation erosion resistance enhancement of cast Ni-Al bronze by laser surface melting," *Journal of Iron and Steel Research International*, 2021.

[6] S. Hong, J. Lin, Y. Wu et al., "Cavitation erosion characteristics at various flow velocities in NaCl medium of carbide-based cermet coatings prepared by HVOF spraying," *Ceramics International*, vol. 47, no. 2, pp. 1929–1939, 2021.

[7] S. Hong, Y. Wu, J. Wu et al., "Microstructure and cavitation erosion behavior of HVOF sprayed ceramic-metal composite coatings for application in hydro-turbines," *Renewable Energy*, vol. 164, pp. 1089–1099, 2021.

[8] Y. Wang, H. Liu, S. Yuan, M. Tan, and K. Wang, "Experimental testing on cavitation vibration and noise of centrifugal pumps under off-design conditions," *Transactions of the Chinese Society of Agricultural Engineering*, vol. 28, no. 2, pp. 35–38, 2012.

[9] H. Wang, B. Long, C. Wang, C. Han, and L. Li, "Effects of the impeller blade with a slot structure on the centrifugal pump performance," *Energies*, vol. 13, no. 7, pp. 1628–1628, 2020.

[10] C. E. Brennen, *Cavitation and Bubble Dynamic*, Cambridge university press, 2013.

[11] W. Zhou, N. Qiu, L. Wang, B. Gao, and D. Liu, "Dynamic analysis of a planar multi-stage centrifugal pump rotor system based on a novel coupled model," *Journal of Sound and Vibration*, vol. 434, pp. 237–260, 2018.

[12] D. Tan, Y. Li, I. Wilkes, E. Vagnoni, R. L. Miorini, and J. Katz, "Experimental investigation of the role of large scale Cavitating Vortical Structures in performance breakdown of an axial Waterjet pump," *Journal of Fluids Engineering*, vol. 137, no. 11, article 111301, 2015.

[13] M. Motley, B. Savander, and Y. Young, "Influence of Spatially Varying Flow on the Dynamic Response of a Waterjet inside an SES," *International Journal of Rotating Machinery*, vol. 2014, Article ID 275916, 18 pages, 2014.

[14] L. Yun, Z. Yan, C. Jianping, Z. Rongsheng, and W. Dezhong, "A cavitation performance prediction method for pumps: Part2-sensitivity and accuracy," *Nuclear Engineering and Technology*, vol. 53, no. 11, pp. 3612–3624, 2021.

[15] Y. Long, C. Feng, L. Wang, D. Wang, Y. Cai, and R. Zhu, "Experiment on cavitation flow in critical cavitation condition of water-jet propulsion pump," *Journal of Beijing University of Aeronautics and Astronautics*, vol. 45, no. 8, pp. 1512–1518, 2019.

[16] H. Wu, D. Tan, R. L. Miorini, and J. Katz, "Three-dimensional flow structures and associated turbulence in the tip region of a waterjet pump rotor blade," *Experiments in Fluids*, vol. 51, no. 6, pp. 1721–1737, 2011.

[17] J. W. Lindau, D. A. Boger, R. B. Medvitz, and R. F. Kunz, "Propeller cavitation breakdown analysis," *Journal of Fluids Engineering*, vol. 127, no. 5, pp. 995–1002, 2005.

[18] J. Katz, "Cavitation phenomena within regions of flow separation," *Journal of Fluid Mechanics*, vol. 140, pp. 397–436, 1984.

[19] Q. Guo, X. Huang, and B. Qiu, "Numerical investigation of the blade tip leakage vortex cavitation in a waterjet pump," *Ocean Engineering*, vol. 187, 2019.

[20] R. Huang, B. Ji, X. Luo, Z. Zhai, and J. Zhou, "Numerical investigation of cavitation-vortex interaction in a mixed-flow waterjet pump," *Journal of Mechanical Science and Technology*, vol. 29, no. 9, pp. 3707–3716, 2015.

[21] R. Huang, W. Ye, Y. Dai et al., "Investigations into the unsteady internal flow characteristics for a waterjet propulsion

system at different cruising speeds," *Ocean Engineering*, vol. 203, 2020.

[22] R. Huang, A. Yu, B. Ji, J. Zhou, Z. Zhai, and X. Luo, "Cavitating flow features in a water-jet pump under different upstream conditions," in *16th International Symposium on Transport Phenomena and Dynamics of Rotating Machinery*, Honolulu, United States, 2016.

[23] R. Huang, Y. Dai, X. Luo, Y. Wang, and C. Huang, "Multi-objective optimization of the flush-type intake duct for a waterjet propulsion system," *Ocean Engineering*, vol. 187, 2019.

[24] S. Xu, X. Long, B. Jin, and G. Li, "Investigation on the mechanism between vortex and cavitation in an axial water-jet pump," *Journal of Harbin Engineering University*, vol. 41, no. 7, pp. 951–957, 2020.

[25] N. Qiu, W. Zhou, B. Che, D. Wu, L. Wang, and H. Zhu, "Effects of microvortex generators on cavitation erosion by changing periodic shedding into new structures," *Physics of Fluids*, vol. 32, no. 10, 2020.

[26] T. Momma and A. Lichtarowicz, "A study of pressures and erosion produced by collapsing cavitation," *Wear*, vol. 186-187, pp. 425–436, 1995.

[27] J. Franc, M. Riondet, A. Karimi, and G. L. Chahine, "Impact load measurements in an erosive cavitating flow," *Journal of Fluids Engineering*, vol. 133, no. 12, 2011.

[28] R. Knapp, "Recent investigations of the mechanics of cavitation and cavitation damage," *Transactions of the ASME*, vol. 77, pp. 1045–1054, 1955.

[29] M. Dular, O. C. Delgosha, and M. Petkovšek, "Observations of cavitation erosion pit formation," *Ultrasonics Sonochemistry*, vol. 20, no. 4, pp. 1113–1120, 2013.

[30] J. Wang, H. Liu, and M. Dular, "Experiment on cavitation erosion mechanism of centrifugal hydraulic cavitation generator," *Transactions of the Chinese Society of Agricultural Engineering*, vol. 33, no. 14, pp. 49–55, 2017.

[31] N. Ochiai, Y. Iga, M. Nohmi, and T. Ikohagi, "Study of quantitative numerical prediction of cavitation erosion in cavitating flow," *Journal of Fluids Engineering*, vol. 135, no. 1, 2013.

[32] A. Peters, H. Sagar, U. Lantermann, and O. el Moctar, "Numerical modelling and prediction of cavitation erosion," *Wear*, vol. 338-339, pp. 189–201, 2015.

[33] A. Peters, U. Lantermann, and O. el Moctar, "Numerical prediction of cavitation erosion on a ship propeller in model- and full-scale," *Wear*, vol. 408-409, pp. 1–12, 2018.

[34] F. Pereira, *Prediction de l'erosion de cavitation: approche energetique, [Ph.D. thesis]*, Ecole Polytechnique Federale de Lausanne, 1997.

[35] R. Fortes-Patella, G. Challier, J. Reboud, and A. Archer, "Energy balance in cavitation erosion: from bubble collapse to indentation of material surface," *Journal of Fluids Engineering*, vol. 135, no. 1, 2013.

[36] M. Dular and O. Coutier-Delgosha, "Numerical modelling of cavitation erosion," *International Journal for Numerical Methods in Fluids*, vol. 61, no. 12, pp. 1388–1410, 2009.

[37] O. Usta and E. Korkut, "Prediction of cavitation development and cavitation erosion on hydrofoils and propellers by detached eddy simulation," *Ocean Engineering*, vol. 191, 2019.

[38] Y. Long, C. An, R. Zhu, and J. Chen, "Research on hydrodynamics of high velocity regions in a water-jet pump based on experimental and numerical calculations at different cavitation conditions," *Physics of Fluids*, vol. 33, 2021.

[39] H. Wang, Q. Hu, Y. Yang, and C. Wang, "Performance differences of electrical submersible pump under variable Speed Schemes," *International Journal of Simulation Modelling*, vol. 20, no. 1, pp. 76–86, 2021.

[40] L. Shi, J. Zhu, F. Tang, and C. Wang, "Multi-disciplinary optimization design of axial-flow pump impellers based on the approximation model," *Energies*, vol. 13, no. 4, p. 779, 2020.

[41] P. Zwart, A. Gerber, and T. Belamri, "A Two-Phase Flow Model for Predicting Cavitation Dynamics," in *Fifth International Conference on Multiphase Flow*, p. 152, Yokohama, 2004.

[42] J. Zhou, M. Zhao, C. Wang, and Z. Gao, "Optimal design of diversion piers of lateral intake pumping station based on orthogonal test," *Shock and Vibration*, vol. 2021, Article ID 6616456, 9 pages, 2021.

[43] L. Chen, *Study on Cloud Cavitation Control by Bionic Leading-Edge Tubercles on Hydrofoil*, Zhejiang University, Hangzhou, 2020.

[44] L. Zhang, C. Wang, Y. Zhang, W. Xiang, Z. He, and W. Shi, "Numerical study of coupled flow in blocking pulsed jet impinging on a rotating wall," *Journal of the Brazilian Society of Mechanical Sciences and Engineering*, vol. 43, p. 508, 2021.

[45] Y. Zhao, G. Y. Wang, B. Huang, C. L. Hu, G. H. Chen, and Q. Wu, "Vortex dynamic analysis of unsteady cavitating flows around a hydrofoil," *Journal of Ship Mechanics*, vol. 8, pp. 896–904, 2015.

[46] H. Zhu, N. Qiu, C. Wang et al., "Prediction of Cavitation Evolution and Cavitation Erosion on Centrifugal Pump Blades by the DCM-RNG Method," *Scanning*, vol. 2021, Article ID 6498451, 12 pages, 2021.

[47] Z. Li, M. Pourquie, and T. van Terwisga, "Assessment of cavitation erosion with a URANS method," *Journal of Fluids Engineering*, vol. 136, no. 4, 2014.

[48] J. E. Higham, W. Brevis, and C. J. Keylock, "Implications of the selection of a particular modal decomposition technique for the analysis of shallow flows," *Journal of Hydraulic Research*, vol. 56, no. 6, pp. 796–805, 2018.

[49] J. Wang, *Numerical Simulation and Experimental Tests for Cavitation and Induced Erosion in Hydraulic Apparatus*, Jiangsu University, Zhenjiang, 2015.

[50] B. Che, *Research on the Mechanism and Passive Control of Attached Cavitation on Hydrofoil*, Zhejiang University, Hangzhou, 2019.

[51] Y. Zhu, G. Li, R. Wang, S. Tang, H. Su, and K. Cao, "Intelligent fault diagnosis of hydraulic piston pump combining improved lenet-5 and pso hyperparameter optimization," *Applied Acoustics*, vol. 183, article 108336, 2021.

Hindawi
Scanning
Volume 2021, Article ID 6498451, 12 pages
https://doi.org/10.1155/2021/6498451

Research Article

Prediction of Cavitation Evolution and Cavitation Erosion on Centrifugal Pump Blades by the DCM-RNG Method

Han Zhu[1], **Ning Qiu**[1], **Chuan Wang**[2,3], **Qiaorui Si**[1], **Jie Wu**[1], **Fanjie Deng**[1] and **Xiang Liu**[1]

[1]*National Research Center of Pumps, Jiangsu University, Zhenjiang, 212013 Jiangsu, China*
[2]*Hainan Vocational University of Science and Technology, Haikou, 571126 Hainan, China*
[3]*College of Hydraulic Science and Engineering, Yangzhou University, Yangzhou, 225009 Jiangsu, China*

Correspondence should be addressed to Ning Qiu; qiuning@ujs.edu.cn

Received 29 September 2021; Revised 17 October 2021; Accepted 22 October 2021; Published 15 November 2021

Academic Editor: Qiao Yanxin

Cavitation can reduce the efficiency and service life of the centrifugal pumps, and a long-term operation under cavitation conditions will cause cavitation damage on the surface of material. The external characteristic test of the IS65-50-174 single-stage centrifugal pump was carried out. Moreover, the cavitation mechanism under specific conditions was analyzed by numerical simulation. Considering the macroscopic cavitation flow structure in the centrifugal pump, three different cavitation erosion prediction methods were used to predict the erodible areas. The results show that the calculation results obtained by the density correction method (DCM) can well match the flow characteristics of the centrifugal pump under the rated conditions. When the centrifugal pump head drops by 3%, cavitation mainly occurs on the suction surface, and the cavity on the pressure surface is mainly concentrated near the front cover. The cavitation prediction method based on the time derivation of pressure change is not suitable for centrifugal pumps, while the prediction result of the erosive power method is more reasonable than the others. At time 0.493114 s, the maximum erosive power appears on the blade near the volute tongue, and its value is $1.46e-04$ W.

1. Introduction

Cavitation is a common phenomenon in centrifugal pumps. When the centrifugal pump is running, the liquid pressure in local areas will be lower than the saturated vapor pressure at the operation temperature, resulting in cavitation [1]. The area of blade surface where cavitation occurs will be damaged under the repeated action of impact load, as shown in Figure 1. At the same time, it will also cause increased noise and severe vibration of the centrifugal pump [2, 3]. Therefore, it is of great significance to carry out cavitation erosion research on centrifugal pumps [4–6].

So far, researchers from various countries have studied the cavitation erosion by experimental and numerical methods [7–10]. Dular et al. [11] used PIV and PLIF technology to measure the internal cavitation flow field of the centrifugal pump and obtained the transient and time-averaged velocity field and vapor volume fraction distribution around the blade. Bilus and Predin [12] studied the effect of installing a rectifier on the inlet pipe on the cavitation performance of the centrifugal pump through experiments, and the use of the rectifier improved the cavitation state. Bachert et al. [13] used PIV testing technology combined with high-speed cameras to study cloud-like cavitation at the volute tongue of centrifugal pumps and explored the reasons for the deterioration of centrifugal pump performance under high flow rate conditions. Wang et al. [14] studied the cavitation at the inlet of the centrifugal pump impeller and initially obtained the relationship between the cavitation distribution in the impeller and the vibration and noise characteristics of the pump. Fu et al. [15] used high-speed photography and pressure

Figure 1: Cavitation erosion in the centrifugal pump.

pulsation measurement technology to systematically analyze the low-frequency cavitation-induced pulsation characteristics of centrifugal pumps under low flow rate conditions.

It is challenging to use experimental methods to study cavitation and the unsteady evolution of cavitation in complex hydraulic machinery. At the same time, there are also difficulties in accurately measuring the velocity flow field of the reentrant flow, and capturing the vortex structure of the shedding cavity. Compared with the experiment, more flow field details can be obtained by numerical simulation, offering a better explaining of the cavitation mechanism. Based on the three-component continuity equation of liquid phase, vapor phase, and noncondensable gas, Hong [16] constructed a nonlinear cavitation model and calculated the cavitation flow field in the axial flow pump. Caridad et al. [17] used numerical simulation to study the cavitation phenomenon of centrifugal pumps under unsteady-state conditions. The accumulation of cavitation caused blockage of the flow channel and increased hydraulic loss. Through numerical simulation, Tan et al. [18] found that under unsteady conditions, the internal cavitation of the centrifugal pump impeller has less effect on the flow pattern under bean flow rate than low flow rate influence. Wang et al. [19] established the RZGB cavitation model considering the rotation effect, the structural characteristics of large curvature, and the compressibility of the liquid when studying the cavitation flow field in the centrifugal pump.

Based on the microjet method, Peters et al. [20] made a prediction of cavitation erosion on a NACA0009 hydrofoil. Wang [21] proposed a cavitation prediction method based on *Matlab* image processing of cavitation clouds in the centrifugal pump. Their results show that the cavitation location in the centrifugal pump is basically the same as the cavitation erosion area. Li et al. [22] conducted a comparative analysis of the erodible area on the NACA0015 hydrofoil based on the first-order deviation of pressure versus time and proved that this method can better match the erodible area on the hydrofoil. Through experiments, Qiu et al. [23] compared the cavitation erosion of NACA0015 hydrofoils with different leading-edge structures and conducted a quantitative analysis of the cavitation impact energy. Usta et al. [24] compared the differences between the Intensity Function Method, Gray level Method, and Erosive Power Method. Then, they compared and predicted the erosion area on a propeller. The results show that the EPM method has advantages in predicting propeller cavitation erosion.

In this paper, the density-corrected RNG $k-\varepsilon$ model was used for cavitation simulation, and three different cavitation erosion prediction methods were used to predict cavitation erosion on the blade surface of the centrifugal pump.

Table 1: The main parameters of test pump.

Parameter	Value
Design flow rate (Q_d)	50 m^3/h
Design head rise (H_d)	34 m
Rotational speed (n)	2900 rpm
Number of blades	6
Specific speed	88.6
Outlet width of impeller (d)	12 mm
Outlet pipe diameter of pump (D_d)	65 mm
Inlet pipe diameter (D_s)	74 mm
Impeller diameter (D_2)	174 mm

2. Centrifugal Pump Parameters and Experimental Setup

In this paper, a single-stage centrifugal pump of type IS65-50-174 was studied. The main parameters of this test pump are shown in Table 1.

The experiments were finished at the Research Center of Fluid Machinery Engineering Technology of Jiangsu University, and the system is shown in Figure 2. The system is mainly composed of two parts: water circulation circuit and data acquisition system.

3. Numerical Simulation Methods

3.1. Continuity Equation and Momentum Equation. In the simulation, the vapor-liquid two-phase flow is generally assumed to be homogeneous. The Navier-Stokes equation based on the Newtonian fluid was used in this simulation. The equation is formulated in the Cartesian coordinate system as

$$\frac{\partial \rho_m}{\partial t} + \frac{\partial \left(\rho_m u_j\right)}{\partial x_j} = 0,$$

$$\frac{\partial (\rho_m u_i)}{\partial t} + \frac{\partial \left(\rho_m u_i u_j\right)}{\partial x_j} = -\frac{\partial p}{\partial x_i} + \frac{\partial}{\partial x_j} \times \left[(\mu_m + \mu_T) \left(\frac{\partial u_i}{\partial x_j} + \frac{\partial u_j}{\partial x_i} - \frac{2}{3} \frac{\partial u_i}{\partial x_j} \delta_{ij} \right) \right],$$

$$\frac{\partial \rho_l \alpha_l}{\partial t} + \frac{\partial \left(\rho_l \alpha_l u_j\right)}{\partial x_j} = m^+ + m^-,$$

$$\rho_m = \rho_l \alpha_l + \rho_v \alpha_v,$$

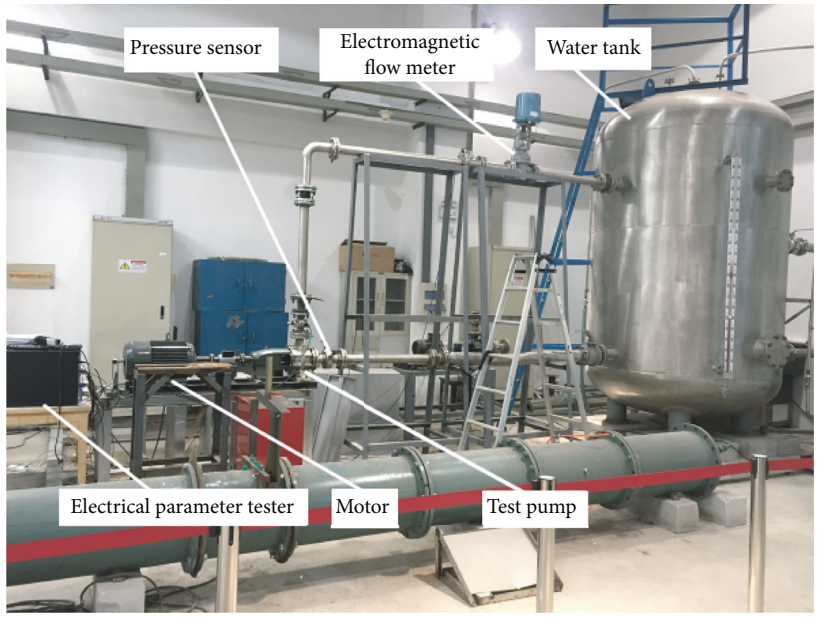

Figure 2: Cavitation test rig.

$$\mu_m = \mu_l \alpha_l + \mu_v \alpha_v, \tag{1}$$

where the subscript i, j indicates the coordinate direction, u indicates the velocity, p indicates the pressure, ρ_l indicates the liquid density, ρ_v indicates the vapor density, α_v indicates the vapor volume fraction, α_l indicates the liquid volume fraction, μ_l indicates the liquid laminar viscosity, μ_v indicates the vapor laminar viscosity, μ_T indicates the turbulent viscosity, m^+ indicates the vapor condensation rate, and m^- indicates the vapor evaporation rate. ρ_m denotes vapor-liquid mixed-phase density, μ_m denotes vapor-liquid mixed-phase laminar viscosity, t indicates the time, x_i, x_j are the coordinates in the i and j directions, and δ_{ij} indicates the shear stress.

3.2. Cavitation Model. The Zwart model [25, 26] is a cavitation model based on the mass transport equation, which describes the cavitation phase change process mainly by establishing the transport relationship between the vapor and liquid phases. Its evaporation rate m^+ and condensation rate m^- are defined as follows:

$$\begin{aligned} m^+ &= C_{\text{dest}} \frac{3\alpha_{\text{nuc}}(1-\alpha_v)\rho_v}{R_B} \left(\frac{2}{3}\frac{p_v - p}{\rho_l}\right)^{1/2}, \quad p < p_v, \\ m^- &= -C_{\text{prod}} \frac{3\alpha_v \rho_v}{R_B} \left(\frac{2}{3}\frac{p - p_v}{\rho_l}\right)^{1/2}, \quad p > p_v. \end{aligned} \tag{2}$$

In the formula, R_B is the bubble radius, α_{nuc} is the volume fraction of gas nuclei, p_v is the saturated vapor pressure, C_{prod} is the rates of steam condensation when the local static pressure is greater than the saturation steam pressure, and C_{dest} is the rate of steam evaporation when the local static pressure is lower than the saturated vapor pressure. The values of the coefficients in the model are [25] $R_B = 1 \times 10^{-6} m$, $C_{\text{prod}} = 0.01$, $C_{\text{dest}} = 50$, and $\alpha_{\text{nuc}} = 1 \times 10^{-4}$.

3.3. Turbulence Model. This simulation was based on the RNG $k-\varepsilon$ turbulence model. To more accurately simulate the development of cavitation in the centrifugal pump, the compressibility of the mixing of the vapor and liquid phases was considered, and the mixed density was corrected by the density corrected method (DCM). Turbulent viscosity is defined as follows:

$$\begin{aligned} f_{\text{DCM}} &= \rho_v + \left(\frac{\rho_m - \rho_v}{\rho_l - \rho_v}\right)^N \cdot (\rho_l - \rho_v), \\ \mu_{\text{T-DCM}} &= \frac{C_\mu k^2}{\varepsilon} f_{\text{DCM}}, \end{aligned} \tag{3}$$

where N is taken as 10 according to literature recommendations [27].

3.4. Numerical Setup and Grid Validation. Water temperature of experiment and simulation was maintained at about 23.5°C. Figure 3 shows the calculation domain and boundary conditions. In order to avoid the inlet and outlet reflux of the calculation domain, an inlet expansion pipe was set before the impeller calculation domain, and an outlet expansion pipe was set after the volute calculation domain. The walls of the extension were all set as nonslip walls. The inlet was set as a pressure inlet with a value of 1 atm. Moreover, the outlet was set as a mass flow rate outlet with a value of 50 m^3/h. The wall surface roughness of the impeller and volute was set to 0.03 mm. Furthermore, the impeller was set as a rotating domain with a speed of 2900 rpm, and the other parts were set as the static domains.

The calculation model was divided into hexahedral structure using *ANSYS ICEM* software. In order to reduce

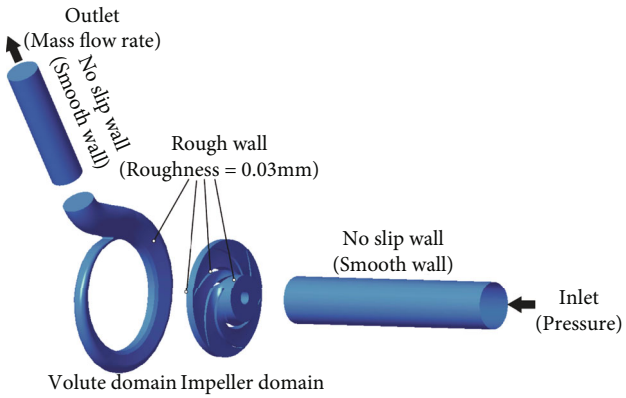

Figure 3: The calculation domain.

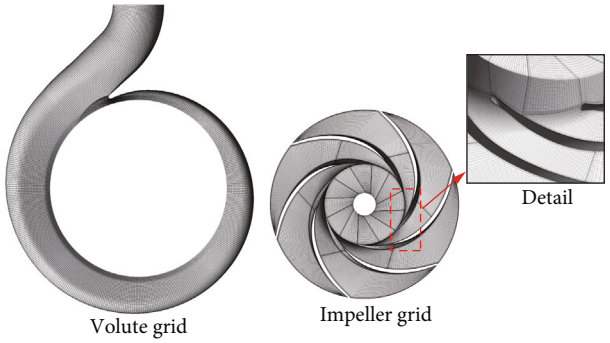

Figure 4: The detail of grid.

Table 2: The information of mesh.

	Grid number
Mesh 1	1429074
Mesh 2	1683736
Mesh 3	2087120
Mesh 4	2538949
Mesh 5	3331173
Mesh 6	4114547

the interference of the grid quality on the simulated performance of the centrifugal pump, the near-wall area of the blade was meshed densely to better control the grid structure of the boundary. The grid details are shown in Figure 4. Considering the influence of the grid on the calculation, the RNG $k-\varepsilon$ turbulence model was used to analyze the grid independence of the computational domain. Table 2 shows the grid information of the computational domain. The change of head is used as the criterion for judging the applicability of the grid.

$$\text{Head} = \frac{P_{\text{out}} - P_{\text{in}}}{\rho g}. \tag{4}$$

Figure 5 shows the head changes under different grid conditions. It can be seen that as the number of grids increases, the head tends to be stable. Considering the computing duration and resources, final option 4 with a mesh

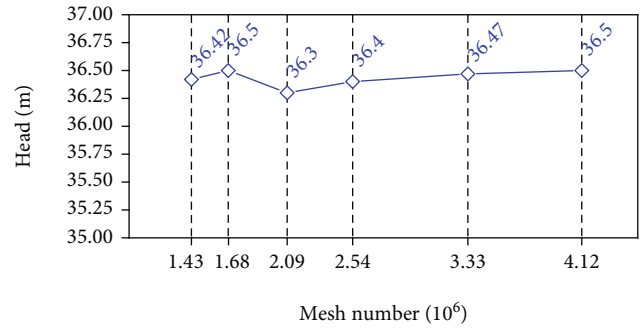

Figure 5: The head under different mesh number.

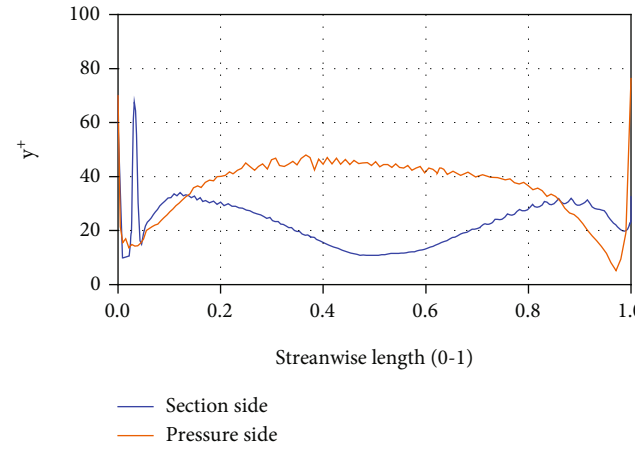

Figure 6: y^+ on the blades.

number of 2538949 was selected for calculation. Under this scheme, the y^+ value of the near-wall surface of the blade is within 100, which meets the calculation requirements of the RNG $k-\varepsilon$ turbulence model, as shown in Figure 6.

4. Results and Discussion

4.1. Experimental Verification and Steady Analysis. Under the conditions of rated flow and speed, the simulated head is 36.39 m and the experimental result is 35.71 m. The relative error is 2%, indicating that the simulation has high reliability.

Figure 7 shows the cavitation performance curve of the test pump. At the rated flow rate, the inlet pressure of the centrifugal pump was reduced by adjusting the vacuum tank. With the pressure gradually reduced, a set of heads and net positive suction heads were obtained, and the cavitation performance curve can be obtained. The net positive suction head calculation formula is

$$\text{NPSH}_a = \frac{p_s}{\rho g} + \frac{v_s^2}{2g} - \frac{p_v}{\rho g}. \tag{5}$$

In engineering, it is generally believed that when the head drops by 3%, the cavitation in the pump is in a critical state, and the performance of the centrifugal pump drops sharply at this state. It can be seen from Figure 7 that the

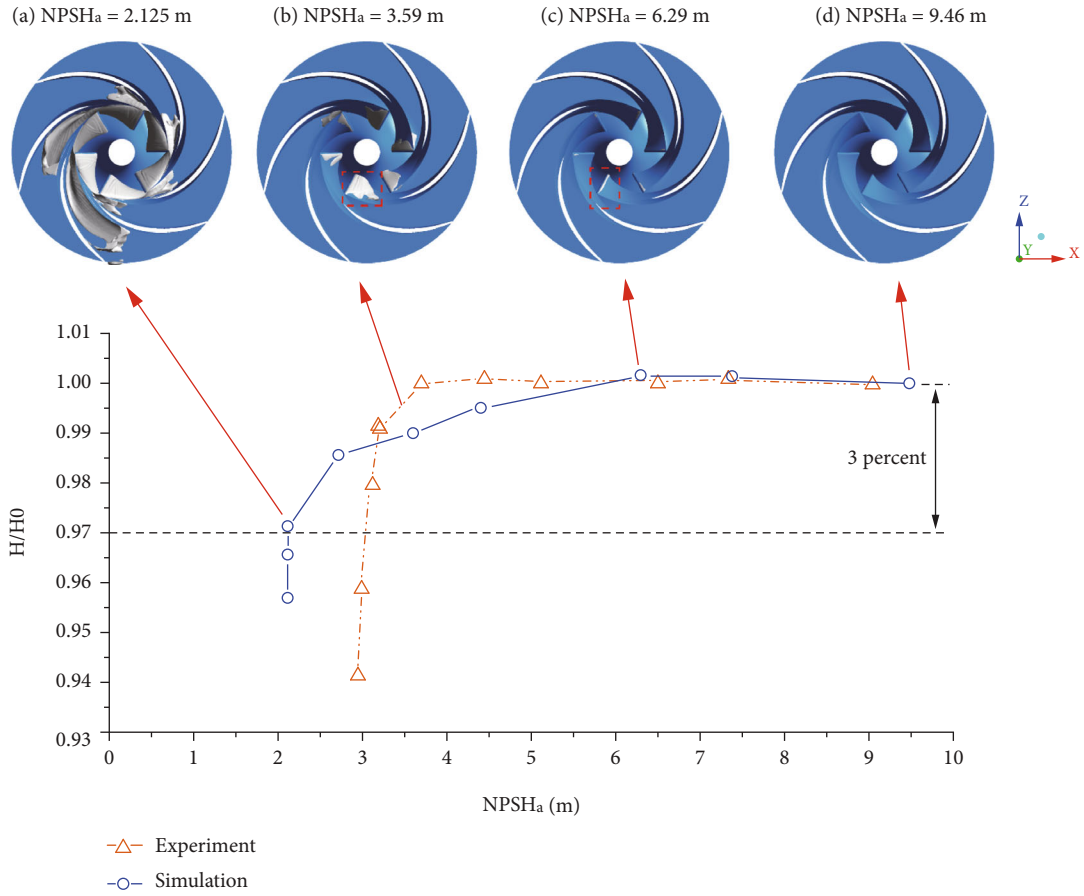

Figure 7: Cavitation performance curve. (vapor volume fraction is used for showing the cavitation evolution; isosurface = 0.1)

experimental results show that the net positive suction head is about 3 m when the head drops by 3%, and the simulation result is about 2.12 m. The critical $NPSH_a$ obtained by simulation is slightly smaller than the experimental result. The reason may be that the simulation calculation is in an ideal working state with less interference. Figures 7(a)–7(d) show the simulated cavitation distribution under different $NPSH_a$. In the initial stage, when $NPSH_a = 9.46$ m, there is no cavitation in the centrifugal pump. As the inlet pressure decreases, the $NPSH_a$ drops to 6.29 m. A slender cavitation zone attached to the suction surface appears on the inlet side of the blade. When the pressure is further reduced, the covered area of the cavity attached to the blade becomes larger, which affects the stability of the flow in the pump to a certain extent, resulting in a drop in the head of the centrifugal pump, as shown in Figure 7(c). At this state, the head is about 99% of the noncavitation head. During the evolution of cavitation, the cavity will gradually become larger and thicker. When $NPSH_a = 2.125$ m, the centrifugal pump head is 3% lower than the noncavitation, as can be seen in Figure 7(d). At this state, the cavitation area fills the entire flow channel and the blocking directly leads to a sharp drop in pump performance.

4.2. Analysis of the Unsteady Cavitation Performance. An unsteady simulation of the internal flow field when $NPSH_a = 2.125$ m under the rated flow was performed. The total duration of unsteady calculation was set to 0.4138 s (the time required for 20 cycles of the impeller rotation), and the time step was set to 0.00022989 s (the case calculated after each 1/90 cycle of impeller rotation). One to ten times iteration was chosen to make the calculation reach the convergence accuracy. The convergence accuracy was set to 0.0001 to ensure the reliability of unsteady calculations. After the impeller rotated 20°, a result file was saved.

Figure 8 shows the liquid phase streamlines and cavitation volume fraction at span = 0.5 during one cycle of the impeller rotation. The streamline near the pressure surface of the blade is neat, but the streamline near the suction surface has some vortexes, as shown in the red dashed area in the figure. The evolution of the vortexes presents obvious unsteady characteristics. A large recirculation zone appears near the exit of the flow channel E. When the time progresses from 2/6 T to 3/6 T, the three vortexes in the flow channel E merge one again and continue to grow over time, while the center of the vortex moves to the outlet of the flow channel. The existence of vortexes reflects the instability of the flow. And the instability of flow is an important reason that affects the performance of the centrifugal pump, especially the drop in head and efficiency. It can be seen from the figure that there is an obvious boundary between the vortex structure and the cavitation structure, and the vortex zone appears behind the vapor phase region. Cavitation occurs on the suction surface of the blade and develops

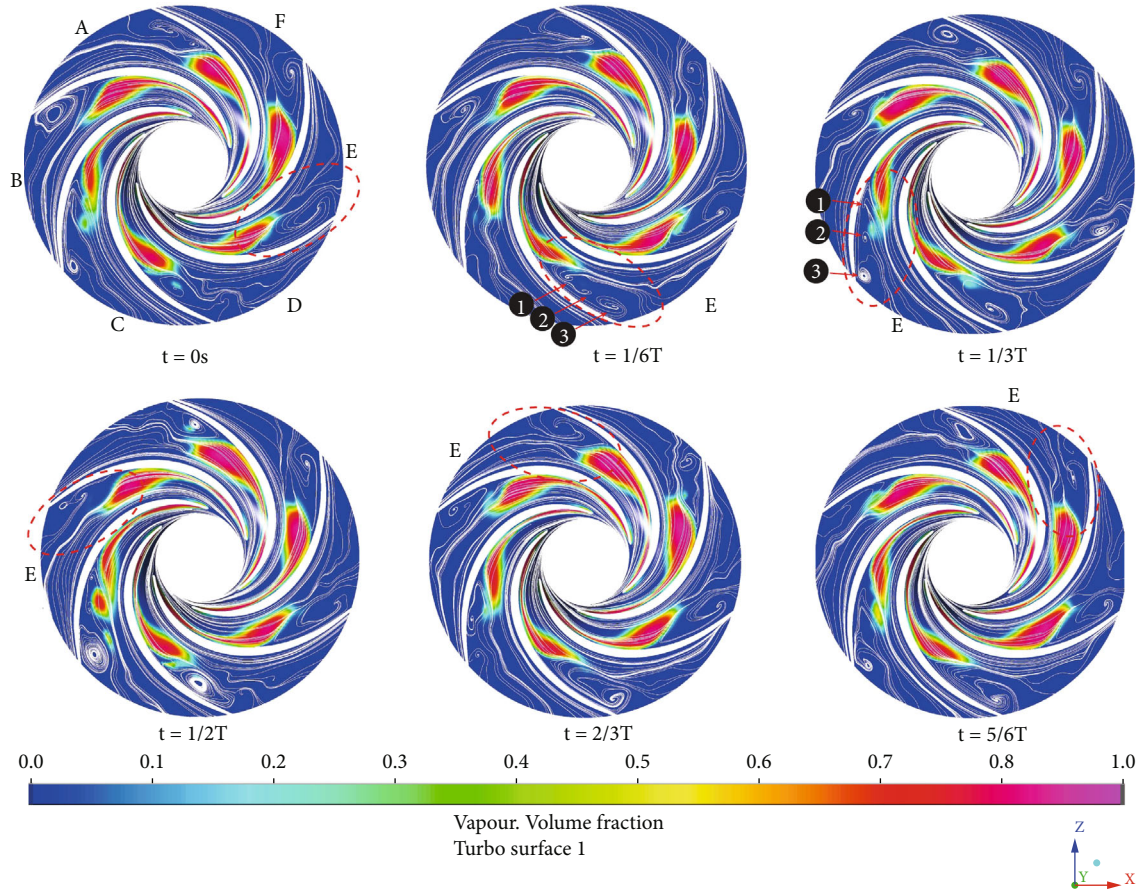

Figure 8: The streamline of water superficial velocity and the vapor volume fraction on span = 0.5 turbo surface.

backward. It is attached to the blades and gradually becomes longer and thicker. At the same time, the attached cavity will roll away from the blade in the closed area of the cavitation at the tail and begin to block the flow path due to the rotation of the impeller. The existence of cavities changes the flow filed, and a velocity vortex is formed behind the cavities.

Figure 9 shows the mean value distribution of each parameter in the impeller shaft surface at a typical time t = 3/6 T. It can be seen from Figures 9(a) and 9(b) that water enters from the impeller inlet and the pressure is low. With the rotation of the blades, the pressure in the flow channel shows an overall upward trend and exceeds 80,000 Pa at the impeller outlet. The fluid velocity near the hub is relatively low, maintaining between 0 and 7 m/s. A certain degree of backflow exists, resulting in lower pressure in this area than in other areas of the impeller inlet, as shown in region 2. There is irregular low-pressure region 1 near the front cover, and cavitation will mainly occur in this area, as shown in Figure 9(c). At the same time, it can be seen that at a position closer to the outlet, a certain range of low-speed area appears. Some vortexes appear in the middle and downstream of the impeller flow channel. Due to the unstable flow, the average velocity in this area is low. It can be seen from Figure 9(c) that the cavitation is irregularly distributed and is basically consistent with the shape of the low-pressure zone. The most severe area of cavitation is located near the front cover, and the cavitation volume fraction gradually decreases from the front cover to the rear cover. There is only a small amount of cavitation at the root of the blade near the rear cover.

Figure 9(d) shows the expanded view of the cavitation volume fraction on the blade at this moment. It can be seen from the figure that on the cross section of span = 0.2, cavitation is mainly distributed on the suction surface of the blade, in the form of attached cavitation. On the cross-section of span =0.5, the attached cavities on the suction surface become longer in the chord length direction of the blade and shell at the closure of the attached cavities. A small area of cavitation appears on the pressure side of the blade inlet. On the cross-section of span = 0.8, the cavitation on the pressure side of the blade is severe. And then, cavitation on the pressure side and cavitation on the suction side gather together, completely blocking the flow channel.

Figure 10 shows the volume fraction distribution of cavitation on different spans of a typical blade. Comparing Figures 10(a) and 10(b), it can be seen that in the same span, the cavitation coverage length of the suction surface is greater than that of the pressure surface, indicating that cavitation mainly occurs on the suction surface of the blade. It can be seen from Figure 10(a) that the cavitation volume fraction on the span = 0.8 is greater than span =0.5 and 0.2 when streamwise length is between 0 and 0.4. The maximum cavitation volume fraction is 0.94 at span = 0.8, the maximum cavitation volume fraction is 0.93 at span = 0.5, and

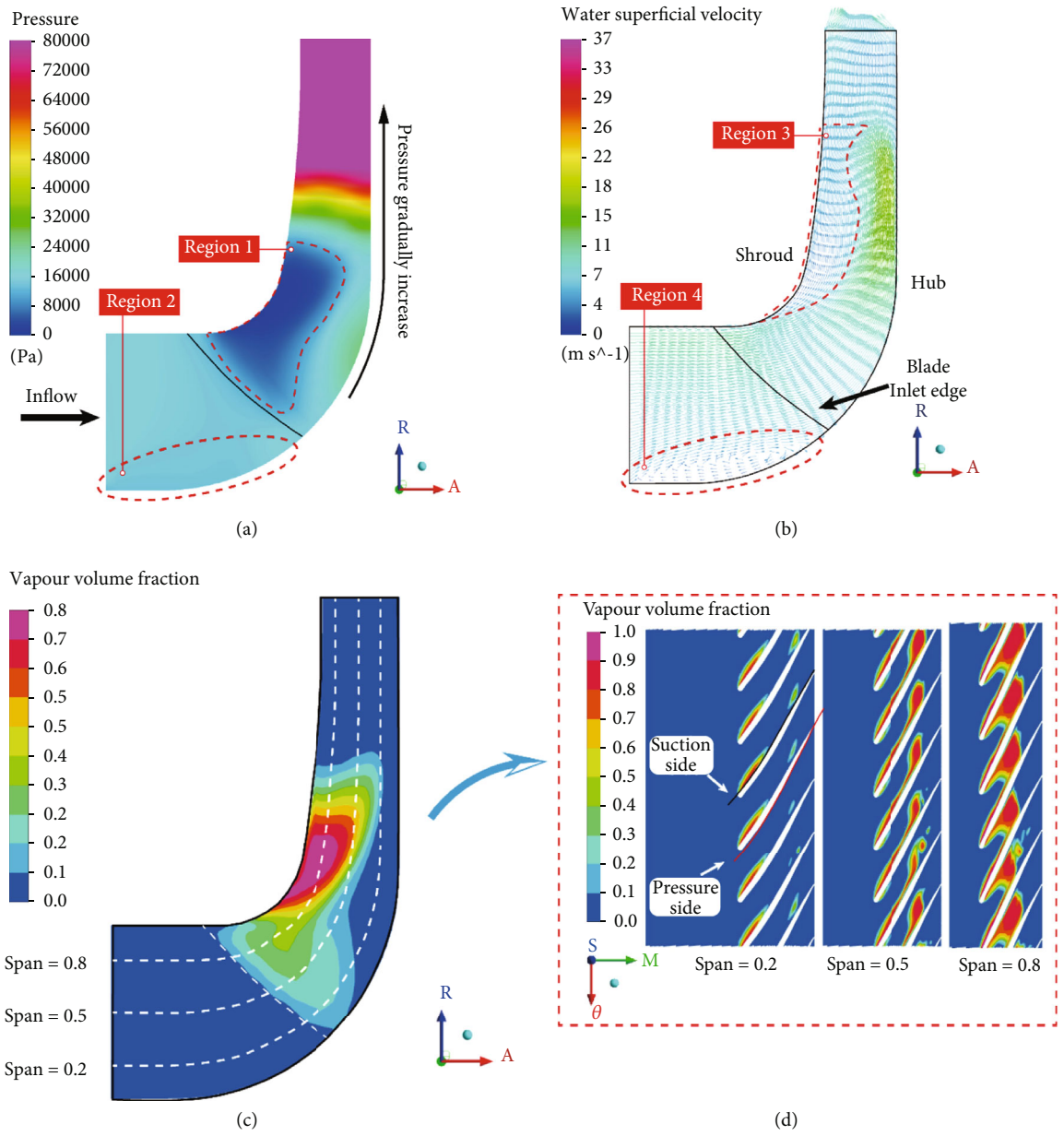

FIGURE 9: The mean distribution on the impeller shaft surface. (a) Pressure. (b) Velocity. (c) Vapor volume fraction.

the maximum cavitation volume fraction is 0.89 at span = 0.2. The three maximum values all appear near the inlet edge of the blade. As the streamline length moves from the inlet to the outlet, the cavitation volume fraction gradually decreases and then increases again. The secondary peak of the cavitation volume fraction at span = 0.8 is 0.81, and the secondary peak at span = 0.5 is 0.76, and the secondary peak at span = 0.2 is only 0.26. It can be seen from Figure 10(b) that the cavitation volume fraction on the pressure surface span = 0.8 is above zero with a streamwise length between 0 and 0.4, and on the span = 0.5, it is streamwise distributed between 0 and 0.2; and the streamwise distribution is between 0 and 0.07 at span = 0.2. These indicate that on the pressure surface, cavitation is more likely to occur near the front cover.

4.3. Cavitation Erosion Prediction on Centrifugal Pump Blades. It is based on the simulation method of VOF (Figure 11) to predict cavitation erosion. Cavitation erosion is a microscopic and transient process, but it is also affected by macroscopic flows. From the energy point of view, the collapse of the cavitation bubble will produce a pressure pulse. This pressure wave is one of the factors that cause cavitation damage, as shown in Figure 12. Pressure waves can be generated by the collapse. Based on the hypothesis of Qiu et al. [23, 28–32], the potential energy of the cavity structure is defined as

$$E_{\text{pot}} = \Delta p \times V_{\text{vap}},$$
$$\Delta p = (p - p_{\text{sat}}). \tag{6}$$

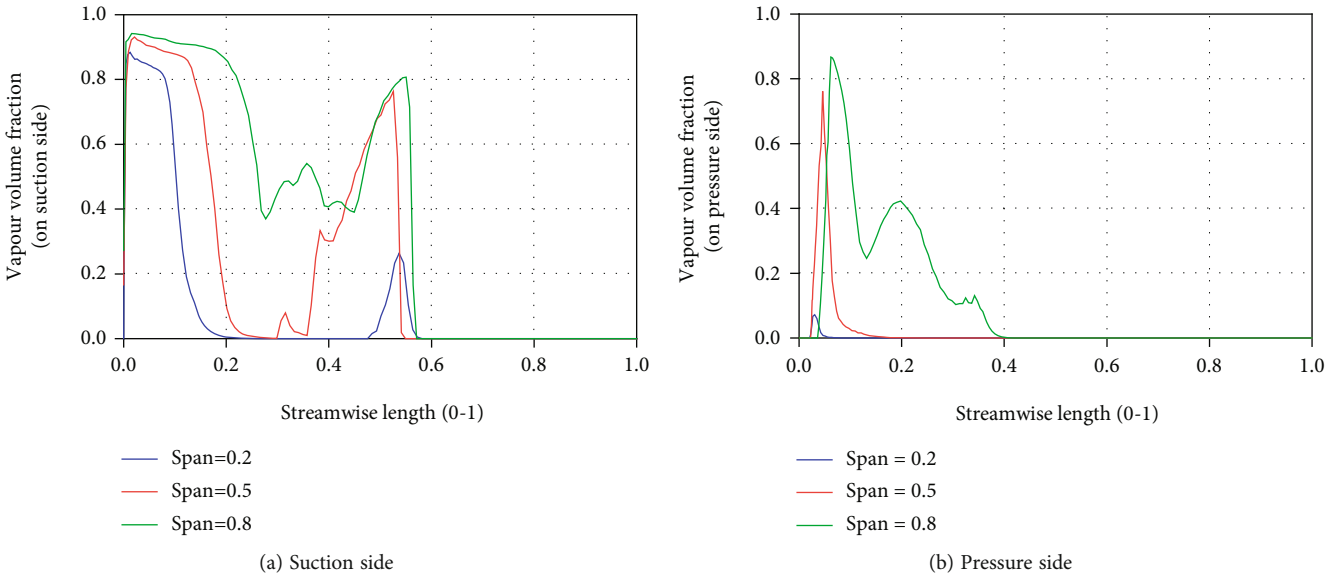

(a) Suction side (b) Pressure side

Figure 10: Distribution of cavitation volume fraction on a typical blade (t = 3/6 T).

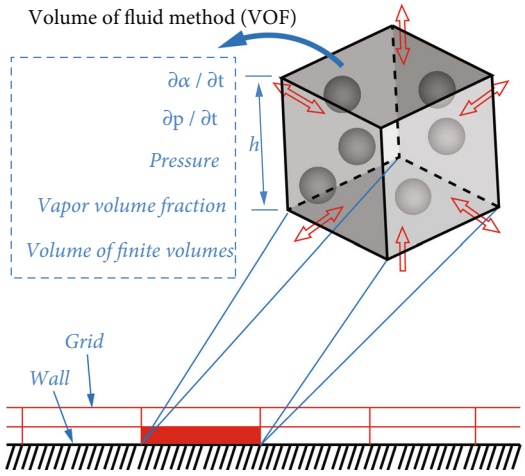

Figure 11: The simulation method based on VOF.

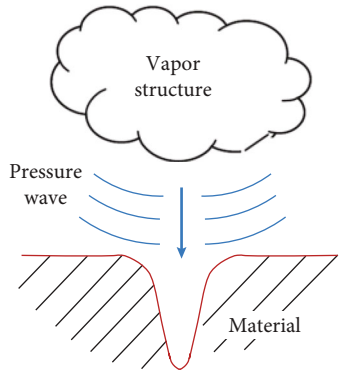

Figure 12: The occurrence of cavitation erosion.

According to the definition of potential energy, the erosive power function can be constructed. The cavitation volume is reduced when cavity collapses and the pressure wave is released. The erosive power function p_{pot} can be defined as

$$p_{pot} = \frac{\partial E_{pot}}{\partial t} = \Delta p \times \frac{\partial V_{vap}}{\partial t} + V_{vap} \times \frac{\partial \Delta p}{\partial t} = (p - p_{sat}) \times V_{cell} \times \frac{\partial \alpha}{\partial t} + V_{cell} \times \alpha \times \frac{\partial p}{\partial t}, \quad \text{if } P_{pot} \geq \varepsilon_{pot}, \tag{7}$$

$$\alpha = \frac{V_{vap}}{V_{cell}} = \frac{\rho - \rho_l}{\rho_v - \rho_l}. \tag{8}$$

Li et al. [22] used the method of pressure change rate, and the cavitation intensity function $I_{pressure}$ is defined as

$$I_{pressure} = \frac{dp}{dt}, \quad \text{if } I_{pressure} \geq \varepsilon_{pressure}. \tag{9}$$

Dular et al. [11] proposed a method for predicting cavitation erosion based on the volume of the cavity. The cavitation erosion function I_{vapor} is defined as

$$I_{vapor} = \frac{dV_v}{dt}(p - p_v), \quad \text{if } I_{vapor} \geq \varepsilon_{vapor}. \tag{10}$$

In the formula, p is the pressure surrounding the vapor (Pa); p_{sat} is the saturated steam pressure (Pa); V_{vap} is the vapor volume (m^3); V_{cell} is the volume of the grid (m^3); α is vapor volume fraction; and $\varepsilon_{pressure}$, ε_{pot}, and ε_{vapor} are threshold.

Figure 13 shows the time evolution of erosion parameters on a typical blade. It can be seen from the figure that the values of *surface-averaged dp/dt* and *surface-averaged d a/dt* present obvious periodic characteristics, and the time of each cycle is about 0.0207 s, which is consistent with the time of one revolution of the impeller. This phenomenon

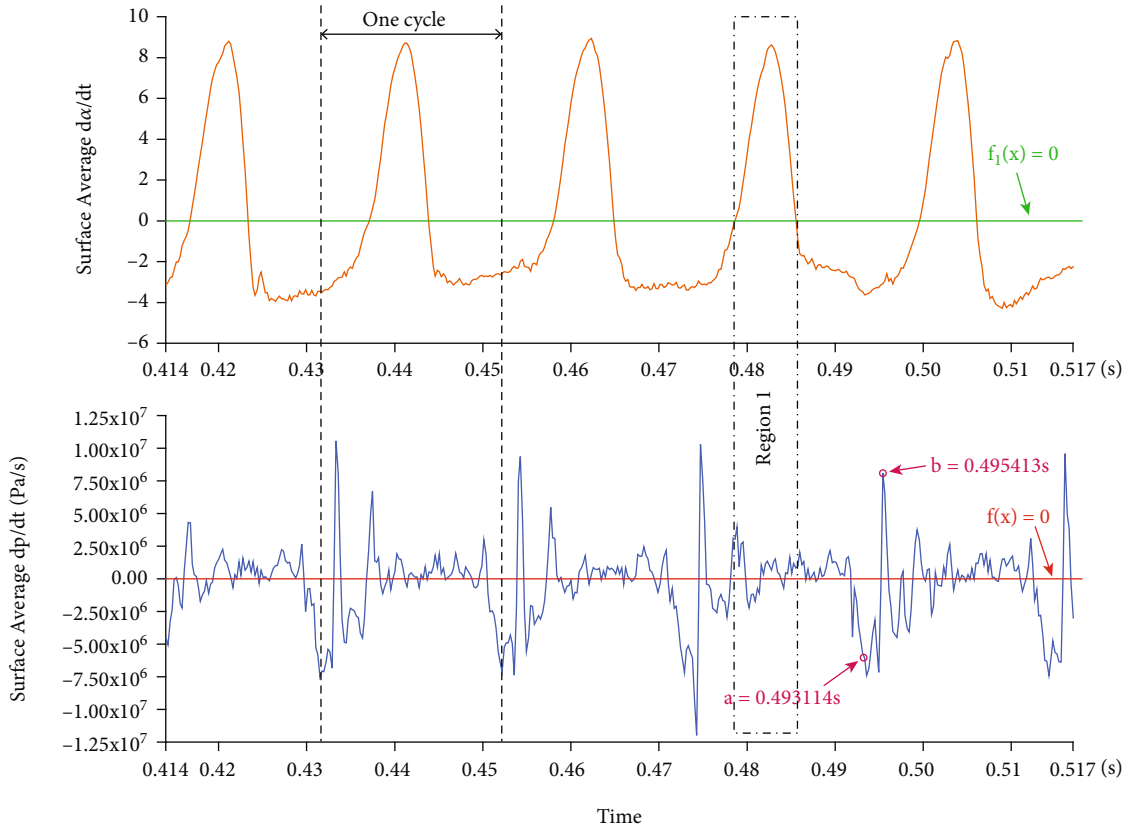

Figure 13: Time evolution of erosion parameters on a typical blade.

reflects the unsteady characteristics of the cavitation in the pump. With the rotation of the impeller, the cavitation in the pump changes continuously. *Surface-averaged da/dt* fluctuates around $f_1(x) = 0$. When the value is greater than 0, the cavitation coverage area near the blade becomes larger. Similarly, *surface-averaged dp/dt* fluctuates around $f(x) = 0$. When the value is less than 0, it indicates that at this moment, the covered cavity has caused the average surface pressure to decrease. The fluctuation of *surface-averaged dp/dt* is small when the value of *surface-averaged da/dt* is above 0, as shown in region 1 in the figure. When the *surface-averaged da/dt* is less than 0, the cavitation coverage area decreases, and the *surface-averaged dp/dt* appears maximum and minimum values in a single cycle. In order to better predict the cavitation erosion situation in the pump, as shown in Figure 14, two typical moments $a = 0.493114$ s and $b = 0.495413$ s are selected for analysis. The selected typical blade is located at the H position at time *a* and h position at time *b*.

Based on the simulation results, three methods are used to predict the cavitation erosion distribution on a typical blade, and the thresholds are set to 0. The result is shown in Figure 15. It can be seen from the figure that the erodible area predicted by I_{pressure} is in the middle and downstream of the blade (shown in region 3 in the figure), and there is no cavitation coverage in this area. At the same time, there is a small erodible area at the entrance of the blade (shown in region 1 in the figure). Compared with Figure 15(1), it

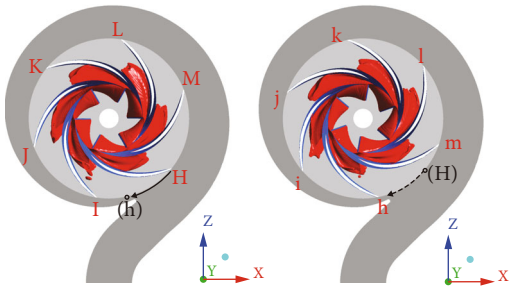

Figure 14: Location of blades at typical times.

is found that there is also an erodible area near the cavitation closing line of the pressure surface (shown in region 2 in the figure). The erosion area predicted by the I_{pressure} method is quite different: the erosion area in the centrifugal pump obtained from the experiment mainly exists in the part covered by the cavitation. Therefore, this method is not suitable for predicting the cavitation erosion area in the centrifugal pump. Figure 15(3) shows the cavitation erosion results obtained by using the I_{vapor} prediction method. From the figure, it can be seen that at time *a* and time *b*, the erodible area predicted by this method is smaller than by the other two methods. Compared with Figure 15(1), the erosion area is mainly concentrated near the vapor-liquid boundary line, which is more obvious near the boundary between the covers and the blade (region 4 in the figure). There are some point-like erodible areas near the cavitation closing line (as

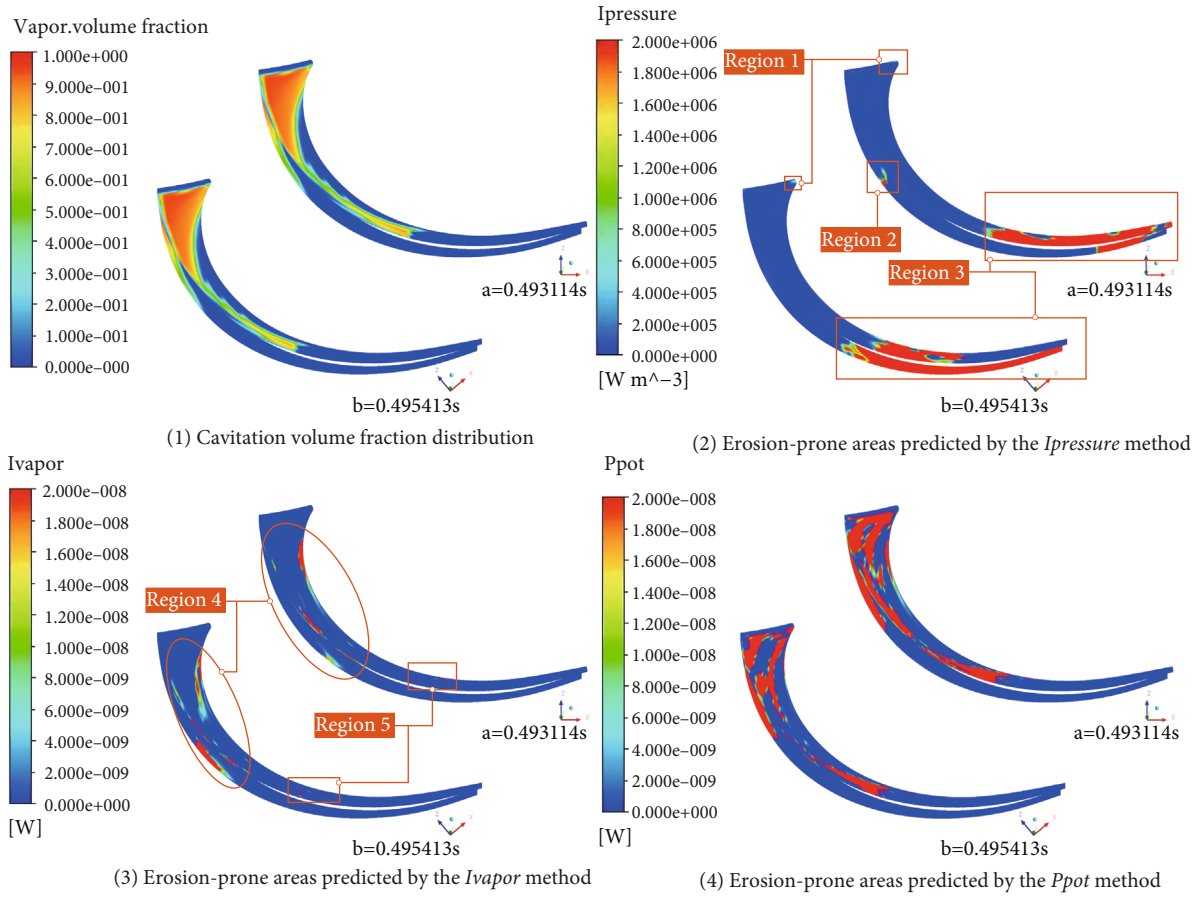

Figure 15: Cavitation erosion prediction results on a typical blade.

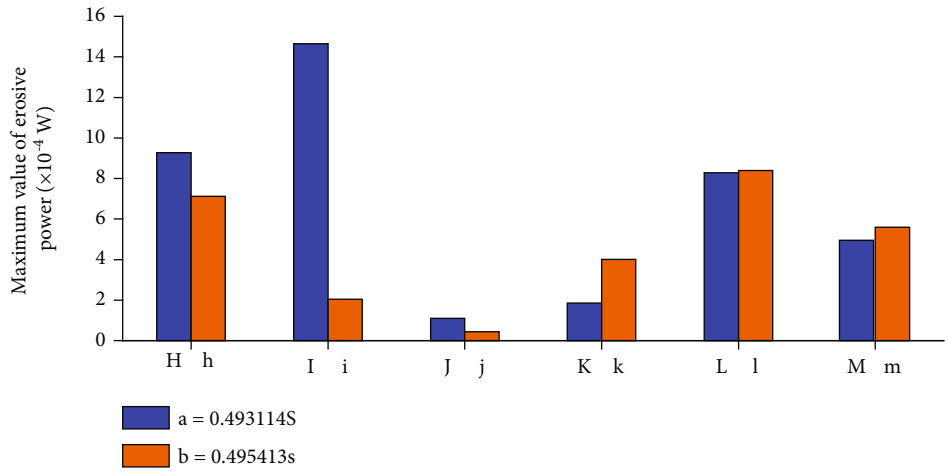

Figure 16: Maximum erosive power on blades.

shown in region 5 in the figure). The trend of the erodible area predicted by this method is basically consistent with the results obtained by other scholars, but it cannot capture the erosion in the cavitation coverage area. Figure 15(4) shows the erosion area predicted by using the erosive power method. It can be observed from the figure that the erosion area develops from the blade inlet to the blade outlet, and the area covered by cavitation shows erosion, which is consistent with the trend of the experimental results of Wang et al. [19, 21]. Compared with the other two methods, this method has advantages in predicting the erodible area in the centrifugal pump. The erosive power method can also be used to quantitatively analyze the erosive power on different blades. Figure 16 shows the statistical results of the maximum erosive power on the blade at different positions at times *a* and *b*.

It can be observed from Figure 16 that, when the blade rotates from time a to time b, the erosive power of the blades at positions H, I, and J becomes smaller, while the erosive power at positions K, L, and M becomes larger. At time a, the maximum value of erosive power on the blades appears on the blade at position I, and its value is $1.46e-04$ W. The minimum value appears on the blade at position J, and its value is $1.10e-05$ W. At time b, after the blades have rotated 40°, the maximum value of the blades appears at position l, and the minimum value of $4.40e-06$ W appears on the blade at position j. At time b, the blade at position j rotated by the blade at position J at time a. This shows that, after being rotated to 40°, the minimum value still appears on the same blade. Consider the dp/dt term in formula (7):

$$\frac{dp}{dt} = \frac{p_t - p_{t-i}}{i}. \tag{11}$$

In the formula, $i = 0.00022989$ s represents the time interval of one step of simulation calculation.

When the blade passes near the tongue, due to the sudden change of the flow channel, the pressure near this position has suddenly increased. Therefore, it is predicted that there is a higher value of erosive power near the position I at time a. At the next moment, the flow path gradually becomes larger, and there is no longer a sudden increase in pressure. Therefore, the predicted erosive power is lower.

5. Conclusion

The unsteady cavitation in the centrifugal pump is studied and analyzed by the method of combining experiment and numerical simulation, and the results show that

(1) the calculated results of the DCM method with a compressibility correction of the turbulence model match with the experimental results well, especially under rated conditions

(2) the existence of cavitation in the centrifugal pump causes the blockage of the flow channel and the generation of vortexes, which leads to the decline of the performance of the centrifugal pump

(3) when the head of the centrifugal pump drops by 3%, cavitation is mainly concentrated on the blades near the front cover

(4) the pressure derivative and volume fraction derivative on the typical blade show a periodic change. The change period is 0.0207 s, which is consistent with the rotation cycle of the impeller

(5) comparing the three cavitation erosion prediction methods, it is found that the cavitation erosion prediction method based on the rate of pressure change is not suitable for centrifugal pumps, and the erosion area predicted by the erosive power method is more reasonable. At $a = 0.493114$ s, the maximum erosive power appears on the blade near the separating tongue, and its value is $1.46e-04$ W

In a future work, it is necessary to set a cavitation erosion experiment. The simulated and experimental results will be compared, and the pulse energy by cavitation will be quantified. These would provide more theoretical support for engineering application.

Data Availability

The data that support the findings of this study are available from the corresponding author upon reasonable request.

Conflicts of Interest

The authors declare that they have no conflicts of interest.

Acknowledgments

This study is supported by the National Natural Science Foundation of China (No. 51806082 and No. 51976079), the National Key Research and Development Program of China (No. 2020YFC1512403), China Postdoctoral Science Foundation (No. 2020M671363 and No. 2021T140282), Postdoctoral Science Foundation of Jiangsu Province (No. 2020Z298), and Entrepreneurial Doctor Program of Jiangsu Province (No. 18SCBS016).

References

[1] J. P. Franc and J. M. Michel, *Fundamentals of Cavitation, vol. 76*, Springer, 2004.

[2] L. Agostino and M. V. Salvetti, *Fluid Dynamics of Cavitation and Cavitating Turbopumps*, Springer, 2007.

[3] S. Pan and X. Peng, *Physical Mechanism of Cavitation*, National Defense Industry Press, Beijing, China, 2013.

[4] Z. X. Chen, H. X. Hu, X. M. Guo, and Y. G. Zheng, "Effect of groove depth on the slurry erosion of V-shaped grooved surfaces," *Wear*, vol. 488-489, article 204133, 2022.

[5] W. Zhou, N. Qiu, L. Wang, B. Gao, and D. Liu, "Dynamic analysis of a planar multi-stage centrifugal pump rotor system based on a novel coupled model," *Journal of Sound and Vibration*, vol. 434, pp. 237–260, 2018.

[6] H. Wang, B. Long, C. Wang, C. Han, and L. Li, "Effects of the impeller blade with a slot structure on the centrifugal pump performance," *Energies*, vol. 13, no. 7, article 1628, 2020.

[7] Q. N. Song, Y. Tong, H. L. Li et al., "Corrosion and cavitation erosion resistance enhancement of cast Ni-Al bronze by laser surface melting," *Journal of Iron and Steel Research International*, 2021.

[8] Z. X. Li, L. M. Zhang, A. L. Ma et al., "Comparative study on the cavitation erosion behavior of two different rolling surfaces on 304 stainless steel," *Tribology International*, vol. 159, article 106994, 2021.

[9] L. M. Zhang, Z. X. Li, J. X. Hu et al., "Understanding the roles of deformation-induced martensite of 304 stainless steel in different stages of cavitation erosion," *Tribology International*, vol. 155, article 106752, 2021.

[10] L. Shi, J. Zhu, F. Tang, and C. Wang, "Multi-Disciplinary optimization design of axial-flow pump impellers based on the approximation model," *Energies*, vol. 13, no. 4, p. 779, 2020.

[11] M. Dular, R. Bachert, B. Stoffel, and B. Širok, "Experimental evaluation of numerical simulation of cavitating flow around hydrofoil," *European Journal of Mechanics-B/Fluids*, vol. 24, no. 4, pp. 522–538, 2005.

[12] I. Bilus and A. Predin, "Numerical and experimental approach to cavitation surge obstruction in water pump," *International Journal of Numerical Methods for Heat &Fluid Flow*, vol. 19, no. 7, pp. 818–834, 2009.

[13] R. Bachert, B. Stoffel, and M. Dular, "Unsteady cavitation at the tongue of the volute of a centrifugal pump," *Journal of Fluids Engineering*, vol. 132, no. 6, article 061301, 2010.

[14] Y. Wang, H. Liu, S. Yuan, M. Tan, and K. Wang, "Experimental test on cavitation vibration and noise of centrifugal pumps under non-design conditions," *Journal of Agricultural Engineering*, vol. 28, no. 2, pp. 35–38, 2012.

[15] Y. Fu, J. Yuan, S. Yuan et al., "Numerical and experimental analysis of flow phenomena in a centrifugal pump operating under low flow rates," *Journal of Fluids Engineering*, vol. 137, no. 1, article 011102, 2015.

[16] F. Hong, *Application of Nonlinear Cavitation Model in Numerical Calculation of Hydraulic Machinery Cavitation, [Ph.D. thesis]*, Jiangsu University, 2016.

[17] J. Caridad, M. Asuaje, F. Kenyery, A. Tremante, and O. Aguillón, "Characterization of a centrifugal pump impeller under two-phase flow conditions," *Journal of Petroleum Science and Engineering*, vol. 63, no. 1-4, pp. 18–22, 2008.

[18] L. Tan, B. Zhu, S. Cao, Y. Wang, and B. Wang, "Numerical simulation of unsteady cavitation flow in a centrifugal pump at off-design conditions," *Proceedings of the Institution of Mechanical Engineers, Part C: Journal of mechanical engineering science*, vol. 228, no. 11, pp. 1994–2006, 2014.

[19] J. Wang, Y. Wang, H. Liu, Q. Si, and M. Dular, "Rotating corrected based cavitation model for a centrifugal pump," *Journal of Fluids Engineering*, vol. 140, no. 11, article 111301, 2018.

[20] A. Peters, H. Sagar, U. Lantermann, and O. el Moctar, "Numerical Modelling and Prediction of Cavitation Erosion," *Wear*, vol. 338-339, pp. 189–201, 2015.

[21] J. Wang, *Numerical Simulation and Experimental Tests for Cavitation and Induced Erosion in Hydraulic Apparatus*, Jiangsu University, Zhenjiang, China, 2015.

[22] Z. Li, M. Pourquie, and T. Van Terwisga, "Assessment of cavitation erosion with a URANS method," *Journal of Fluids Engineering*, vol. 136, 2014.

[23] N. Qiu, W. Zhou, B. Che, D. Wu, L. Wang, and H. Zhu, "Effects of microvortex generators on cavitation erosion by changing periodic shedding into new structures," *Physics of Fluids*, vol. 32, no. 10, article 104108, 2020.

[24] O. Usta and E. Korkut, "Prediction of cavitation development and cavitation erosion on hydrofoils and propellers by Detached Eddy Simulation," *Ocean Engineering*, vol. 191, article 106512, 2019.

[25] P. Zwart, A. Gerber, and T. Belamri, "A two-phase flow model for predicting cavitation dynamics," in *Fifth International Conference on Multiphase Flow*, Yokohama, Japan, 2004.

[26] H. Wang, Z. Qian, D. Zhang, T. Wang, and C. Wang, "Numerical study of the normal impinging water jet at different impinging height, based on Wray–Agarwal turbulence model," *Energies*, vol. 13, no. 7, article 1744, 2020.

[27] B. Huang, G. Wang, and Y. ZHAO, "Numerical simulation unsteady cloud cavitating flow with a filter-based density correction model," *Journal of Hydrodynamics*, vol. 26, no. 1, pp. 26–36, 2014.

[28] M. S. Chapman and R. B. Plesset, "Thermal effects in the free oscillation of gas bubbles," *Journal of Basic Engineering*, vol. 93, no. 3, pp. 373–376, 1971.

[29] R. B. Plesset and M. S. Chapman, "Collapse of an initially spherical vapour cavity in the neighbourhood of a solid boundary," *Journal of Fluid Mechanics*, vol. 47, no. 2, pp. 283–290, 1971.

[30] M. Dular and O. Coutier-Delgosha, "Numerical modelling of cavitation erosion," *International Journal for Numerical Methods in Fluids*, vol. 61, no. 12, pp. 1388–1410, 2009.

[31] J. R. Blake, "The Kelvin impulse: application to cavitation bubble dynamics," *The Journal of the Australian Mathematical Society. Series B. Applied Mathematics*, vol. 30, no. 2, pp. 127–146, 1988.

[32] F. Pereira, *Prediction de l'erosion de cavitation: approche energetique, [Ph.D. thesis]*, Ecole Polytechnique Federale de Lausanne, 1997.

Hindawi
Scanning
Volume 2021, Article ID 1131858, 8 pages
https://doi.org/10.1155/2021/1131858

Research Article

Thermochemical Recycling of Oily Sludge by Catalytic Pyrolysis: A Review

Xiaojing Di,[1] **Haodan Pan**,[1] **Donghao Li**,[1] **Hongxiang Hu**,[2] **Zhiyong Hu**,[1] **and Yulin Yan**[3]

[1]*College of Petroleum Engineering, Liaoning Petrochemical University, Fushun 113301, China*
[2]*CAS Key Laboratory of Nuclear Materials and Safety Assessment, Institute of Metal Research, Chinese Academy of Sciences, Shenyang 110016, China*
[3]*The Shale Oil Plant of Fushun Mining Group Co., Ltd., Fushun 113115, China*

Correspondence should be addressed to Haodan Pan; panhaodan@126.com and Hongxiang Hu; hxhu@imr.ac.cn

Received 18 September 2021; Accepted 20 October 2021; Published 31 October 2021

Academic Editor: Jian Chen

The main methods of treating oily sludge at home and abroad and the current research status of oily sludge pyrolysis technology are briefly described, and four commonly used catalysts are introduced: metals, metal compounds, molecular sieves, metal-supported molecular sieves, and biomass catalysts for oily sludge. The influence of pyrolysis, the pyrolysis mechanism, and the product composition of oily sludge with the addition of different catalysts are also discussed. Finally, the development direction of preparing new catalysts and the mixed use of multiple catalysts is proposed as a theory to provide for the efficient and reasonable utilization of oily sludge.

1. Introduction

1.1. Source and Ingredients of Oily Sludge. Crude oil is the blood of industry and an important strategic resource in the development of the national economy. The oil oily sludge is inevitably produced during the storage, transportation, and refining development process of the entire petroleum industry. It is characterized by high oil content, fine particles, high viscosity, and difficulty in dehydration and transportation. The composition of oily sludge is extremely complex, containing high concentrations of total petroleum hydrocarbons, and heavy metals, such as copper, zinc, chromium, mercury, chemical additives, and pathogenic microorganisms. According to research, the oil content of oily sludge is between 10% and 50%, and the water content is between 40% and 90%, accompanied by a certain amount of solids.

The output of oily sludge is increasing year by year. According to statistics, the total amount of oily sludge produced in the world every year reaches 60 million tons [1–3], and with the deep development of most oil fields, the output of oily sludge will continue to increase. According to the source, oily sludge can be divided into oilfield oily sludge (OOS), storage and transportation oily sludge (STOS), refinery oily sludge (ROS), and accidental oily sludge (AOS). Different oily sludges differ in properties. Selecting the corresponding oily sludge treatment method according to its nature is a task that must be completed at present.

1.2. Treatment Method. At present, domestic and foreign methods for treating oily sludge include thermochemical cleaning technology, solvent extraction technology, and biological treatment technology.

1.2.1. Thermochemical Cleaning. Thermochemical cleaning technology is a method of adding hot water and chemical reagents to oily sludge to change the properties of the oil phase and liquid phase to extract oil. Most of the thermochemical cleaning technology treats oily sludge incompletely, and it is difficult to meet the demand. Therefore, its method will be combined with biological treatment

technology, using thermochemical cleaning as pretreatment to refine crude oil and biological treatment technology to achieve harmless treatment of its products. Duan et al. [4] evaluated the cleaning effect by using the interfacial tension (IFT) method and found that when the mixture ratio of Na_2CO_3, AEO-9, and rhamnolipid is 5 : 1 : 0.5, the IFT can be reduced to 0.064 mN/m as low as possible. When the concentration of the mixture is 2 wt%, the cleaning agent aqueous solution/oily sludge is 3 : 1, the cleaning time is 40 minutes, the cleaning temperature is 50°C, and the residues on the cleaned solids are analyzed. The oil is mainly passed through the layer adsorption, where its adsorbed on the solid, and the residue is paraffin and polycyclic aromatic hydrocarbons. Wang et al. [5] achieved the three-phase separation of oil, mud, and water through precipitation and swirling and used gel permeation chromatography (GPC) to characterize the migration of the oil phase. As the cleaning solvent/oil ratio increased from 1 : 2 to 5: 1, the molecular weight of the upper layer is reduced from 1044 to 846, and the solvent is a necessary condition for separating the oil phase. Jing et al. [6] used AEO-9, DBS, Na_2SiO_3-$9H_2O$, and other surfactant solutions to test the best solution for washing oily sludge. Because Na_2SiO_3-$9H_2O$ is easy to disperse, the residual oil rate is the lowest, only about 1.6%, and the washing effect is the best. Compared with other technologies, chemical cleaning technology has the advantages of simple process, low cost, and high reliability, and most of the solutions can be recycled, which can avoid secondary pollution.

1.2.2. Solvent Extraction Technology. The solvent extraction process is widely used as an operating technology to remove semivolatile and volatile organic compounds from oily sludge. The oily sludge is mixed with the solvent in a certain ratio, and the oil is extracted by the solvent and then recovered by distillation. Commonly used solvents include methyl ethyl ketone (MEK), reformed oil, liquefied petroleum gas (LPGC), hexane, xylene, and other organic solvents, which can be recycled. Due to the large consumption of solvents, high costs, and possible new environmental pollution, in recent years, researchers have devoted themselves to the development of new solvents such as supercritical liquids to replace traditional organic solvents. The extraction process is faster than traditional organic solvents, but when the processing volume is too large, the efficiency drops [7]. Lam et al. [8] summarized recent solvent extraction experiments and found that solvent extraction has the disadvantage of inconvenient recovery of waste oil.

Khan et al. [9] developed supercritical fluid solvents instead of traditional chemical solvents. This technology can remove metal impurities, break emulsions, and complete petroleum extraction without the use of catalysts and hydrogen. The oil recovery rate can reach 78%; though, the quality content is reduced by 98.5%. The RAG layer conversion of supercritical fluids has created a new method in the field of nontraditional crude oil refining. This process is suitable for oil refineries to efficiently extract oil recovery fluid. Hu et al. [10] used solvents to extract the petroleum in the oily sludge and performed thermogravimetric analysis on the oily sludge, the extracted crude oil, and the residual oily sludge. The temperature range of the extracted crude oil was 200-550°C. However, the characteristics of the initial oily sludge still remain, indicating that the extraction is not complete, and there is still value for further development. Compared with other technologies, the solvent extraction method has a higher oil recovery rate, thorough treatment of oily sludge, lower extraction temperature, energy saving, and mild operating conditions, and the extraction agent does not need to be regenerated. It is a clean, economical, and effective oily pollution.

In mud treatment technology, the extractant is volatile and toxic, and the tightness of the equipment is strictly required during operation, which leads to high processing costs. At present, the extraction method is considered to be an efficient method for treating oily sludge. To solve the shortcomings of the above method, it is necessary to pretreat the oily sludge and select a suitable extractant as the goal of indepth requirements shortly.

1.2.3. Biological Treatment Technology. Biological treatment is a process that uses microorganisms to decompose the hydrocarbons in the oily sludge into carbon dioxide and water to achieve harmlessness [11]. Most of the petroleum products in oil oily sludge can be decomposed by microorganisms, and the decomposition rate is mainly affected by the composition of hydrocarbons. There are three types of biological treatment: land cultivation, composting, and bioreactor method. Zare et al. [12] concluded that most of the petroleum substances in the oily sludge can be decomposed by microorganisms, and the decomposition speed varies with the types of hydrocarbons. Alkanes are the most easily decomposable hydrocarbons; in contrast to asphaltenes, microorganisms can directly decompose without additional conditions, but the natural decomposition by microorganisms is very slow. Ji et al. [13] optimized the activity and stability of the formate dehydrogenase gene Cbfdh by using Box-Behnken, and the Cbfdh activity reached 12.2. Using Cbfdh to degrade 10% (w/w) oily sludge for 12 hours; the degradation rate could reach 35.6%. CbFDH makes full use of lactose in Escherichia coli BL21 to accelerate crude oil degradation, and its Cbfdh efficiency and cost are better than current microbial strains. Compared with other methods, the biological treatment method is not expensive, has low safety pollution, and has strong transferability.

1.2.4. Heat Treatment Technology. Traditional oily sludge treatment methods are mainly landfilling, composting, and incineration. The landfill method is to fill, cover, and compact the oily sludge into a prepared pit, make it undergo biological, physical, and chemical changes, decompose organic matter, and achieve the purpose of reduction and harmlessness. Landfilling has low cost and easy operation and is generally regarded as a general solution for oily sludge treatment. Compost can decompose organic materials into organic fertilizer for agriculture. Hu et al. [14] summarized the disadvantages of the composting method, which covers a large area and is easily affected by natural conditions such as rainfall and temperature. Incineration is considered to be

the most effective method to reduce the volume of oily sludge, which can significantly reduce the amount of waste. Gong et al. [15] burned oily sludge in a tube furnace and used the software FactSage to calculate the thermodynamic balance of the process. As the incineration temperature increased from 800°C to 1000°C, Cr, Pb, Cu, Zn, Ni, etc, the release rate of heavy metals gradually increased. When the temperature exceeded 1000°C and the excess air ratio increased from 1.0 to 1.4, the release rates of Cr, Pb, Cu, Zn, and Ni decreased first and then stabilized. Guo et al. [16] found that incineration decomposes the oil and other organic pollutants in oily sludge into small molecules, such as H2O and CO2. Zhou [17] concluded through experiments that the incineration temperature should be controlled above 850°C to avoid the production of dioxins. Although heat treatment has certain advantages, there are certain problems in terms of oily sludge treatment effect, cost, applicability, and secondary pollution.

Traditional oily sludge treatment methods include landfill, composting, and incineration, which occupy a large area, are costly, and are likely to cause secondary pollution. Some emerging treatment methods, such as solvent extraction technology and biological treatment technology, will not cause secondary pollution, but there are disadvantages such as high cost and long cycle. Pyrolysis is therefore gradually being valued and widely used due to its fast processing, good effect, and availability of residues.

2. Research Progress of Catalytic Pyrolysis of Oily Sludge

2.1. Pyrolysis and Catalytic Pyrolysis. Pyrolysis technology means that the oily sludge is heated to a certain temperature under anaerobic conditions to separate the hydrocarbons and recover them through phase separation. The recovered gas phase is methane, carbon dioxide, etc., the liquid phase is mainly fuel and water at room temperature, and the solid phase is inorganic minerals and carbon residue. In this process, organic components are transformed into pyrolysis oil, gas products, and carbonaceous residues. After pyrolysis, the oily sludge is gradually mineralized, as shown in Figures 1–3 [18]. The thermal conversion process of oily sludge is divided into two stages: first, the evaporation stage when the temperature is lower than 350°C, low-boiling light hydrocarbons volatilize from the oily sludge. The second stage is the parallel-sequential reaction stage, and when the temperature exceeds 350°C, heavy oil will start to crack. Hydrocarbons will generate free radicals due to thermal activation at around 400°C, and a series of free radical reactions will occur. On the one hand, it will proceed towards the cracking of small-molecule hydrocarbons while it proceed towards the condensation direction of coking and finally produce oil, water, noncondensable gas, and coke [19]. In comparison, the pyrolysis method has the advantages of faster processing speed, more thorough oily sludge treatment, and recyclable oil and gas and residues. However, it also has large investments, high energy consumption, high equipment requirements, and more complicated operations. Improper disposal is prone to defects such as secondary pollution and potential safety hazards.

In response to the problems of pyrolysis of oily sludge, researchers have focused on further improving the yield and quality of pyrolysis products by adjusting the process conditions of the pyrolysis process. Gong et al. [20] studied the pyrolysis temperature of oil oily sludge in a tube furnace and the influence of different atmospheres (N2/CO2) on the pyrolysis behavior of oily sludge. CO_2 can promote the pyrolysis of OS and reduce the coke yield. As the pyrolysis temperature increases, the light fraction (gasoline, diesel) in the oil decreases, the heavy fraction also increases, while the content of CH_4, C_2H_4, $C_{4\text{-}6}$, and C_{6+} increases, and the content of C_2H_6, C_3H_8, and C_3H_6 decreases. Lin et al. [21] studied the copyrolysis of oily sludge and rice husk at a weight ratio of 2 : 1, the increase in the content of SARA (saturates, aromatics, resins, asphaltenes) saturates and aromatics, and the reduction of heavy fractions and improve the quality of oil solution. The concentration of chain hydrocarbons increased, and the content of oxygenated compounds decreased by 46-93%. As the synergistic reaction promotes the secondary reaction, pyrolysis tends to produce more H_2, CO, and C_1-C_2 hydrocarbons.

Regarding the adjustment of pyrolysis process conditions to promote pyrolysis of oily sludge, such as catalytic pyrolysis, it has shown great development potential and research prospects due to its high treatment efficiency and low pollution. Adding a catalyst in the pyrolysis process can have a positive effect on the pyrolysis products of oily sludge, that is, the oil and gas yields increase, and the oil quality is improved, while the residue reduces [22, 23]. It can also change the pyrolysis reaction conditions to make the time required for pyrolysis shorter, and the temperature is lowered. For the same oily sludge, different catalysts are pyrolyzed and catalyzed, and the products after pyrolysis have different degrees of influence. Therefore, it is very important to determine the results of the experiment and choose the appropriate catalyst.

2.2. Research Progress of Catalysts for the Catalytic Pyrolysis of Oily Sludge. Common catalysts for pyrolysis of oily sludge include: metals, metal compounds, molecular sieves, and biomass.

2.2.1. Metal. Metal element catalysts are mainly transitioned metal elements, including Ni, Fe, Cu, and Al, and are generally loaded on a carrier to improve the pyrolysis efficiency of oily sludge [24, 25]. Metal catalysts can increase the generation of pyrolysis gas [26].

Li et al. [27] mixed oily sludge and steel slag for reaction, which can recover oil and gas and is accompanied by iron generation. As the two react together, the steel slag undergoes a reduction reaction at high temperatures to produce iron. The reduced iron acts as a catalyst for the pyrolysis of oily sludge. Compared with the pyrolysis of oily sludge alone, the production of CO2 and H2 is significantly increased. Lin et al. [28] proposed an innovative method to prepare Fe-char from oil oily sludge and apply it to the catalytic cracking of heavy oil in oily sludge. The conversion

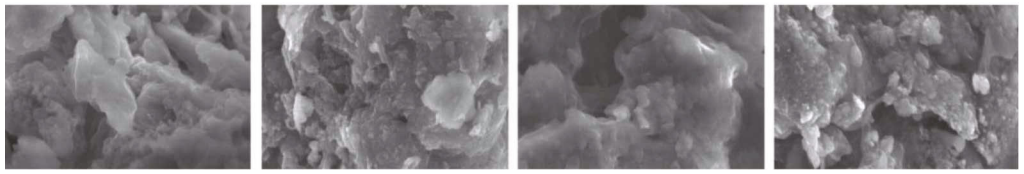

Figure 1: Changes in the apparent morphology of raw oily sludge and oily sludge after pyrolysis at 450°C, 750°C, and 950°C for 0 weeks [18].

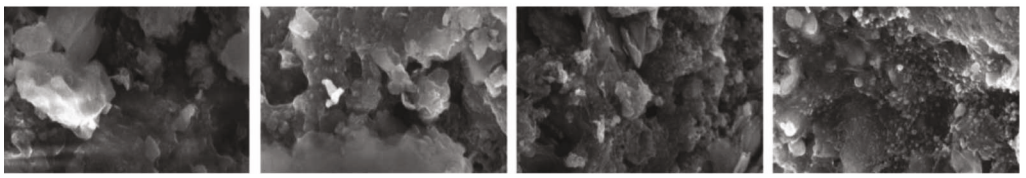

Figure 2: Changes in the apparent morphology of the original oily sludge and oily sludge after pyrolysis at 450, 750, and 950°C for 2 weeks [18].

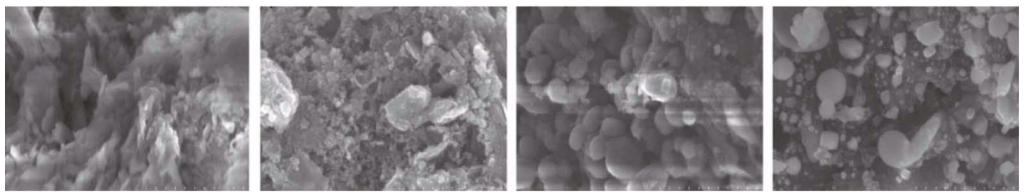

Figure 3: Changes in the apparent morphology of raw oily sludge and oily sludge after pyrolysis at 450°C, 750°C, and 950°C for 4 weeks [18].

efficiency of char900 formed at 900°C is higher than that of char600 formed at 600°C. By using char900, the H_2 and CO yields are significantly improved. The oil conversion rate of using char900 at 800°C can reach 95.8%, Fe°. It plays an important role in promoting hydrocarbon reforming and water gas shift (WGS) reactions. Song et al. [29] innovated a method of combining oil oily sludge and steel slag to improve the quality of the oil. Thermogravimetric analysis (TG) was used to characterize the characteristics of pyrolysis oil, and the effect of steel slag on the product H_2 during the pyrolysis of oily sludge was analyzed. The addition of steel slag increases the weight loss rate of oil sludge and promotes the production of H_2 and CH_4. When 15% steel slag is added, the H_2 yield increases from 26.43% to 30.41%, and the CH_4 yield increases from 34.65% to 43.38%. The pyrolysis of oily sludge is 3 times. At the same time, it is feasible to use a magnetic separator to separate steel slag and oily sludge after the experiment, and this scheme has a certain potential. Metals play a positive role in the pyrolysis of oily sludge, but due to high cost, it is therefore necessary to choose this type of catalyst based on actual conditions.

2.2.2. Metal Compounds. The metal compound is a catalyst mainly composed of light metals, such as compounds of Al, Na, Ca, K, etc. Metal oxides have excellent redox characteristics and high catalytic activity [26, 30]. Compared with ordinary zeolite molecular sieve catalysts, metal oxide catalysts are easy to obtain; so, metal oxide catalysts have a high-cost performance.

Kwon et al. [22] found that adding CaCO3 to the oily sludge cannot only increase the CO generation rate but also reduce the yield of polycyclic aromatic hydrocarbons from 36.6% to 29.6%. The CO2 generated by the heating of CaCO3 enhances the thermal cracking of volatile organic carbon during the pyrolysis of OS and provides a source of C and O, thereby increasing the yield of CO. The addition of CaCO3 can improve the efficiency of converting solids into gases, thereby reducing the production of harmful substances. Lin et al. [31] explored the effect of KOH on the pyrolysis of different oily sludges and used gel permeation chromatography (GPC), rheometer, and gas chromatography-mass spectrometry (GC-MS) to characterize pyrolysis oil products. When added, oil yield and oil viscosity are reduced, and gas and solid products and calorific value are increased. KOH can promote the formation of compounds in pyrolysis oil and inhibit the formation of asphalt. KOH promotes the improvement of oil quality with low molecular weight, low viscosity, and high calorific value. Huang et al. [32] studied the effect of adding Fe2O3 on the composition and content of solid-liquid gas produced by oily sludge pyrolysis. Its Fe2O3 increased the gas produced from 8.69 wt% to 11.62 wt%, and the oil increased from 32.54 wt% to 38.74 wt%. The generated char is reduced from 58.77 wt% to 49.64 wt%. This catalyst accelerates the formation of gas, oil, and char, but does not affect the components in the oil. Sun et al. [33] proposed a pyrolysis scheme of fully mixed biomass-coated alumina and pyrolyzed oily sludge and studied the effect of temperature and alumina on pyrolysis. The yield and component distribution of noncondensable gas products are more significantly affected by temperature. When the mass ratio of alumina to oily sludge at 500°C is 1 : 35, the maximum liquid production is

Table 1: The advantages and disadvantages of different types of catalysts and suggestions [26].

Catalyst type	Advantage	Shortcoming	Suggest
Metal	Good effect	Expensive, causing secondary pollution	Use according to actual conditions, and use metal waste when appropriate
Metal compound	Variety and easy access	Different metal oxides have different effects on the pyrolysis of oily sludge; so, it is necessary to find a suitable metal oxide	Exploring the metal compounds required by the corresponding oily sludge
Molecular sieve	Not only can be used as a catalyst, but also other catalysts can be supported, so that the catalytic effect is better, and the reaction system is not required.	High price, prone to coking, high pyrolysis temperature	Explore suitable process conditions and carry out catalyst regeneration treatment to extend catalyst life
Biomass	It is not easy to cause secondary pollution, the price is cheap, and the two sides have a coordinated reaction, which promotes a more comprehensive pyrolysis	It is necessary to find suitable biomass for synergistic reaction. Some biomass not only does not promote the reaction but also inhibits the reaction from proceeding.	Explore the biomass that is conducive to the pyrolysis of different oily sludges

48.44 wt.%. As the temperature increases, the liquid product undergoes secondary cracking, and CO_2 and H_2 increase. In summary, compared with metal catalysts, metal compound catalysts cannot only increase the yield of pyrolysis gas but also increase the yield of hydrocarbons and their pyrolysis oil compounds. Such catalysts are easy to obtain, and different metal compounds have different effects on the pyrolysis of oily sludge, which need to be selected according to specific needs.

2.2.3. Molecular Sieves and Metal-Supported Molecular Sieve Catalysts. Molecular sieves are a kind of aluminosilicate crystals with regular microporous structure [34], and they are widely used in X type, Y type, ZSM-5 type, MCM-41 type, and so on [26, 35].

Molecular sieves are widely used in heterogeneous catalysis and as catalyst carriers due to their advantages in pores and large specific surface area. However, many molecular sieves are relatively weak in acidity with low surface density, resulting in low catalytic activity. Therefore, the application of mesoporous molecular sieves to catalytic reactions is not ideal. To improve its acidity and catalytic performance, domestic and foreign researchers have used metals or metals. Oxides and other compounds with catalytic effects are introduced into the molecular sieve, which not only takes advantage of the pore advantage of the molecular sieve but also takes advantage of the special properties such as the high activity of the oxide. Jia et al. [36] prepared Fe/Al pillared bentonites with different Fe/Al mass ratios as oily sludge pyrolysis catalysts and used X-ray diffraction (XRD), N2 adsorption, and NH3-TPD to characterize their pyrolysis products. As the ratio of Fe/Al increases, the oil yield first increases and then decreases. When Fe/Al is 2.0 wt%, the oil yield reaches the maximum with a value of 52.46%. This catalyst can not only increase the oil yield but also increase the formation of CH4. Yu et al. [37] used the impregnation method to synthesize molecular sieve Al-MCM-41 and studied the influence of the catalyst concentration on the pyrolysis of oil oily sludge. As the catalyst concentration increases from 0.5% to 1%, the pyrolysis oil recovery rate increases significantly, reaching the maximum value of 83.48%. After that, the recovered oil did not change much with the increase in catalyst concentration. Lin et al. [38] used HZSM-5 and Zn/HZSM-5 to catalytically pyrolyze oily sludge in a two-stage tubular fixed-bed reactor to recover aromatic hydrocarbons. Through XRD, Fourier transform infrared (FTIR), N_2 adsorption, and NH_3-TPD characterize the physical and chemical properties of HZSM-5 zeolite before and after Zn loading. Gas chromatography-mass spectrometry was used to analyze the effects of different residence times and modified HZSM-5 on pyrolysis products. As the residence time increased from 1 second to 7.6 seconds, the total aromatics yield also increased from 48.7% to 92.2%. When the residence time is 1.9 seconds, the catalytic effect of Zn/HZSM-5 on the pyrolysis of oily sludge was studied. The incorporation of 3% Zn increased the total aromatic products from 58.7% to 81.0%, and the H_2 and CO_2 yields were significantly improved. In summary, compared to other catalysts, the catalytic effect of supported catalysts is more significant. Compared with ordinary molecular sieves, the catalytic effect of molecular sieves loaded with other catalysts is doubled, and the addition of metals or metal oxides further enhances the catalytic effect of molecular sieves. However, the disadvantage is that the price is high, there is a problem of coking during the reaction, and the temperature of the catalytic pyrolysis reaction is lowered but still above 400°C. How to further improve the low-temperature catalytic efficiency of molecular sieve catalysts can be regarded as the next research goal, and appropriate reaction processes should be selected to prolong the service life of the catalyst, or regeneration treatment should be carried out to improve its use efficiency.

2.2.4. Biomass. The essence of copyrolysis of oily sludge and biomass is to catalyze and strengthen the pyrolysis of oily sludge, enhance the rate of oil and gas recovery, and improve the oil and gas quality. Common biomass catalysts include rice husks, walnut husks, wood chips, and apricot husks [39].

Zhao et al. [40] studied the effects of rice husks, walnut husks, wood chips, and apricot husks on the pyrolysis of oily sludge. As the biomass increases, its dehydration efficiency increases, and the oil recovery rate also increases. The main reason is that biomass can eliminate uneven heat transfer and provide the heat required for pyrolysis. After comparing the pyrolysis products, it is found that the oil recovery rate is sawdust>rice husk>apricot husk>walnut husk. Lin et al. [21] studied the copyrolysis of oily sludge and rice husk and performed SARA and gas chromatography/mass spectrometry tests on the results. SARA concluded that the interaction between the two increases the content of saturated hydrocarbons and aromatics, resulting in a reduction in heavy fractions and an increase in oil quality. Through the gas chromatography/mass spectrometry analysis of the experiment, it is found that the interaction increases the concentration of chain hydrocarbons, CO and C_1-C_2 hydrocarbons, and H2 (from 22.2% to 55.6%), but reduces H_2S. It is mainly attributed to the ash content of biomass and the catalysis of alkali metals. Jin et al. [41, 42] mixed pyrolysis of bamboo sawdust and oily sludge at 400-600°C. Copyrolysis reduced carbon production. In addition, the two copyrolysis promoted the conversion of toxic metals into a more stable state at 600°C. After copyrolysis, Cu and Zn in the stable state of the residue are 3.2 times the pyrolysis of the oily sludge alone. Compared with other catalysts, this catalyst is mostly domestic wastes; so, it is cheap, and conducive for the formation of pyrolysis gas, and can transform potentially toxic metals into a more stable state. Therefore, it is suitable for treating metal-polluted oilfields: a safe and feasible way.

3. Comparison of Different Types of Catalysts

The advantages and disadvantages of different types of catalysts and suggestions are shown in Table 1. The adaptability, advantages, and disadvantages of different types of catalysts are different, and suitable catalysts should be selected according to the treatment object, target product, and cost requirements.

4. Prospects for Catalytic Pyrolysis Technology of Oily Sludge

The composition of oily sludge is very complex. If it is not treated in time, it will not only cause different levels of environmental pollution but also bring huge economic losses. Therefore, it is urgent to find a harmless treatment method for oily sludge. Suggestions are given below:

(1) The main catalysts for oily sludge pyrolysis include metals and their compounds, molecular sieves, and biomass. Various catalysts have different effects due to their different objectives. For the selection of catalysts for experiments, suitable catalysts should be selected according to experimental requirements, results, and process conditions

(2) Focus on studying the mechanism of catalysts, develop environmentally friendly and efficient catalysts, and use lower cost and energy consumption to obtain higher quality target products

(3) Indepth study of waste recovery and utilization to prepare catalysts to realize energy recycling. Carry out research on the copyrolysis of oily sludge with other biomass and waste, and the two sides have a synergistic effect to promote the reaction and increase the target yield

(4) According to the nature of oily sludge emission standards and the comprehensive requirements of environmental protection and economy, there is a need to explore the combined use of multiple catalysts to achieve good catalytic effects

Data Availability

The authors confirm that the data supporting the findings of this study are available within the article.

Conflicts of Interest

The authors declare that they have no conflicts of interest.

Authors' Contributions

Xiaojing Di contributed to the experiment, methodology, and writing-original draft preparation. Haodan Pan contributed to the writing-reviewing, investigation, and data curation. Donghao Li contributed to the experiment and methodology. Hongxiang Hu contributed to the supervision and validation. Zhiyong Hu contributed to the reviewing, validation, and suggestion. Yulin Yan contributed to the methodology, reviewing, and suggestion.

References

[1] S. Cheng, Y. Wang, N. Gao, F. Takahashi, A. Li, and K. Yoshikawa, "Pyrolysis of oil sludge with oil sludge ash additive employing a stirred tank reactor," *Journal of Analytical and Applied Pyrolysis*, vol. 120, pp. 511–520, 2016.

[2] M. Hassanzadeh, L. Tayebi, and H. Dezfouli, "Investigation of factors affecting on viscosity reduction of sludge from Iranian crude oil storage tanks," *Petroleum Science*, vol. 15, no. 3, pp. 634–643, 2018.

[3] M. Lashkarbolooki and S. Ayatollahi, "Effects of asphaltene, resin and crude oil type on the interfacial tension of crude oil/brine solution," *Fuel*, vol. 223, pp. 261–267, 2018.

[4] M. Duan, X. Wang, S. Fang, B. Zhao, C. Li, and Y. Xiong, "Treatment of Daqing oily sludge by thermochemical cleaning method," *Colloids and Surfaces A-Physicochemical and Engineering Aspects*, vol. 554, pp. 272–278, 2018.

[5] J. Wang, X. Han, Q. Huang, Z. Ma, Y. Chi, and J. Yan, "Characterization and migration of oil and solids in oily sludge during centrifugation," *Environmental Technology*, vol. 39, no. 10, pp. 1350–1358, 2018.

[6] G. Jing, T. Chen, and M. Luan, "Studying oily sludge treatment by thermo chemistry," *Arabian Journal of Chemistry*, vol. 9, pp. S457–S460, 2016.

[7] M. M. I. Al-Doury, "Treatment of oily sludge using solvent extraction," *Petroleum Science and Technology*, vol. 37, no. 2, pp. 190–196, 2019.

[8] S. S. Lam, R. K. Liew, A. Jusoh, C. T. Chong, F. N. Ani, and H. A. Chase, "Progress in waste oil to sustainable energy, with emphasis on pyrolysis techniques," *Renewable & Sustainable Energy Reviews*, vol. 53, pp. 741–753, 2016.

[9] M. K. Khan, B. Sarkar, H. Zeb, M. Yi, and J. Kim, "Simultaneous breaking and conversion of petroleum emulsions into synthetic crude oil with low impurities," *Fuel*, vol. 199, pp. 135–144, 2017.

[10] J. Hu, J. Gan, J. Li et al., "Extraction of crude oil from petrochemical sludge: characterization of products using thermogravimetric analysis," *Fuel*, vol. 188, pp. 166–172, 2017.

[11] Z. Wang, Z. Zhao, Z. Wang, X. Li, and Z. Chu, "Application and development of pyrolysis technology in petroleum oily sludge treatment," *Environmental Engineering Research*, vol. 26, no. 1, pp. 82–90, 2021.

[12] N. Zare, B. Bonakdarpour, M. A. Amoozegar et al., "Using enriched water and soil-based indigenous halophilic consortia of an oilfield for the biological removal of organic pollutants in hypersaline produced water generated in the same oilfield," *Process Safety and Environmental Protection*, vol. 127, no. B, pp. 151–161, 2019.

[13] L. Ji, X. Fu, M. Wang et al., "Enzyme cocktail containing NADH regeneration system for efficient bioremediation of oil sludge contamination," *Chemosphere*, vol. 233, pp. 132–139, 2019.

[14] G. Hu, J. Li, and G. Zeng, "Recent development in the treatment of oily sludge from petroleum industry: a review," *Journal of Hazardous Materials*, vol. 261, pp. 470–490, 2013.

[15] Z. Gong, Z. Wang, and Z. Wang, "Study on migration characteristics of heavy metals during oil sludge incineration," *Petroleum Science and Technology*, vol. 36, no. 6, pp. 469–474, 2018.

[16] P. Guo, Z. Liu, Y. Li, J. Wu, and C. Hu, "Analysis on oily sludge treatment technology," *DONGFANG ELECTRIC*, vol. 33, no. 131, pp. 6–9, 2019.

[17] F. Zhou, "Research and practice of dioxin control in domestic waste incineration power plant," *Environmental Sanitation Engineering*, vol. 27, no. 6, pp. 93–96, 2019.

[18] H. Peng, Y. Wu, T. Guan et al., "Sludge aging stabilizes heavy metals subjected to pyrolysis," *Ecotoxicology and Environmental Safety*, vol. 189, pp. 109984–109989, 2020.

[19] W. Song, J. E. Vidonish, R. Kamath et al., "Pilot-scale pyrolytic remediation of crude-oil-contaminated soil in a continuously-fed reactor: treatment intensity trade-offs," *Environmental Science & Technology*, vol. 53, no. 4, pp. 2045–2053, 2019.

[20] Z. Gong, A. Du, Z. Wang, P. Fang, and X. Li, "Experimental study on pyrolysis characteristics of oil sludge with a tube furnace reactor," *Energy & Fuels*, vol. 31, no. 8, pp. 8102–8108, 2017.

[21] B. Lin, Q. Huang, and Y. Chi, "Co-pyrolysis of oily sludge and rice husk for improving pyrolysis oil quality," *Fuel Processing Technology*, vol. 177, pp. 275–282, 2018.

[22] E. E. Kwon, T. Lee, Y. S. Ok, D. C. W. Tsang, C. Park, and J. Lee, "Effects of calcium carbonate on pyrolysis of sewage sludge," *Energy*, vol. 153, pp. 726–731, 2018.

[23] X. Liu, H. Pan, C. Guo, X. di, and H. Hu, "Effect of double transition metal salt catalyst on Fushun oil shale pyrolysis," *Scanning*, vol. 2020, 14 pages, 2020.

[24] K. Zheng, H. Hu, F. Chen, and Y. Zheng, "Failure analysis of the blackwater regulating valve in the coal chemical industry," *Engineering Failure Analysis*, vol. 125, p. 105442, 2021.

[25] L. Pang, Z. B. Wang, M. H. Lu, Y. Lu, X. Liu, and Y. G. Zheng, "Inhibition performance of benzimidazole derivatives with different heteroatoms on the under-deposit corrosion of carbon steel in CO_2-saturated solution," *Corrosion Science*, vol. 192, pp. 109841–109863, 2021.

[26] Y. Yang, C. Xu, K. Tong, D. Ma, X. Zhao, and Y. Xu, "Research progress of sludge pyrolysis catalyst," *Chemical Environmental Protection*, vol. 40, no. 6, pp. 580–585, 2020.

[27] P. Li, X. Zhang, J. Wang et al., "Process characteristics of catalytic thermochemical conversion of oily sludge with addition of steel slag towards energy and iron recovery," *Journal of Environmental Chemical Engineering*, vol. 8, no. 4, pp. 103911–103911, 2020.

[28] B. Lin, Q. Huang, Y. Yang, and Y. Chi, "Preparation of Fe-char catalyst from tank cleaning oily sludge for the catalytic cracking of oily sludge," *Journal of Analytical and Applied Pyrolysis*, vol. 139, pp. 308–318, 2019.

[29] Q. Song, H. Zhao, J. Jia et al., "Characterization of the products obtained by pyrolysis of oil sludge with steel slag in a continuous pyrolysis-magnetic separation reactor," *Fuel*, vol. 255, pp. 1–12, 2019.

[30] Y. Qiao, S. Sheng, L. Zhang et al., "Friction and wear behaviors of a high nitrogen austenitic stainless steel Fe-19Cr-15Mn-0.66N," *Journal of Mining and Metallurgy Section B-Metallurgy*, vol. 57, no. 2, pp. 285–293, 2021.

[31] B. Lin, J. Wang, Q. Huang, and Y. Chi, "Effects of potassium hydroxide on the catalytic pyrolysis of oily sludge for high-quality oil product," *Fuel*, vol. 200, pp. 124–133, 2017.

[32] Z. Huang, L. Qin, Z. Xu, W. Chen, F. Xing, and J. Han, "The effects of Fe_2O_3 catalyst on the conversion of organic matter and bio-fuel production during pyrolysis of sewage sludge," *Journal of the Energy Institute*, vol. 92, no. 4, pp. 835–842, 2019.

[33] Y. Sun, B. Jin, W. Wu et al., "Effects of temperature and composite alumina on pyrolysis of sewage sludge," *Journal of Environmental Sciences*, vol. 30, pp. 1–8, 2015.

[34] H. Wang, H. Jia, L. Wang, and H. Chen, "The catalytic effect of modified bentonite on the pyrolysis of oily sludge," *Petroleum Science and Technology*, vol. 33, no. 13-14, pp. 1388–1394, 2015.

[35] Z. X. Chen, H. X. Hu, Y. G. Zheng, and X. M. Guo, "Effect of groove microstructure on slurry erosion in the liquid-solid two- phase flow," *Wear*, vol. 466-467, p. 203561, 2021.

[36] H. Jia, S. Zhao, X. Zhou, C. Qu, D. Fan, and C. Wang, "Low-temperature pyrolysis of oily sludge: roles of Fe/Al-pillared bentonites," *Archives of Environmental Protection*, vol. 43, no. 3, pp. 82–90, 2017.

[37] T. Yu, H. Hu, F. Wang, C. QU, J. LI, and B. YANG, "Effects of molecular sieves on the catalytic pyrolysis of oily sludge," *University Politehnica of Bucharest Scientific Bulletin Series B-Chemistry and Materials Science*, vol. 82, no. 4, pp. 133–146, 2020.

[38] B. Lin, J. Wang, Q. Huang, M. Ali, and Y. Chi, "Aromatic recovery from distillate oil of oily sludge through catalytic pyrolysis over Zn modified HZSM-5 zeolites," *Journal of Analytical and Applied Pyrolysis*, vol. 128, pp. 291–303, 2017.

[39] L. M. Zhang, Z. X. Li, J. X. Hu et al., "Understanding the roles of deformation-induced martensite of 304 stainless steel in

different stages of cavitation erosion," *Tribology International*, vol. 155, p. 106752, 2021.

[40] S. Zhao, X. Zhou, C. Wang, and H. Jia, "Dewatering and low-temperature pyrolysis of oily sludge in the presence of various agricultural biomasses," *Environmental Technology*, vol. 39, no. 21, pp. 2715–2723, 2018.

[41] J. Jin, M. Wang, Y. Cao et al., "Cumulative effects of bamboo sawdust addition on pyrolysis of sewage sludge: biochar properties and environmental risk from metals," *Bioresource Technology*, vol. 228, pp. 218–226, 2017.

[42] Y. Qiao, X. Wang, L. Yang et al., "Effect of aging treatment on microstructure and corrosion behavior of a Fe-18Cr-15Mn-0.66N stainless steel," *Journal of Materials Science & Technology*, vol. 107, pp. 197–206, 2022.

Hindawi
Scanning
Volume 2021, Article ID 6759176, 6 pages
https://doi.org/10.1155/2021/6759176

Review Article

Progress in Catalytic Pyrolysis of Oil Shale

Donghao Li[1], **Haodan Pan**[1], **Xiaojing Di**[1], **Xiaoyang Liu**[2] and **Hongxiang Hu**[3]

[1]*College of Petroleum Engineering, Liaoning Petrochemical University, Fushun 113301, China*
[2]*Thermal Power Plant of PetroChina Fushun Petrochemical Company, Funshun 113301, China*
[3]*CAS Key Laboratory of Nuclear Materials and Safety Assessment, Institute of Metal Research, Chinese Academy of Sciences, Shenyang 110016, China*

Correspondence should be addressed to Haodan Pan; panhaodan@126.com and Hongxiang Hu; hxhu@imr.ac.cn

Received 30 August 2021; Accepted 21 September 2021; Published 7 October 2021

Academic Editor: Jian Chen

This paper briefly describes the research status of oil shale pyrolysis technology and the main factors affecting oil shale pyrolysis, with emphasis on four kinds of commonly used catalysts: The effects of natural minerals, metal compounds, molecular sixes, and supported catalysts on the pyrolysis of oil shale were discussed. The changes of the pyrolysis mechanism and product composition of oil shale with the addition of different catalysts were discussed. Finally, the development direction of preparation of new catalysts was discussed, in order to provide a prospect for the development and utilization of unconventional and strategic alternative energy resources around the world.

1. Introduction

With the continuous decline of petroleum supply and the increase of petroleum product cost, how to solve the energy problem has become a big problem of urgency. Shale oil, the pyrolysis product of oil shale, is considered as a substitute for crude oil, and the utilization of this resource can alleviate the shortage of crude oil supply. Oil shale is an unconventional oil and gas resource, which is a nonrenewable energy source like oil, natural gas, and coal. It is rich in reserves and has great potential for industrial application [1]. The world is rich in oil shale reserves, up to 689 billion tons of shale oil. The United States has the largest oil shale reserves at 530.5 billion tons. China's reserves are 47.6 billion tons [2].

Because kerogen in oil shale is completely solid in its natural state, it cannot be directly mined. Kerogen in oil shale can be converted into liquid shale oil only by pyrolysis [2]. However, kerogen in oil shale conversion efficiency is low and affects the quality of shale oil, resulting in oil instability and high viscosity. Therefore, in order to promote the conversion of kerogen macromolecules, researchers used different types of catalysts to carry out catalytic pyrolysis, so as to improve the conversion efficiency of kerogen.

2. Research Status of Oil Shale Pyrolysis Technology

2.1. Application of Oil Shale Pyrolysis Technology. Oil shale pyrolysis technology mainly includes ectopic and in situ methods. Ectopic methods include oil shale extraction, grinding, screening, and pyrolysis. The in situ method involves heating and then pyrolyzing oil shale in geological formations [1, 2]. Therefore, many types of distiller have been derived in industry. Fushun distiller in China, Kiviter distiller in Estonia, and Petrosix distiller in Brazil have been successfully implemented and widely used [3].

Taking Fushun-type retorting technology as an example, the oil shale retorting process (OSR-GHC) with gas heat carrier has some disadvantages, such as low oil yield and low energy efficiency, which lead to low economic benefit [4]. Therefore, more and more attentions were paid to this technology of solid heat carrier retorting.

Different from the oil shale retorting process, the oil shale retorting process using solid heat carrier technology (OSR-SHC) uses a thermal cycle to provide heat for the oil shale retorting reaction. Compared with gas heat carrier retorting technology, the OSR-SHC process has many advantages: it can make the retorting air distribution

uniform and reduce the flow resistance. Increase shale oil yield to 90%. Increase resource utilization rate, good economy, and reduce environmental pollution [5].

2.2. Factors Affecting Oil Shale Pyrolysis. The pyrolysis of oil shale is affected by many factors, among which the technological conditions (including pyrolysis temperature, residence time, heating rate, and pressure) have the most significant influence on its pyrolysis [6].

2.2.1. Influence of Pyrolysis Temperature. The final pyrolysis temperature of oil shale has a complex influence on the pyrolysis process. The yield of shale oil, the composition of shale oil, the composition of pyrolytic semicoke, and secondary cracking of pyrolysis products are all related to the final pyrolysis temperature.

Wang et al. [7] studied the effect of water vapor on the temperature in pyrolysis of oil shale as a heat-carrying fluid and found that between 382°C and 555°C, the permeability increased significantly with the increase of temperature, which was conducive to pyrolysis. Geng et al. [8] have studied the evolution of pore fractures using X-ray computed tomography (Figures 1–4). The results show that the porosity increases, and the degree of pyrolysis intensifies with the increase of temperature. From 300°C to 500°C, the most significant increases.

2.2.2. Influence of Heating Time. Hydrothermal pretreatment affects the yield of oil shale pyrolysis products. The semicoke yield of oil shale increases, and the gas and water yield decreases. The shale oil yield can reach the maximum after 2 h hydrothermal pretreatment, and the oil produced from oil shale pyrolysis has higher energy [9]. Yang et al. [10] studied the influence of heat injection time on the quality of oil and gas products. When the injection temperature is controlled at 555°C, the quality of shale oil formed by oil shale cracking reaches the highest at 3 h of injection.

2.2.3. Influence of Heating Rate. The effect of heating rate on shale oil production is small, corresponding to oil production in the range of 10.4-11%. With the acceleration of the heating rate, oil production increases while gas production decreases slightly [11]. Lu et al. [12] and Bai et al. [13] studied the pyrolysis process of oil shale. The influence of heating rate (5°C/min, 10°C/min, 20°C/min, and 50°C/min) was considered. The increase of heating rate can transfer the characteristic parameters of oil shale pyrolysis to the high temperature but has no effect on the total mass loss.

2.2.4. Influence of Pressure. The influence of increasing pressure on the pyrolysis of organic matter depends on the amount of increasing pressure. Different increasing pressure values will have different effects and even block phenomena. The high-pressure thermogravimetric analysis of oil shale pyrolysis shows that the volatilization temperature of hydrocarbon increases with the increase of pyrolysis pressure. With the increase of pyrolysis pressure, oil production rate decreases, and gas production rate increases [14, 15].

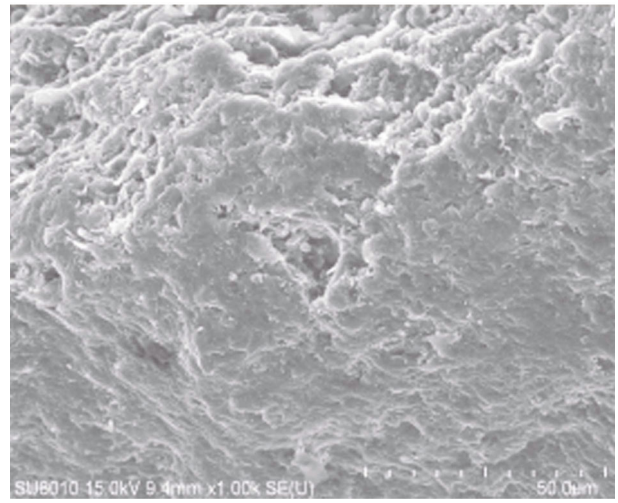

Figure 1: Pore size at 300°C.

3. Research Progress on Catalytic Pyrolysis of Oil Shale

Different parameters and conditions of catalytic pyrolysis of oil shale have been studied by using different catalysts. At present, the catalysts used in the catalytic pyrolysis of oil shale mainly include the following four types: natural minerals, metal compounds, molecular sieves, and supported catalysts.

3.1. Natural Minerals. As a kind of inorganic and organic sedimentary rock, the oil shale itself contains a variety of natural mineral components. Natural minerals such as quartz, clay minerals, feldspar, and pyrite are closely combined with organic matter in oil shale, which has a great influence on the pyrolysis process.

Oil shale is composed of organic and inorganic minerals. Inorganic minerals usually account for 50-85 wt% of oil shale, mainly including silicates, carbonates, quartz, and pyrite. Inorganic minerals have a certain influence on the pyrolysis of oil shale [16]. Zhao et al. [16] and Chang et al. [17] used acid to treat oil shale in batches in order to better understand the interaction between organic matter and inorganic minerals during oil shale pyrolysis. Hydrochloric acid effectively eliminates carbonate minerals, hydrofluoric acid effectively dissolves silicate minerals, and nitric acid removes pyrite. It was found that the shale oil production rates of original, carbonate-free, and carbonate-silicate oil shale samples were 50.4 wt.%, 44.3 wt.%, and 50.3 wt.%, respectively, indicating that carbonates promoted shale oil production and acted as catalysts in kerogen pyrolysis because their elimination from oil shale reduced hydrocarbon production [18]. The rate of shale oil production is reduced by silicates. This suggests that carbonates catalyze, sulfates catalyze, and the decomposition of kerogen also decreases with the increase of silicate. In addition, H_2SO_4 treatment can reduce the initial temperature and improve the pyrolysis efficiency of oil shale, which is economical [19].

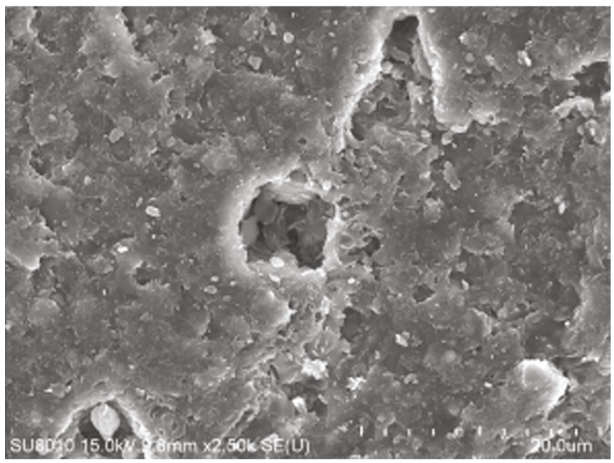

Figure 2: Pore size at 400°C.

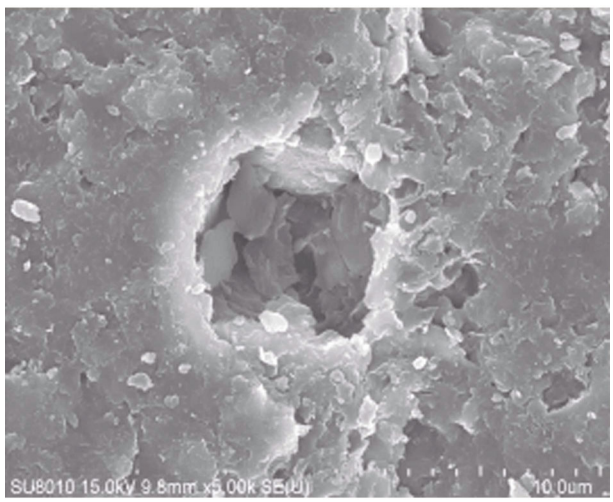

Figure 3: Pore size at 450°C.

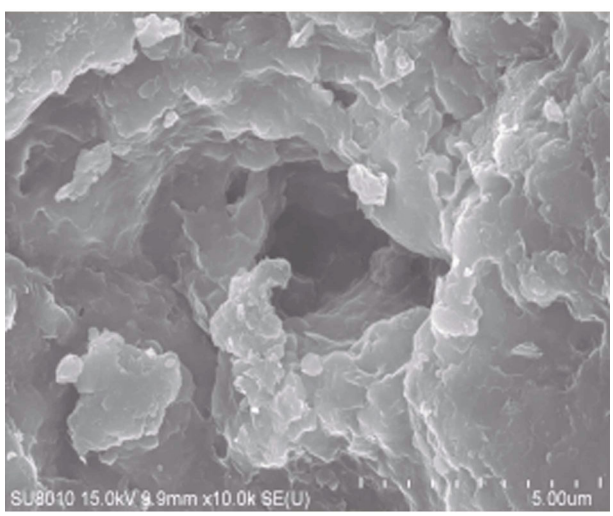

Figure 4: Pore size at 500°C.

Lu et al. [20] used HCL-HF to treat Huadian oil shale to better understand the interaction between organic matter and minerals in the pyrolysis process of oil shale. Mineral compounds have little effect on the decomposition of organic matter but have an effect on volatile matter reactions. It was found that $CaCO_3$, kaolinite, and TiO_2 had little effect on the volatiles reaction, while K_2CO_3, Na_2CO_3, and $MnCO_3$ promoted the volatiles reaction. In the process of catalytic pyrolysis of oil shale, the alkyl side chains of carbonate are disconnected, more hydrocarbons and toluene are generated, and benzene and H_2 are generated by dehydrogenation of long-chain aliphatic hydrocarbons. The action sequence of carbonate is $K_2CO_3 > Na_2CO_3 > Mn_2CO_3$.

The copyrolysis behavior of kerogen and montmorillonite showed that montmorillonite significantly improved the pyrolysis characteristics of kerogen. Therefore, montmorillonite can be considered as a potential natural catalyst [21]. Jiang et al. [22] studied the catalytic pyrolysis characteristics of oil shale mixed with montmorillonite and $CoCl_2{\cdot}6H_2O$. It was found that montmorillonite and cobalt chloride promoted decarboxylation reaction, and free radical reaction decreased acid yield and increased aliphatic hydrocarbon yield. The relative content of aliphatic hydrocarbons increased from 41.55% to 51.27%. This indicates that the combined use of montmorillonite and cobalt chloride is beneficial to the improvement of pyrolysis characteristics of oil shale and the formation of low molecular weight hydrocarbon fuels. Moreover, with the increase of montmorillonite ratio, shale oil yield increases, and the presence of cobalt chloride further promotes the deep pyrolysis of oil shale. When the cobalt chloride/montmorillonite mass ratio was 1 : 5, the maximum yield of liquid fuel increased by about 3.5 wt%.

Shi et al. [23] studied the influence of shale ash on the oil shale pyrolysis process. It is found that shale ash has little effect on product yield, but a great effect on gas and oil composition. Under the action of shale ash, the production of H_2 and CH_4 increased, but CO_2 decreased significantly. It reduces the aliphatic content in shale oil, shortens the chain length of the aliphatic group, but promotes the formation of aromatic hydrocarbon. This effect increases with the increase of shale ash content. Shale oil production is rising.

3.2. Metal Compounds. Metal compounds including metal oxides, metal sulfides, and metal salts have the advantages of simple preparation and high activity. Therefore, the effect of metal compounds on the yield and quality of liquid products has been studied extensively. Studies have found that Fe, Ca, Zn, Ni, and other metal oxides and chloride can accelerate the pyrolysis of oil shale and promote the generation of hydrogen-free radicals and the lightening of shale oil [24].

After the Fe_2O_3 catalyst was added and the $CaCO_3$ catalyst was added, the shale oil yield also increased in the pyrolysis process, but the shale oil yield was 1.02 times and 1.01 times, respectively. Therefore, Fe_2O_3 has a stronger catalytic effect on oil shale pyrolysis [24]. Lu et al. [12] selected CH_3COONa, $(CH_3COO)_2Ca$, and MgO as oil shale catalysts to study their pyrolysis behavior and characteristics of

pyrolysis products. The results show that the three catalysts can improve the shale oil and gas production rate. These catalysts redirect the pyrolysis process and improve the yield of shale oil and pyrolysis gas. CH_3COONa and MgO make the precipitation temperature of oil shale lower than that of the original sample, thus, reducing the activation energy of oil shale pyrolysis. Kang et al. [25] and Kang et al. [26] extracted Huadian oil shale and added different Fe compounds. After adding $FeCl_3$, the yield of shale oil from oil shale pyrolysis within 20 hours increased by 58.5%, and the time required for shale oil to produce the maximum oil decreased by 43%. This suggests that $FeCl_3$ accelerates the decomposition of asphaltenes in residual bitumen by promoting the cleavage of heterotopic bonds and triggering the pyrolysis reaction of kerogen. The presence of $FeCl_3$ inhibited the condensation polymerization of kerogen and promoted the ring-opening reaction of the aromatic structure. At 350°C, within 20 hours after $FeCl_2$ was added, the concentration of asphalt obtained was 0.08 mol/L, 50.5% higher than that of pure water. The addition of $FeCl_2$ reduced the time required to reach the maximum yield of bitumen by 43%. The results show that $FeCl_2$ solution extraction is an efficient method for in situ extraction of oil shale.

Jiang et al. [27] and Chang et al. [28] studied the effects of several transition metal salts such as $FeCl_2{\cdot}4H_2O$, $CoCl_2{\cdot}6H_2O$, $NiCl_2{\cdot}6H_2O$, $MnSO_4{\cdot}H_2O$, and $ZnCl_2$ on oil shale pyrolysis based on thermal decomposition characteristics, product yield, and composition of oil shale. It is concluded that these metal salts can promote the secondary cracking of shale oil, reduce oil production, and increase the production of pyrolysis gas. Metal salts can also catalyze the aromatization of aliphatic hydrocarbons to produce aromatic hydrocarbons. When $MnSO_4{\cdot}H_2O$ and $CoCl_2{\cdot}6H_2O$ are loaded with 0.1%$MnSO_4{\cdot}H_2O$ and $CoCl_2{\cdot}6H_2O$, the initial precipitation temperature of oil shale is lower than that of the original sample. In the second stage of pyrolysis (430~520°C), the activation energy decreases by 3.621 kJ/mol and 5.964 kJ/mol, respectively, and the oil yield increases by 0.44% and 0.53%, respectively, at 520°C. Meanwhile, $NiCl_2{\cdot}6H_2O$ can also promote oil shale pyrolysis. $FeCl_2{\cdot}4H_2O$ and $ZnCl_2$ have little effect on the decomposition behavior of oil shale. Metal salts can also catalyze the aromatization of aliphatic hydrocarbons to produce aromatic hydrocarbons.

3.3. Molecular Sieve. Molecular sieve has a special pore structure and is widely used in the chemical process industry as a new catalyst. The commonly used molecular sieves are mainly SAPO-11 molecular sieve, aluminum phosphate molecular sieve, ZSM-5 molecular sieve, TS molecular sieve, MCM molecular sieve, SBA molecular sieve, etc.

In addition, the molecular sieve can be entered according to the size of the order, but also has the advantages of uniform aperture structure, large specific surface area, high surface polarity, and stable structure. If the metal ions are doped in the molecular sieve, the acidity and REDOX characteristics will be affected. MCM-41 has a catalytic effect on the pyrolysis of oil shale and is widely used in hydrocarbon conversion processes, including aromatics dealkylation, cracking, and hydrocracking. MCM-41 has a unique cracking selectivity that can increase shale oil production [29].

ZSM-5 zeolite catalyst was added into the reactor to process the steam generated from the pyrolysis of oil shale. The effects of zeolite catalysts on the yield and composition of derived oil and gas were studied. The main gases produced by the pyrolysis of oil shale are carbon dioxide, carbon monoxide, hydrogen, methane, C_2H_4, C_2H_6, C_3H_6, and a small number of other hydrocarbon gases. After catalysis, the concentration of all hydrocarbon gases increased. But the oil yield is reduced, which leads to higher gas yield and coke formation on the catalyst. The total nitrogen and sulfur contents in oil were significantly reduced by 67% for nitrogen and 56% for sulfur [30]. Chang et al. [31] conducted catalytic pyrolysis of Huadian oil shale using ZSM-5 (SAR = 25, 38, 50) as a catalyst. Pyrolysis experiments were carried out in ZSM-5 (10 wt%) oil shale. The results showed that the ZSM-5 catalyst reduced the shale oil yield from 9.33 wt% to 6 wt%. The content of aromatic hydrocarbons in shale oil increased from 2.88% to more than 20%. The contents of aromatic hydrocarbons of ZSM-5-25 and ZSM-5-38 are 59.39% and 56.46%, respectively, which are suitable catalysts for catalytic pyrolysis. Compared with ZSM-5-38, ZSM-5-25 catalyzed less monocyclic aromatic hydrocarbons and more polycyclic aromatic hydrocarbons.

Park [32] studied the pyrolysis and catalytic pyrolysis of black pine (BPW) and cook oil shale (KOS) on acidic zeolite by gas chromatography-mass spectrometry. The results of gas chromatography-mass spectrometry (GC-MS) showed that oxygen-containing compounds and light hydrocarbons were generated from black pine and cook oil shale during noncatalytic pyrolysis. These oxygen-containing compounds and light hydrocarbons are converted to aromatic hydrocarbons over acidic zeolite by catalytic pyrolysis. The catalytic pyrolysis efficiency of BPW and KOS on HZSM-5 is up to 56%.

3.4. Supported Catalysts. Load type catalyst consists of active component and carrier of two parts; the load on the carrier was promoted after the dispersion of active components and can reduce the dosage; the carrier who is usually a big specific surface area and thermal stability of good material, such as natural ores and molecular sieve; and they can not only separate as a catalyst but also can be the carrier of catalyst. The active ingredients are mainly composed of one or several kinds of Fe, Co, Mo, Ni, etc. The supported catalyst support and active component also show a synergistic effect in some specific reactions.

Shale ash has a catalytic effect on oil shale pyrolysis and has a good adsorption capacity. As the grain size of shale ash decreased from 1.25 mm to 0.20 mm, the shale coke yield decreased slightly and the total volatile product yield increased. The addition of 0.20 mm shale ash is the best for improving shale oil production rate and kerogen conversion to volatile products [33]. Lu et al. [34] studied the effect of Fushun oil shale and shale ash loaded with different transition metal salts ($ZnCl_2$, $NiCl_2{\cdot}6H_2O$, and $CuCl_2{\cdot}2H_2O$) on pyrolysis. The transition metal salt catalyst supported by shale ash can reduce the initial pyrolysis temperature of oil

shale, and the catalytic effect is enhanced with the increase of transition metal salt loading in the range of 0.1-3.0 wt%. Different transition metal salts have different catalytic effects. $CuCl_2{\cdot}2H_2O$ has the most obvious catalytic effect among the three excessive metal salts. The loading of transition metal salts on shale ash not only increases the content of oxygen-containing compounds but also promotes the cracking and aromatization of aliphatic hydrocarbons to form short-chain aliphatic hydrocarbons and aromatic hydrocarbons. The catalytic sequence of transition metal salts is $CuCl_2 \cdot 2H_2O > NiCl_2 \cdot 6H_2O > ZnCl_2$. Liu et al. [35] studied using shale ash (SA) as support, Cu-Ni transition metal salts with different ratios of Cu/Ni are 1 : 0, 2 : 1, 1 : 1, and 1 : 2, 0 : 1 to investigate the effects of different ratios of transition metal salts on the pyrolysis behavior and characteristics of Fushun oil shale. The results show that the temperature corresponding to the maximum weight loss rate decreases by 12.9°C, 4.0°C, and 3.6°C, respectively, and the apparent activation energy of pyrolysis decreases by 35.2%, 33.9%, and 29.6% with the addition of Cu_0Ni_1/SA catalyst, respectively. The addition of Cu_0Ni_1/SA and Cu_2Ni_1/SA further improved the shale oil yield by 3.5% and 3.1%, respectively.

After hydrodesulfurization, the calorific value and viscosity of shale oil are improved obviously. Catalysts used for modification are always inactivated by coke deposition, but in situ high-temperature treatment in the air effectively removes the coke from the catalyst surface to make it highly active after the devulcanization operation. Zhang et al. [36] and Qiao et al. [37] used Ni-Mo/Al_2O_3 catalyst to conduct fixed-bed mild hydrotreating for shale oil. The results show that under the condition of catalytic hydrodesulfurization, the sulfur removal rate of shale oil is 84.6%, and the yield of upgraded high-quality oil is up to 96.2%. After hydrodesulfurization, the calorific value and viscosity of shale oil are improved obviously.

4. Prospect of Catalytic Pyrolysis Technology of Oil Shale

Researchers have carried out a large number of studies on various factors affecting oil shale pyrolysis and achieved fruitful results. The optimum conditions involving pyrolysis temperature, heating rate, residence time, and pressure have been determined.

The future research direction of oil shale pyrolysis will focus on catalysts: (1) further research on alkali metal, alkaline earth metal, and molecular sieve catalysts; (2) the supported catalyst was designed with molecular sieve, montmorillonite, and Al2O3 as the carrier; (3) the corresponding catalysts were designed by deeply understanding the macroscopic and microscopic structural characteristics of oil shale in different areas, and the catalytic cracking mechanism was studied. At present, there have been researches on binary supported catalysts based on single active component supported catalysts, but there are still few types of research in this aspect. In the future, with further research, there will be more binary or even multiple supported catalysts or more complex catalysts to promote the development and progress of the oil shale industry.

Data Availability

The review article's data used to support the findings of this study are included within the article.

Conflicts of Interest

The authors declare that they have no conflicts of interest.

References

[1] H. Li, G. Li, Q. Yang, and H. Zhou, "Modeling and performance analysis of shale oil and methane cogeneration by oil shale pyrolysis integrated with a pyrolysis gas methanation process," *Energy & Fuels*, vol. 34, no. 9, pp. 11690–11698, 2020.

[2] Z. Kang, Y. Zhao, and D. Yang, "Review of oil shale in-situ conversion technology," *Applied Energy*, vol. 269, no. 1, p. 115121, 2020.

[3] M. Mu, X. Han, and X. Jiang, "Combined fluidized bed retorting and circulating fluidized bed combustion system of oil shale: 3. Exergy analysis," *Energy*, vol. 151, pp. 930–939, 2018.

[4] Q. Yang, Y. Qian, A. Kraslawski, H. Zhou, and S. Yang, "Advanced exergy analysis of an oil shale retorting process," *Applied Energy*, vol. 165, no. 1, pp. 405–415, 2016.

[5] Q. Yang, Y. Qian, A. Kraslawski, H. Zhou, and S. Yang, "Framework for advanced exergoeconomic performance analysis and optimization of an oil shale retorting process," *Energy*, vol. 109, no. 15, pp. 62–76, 2016.

[6] T. Saif, Q. Lin, B. Bijeljic, and M. J. Blunt, "Microstructural imaging and characterization of oil shale before and after pyrolysis," *Fuel*, vol. 197, no. 1, pp. 562–574, 2017.

[7] L. Wang, D. Yang, and Z. Kang, "Evolution of permeability and mesostructure of oil shale exposed to high- temperature water vapor," *Fuel*, vol. 290, p. 119786, 2021.

[8] Y. Geng, W. Liang, J. Liu, M. Cao, and Z. Kang, "Evolution of pore and fracture structure of oil shale under high temperature and high pressure," *Energy & Fuels*, vol. 31, no. 10, pp. 10404–10413, 2017.

[9] H. Jiang, S. Deng, J. Chen et al., "Effect of hydrothermal pretreatment on product distribution and characteristics of oil produced by the pyrolysis of Huadian oil shale," *Energy Conversion and Management*, vol. 143, no. Jul., pp. 505–512, 2017.

[10] D. Yang, L. Wang, Y. Zhao, and Z. Kang, "Investigating pilot test of oil shale pyrolysis and oil and gas upgrading by water vapor injection," *Journal of Petroleum Science and Engineering*, vol. 196, p. 108101, 2021.

[11] X. Lan, W. Luo, Y. Song, J. Zhou, and Q. Zhang, "Effect of the temperature on the characteristics of retorting products obtained by Yaojie oil shale pyrolysis," *Energy & Fuels*, vol. 29, no. 12, pp. 7800–7806, 2015.

[12] Y. Lu, Y. Wang, Q. Wang, J. Zhang, Y. Zhao, and Y. Zhang, "Investigation on the catalytic effect of AAEMs on the pyrolysis characteristics of Changji oil shale and its kinetics," *Fuel*, vol. 267, no. 1, p. 117287, 2020.

[13] F. T. Bai, Y. H. Sun, Y. M. Liu, M. Guo, and J. Zhao, "Characteristics and kinetics of Huadian oil shale pyrolysis via non-isothermal thermogravimetric and gray relational analysis," *Combustion Science and Technology*, vol. 192, no. 3, pp. 471–485, 2020.

[14] E. C. Corredor and M. D. Deo, "Effect of vapor liquid equilibrium on product quality and yield in oil shale pyrolysis," *Fuel*, vol. 234, no. 15, pp. 1498–1506, 2018.

[15] B. Baruah and P. Tiwari, "Effect of high pressure on nonisothermal pyrolysis kinetics of oil shale and product yield," *Energy & Fuels*, vol. 34, no. 12, pp. 15855–15869, 2020.

[16] X. Zhao, X. Zhang, Z. Liu, Z. Lu, and Q. Liu, "Organic matter in Yilan oil shale: characterization and pyrolysis with or without inorganic minerals," *Energy & Fuels*, vol. 31, no. 4, pp. 3784–3792, 2017.

[17] Z. Chang, M. Chu, C. Zhang, S. Bai, H. Lin, and L. Ma, "Influence of inherent mineral matrix on the product yield and characterization from Huadian oil shale pyrolysis," *Journal of Analytical and Applied Pyrolysis*, vol. 130, pp. 269–276, 2018.

[18] H. Faisal, K. S. Katti, and D. R. Katti, "Modeling the behavior of organic kerogen in the proximity of calcite mineral by molecular dynamics simulations," *Energy & Fuels*, vol. 34, no. 3, pp. 2849–2860, 2020.

[19] Z. Zhang, L. Zhao, L. Zhuang, Y. Li, and H. Zhang, "The effect of acid treatment on pyrolysis of Longkou oil shale," *Energy Sources, Part A: Recovery, Utilization, and Environmental Effects*, vol. 41, no. 13, pp. 1605–1614, 2019.

[20] Z. Lu, X. Zhao, Z. Liu, and Q. Liu, "Mutual influences between organic matter and minerals during oil shale pyrolysis," *Energy & Fuels*, vol. 33, no. 3, pp. 1850–1858, 2019.

[21] M. Hu, Z. Cheng, M. Zhang et al., "Effect of calcite, kaolinite, gypsum, and montmorillonite on Huadian oil shale kerogen pyrolysis," *Energy & Fuels*, vol. 28, no. 3, pp. 1860–1867, 2014.

[22] H. Jiang, W. Hong, Y. Zhang et al., "Behavior, kinetic and product characteristics of the pyrolysis of oil shale catalyzed by cobalt-montmorillonite catalyst," *Fuel*, vol. 269, no. 1, p. 117468, 2020.

[23] W. Shi, Z. Wang, W. Song, S. Li, and X. Li, "Pyrolysis of Huadian oil shale under catalysis of shale ash," *Journal of Analytical and Applied Pyrolysis*, vol. 123, no. Jan., pp. 160–164, 2017.

[24] S. Wang, L. Song, and X. Jiang, "Catalytic effects of FE- AND ca-based additives on gas evolution during pyrolysis of Dachengzi oil shale of China," *Oil Shale*, vol. 35, no. 1, p. 39, 2018.

[25] S. Kang, Y. Sun, M. Qiao et al., "The enhancement on oil shale extraction of $FeCl_3$ catalyst in subcritical water [J]," *Energy*, vol. 238, p. 121763, 2022.

[26] S. Kang, Y. Sun, S. Deng et al., "Extraction of Huadian oil shale in subcritical $FeCl_2$ solution," *Fuel Processing Technology*, vol. 211, p. 106571, 2021.

[27] H. Jiang, L. Song, Z. Cheng et al., "Influence of pyrolysis condition and transition metal salt on the product yield and characterization via Huadian oil shale pyrolysis," *Journal of Analytical and Applied Pyrolysis*, vol. 112, no. Mar., pp. 230–236, 2015.

[28] Z. CHANG, M. CHU, C. ZHANG, S. BAI, and L. MA, "Investigation of the effect of selected transition metal salts on the pyrolysis of Huadian oil shale, China," *Oil Shale*, vol. 34, no. 4, p. 354, 2017.

[29] A. Schwanke and S. Pergher, "Lamellar MWW-type zeolites: toward elegant nanoporous materials," *Applied Sciences*, vol. 8, no. 9, p. 1636, 2018.

[30] Y. Tian, M. Li, D. Lai, Z. Chen, S. Gao, and G. Xu, "Characteristics of oil shale pyrolysis in a two-stage fluidized bed," *Chinese Journal of Chemical Engineering*, vol. 26, no. 2, pp. 407–414, 2018.

[31] Z. Chang, Y. Qu, Z. Gu et al., "Production of aromatic hydrocarbons from catalytic pyrolysis of Huadian oil shale using ZSM-5 zeolites as catalyst," *Journal of Analytical and Applied Pyrolysis*, vol. 104990, p. 104990, 2020.

[32] Y. K. Park, M. Z. Siddiqui, S. Karagöz, T. U. Han, A. Watanabe, and Y. M. Kim, "In-situ catalytic co-pyrolysis of kukersite oil shale with black pine wood over acid zeolites," *Journal of Analytical and Applied Pyrolysis*, vol. 155, p. 105050, 2021.

[33] X. Ge, S. Wang, and X. Jiang, "Catalytic effects of shale ash with different particle sizes on characteristics of gas evolution from retorting oil shale," *Journal of Thermal Analysis and Calorimetry*, vol. 138, no. 2, pp. 1527–1540, 2019.

[34] H. Lu, F. Jia, C. Guo, H. Pan, X. Long, and G. Liu, "Effect of shale ash-based catalyst on the pyrolysis of Fushun oil shale," *Catalysts*, vol. 9, no. 11, p. 900, 2019.

[35] X. Liu, H. Pan, C. Guo, X. di, and H. Hu, "Effect of Double Transition Metal Salt Catalyst on Fushun Oil Shale Pyrolysis," *Scanning*, vol. 2020, 14 pages, 2020.

[36] M. Zhang, C. Wang, K. Wang et al., "Gentle hydrotreatment of shale oil in fixed bed over Ni- Mo/Al_2O_3 for upgrading," *Fuel*, vol. 281, p. 118495, 2020.

[37] Y. X. Qiao, S. L. Sheng, L. M. Zhang et al., "Friction and wear behaviors of a high nitrogen austenitic stainless steel Fe-19Cr-15Mn-0.66N," *Journal of Mining and Metallurgy, Section B: Metallurgy*, vol. 57, no. 2, pp. 285–293, 2021.

Hindawi
Scanning
Volume 2021, Article ID 6661872, 10 pages
https://doi.org/10.1155/2021/6661872

Research Article

Effect of Cu^{2+} on Corrosion Behavior of A106B Carbon Steel and 304L Stainless Steels in Seawater

Kewei Fang,[1] **Chengtao Li**,[1] **Shuai Dong**,[1] **Dubao Zhang**,[1] **Xiangfeng Wu**,[1] **and Hongxiang Hu**[2]

[1]*Suzhou Nuclear Power Research Institute, Suzhou 215004, China*
[2]*CAS Key Laboratory of Nuclear Materials and Safety Assessment, Institute of Metal Research, Chinese Academy of Sciences, Shenyang 110016, China*

Correspondence should be addressed to Kewei Fang; fangkewei@cgnpc.com.cn and Hongxiang Hu; hxhu@imr.ac.cn

Received 5 August 2021; Accepted 24 August 2021; Published 6 October 2021

Academic Editor: Jian Chen

The corrosion behaviors of A106B carbon steel and 304L stainless steel (SS) in seawater with different Cu^{2+} concentrations were studied by the immersion test and the potentiodynamic polarization test. The results showed that with the increasing Cu^{2+} concentration, the mass lot rates of A106B and 304L SS all increased in the immersion test, and compared with A106B, the mass lot rates of 304L SS were all smaller. In the potentiodynamic polarization test, following the concentration of Cu^{2+} increased, the corrosion potential of A106B firstly shifted negatively; then, when Cu^{2+} increased to 100 ppm, the polarization curve moved to the upper right direction; namely, both the corrosion potential and corrosion electrical density increased. The corrosion potential of 304L SS increased with the increasing Cu^{2+}, and the passive region was reduced; the pitting sensitivity improved.

1. Introduction

The important plant water system (SEC system), i.e., the safety plant water system, function was to transfer the heat from the structures, systems, and components related to safety to the final sink-seawater under normal operation and accident conditions. The system consisted of SEC pumps, shellfish traps, various values and pipes, and RRI/-SEC plate heat exchangers [1].

In the existing nuclear power plants, the SEC pipes were made of stainless steel [2, 3], carbon steel lined with coating, rubber, plastic or cement mortar, and resin pipes. During the service of the SEC pipes, the addition of the cupric fungicide to prevent microbial corrosion, the corrosion of copper components, or other reasons could lead to the local enrichment of Cu^{2+} in the SEC system and the precipitation of Cu on the surface of components; the interaction between Cu^{2+} and seawater may accelerate the corrosion of SEC system material, even leading to the breaking of the components and inducing the addition of Cu^{2+} into the secondary circuit system.

Presently, the corrosion of steels in seawater had been widely investigated all over the world [4–20], and the influence of Cu^{2+} on material corrosion is mainly focused on different materials in nonseawater environment, such as steel [21–30], aluminum alloy [31, 32], 690 alloy [33], and copper alloy [34]. However, the works focused on the corrosion behavior of steels in seawater containing Cu^{2+} and the influence of the Cu^{2+} and copper oxides on the corrosion of the equipment in the secondary circuit system were little reported [35]. Therefore, the corrosion behaviors of steels in seawater containing Cu^{2+} were studied by the immersion test, potentiodynamic polarization, and SEM observation, which could provide a certain basis and guidance for the operation of nuclear power stations.

2. Experimental Detail

The materials used in the present work were A106B carbon steel and 304L stainless steel (SS). The chemical compositions (wt.%) of A106B and 304L SS are listed in Table 1.

Table 1: The chemical compositions of A106B and 304L SS (wt.%).

	C	Si	Mn	P	S	Cr	Ni	Mo	Cu	Fe
A106B	0.23	0.35	0.62	0.023	0.012	0.21	0.14	0.07	0.18	Bal.
304L SS	0.025	0.27	1.38	0.017	0.002	18.04	8.08	0.05	0.07	Bal.

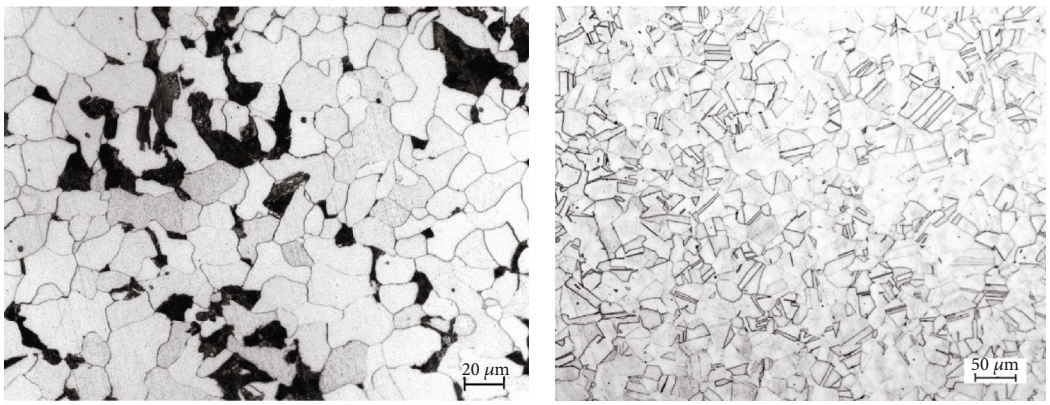

(a) (b)

Figure 1: OM microstructure of (a) A106B and (b) 304L SS.

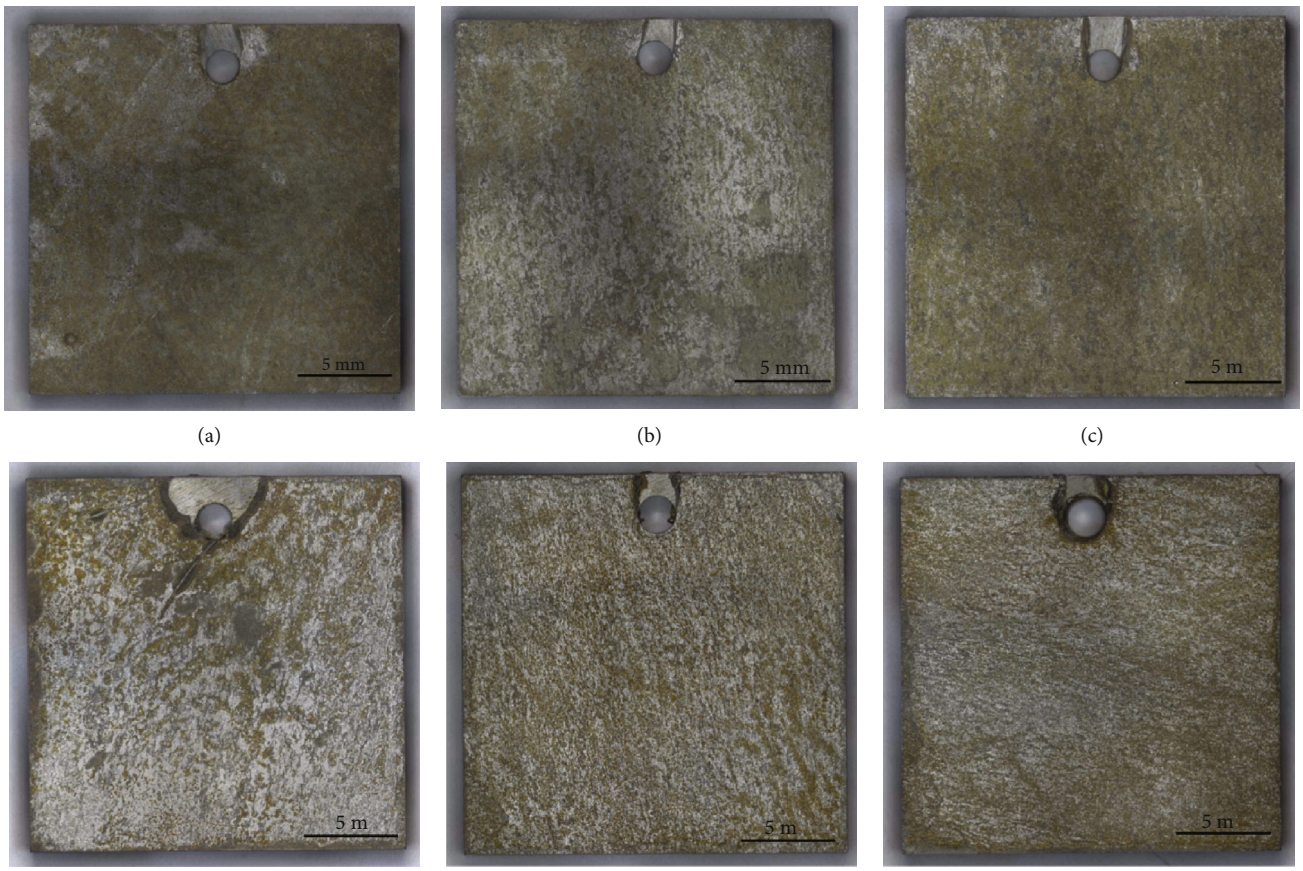

(a) (b) (c)

(d) (e) (f)

Figure 2: Corrosion morphologies of A106B after the immersion test: (a) 0 ppm, (b) 10 ppm, (c) 50 ppm, (d) 100 ppm, (e) 500 ppm, and (f) 1000 ppm.

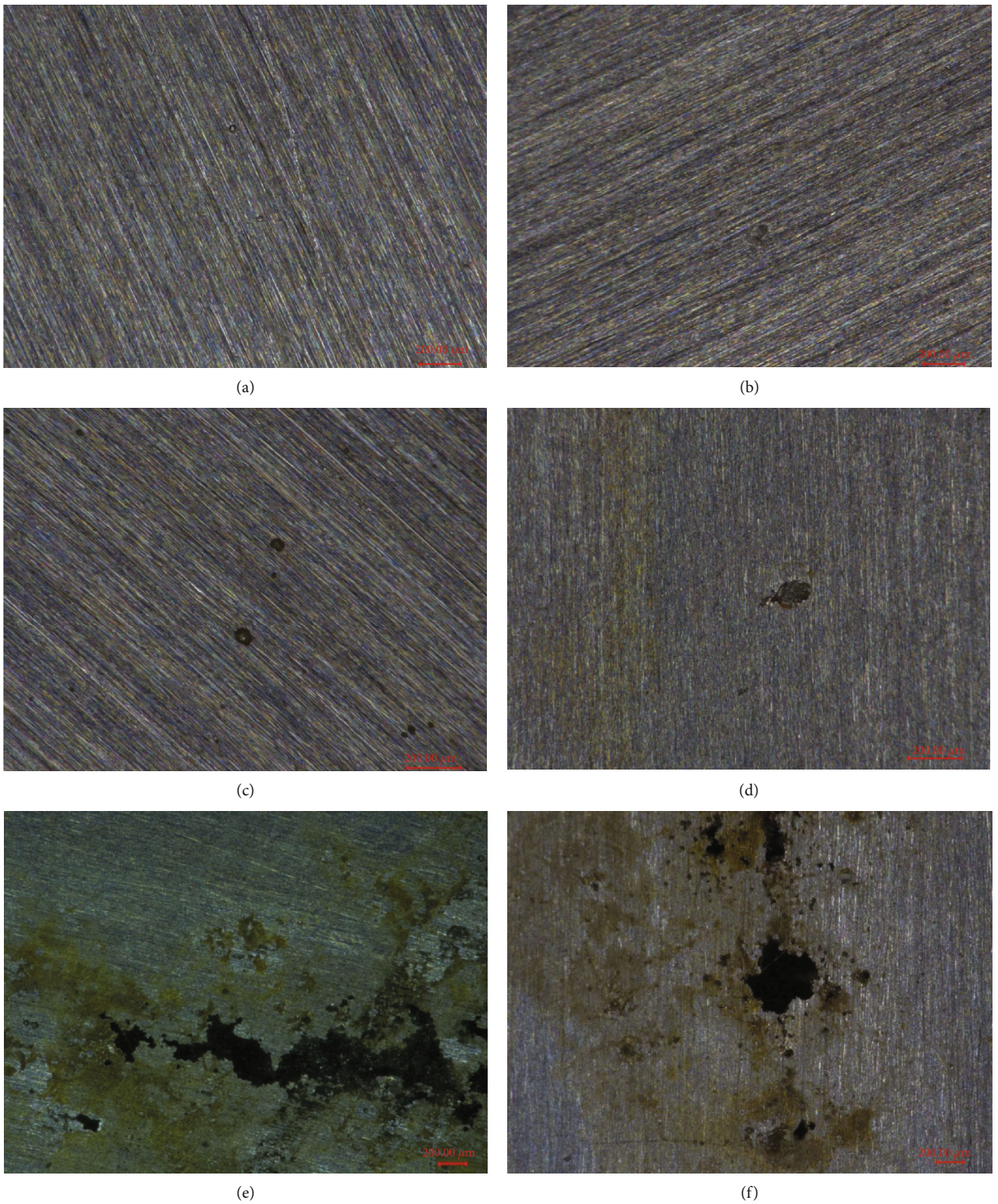

(a) (b) (c) (d) (e) (f)

Figure 3: Morphologies of 304L SS after the immersion test: (a) 0 ppm, (b) 10 ppm, (c) 50 ppm, (d) 100 ppm, (e) 500 ppm, and (f) 1000 ppm.

As shown in Figure 1(a), the optical microstructure (OM) of A106B was ferrite and pearlite biphasic structure, among which the black lamellar structure was pearlite phase. The microstructure of 304L SS is listed in Figure 1(b), which was a typical austenitic structure with twins. A106B was eroded by 4% nitrate alcohol and ethanol, respectively; then, they were analyzed by an optical microscope. 304L SS was electrolytically etched in 10% oxalic acid reagent at 10 V for 60 s for the microstructural observations.

The materials were cut into sheets with a dimension of 20 mm × 20 mm × 3 mm. Prior to the experiment, the surface of the samples was polished to 800# with sandpaper,

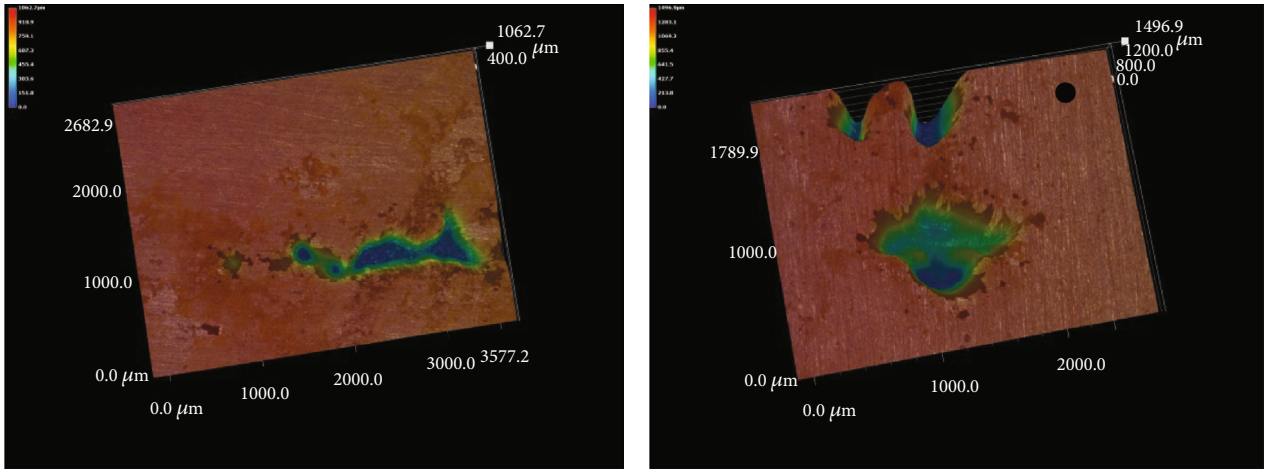

(a) (b)

Figure 4: 3D corrosion pit morphologies of 304L SS: (a) 500 ppm and (b) 1000 ppm.

then cleaned with deionized water, acetone, and anhydrous ethanol, then air-dried. The quality was weighted and size measured after the samples. The test solutions were seawater solutions with different concentrations of Cu^{2+}; the concentrations of Cu^{2+} were 10, 50, 100, 500, and 1000 ppm, respectively; the test period was 168 h, and the test temperature was 50°C. Before and after the immersion tests, the specimen was weighed using an electronic balance with an accuracy of 0.01 mg. The corrosion rate (C_R) was calculated based on the mass loss, Δm, using Equation (1) after a given period [1]:

$$C_R = \frac{\Delta m_1 + \Delta m_2 + \Delta m_3 + \Delta m_4 + \Delta m_5}{5 \cdot S \cdot t}, \quad (1)$$

where Δm_1, Δm_2, Δm_3, Δm_4, and Δm_5 represent the mass loss of the five samples used (mg), S is the surface area of the sample (10.4 cm^2), and t is the total test duration (168 h).

The exposed area of the sample in the test of the potentiodynamic polarization was 1 cm^2. Before the experiment, the surface of the samples was polished down to 800# with sandpaper and then cleaned using deionized water, acetone, and anhydrous ethanol. The potentiodynamic polarization test was carried out using the CS310 electrochemical workstation; the detailed introduction of the electrochemical experimental design methods was presented in the literature [1, 2]. The test solution was consistent with the immersion test, and the test temperature was 25°C. Before the test, the working electrode was immersed in the solution for 30 min and then −400 mV below the corrosion potential and terminated when the current density of 10 mA/cm^2 was reached with a scanning rate of 20 mV/min.

3. Results and Discussion

3.1. Corrosion Morphologies of A106B. Figure 2 presents the corrosion morphologies of A106B after the immersion test in tested solutions. A106B presented uniform corrosion in seawater of different concentrations of Cu^{2+}. After the test in solution without Cu^{2+}, the matrix surface of the sample

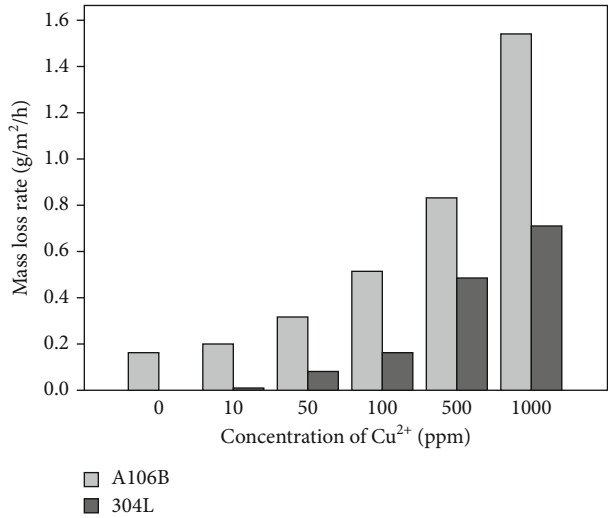

Figure 5: The weight loss rate of A106B and 304L SS after the immersion test.

was relatively flat; with the addition of Cu^{2+}, small and shallow pits appeared, and with the increase of the concentration of Cu^{2+}, the amount of the pits increased. After the test, a small number of tan corrosion products adhered to the matrix surface.

Figures 3 and 4 present the corrosion morphologies of 304L SS after the immersion test. The corrosion pits all appeared on the matrix surface of the samples; without the Cu^{2+}, there were only few shallow pits, and the size of the pits were small, with a few microns; with the increase of the concentration of Cu^{2+}, the amount and size of the pits both increased; the maximum depth of the pits in seawater of 500 ppm and 1000 ppm Cu^{2+} could be as deep as 1000 and 1500 microns, respectively.

3.2. Corrosion Rate of A106B and 304L SS. Figure 5 presents the mass loss rate of A106B and 304L SS after the immersion test. As is seen in Figure 5, the mass loss rate of A106B

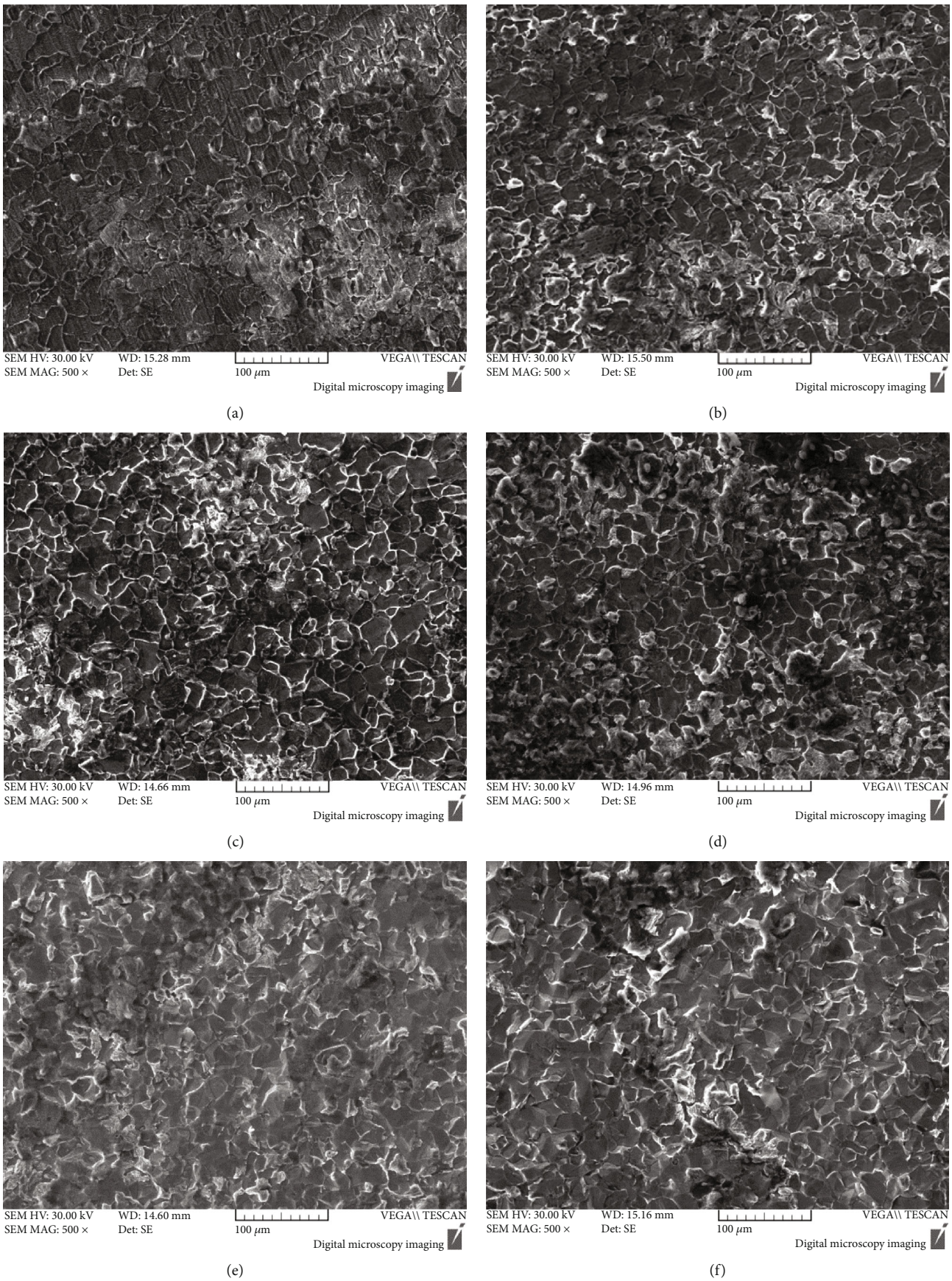

Figure 6: Morphologies of A106B after the immersion test: (a) 0 ppm, (b) 10 ppm, (c) 50 ppm, (d) 100 ppm, (e) 500 ppm, and (f) 1000 ppm.

largely increased with the increase of the concentration of Cu^{2+}. The mass loss rate in seawater without the Cu^{2+} was 0.163 g·m^{-2}·h^{-1}; the mass loss rate in seawater of 10, 50, 100, 500, and 1000 ppm Cu^{2+} increased by 0.23, 0.97, 2.14, 4.12, and 8.47 times, respectively. The mass loss rate of 304L SS in seawater without the Cu^{2+} is about 0.0012 g·m^{-2}·h^{-1}. However, the mass loss rate in seawater of 10 ppm, 50 ppm, 100 ppm, 500 ppm, and 1000 ppm Cu^{2+} increased by 6, 67, 139, 404, and 591 times, respectively. The presence of Cu^{2+} significantly increased the corrosion rate of 304L SS in seawater.

3.3. Corrosion Morphologies of A106B and 304L SS. Figure 6 presents the SEM surface morphologies of A106B after the immersion test in seawater solution of different concentrations of Cu^{2+}. The morphologies of different concentrations of Cu^{2+} had no significant difference; the matrix was relatively flat with some small particles. The EDS analysis showed that the matrix surface mainly consisted of Fe and a small amount of O, the content of Cu was little, which indicated that the precipitated Cu and other corrosion products were very loose, and there were basically no residual corrosion products attached on the matrix. Figure 7 presents the EDS result on the surface of A106B, which indicated that the surface of A106B was rich in Fe and O elements.

Figure 8 shows the SEM microscopic morphology of 304L stainless steel after the corrosion test in seawater of different concentrations of Cu^{2+}. Without the Cu^{2+}, the pitting corrosion initiation formed, the concentration of Cu^{2+} increased to 10 ppm, and a small number of corrosion pits with a few microns to tens of micron in size appeared; with the increase of the concentration of Cu^{2+}, the size of the corrosion pits increased; when the concentration of Cu^{2+} increased to 100 ppm, the size of the corrosion pits had been more than 100 microns, which indicated the sample suffered from heavy pitting corrosion.

3.4. Potentiodynamic Polarization. Figure 9 shows the potentiodynamic polarization curves of A106B in tested solutions. As is seen in Figure 10, the concentration of Cu^{2+} had a significant influence on the corrosion behavior of A106B. With the increase of the concentration of Cu^{2+}, the corrosion potential decreased and the corrosion current density increased firstly; compared with that without Cu^{2+}, E_{corr} of A106B in tested solutions initially shifted to a more negative potential and then subsequently increased to negative potential when the concentration of Cu^{2+} is higher than 100 ppm. The corrosion potential (E_{corr}) for A106B in seawater without Cu^{2+} is -648 mV_{SCE}; when the concentration of Cu^{2+} increased to 10 ppm, E_{corr} decreased by about 10 mV; when increased to 50 ppm, it decreased by 65 mV_{SCE}; when increased more than 100 ppm, the potentiodynamic polarization curves moved significantly up to the right; namely, both the corrosion potential and the corrosion current density largely increased. Meanwhile, with the increase of the concentration of Cu^{2+}, the cathode control became the diffusion control of Cu^{2+}.

The corrosion potential was a mixed potential formed by the coupling of anodic dissolution reaction and cathode depolarizer reduction reaction, which was between the anodic reaction equilibrium potential and cathode reduction reaction equilibrium potential. In seawater solution without Cu^{2+}, the cathode reaction was the reduction of O_2, as the equilibrium potential of electrode reaction $Cu \rightleftharpoons Cu^{2+} + 2e^-$ was higher than that of $Fe \rightleftharpoons Fe^{2+} + 2e^-$; when the Cu^{2+} was added, the cathode reactions on the surface of A106B included both the reduction reactions of O and Cu^{2+}; namely, in the seawater containing Cu^{2+}, there were two depolarizing agents, O_2 and Cu^{2+}, which made the A106B suffer from corrosion.

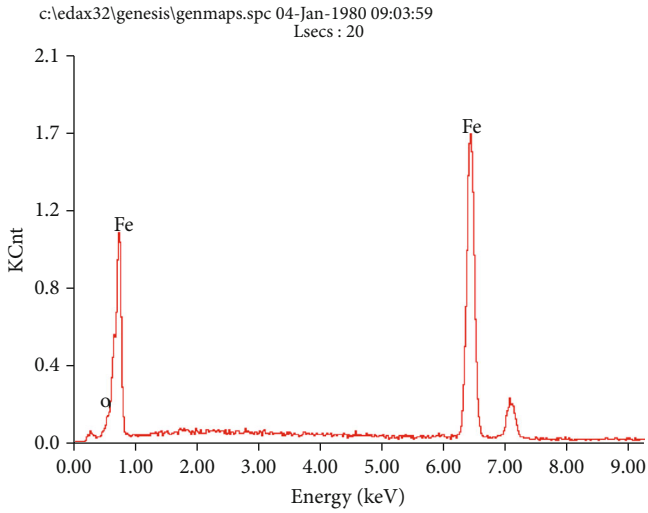

Figure 7: EDS on the surface of A106B after the immersion test at 100 ppm Cu solution.

The equilibrium potential (for standard hydrogen potential) of electrode reaction $Cu \rightleftharpoons Cu^{2+} + 2e^-$ could be calculated through the Nernst equation:

$$E_{e(Cu/Cu^{2+})} = E^{\theta}_{(Cu/Cu^{2+})} + \frac{RT}{2F} \ln c_{Cu^{2+}}, \quad (2)$$

where $E_{e(Cu/Cu^{2+})}$ is the equilibrium potential of electrode reaction $Cu \rightleftarrows Cu^{2+} + 2e$ and $E^{\theta}_{Cu/Cu^{2+}}$ is the standard potential of electrode reaction $Cu \rightleftarrows Cu^{2+} + 2e$, where R is ideal gas constant, 8.314 J/(K·mol), T is thermodynamic temperature (K), F is Faraday constant, 96500 C, and $c_{Cu^{2+}}$ is the concentration of Cu^{2+} (mol/cm^3).

As known, $E^{\theta}_{Cu/Cu^{2+}}$ was known as 0.345 V (SHE), $E^{\theta}_{OH^-/O_2}$ was 0.401 V (SHE), so when the concentration of Cu^{2+} was low, the cathode reaction was mainly the reduction of O_2; the two intercoupling cathode reactions accelerated the anodic dissolution reaction rate; meanwhile, a small amount of Cu was precipitated on the surface of the sample, which formed the Fe-Cu corrosion galvanic cells and also accelerated the anodic dissolution reaction. With the increase of the concentration of Cu^{2+}, $E_{e(Cu/Cu^{2+})}$ increased constantly and finally increased higher than $E^{\theta}_{OH^-/O_2}$, the cathode reaction was changed from mainly the reduction of O_2 to mainly the reduction of Cu^{2+}, a large amount of

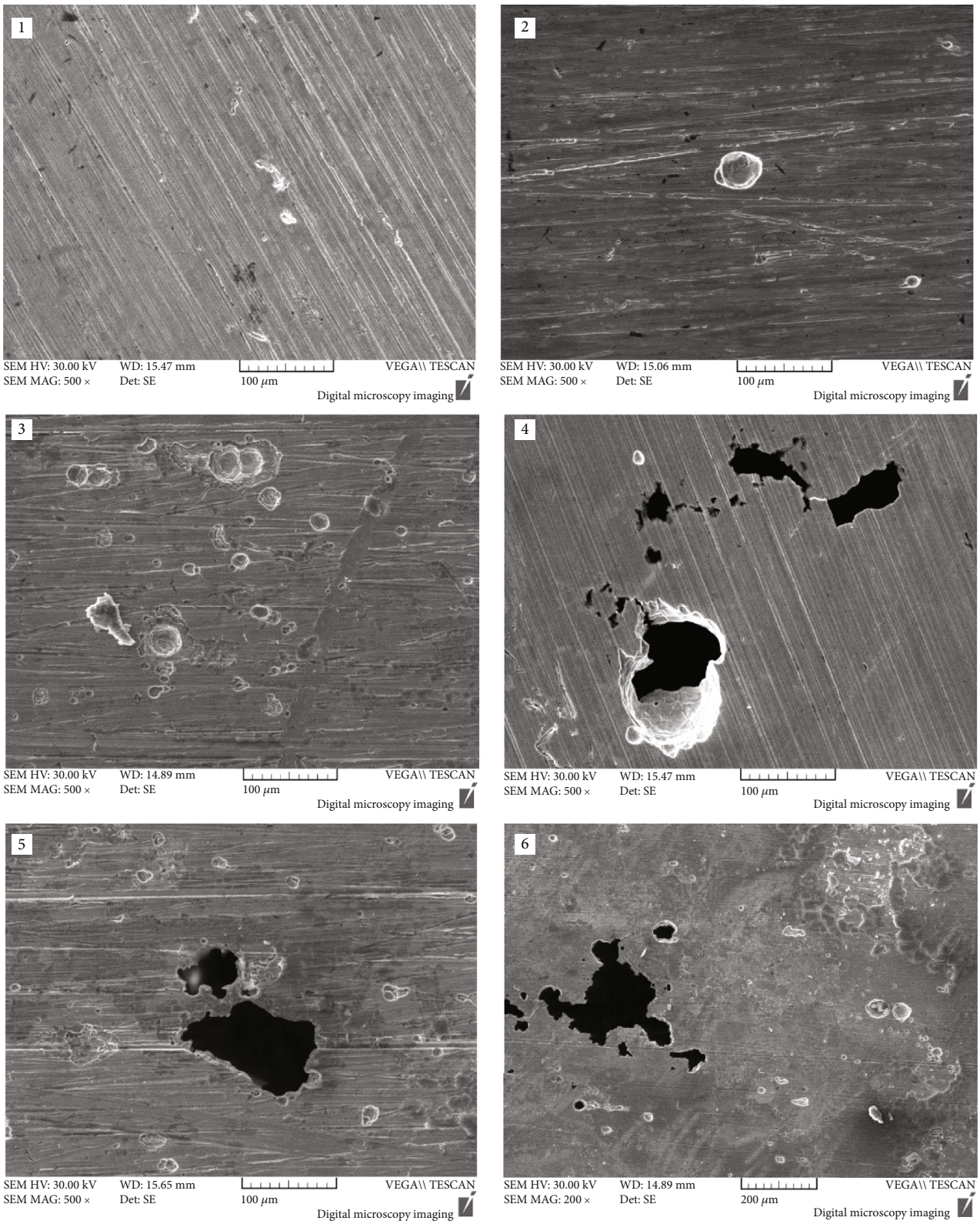

Figure 8: Morphologies of 304L SS after the immersion test: (1) 0 ppm; (2) 10 ppm; (3) 50 ppm; (4) 100 ppm; (5) 500 ppm; (6) 1000 ppm.

Cu was precipitated on the surface, and a large number of Fe-Cu corrosion galvanic cells were formed, which largely increased the anodic dissolution rate. This was also the reason why there were many small corrosion pits on the surface, but the macroscopic corrosion morphology was characterized by uniform corrosion.

Figure 10 shows the potentiodynamic polarization curves of 304L SS in tested solutions. As can be seen, with

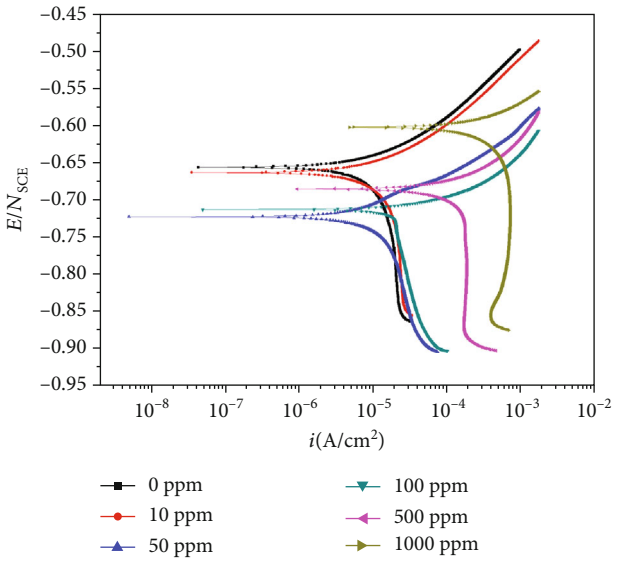

Figure 9: Potentiodynamic polarization curves of A106B in tested solutions.

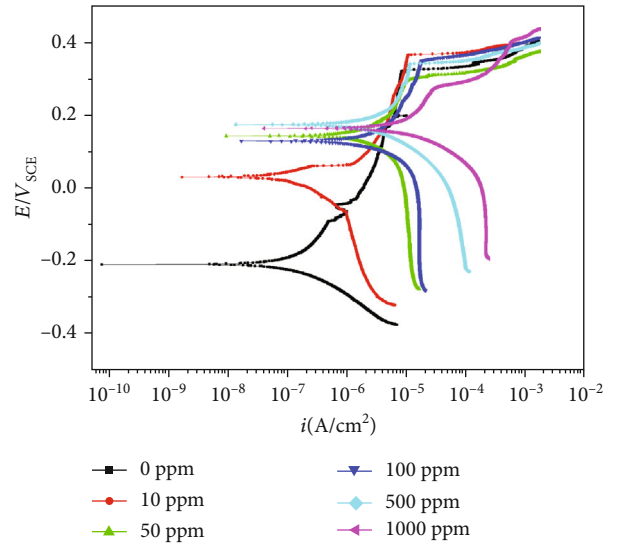

Figure 10: Potentiodynamic polarization curves of 304L SS in tested solutions.

the increase of the concentration of Cu^{2+}, the potentiodynamic polarization curves moved up to the right; the corrosion potential and corrosion current density increased. Due to the existence of the pass passivation film, the anodic dissolution rate was quite low and the anode reaction equilibrium potential had no significant change; with the increase of the concentration of Cu^{2+}, the cathode reaction rate was accelerated and the cathode reaction equilibrium potential increased, and an anode reaction and two cathodic reactions coupled and polarized each other, finally leading to the increase of the corrosion potential and corrosion current density. Meanwhile, a small amount of Cu was precipitated on the surface of the sample, which also formed the Fe-Cu galvanic cells, making the stability of the passivation film decreased; the more the number of Fe-Cu galvanic cells increased, the more obvious the stability of the passivation film decreased; thus, the passivation zone significantly narrowed, and the pitting corrosion sensitivity e significantly increased; once the passivation film was broken locally, the fresh metal substrate was exposed; the corrosion pits formed and developed under the combined action of Cl^- and Cu^{2+}.

4. Conclusion

(1) The results of the immersion test showed that A106B presented uniform corrosion in seawater of different concentrations of Cu^{2+}; with the increase of the concentration of Cu^{2+} to 10 ppm, 50 ppm, 10 0 ppm, 500 ppm, and 1000 ppm, the corrosion weight loss rate increased by 0.23, 0.97, 2.14, 4.12, and 8.47 times, respectively

(2) 304L SS presented pitting corrosion in seawater of different concentrations of Cu^{2+}; with the increase of the concentration of Cu^{2+} to 10 ppm, 50 ppm, 100 ppm, 500 ppm, and 1000 ppm, the corrosion weight loss rate increased by 6, 67, 139, 404, and 591 times, respectively; the amount and size of the corrosion pits both increased. Compared with the behaviors of A106B in the immersion test, the mass lot rates of 304L SS were all lower

(3) The results of potentiodynamic polarization curves of A106B showed that with the increase of the concentration of Cu^{2+}, the corrosion potential decreased firstly; when increased to more than 100 ppm, both the corrosion potential and the corrosion current density largely increased. Meanwhile, the cathode reaction was altered from mainly the reduction of O_2 to mainly the reduction of Cu^{2+}

(4) The results of potentiodynamic polarization curves of 304L showed that with the increase of the concentration of Cu^{2+}, the corrosion potential and corrosion current density increased, the passivation zone significantly narrowed, and the pitting corrosion sensitivity significantly increased

Data Availability

The data used to support the findings of this study are available from the corresponding authors upon request.

Conflicts of Interest

The authors declare that they have no conflict of interest.

Acknowledgments

The authors acknowledge the financial support of the National key research and development program (No. 2016YFB0700404).

References

[1] L. L. Li, Z. B. Wang, S. Y. He, and Y. G. Zheng, "Correlation between depassivation and repassivation processes determined by single particle impingement: its crucial role in the phenomenon of critical flow velocity for erosion-corrosion," *Journal of Materials Science & Technology*, vol. 89, pp. 158–166, 2021.

[2] L. M. Zhang, Z. X. Li, J. X. Hu et al., "Understanding the roles of deformation-induced martensite of 304 stainless steel in different stages of cavitation erosion," *Tribology International*, vol. 155, 2021.

[3] H. Ju, W. H. Xu, J. J. Chen, D. L. Zhang, G. M. Liu, and J. Z. Duan, "Electrochemical investigation of under-deposit corrosion behavior for aluminum brass in artificial seawater," *Corrosion*, vol. 76, no. 11, pp. 1050–1063, 2020.

[4] H. Y. Tian, M. D. Chen, F. Ge, K. Song, X. Wang, and Z. Y. Cui, "Hydrogen permeation and stress corrosion cracking of heat-affected zone of E690 steel under the combined effect of sulfur species and cathodic protection in artificial seawater," *Construction and Building Materials*, vol. 296, p. 123721, 2021.

[5] Y. X. Qiao, S. L. Sheng, L. M. Zhang et al., "Friction and wear behaviors of a high nitrogen austenitic stainless steel Fe-19Cr-15Mn-0.66N," *Journal of Mining and Metallurgy, Section B: Metallurgy*, vol. 57, no. 2, pp. 285–293, 2021.

[6] Y. X. Qiao, Y. P. Chen, L. L. Li et al., "Corrosion behavior of a nickel-free high-nitrogen stainless steel with hydrogen charging," *JOM*, vol. 73, no. 4, pp. 1165–1172, 2021.

[7] Y. Y. Shen, Y. H. Dong, L. H. Dong, and Y. S. Yin, "Corrosion inhibition effect of microorganism on 5754 Al alloy in seawater," *Aata Metallurgica Sinica*, vol. 56, no. 12, pp. 1681–1689, 2020.

[8] P. F. Xu, X. G. Feng, X. Y. Lu, and C. Chen, "Effect of calcium phytate on the corrosion behavior of 304 stainless steel as coral concrete reinforcement in a 3.5% sodium chloride solution," *International Journal of Electrochemical Science*, vol. 15, no. 12, pp. 12244–12251, 2020.

[9] Z. W. Chen, W. T. Xia, C. Q. Yao, Z. F. Lin, W. Zhang, and W. H. Li, "Research on the metal corrosion process in the sea mud/seawater/atmosphere interface zone," *Coatings*, vol. 10, no. 12, p. 1219, 2020.

[10] Y. Ogawa, S. Suzuki, N. Taniguchi, M. Kawasaki, H. Suzuki, and R. Takahashi, "Corrosion resistance of a cast steel overpack for high-level radioactive waste disposal in Japan," *Materials and Corrosion*, vol. 72, no. 1–2, pp. 52–66, 2021.

[11] A. Elshami, S. Bonnet, A. Khelidj, and L. Sail, "Effectiveness of corrosion inhibitors in simulated concrete pore solution," *European Journal of Environmental and Civil Engineering*, vol. 24, no. 13, pp. 2130–2150, 2020.

[12] Z. X. Chen, H. X. Hu, Y. G. Zheng, and X. M. Guo, "Effect of groove microstructure on slurry erosion in the liquid-solid two- phase flow," *Wear*, vol. 466-467, p. 203561, 2021.

[13] L. Benea, N. Simionescu, and L. Mardare, "The effect of polymeric protective layers and the immersion time on the corrosion behavior of naval steel in natural seawater," *Journal of Materials Research and Technology*, vol. 9, no. 6, pp. 13174–13184, 2020.

[14] D. P. Wang, H. T. Zhang, P. Y. Guo, B. A. Sun, and Y. X. Wang, "Nanoscale periodic distribution of energy dissipation at the shear band plane in a Zr-based metallic glass," *Scripta Materialia*, vol. 197, p. 113784, 2021.

[15] Y. B. Kim and S. J. Kim, "Erosion corrosion characteristics of Al5052-O and Al6061-T6 aluminum alloys with flow rate of seawater," *Corrosion Science and Technology*, vol. 18, 2019.

[16] L. F. Gao and M. Du, "Pitting corrosion behavior of 304 stainless steel in desalination seawater," *Corrosion Science and Protection Technology*, vol. 29, no. 1, pp. 8–14, 2017.

[17] B. B. Chernov, I. A. Chaves, A. M. Nugmanov, and R. E. Melchers, "Corrosion performance of low alloy steels in sub-arctic natural seawater," *Corrosion*, vol. 74, no. 12, pp. 1466–1475, 2018.

[18] Y. Z. Mao, Y. H. Wei, H. T. Zhao, C. X. Lv, H. J. Cao, and J. Li, "Corrosion behavior of epoxy-coated rebar with pinhole defect in seawater concrete," *Acta Metallurgica Sinica-Einglish Letters*, vol. 31, no. 11, pp. 1171–1182, 2018.

[19] B. S. Zhang, Q. Dong, Z. Ba, S. Zhu, Y. Han, and Z. Wang, "Electrochemical corrosion behavior of plasma-sprayed FeCrNiMoCBSi amorphous/nanocrystalline coatings in simulated seawater medium," *Journal of Materials Engineering and Performance*, vol. 27, no. 11, pp. 6227–6236, 2018.

[20] F. L. Ma, J. Li, Z. Zeng, and Y. Gao, "Tribocorrosion behaviour of F690 and 316L steel in artificial seawater," *Lubrication Science*, vol. 30, no. 7, pp. 365–375, 2018.

[21] J. Aguirre and M. Walczak, "Effect of dissolved copper ions on erosion-corrosion synergy of X65 steel in simulated copper tailing slurry," *Tribology International*, vol. 114, pp. 329–336, 2017.

[22] Q. Qu, G. Gao, H. Guo, L. Li, and Z. Ding, "Co-effect of bis (cyclo-hexanone) oxalyldihydrazone and copper (II) ion on the corrosion of cold rolled steel in 0.5 M hydrochloric acid solution," *Materials and Corrosion*, vol. 62, no. 8, pp. 778–785, 2011.

[23] M. A. Migahed, M. A. Hegazy, and A. M. al-Sabagh, "Synergistic inhibition effect between Cu^{2+} and cationic gemini surfactant on the corrosion of downhole tubing steel during secondary oil recovery of old wells," *Corrosion Science*, vol. 61, no. 8, pp. 10–18, 2012.

[24] H. Tanaka, A. Miyafuji, T. Ishikawa, and T. Nakayama, "Influence of Ni(II), Cu(II) and Cr(III) on the formation, morphology and molecular adsorption properties of α-FeOOH rust particles prepared by aerial oxidation of neutral Fe(II) solutions," *Advanced Powder Technology*, vol. 29, no. 1, pp. 9–17, 2018.

[25] P. P. Li, H. L. Zhang, M. Z. Xia, F. Y. Wang, S. D. Zhu, and W. Lei, "The synergistic effect and microscopic mechanism of co-adsorption of three emerging contaminants and copper ion on gemini surfactant modified montmorillonite," *Ecotoxicology and Environmental Safety*, vol. 184, 2019.

[26] Q. Li, D. P. Zhang, S. Hu, Z. Y. Chen, and X. P. Guo, "Effect of the ion selectivity of a precipitate membrane on the corrosion of carbon steel in Cu^{2+}-containing solution," *Materials Chemistry and Physics*, vol. 243, 2020.

[27] G. N. Mu, T. P. Zhao, M. Liu, and T. Gu, "Effect of metallic cations on corrosion inhibition of an anionic surfactant for mild steel," *Corrosion*, vol. 52, no. 11, pp. 853–856, 1996.

[28] J. Liu, A. Alfantazi, and E. Asselin, "Influence of cupric, ferric, and chloride on the corrosion of titanium in sulfuric acid solutions up to 85°C," *Corrosion*, vol. 70, no. 1, pp. 29–37, 2014.

[29] L. Fan, J. T. Zhang, H. Wang et al., "Effects of trace Cl^-, Cu^{2+} and Fe^{3+} ions on the corrosion behaviour of AA6063 in ethylene glycol and water solutions," *Acta Metallurgica Sinica-English Letters*, 2021.

[30] D. Kameli, N. Aliouane, H. Hammache-Makhloufi, and L. Makhloufi, "Anti corrosion activity of ethylene tetra phosphonic acid-Cu^{2+} system on carbon steel in H2SO4SOLUTION," *Surface Review and Letters*, vol. 27, no. 7, p. 1950180, 2020.

[31] A. E. El Meleigy, "Influence of copper ions on the corrosion behaviour of aluminium," *Egyptian Journal of Chemistry*, vol. 49, no. 3, pp. 299–313, 2006.

[32] M. Ahmed, Y. M. Qi, L. L. Zhang et al., "Influence of Cu^{2+} ions on the corrosion resistance of AZ31 magnesium alloy with microarc oxidation," *Materials*, vol. 13, no. 11, p. 2647, 2020.

[33] Z. Lin, S. Qiu, J. Xiao, Z. Fu, and Y. Chen, "Effects of Cl^- and Cu^{2+} on stress corrosion cracking of alloy 690," *Nuclear Power Engineering*, vol. 36, no. 1, pp. 50–54, 2015.

[34] C. M. Giordano, G. S. Duffó, and J. R. Galvele, "The effect of Cu^{2+} concentration on the stress corrosion cracking susceptibility of α-brass in cupric nitrate solutions," *Corrosion Science*, vol. 39, no. 10-11, pp. 1915–1923, 1997.

[35] T. Aoyama, H. Ogawa, C. Kato, and F. Ueno, "Decrease in pitting corrosion resistance of extra-high-purity type 316 stainless-steel by Cu^{2+} in NaCl," *Metals*, vol. 11, no. 3, p. 511, 2021.

Hindawi
Scanning
Volume 2021, Article ID 7019861, 8 pages
https://doi.org/10.1155/2021/7019861

Research Article

Fracture Analysis and Fatigue Strength Calculation of Anchor Bolt Used in Circulating Water Pump in Nuclear Power Plant

Qiang Chen, Shuai Zu, Yinhui Che, Dongxiong Feng, and Yang Li

Suzhou Nuclear Power Research Institute Co., Ltd., Shenzhen 518120, China

Correspondence should be addressed to Qiang Chen; rcachen@163.com

Received 5 August 2021; Accepted 9 September 2021; Published 4 October 2021

Academic Editor: Jian Chen

A circulating water pump is a key equipment of cooling systems in nuclear power plants. Several anchor bolts were broken at the inlet rings of the same type of pumps. The bolts were turned by a special material for seawater corrosion protection. There were obvious turning tool marks at the root of the thread, which was considered as the source of the crack. The fatigue crack extended to the depth of the bolt, causing obvious radiation stripes on the fracture surface, which was a typical fatigue fracture. Obvious overtightening characteristics were found at the head of the broken bolt. Fracture and energy spectrum analysis showed that the bolt was not corroded. The axial vibration of the pump was measured. The static tensile stress along the bolt axis caused by the preload, the axial tensile stress caused by the axial vibration, and the torsional stress were calculated, respectively. According to the fatigue strength theory, the composite safety factor of the bolt fatigue strength was 1.37 when overtightening at 1.2 times the design torque, which was less than the allowable safety factor of 1.5-1.8, so the bolt was not safe, which further verified the conclusion of fracture analysis. The reason for the low safety factor was caused by the overtightening force. The improvement method was to control the bolt preload or increasing the bolt diameter.

1. Introduction

A cooling water pump is a very important equipment in nuclear power plants. During overhaul, it was found that the fixing bolts of the embedded parts of four CR1QS1 pumps were broken. The pump is a single-stage, vertical, bottom-suction concrete volute centrifugal pump. The pumps were fixed on the concrete embedded parts with 8 M12 × 1.75 hexagon socket bolts through the mouth ring, as shown in Figure 1. The purpose of the protective cap is to protect the bolt from erosion. The working medium of the pump is sea water.

The common failure modes of bolt fracture are fatigue fracture, stress corrosion cracking, and overload fracture. Due to the large stress concentration of a bolt thread, it is easy for a fatigue source to form at the root, and the possibility of fatigue fracture is high. The bolt fracture studied by González et al. occurred at the second turn of the screw thread, which was caused by hydrogen embrittlement [1]. The bolt studied by Shafiei and Kazempour-Liaisi had M23C6 carbide, which was the source of the fatigue crack. The crack propagates along the grain boundary, and finally, fatigue fracture occurs [2]. Li et al. found that surface decarburization of the bolts and stress concentration at the bolt thread neck decreased the fatigue strength [3]. Wu et al. studied the corrosion fracture mechanism of cable bolts [4]. The fracture had general fatigue fracture characteristics. There were corrosion fatigue crack sources and radial fatigue crack propagation traces. Hydrogen-assisted stress corrosion cracking was the main fracture mechanism of cable bolts failure. The fatigue crack source of the bolt-sphere joint was pitting caused by corrosion [5]. Wen et al. [6] studied the fracture of a 20MnTiB steel high-strength bolt. Microdefects were found near the bottom of the thread. Considerable stress and corrosion accelerated the crack propagation of the bolt. The working capacity of a rock bolt decreased by 25-50% when it worked under the condition of rock and groundwater corrosion [7].

It is generally believed that the fatigue strength of bolts is only related to the stress amplitude. The fatigue strength only studied the stress amplitude of bolt tensile stress [7–10]. For example, the bolt fatigue strength condition

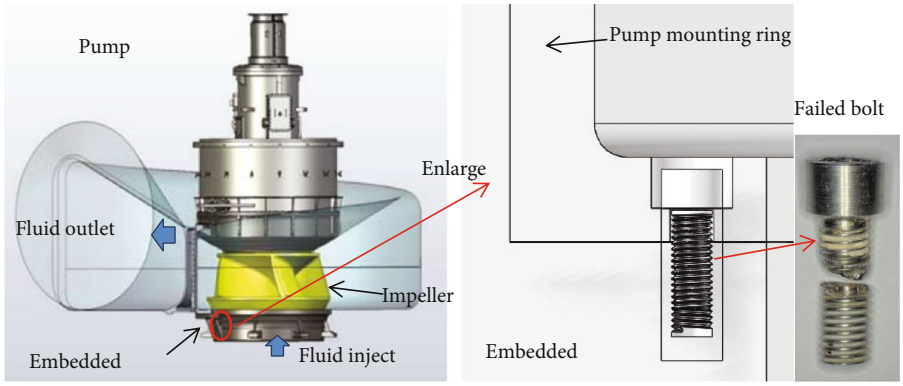

(a) Overall structure diagram of pump (b) Enlarged diagram of failed bolt location

Figure 1: Structure of embedded parts under circulating water pump.

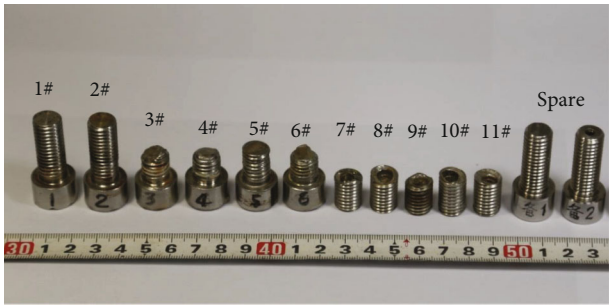

Figure 2: Bolts in service and spare parts.

was that the allowable stress amplitude was equal to 90 MPa [8], and the fatigue curve studied was the $\Delta\sigma - N$ curve [9]. However, in practice, many examples showed that the failure of bolts was related to the average stress (i.e., bolt preload) [11, 12]. The reason for a bolt fracture was that the safety factor is insufficient due to excessive preload [11, 12]. The safety factor of static strength is obtained by preloading, the safety factor of variable stress is obtained by strain, and the safety factor is modified by Goodman's theory [13].

In this paper, the fracture analysis, mechanical property analysis, and energy spectrum analysis of the broken bolt are carried out. At the same time, the fatigue strength of the bolt is calculated, the failure causes are found out, and the improvement suggestions are put forward. Finally, the calculation method of the bolt fatigue strength is proposed.

2. Fracture Analysis of Bolt

2.1. Fracture Analysis. The bolts in service are shown in Figure 2, in which Nos. 1 and 2 were the unbroken bolts, Nos. 3-6 were the head of the broken bolts, and Nos. 7-11 were the rest of the broken parts of the broken bolts. Compared with the spares, their surfaces were the same as the serviced bolts, indicating that there was no corrosion.

The fracture of No. 3 bolt in Figure 2 is representative. Take it as an example to illustrate the fracture form of bolts. Figures 3(a) and 3(b) are the overall morphology and local morphology of the No. 3 bolt, respectively. There are obvious radial lines on the edge of the thread teeth, which is the fracture source as the point indicated by the arrow. The fracture source extends to the core, and then the bolt breaks when the crackle reaches the middle. This is the instantaneous fracture zone region, where the section is rough and uneven. The instantaneous breaking zone occupies a relatively large area, indicating that there is a large residual pretightening force when the bolt is broken.

The macromorphology of No. 3 bolt fracture was observed by stereoscope, as shown in Figure 4(a). The fracture was uneven, with the thread teeth about 28°, which was about the direction of principal stress. Further zooming in and observing what is shown by the arrows in Figure 4(b), the source of the cracks is located at the machining tool mark at the root of thread, and there are a lot of microcracks around.

Figure 5(a) is the morphology of the inner hexagon of the head of No. 3 broken bolt. The top of the bolt head is damaged when the sample was taken on site, as shown by the arrow. But the inner hexagon area is damaged during tightening, as shown in the region. Figure 5(b) shows the morphology of the unbroken bolt head, with the inner hexagon of the screw head intact. The comparison shows that the broken bolts have overtightening behavior when they were installed.

Figure 6(a) is the overall graph taken with a Scanning Electron Microscope (SEM), which shows the fracture source by arrow. Figure 6(b) is a micrograph of the expansion zone, which shows typical fatigue fracture characteristics. This shows that the process of fracture propagation also has the effect of alternating stress.

Figure 7 shows the macroimages of four unbroken screws through dye penetrant inspection, and no cracks are found on the surface. The metallographic structures of the unbroken and broken bolts are, respectively, shown in Figures 8(a) and 8(b), which show an austenite + ferrite structure. This conforms to the characteristics of dual phase steel, without obvious abnormality.

2.2. Research on Bolt Metallurgy. The bolts were made of a special material for seawater corrosion protection. Due to the small quantity, they were manufactured by turning.

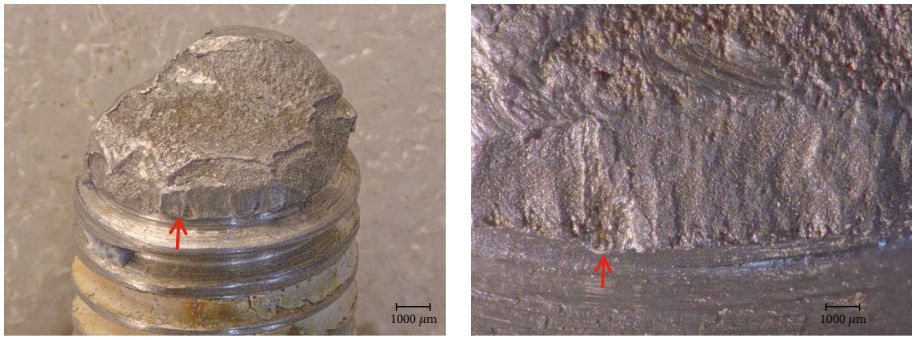

(a) Overall fracture morphology (b) Enlarged morphology of crack source

Figure 3: Fracture of No. 3 bolt in Figure 2.

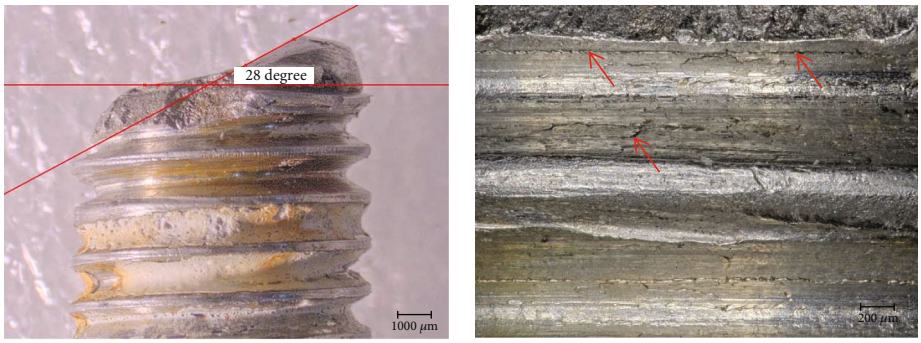

(a) Overall fracture morphology (b) Enlarged morphology of crack source

Figure 4: Macroscopic observation of thread profile of No. 3 bolt.

(a) The broken bolt head of No. 3 (b) The unbroken bolt head onsite

Figure 5: Comparative morphology of hexagon socket head.

The chemical composition meets the ASTM s32760 standard, see Table 1. Using the XHB-3000 Digital Brinell Hardness Tester, the average hardness of bolts is 230-240 HBW, equivalent to grade 8.8 (Chinese national standard GB3098.1), which also meets the requirements of ASTM s32760 of less than 310 HBW.

Using an ONH836 hydrogen, oxygen, and nitrogen analyzer, the contents of gas elements N, H, and O were tested and shown in Table 2. The content of nitrogen meets the requirements of standard value, and the contents of hydrogen and oxygen are also low. In addition, the bolt did not have intergranular stress corrosion cracking, so the bolt fracture had nothing to do with the influence of gas content.

By the AG100KNG universal testing machine, the tensile properties of sample bolts were tested, as shown in Table 3. The results all meet the requirements of standard values, and the mechanical properties are normal. According to the empirical formula recommended in the mechanical design manual, the symmetrical cycle fatigue limit σ_{-1} and torque yield limit τ_s are estimated as follows:

$$\sigma_{-1} \approx 0.28(\sigma_b + \sigma_s) = 0.28 \times (814 + 569) = 387 \text{ MPa}, \quad (1)$$

$$\tau_s \approx 0.58\sigma_s = 0.58 \times 569 = 330 \text{ MPa}.$$

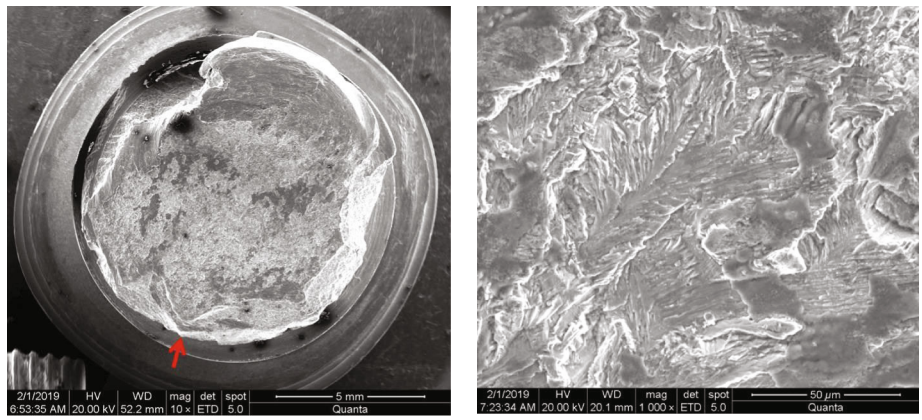

(a) Overall fracture morphology (b) Enlarged morphology of crack source

Figure 6: SEM photos of No. 3 bolt.

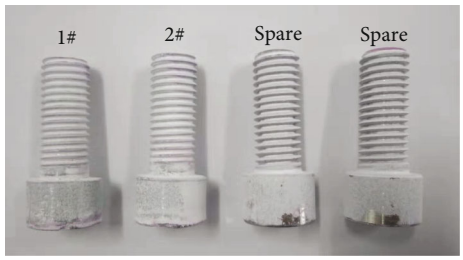

Figure 7: Macroimage of dye penetrant inspection for screws.

2.3. Energy Disperse Spectroscopy Analysis. Table 4 shows the composition of the fracture surface after cleaning by Energy Disperse Spectroscopy (EDS). The result is the same as the previous conclusion in Section 2.1, that is, as can be seen in Figure 2, the broken bolts were as glossy as the spare parts, and there was obviously no corrosion.

3. Calculation of Bolt Fatigue Strength

3.1. Bolt Stress Analysis

3.1.1. Pretightening Stress Calculation. The stress of a bolt includes the preload and the working load. There are two preloads: one is the axial tensile stress and the other is the torsional stress around the axis. The working load acts on the axial direction of the bolt, and the calculation method is shown in Section 3.1.2. This section mainly calculates the tensile stress σ_m and torsional stress τ_m caused by the preload.

The bolts should be tightened when they are installed; that is, they are subject to the preload (tension) and friction torque. When working, it may be subjected to the variable stress of axial tension. In this paper, the finite element method is used to calculate the tensile stress σ_m and torsional stress τ_m by ANSYS Workbench 15.0 software.

The pump and the foundation ring are connected by 8 bolts. The finite element model takes 1 bolt and one eighth of the foundation including the ring and concrete, as shown in Figure 9. According to the equipment maintenance manual, the installation torque of the bolt is 40.5 Nm, the torque coefficient is 0.258, and the calculated preload is 13081 N.

The axial tensile stress and torsional stress of the bolt are shown in Figures 10 and 11, respectively. The axial tensile stress σ_m is 434.05 MPa, and the torsional stress τ_m is 59.29 MPa at design torque. If the overtightening torque reaches 1.2 times the design value, the axial tensile stress σ_m is 520.86 MPa, and the torsional stress τ_m is 71.41 MPa. The inner hexagon of the broken bolt head has been seriously damaged, and the actual torque is far greater than 1.2 times the design value.

3.1.2. Calculation of Bolt Working Stress. When the pump runs, the impeller will have a working load, acting on the bolt axis direction. The stress is a symmetrical cyclic strain produced by the axial vibration when the pump is running. The axial load was obtained by actual measurement. A speed sensor was installed at the bearing, and the excitation spectrum load was the relationship between the speed and the frequency spectrum, as shown in Figure 12.

The workbench random vibration analysis module was used to calculate the stress response of vibration fatigue. The excitation was loaded on the concrete foundation. The finite element equivalent stress diagram is shown in Figure 13, in which the maximum equivalent stress σ_a is 7.3 MPa.

3.2. Bolt Strength Calculation. The axial force of the bolt is similar to that of the shaft, so the formula of the safety factor of fatigue strength is as follows:

$$S_\sigma = \frac{\sigma_{-1}}{(k_\sigma \sigma_a / \varepsilon_\sigma \beta) + \psi_\sigma \sigma_m}, \tag{2}$$

where σ_{-1} is the symmetrical fatigue limit of 387 MPa, as calculated by equation (1). σ_a is the working stress of 7.3 MPa, as calculated in Section 3.1.2. σ_m is the axial stress caused by the pretightening force, as calculated by FEM in Section 3.1.1. k_σ is the stress concentration factor, and take $k_\sigma = 3$ from the mechanical design manual because it was manufactured by turning. ε_σ is the size factor, and take 1 for the M12

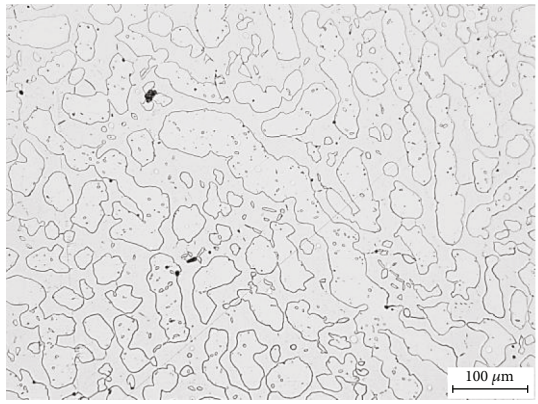

(a) Transverse metallographic structure of No. 2 screw

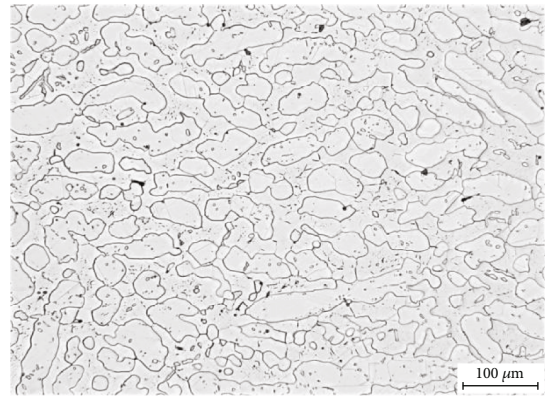

(b) Transverse metallographic structure of No. 11 screw

Figure 8: Microstructure of the sample bolts.

Table 1: Chemical composition of bolts (wt%).

C	Mn	P	S	Si	Cr	Ni	Mo	Cu	W
≤0.030	≤1.00	≤0.030	≤0.010	≤1.00	24.0-26.0	6.0-8.0	3.0-4.0	0.50-1.00	0.50-1.00

Table 2: Gas element test of bolts.

Bolt sample	Gas content (wt%)		
	N	H	O
No. 2	0.28	<0.00006	0.022
No. 10	0.28	0.0001	0.022
Standard value	0.20-0.30	—	—

bolt. β is the enhancement coefficient, and take 1 because of no enhancement. ψ_σ is the stress conversion factor, calculated as follows:

$$\psi_\sigma = \frac{\sigma_{-1}}{\sigma_b} = \frac{387}{814} = 0.475. \tag{3}$$

So, the safety factor of normal stress at design torque is as follows:

$$S_\sigma = \frac{\sigma_{-1}}{(k_\sigma \sigma_a/\varepsilon_\sigma\beta) + \psi_\sigma\sigma_m} = \frac{387}{((3\times 7.3)/(1\times 1)) + 0.475\times 434.05} = 1.7. \tag{4}$$

The safety factor of normal stress at 1.2 times the design torque is as follows:

$$S_\sigma = \frac{\sigma_{-1}}{(k_\sigma \sigma_a/\varepsilon_\sigma\beta) + \psi_\sigma\sigma_m} = \frac{387}{((3\times 7.3)/(1\times 1)) + 0.475\times 520.86} = 1.44. \tag{5}$$

The torsional stress produced by friction during preloading is static stress.

So, the safety factor at design torque is as follows:

$$S_\tau = \frac{\tau_s}{\tau_0} = \frac{330}{59.29} = 5.57. \tag{6}$$

The safety factor of normal stress at 1.2 times the design torque is as follows:

$$S_\tau = \frac{\tau_s}{\tau_0} = \frac{330}{71.41} = 4.62. \tag{7}$$

The composite safety factor at design torque is as follows:

$$S = \frac{S_\sigma S_\tau}{\sqrt{S_\sigma^2 + S_\tau^2}} = \frac{1.7\times 5.57}{\sqrt{1.7^2 + 5.57^2}} = 1.63 \geq [S] = 1.5 \sim 1.8. \tag{8}$$

The safety factor of normal stress at 1.2 times the design torque is as follows:

$$S = \frac{S_\sigma S_\tau}{\sqrt{S_\sigma^2 + S_\tau^2}} = \frac{1.44\times 4.62}{\sqrt{1.44^2 + 4.62^2}} = 1.37 \leq [S] = 1.5 \sim 1.8. \tag{9}$$

According to the mechanical design manual, the allowable safety factor is 1.5~1.8. The composite safety factor at design torque is greater than the lower allowable safety factor. However, when the overtightening torque reaches 1.2 times the design torque, the safety factor has been less than the limit, so the bolt is not safe. The reason for the low composite safety factor is that the safety factor of axial tension is too low, which is 1.44 only. There are two factors affecting the safety factor of axial tension. The first part is the working

Table 3: Test results of tensile properties of sample bolts at room temperature.

	Tensile strength σ_b (MPa)	Yield strength σ_s (MPa)	Elongation (%)	Reduction of area (%)
Mechanical property	814	569	38.5	70
ASTM S32760	≥750	≥550	≥25	—

Table 4: Composition of washed fracture surface.

Element	Weight (%)	Atomic (%)	Test position
C K	6.20	20.20	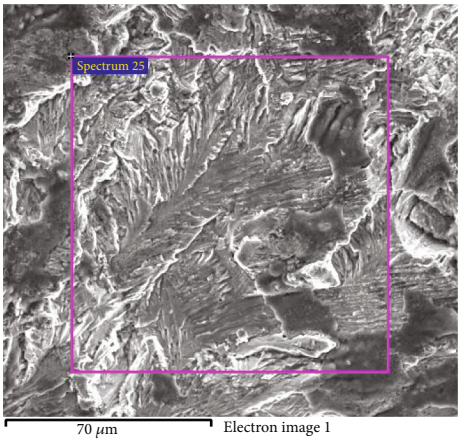
O K	7.39	18.09	
Al K	0.36	0.52	
Si K	0.85	1.18	
Cr K	22.41	16.88	
Mn K	1.18	0.84	
Fe K	54.28	38.06	
Ni K	4.80	3.20	
Mo L	2.53	1.03	
Totals	100.00	100.00	

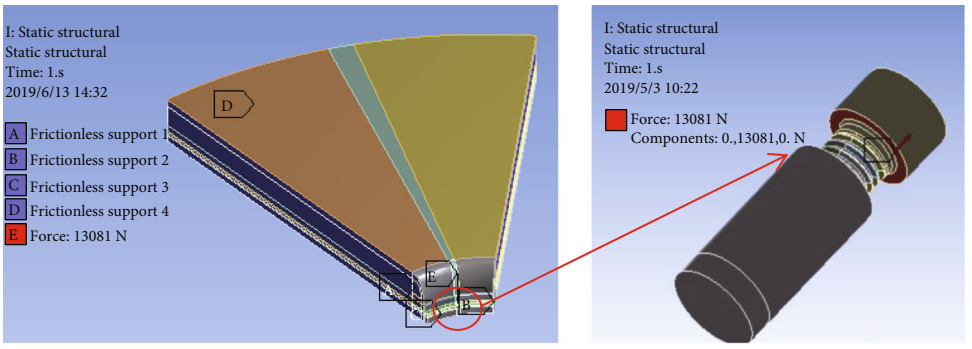

Figure 9: Finite element model.

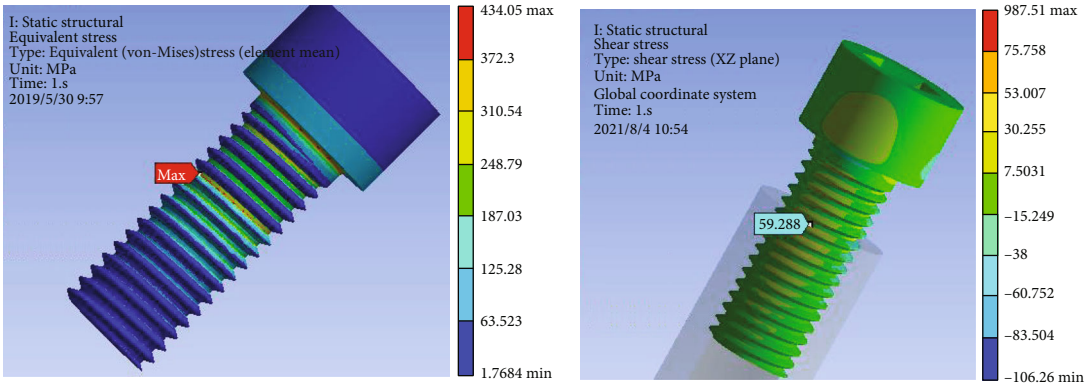

(a) Axial tensile stress of bolt

(b) Bolt torsion stress

Figure 10: Stress value at design torque.

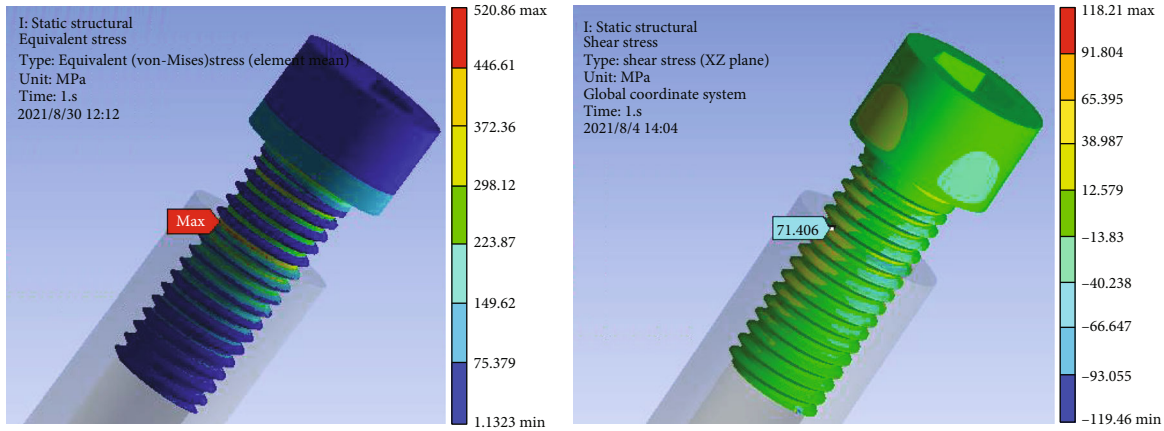

(a) Axial tensile stress of bolt

(b) Bolt torsion stress

Figure 11: Stress value at 1.2 times design torque.

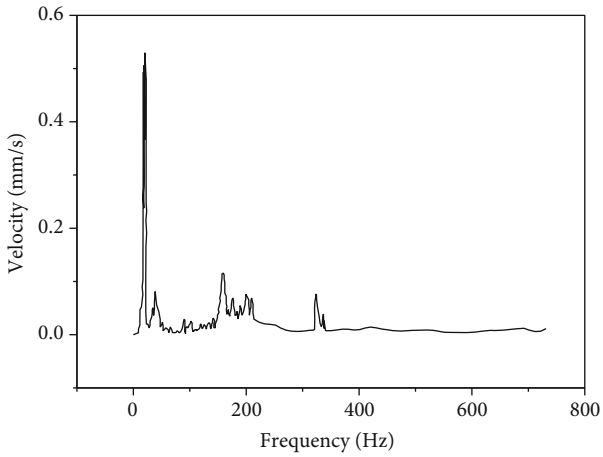

Figure 12: Vibration excitation load spectrum.

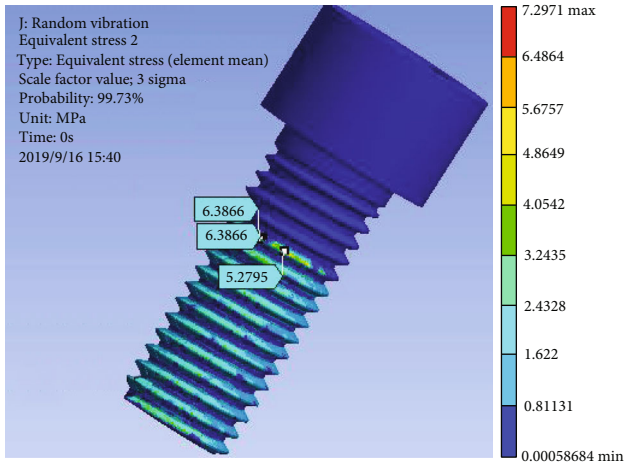

Figure 13: Equivalent stress of bolt.

load, and the other is the preload. The stress caused by the working load is 7.3 MPa only, which is very small. Even if multiplied by the stress concentration factor of 3, 21.9 MPa, it is still very small and not enough to cause failure. However, the stress of 520.86 MPa caused by the preload is relatively large. Therefore, the measure to improve the safety factor is to control the bolt preload or increase the bolt diameter.

4. Conclusion

Through the above analysis of bolt fracture, metallurgy, and strength, the following conclusions can be drawn:

(1) There are obvious crack sources at the root of the thread, and there is an obvious fatigue fracture zone and an instantaneous fracture zone at the cross section. The fatigue fracture zone is typically radial and has typical fatigue fracture characteristics

(2) The bolt safety factor at 1.2 times the design torque is 1.37, which has been less than the allowable safety factor of 1.5-1.8. Therefore, the fatigue strength of bolts is insufficient, and a bolt fracture is due to fatigue failure when the bolt is overtightened

(3) The failure of bolts is not caused by seawater corrosion. The surface of the broken bolt is bright, and there is no trace of corrosion

(4) The key cause of a bolt fracture is too much preload. The measure to improve the safety factor is to control the bolt preload or increase the diameter of the bolt

Data Availability

All data generated or analyzed during this study are included in this article.

Conflicts of Interest

The authors declare that they have no conflicts of interest.

References

[1] P. Valles González, A. P. Muro, and M. García-Martínez, "Failure analysis study on a fractured bolt," *Engineering Failure Analysis*, vol. 109, p. 104355, 2020.

[2] A. Shafiei and H. Kazempour-Liasi, "Failure analysis of gas turbine torque tube bolts," *Engineering Failure Analysis*, vol. 124, p. 105369, 2021.

[3] L. Li and R. Wang, "Failure analysis on fracture of worm gear connecting bolts," *Engineering Failure Analysis*, vol. 36, pp. 439–446, 2014.

[4] S. Wu, J. Li, J. Guo, G. Shi, Q. Gu, and C. Lu, "Stress corrosion cracking fracture mechanism of cold-drawn high-carbon cable bolts," *Materials Science & Engineering A*, vol. 769, p. 138479, 2020.

[5] H. Yuan, H. Liu, X. Ren, X. Zhang, D. Ai, and Y. Luo, "The bearing performance of the bolt-sphere joints with stochastic pitting corrosion damage," *Journal of Constructional Steel Research*, vol. 160, pp. 359–373, 2019.

[6] J. Wen, L. Liua, Q. Jiao, J. Yang, Q. Liu, and C. Lin, "Failure analysis on 20MnTiB steel high-strength bolts in steel structure," *Engineering Failure Analysis*, vol. 118, p. 104820, 2020.

[7] B. Wang, X. Guo, H. Jin, F. Li, and S. Yang, "Experimental study on degradation behaviors of rock bolt under the coupled effect of stress and corrosion," *Construction and Building Materials*, vol. 214, pp. 37–48, 2019.

[8] F. Pan and J. Shouliang, "Research on prevention of bolt fatigue failure based on construction machinery," *Modern manufacturing technology and equipment*, vol. 2, pp. 120-121, 2021, 156.

[9] J. Maljaars and M. Euler, "Fatigue S-N curves of bolts and bolted connections for application in civil engineering structures," *International Journal of Fatigue*, vol. 151, p. 106355, 2021.

[10] J. Jinfeng, H. Haishu, L. Yong, X. Ying, and L. Honggang, "Research progress on fatigue of high strength bolts for flat frame structure," *Building science*, vol. 3, pp. 85–92, 2021.

[11] W. Hui, Z. Chunyu, L. Youliang, H. Wenjie, and L. Shengju, "Strength analysis of blade root bolts in hoisting process of single blade of wind turbine," *Solar energy*, vol. 326, pp. 1–7, 2021.

[12] D. M. Bastidas, A. Gil, U. Martin, J. Ress, J. Bosch, and S. F. Medina, "Failure analysis of boron steel 27MnCrB5-2 structural bolts during tightening of railcar wheel-axle," *Engineering Failure Analysis*, vol. 124, p. 105333, 2021.

[13] Z. Fa, G. Xinfeng, and W. Ningning, "Fatigue analysis of top cover bolts pumped storage power station based on fatigue cumulative damage theory," *Hydropower and pumped storage*, vol. 7, no. 3, pp. 1–6, 2021.

Hindawi
Scanning
Volume 2021, Article ID 6337768, 9 pages
https://doi.org/10.1155/2021/6337768

Research Article

Effect of the Concentration of $SrAl_2O_4$: $Eu^{2+}$and Dy^{3+} (SAO) on Characteristics and Properties of Environment-Friendly Long-Persistent Luminescence Composites from Polylactic Acid and SAO

Zhongjin Ni,[1] Tianyu Fan,[1] Shuyang Bai,[1] Shiyu Zhou,[1] Yan Lv,[1] Yihua Ni,[1] and Bin Xu[2]

[1]*College of Engineering, Zhejiang A&F University, Linan 311300, China*
[2]*College of Materials Science and Engineering, Zhejiang University of Technology, Hangzhou 310014, China*

Correspondence should be addressed to Yihua Ni; zafu_nyh@163.com and Bin Xu; xb13758240912@163.com

Received 23 June 2021; Accepted 1 September 2021; Published 27 September 2021

Academic Editor: Qiao Yanxin

We report luminous polylactic acid (PLA) composite prepared via a solvent casting method using different amounts of phosphor strontium aluminate ($SrAl_2O_4$: Eu^{2+} and Dy^{3+}) (SAO). The reason for doing this is that the changes of fluorescence and mechanical properties in the composites with different SAO contents can be directly evaluated. The SAO particles should have a variety of excellent characteristics in the PLA matrix, among which dispersibility and compatibility are particularly important; so, they can be modified by 3-aminopropyltriethoxysilane (APS) to achieve the target characteristics. The results showed that the fluorescence and mechanical properties were affected by SAO addition. The mechanical properties significantly improved with 5 wt% SAO; further, addition had no impact. And the emission band of fluorescence and phosphorescence is just at the peak of 524 nm. The composites with 15 wt% SAO have the best fluorescence properties. The fluorescence decreased with further doping. Fluorescence decay curves with various amounts of SAO particles show a similar tendency as pure SAO particles; the speed of decrease in afterglow intensity was higher for the first 30 min. In addition, the detailed morphological scanning and study by scanning electron microscope (SEM) showed that the particles had good adhesion to the matrix. In conclusion, the concentration of SAO into the PLA matrix impacts the fluorescence and mechanical properties of a SAO/PLA composite material.

1. Introduction

Long persisting luminescent (LPL) materials have an important feature, and they can continue to emit light for a long time (even hours) after excitation; so, they are often used as inorganic photoluminescent materials, and they are also widely used in energy storage materials and because of the specificity of this characteristic, LPL materials—especially aluminates like $SrAl_2O_4$: Eu^{2+} and Dy^{3+} (SAO) widely used in luminescent ceramics and coatings, as well as in emergency escape clothing and signs [1]. Because of their high luminous efficiency, long persistence time, stable chemical properties, and lack of radiation pollution, SAO phosphors are widely developed [2]. Biodegradable polymers like polylactic acid (PLA) are frequently used with SAO [3, 4]. This sustainable and environment-friendly material has a good prospect in medical materials, home decoration materials, packaging materials, and other fields [5]. Although PLA has excellent processability in many equipment and offers good attachment and strength, however, it is frangible and brittle, which limits its use. Thus, PLA should be modified for most practical applications [4, 6].

Luminous PLA composites can be prepared with SAO to improve their mechanical properties. These composites have excellent phosphorescence, fluorescence, plasticity, elasticity, and self-degradation [7]. Over the last few years, this

material has gained a lot of interest in areas such as radiation detection [8], industrial applications [9, 10], and in vivo imaging [11]. This preserves the properties of the aluminates and improves PLA's mechanical properties.

Here, SAO particles were added to a PLA composite. Samples were processed via solvent casting using different amounts of SAO particles. The effects of SAO content on the microstructure, thermal, tensile, and afterglow properties of SAO/PLA composite were investigated in detail. To enhance the behavior of these composites, SAO particles were treated with a 3-aminopropyltriethoxysilane (APS) coupling agent [12]. The treated SAO particles were then doped at 5, 10, 15, and 20 wt% in a copolymer solution (polyethylene glycol was added to increase the compatibilization of SAO in the PLA matrix). The final product was prepared via solvent casting with characterization of optical properties, mechanical properties, and morphological characteristics.

2. Materials and Methods

2.1. Materials. PLA 4032D was purchased from Nature Works Company. Long-persistent luminescent materials doped with strontium aluminate ($SrAl_2O_4$:Eu^{2+} and Dy^{3+}; SAO) were provided by Zhejiang Minghui Luminescence Technology Company. Polyethylene glycol 2000/PEG2000 was provided by Shanghai Yuanye Biotechnology Company. Dichloromethane solution was provided by Shanghai Aladdin Biotechnology Company. Anhydrous ethylene alcohol was supplied by China Pharmaceutical Group Chemical Reagent Company. Silane coupling agent APS (KH550) was purchased from Linan Karl Biotechnology Company.

2.2. SAO/PLA Composite Material Preparation and Methods

2.2.1. Modification of SAO Particles. The deionized water (20 ml), absolute ethanol (180 ml), and KH550 (2 wt% of the total weight) were added to a 400 ml beaker and mixed by a magnetic stirrer at a speed of 500-700 r/min for 60 min. The sample was magnetic stirred for 1 hour at a speed of 500-700 r/min. The above solution added with SAO was stirred under 60°C at 500-700 r/min. Ethoxy is a special group that can be hydrolyzed in water or solvent to form silanol, and it is also a group contained in KH550. The -OH group of PLA can react with silanol, which in turn makes a stable covalent bond formed on the surface of the PLA polymer [13, 14] (Schemes 1 and 2). The treated SAO was vacuum filtered in a drying box at 80°C for 6 hours.

2.2.2. Preparation of SAO/PLA Composite Materials. The PLA powder was dried for 24 hours at a temperature of about 70 degrees Celsius, and then the solution was stirred adding 0.1 g/mol PLA powder into dichloromethane for 1 hour at 1000-2000 r/min followed by 0.5 g polyethylene glycol and pretreated SAO powder into the solution. Polyethylene glycol disperses the SAO particles to facilitate attachment to the PLA surface [15]. Next, copolymer solutions containing 5, 10, 15, and 20 wt% SAO particles were melt spun. These solutions were stirred by ultrasonic stirring for 30 min, and then each group of solution samples was kept for 12 hours and dried at 60°C for 24 hours.

2.3. Testing and Characterization

2.3.1. XRD Analysis. The XRD patterns of the polymers were collected on a SHIMADZU XRD-6000 diffractometer with a scanning speed of 2°/min (2θ from 5° to 60°) using a nickel-filtered Cu-$K\alpha$ radiation ($\lambda = 1.54056$ Å) as the radiation source (40 kV, 40 mA).

2.3.2. FT-IR Analysis. At room temperature, the infrared spectrum of each powder sample sandwiched between two KBr particles was recorded through a Perkin-Elmer 1100 Model with a wavelength range of 4000 cm^{-1} to 500 cm^{-1} (the spectrum was measured using 32 scans at 4 cm^{-1} resolution).

2.3.3. DSC Analysis. The Netzsch STA 409PC Maia instrument was used for DSC analysis in a nitrogen atmosphere (purge flow rate of 50 mL/min). In order to obtain the curing heat flow curves of the powder samples, different heating rates (such as 5, 10, 15 and 20 K/min) were used in the measurement, while dynamic DSC measurements were made in the thermal sweep range from 40°C to 250°C. Each new sample is about 5-8 mg in an aluminum tray protected by N_2 gas.

2.3.4. TGA Analysis. A thermogravimetric analysis was performed on each sample with an initial weight of approximately 10 mg using the STA 409PC by storing the samples in an open Pt pan with high purity nitrogen as purge gas and raising the temperature from room temperature to 800°C at a heating rate of about 20°C/min.

2.3.5. Tensile Property Test. An electronic universal testing machine (with a 2 KN load cell) manufactured by Meister Industrial Systems Company was used to test the tensile properties of the sample at a crosshead speed of 2 mm/min. Each sample measured 75 mm × 4 mm × 1 mm. A total of 10 samples were used in the experiment and tested repeatedly.

2.3.6. SEM Analysis. Under the acceleration voltage of 15000 V, through Hitachi SU8010 (S-4800-1) field emission scanning electron microscope and then scanning SEM micrographs imaging of the fracture morphology of the impact specimens, the gold thickness was 10 nm. The fracture surfaces were coated with a thin evaporated layer of gold.

2.3.7. Fluorescence Spectrum Analysis. The sample was irradiated for 12 hours under ultraviolet light (wavelength range 320-400 nm, central wavelength 360 nm, power 60 $\mu W/cm^2$). A fluorescence spectrophotometer F97PRO (Shanghai Prism Light Technology Company) was used to measure the fluorescence spectra. The peak value is 524 nm ($\lambda = 524$ nm). The decay curves were obtained by measuring continuously for 1 hour. The fluorescence emission spectra at room temperature and phosphorescence spectra at 1 min were obtained by excitation of the sample with a wavelength of 360 nm.

3. Results and Discussion

3.1. Crystallization Behavior. Figure 1 shows XRD patterns of neat PLA, 5 wt% SAO/PLA, 10 wt% SAO/PLA, 15 wt% SAO/PLA, and 20 wt% SAO/PLA composites. The peaks at $2\theta = 21.8°$, 28.8°, 29.6°, 30.1°, and 34.6° are present in XRD

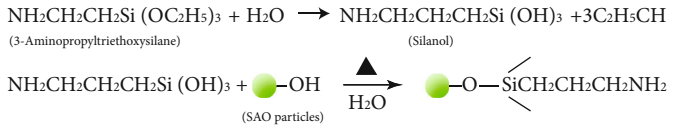

Scheme 1: Hypothetical reaction of KH550 and SAO particles.

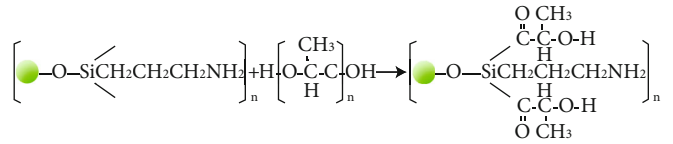

Scheme 2: Crosslinking reaction of silylated SAO with PLA.

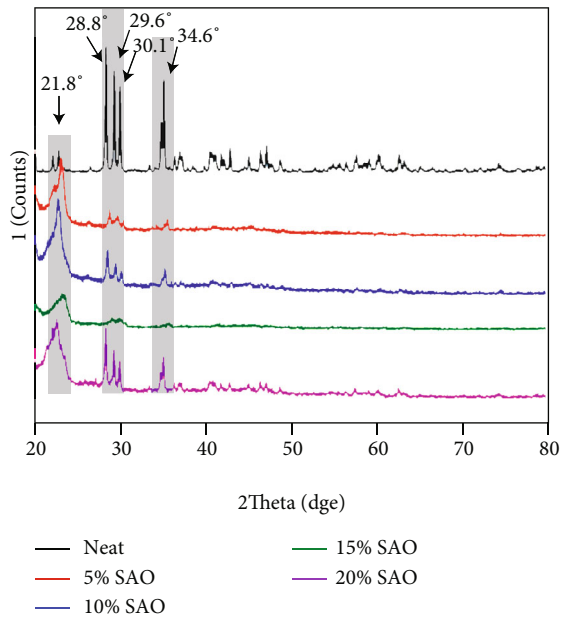

Figure 1: XRD patterns of pure PLA, 5 wt% SAO/PLA, 10 wt% SAO/PLA, 15 wt% SAO/PLA, and 20 wt% SAO/PLA.

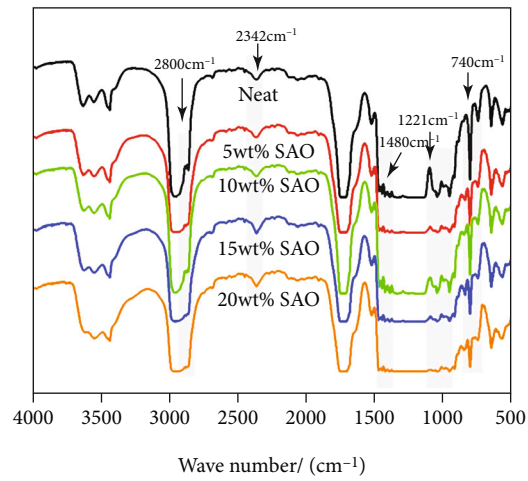

Figure 2: FT-IR spectra of pure PLA, 5 wt% SAO/PLA, 10 wt% SAO/PLA, 15 wt% SAO/PLA, and 20 wt% SAO/PLA.

patterns of SAO particles indicating that the crystal types of the SAO/PLA composite changed upon addition of SAO particles, and its characteristic peak obviously decreased. Moreover, the characteristic peak of PLA/SAO composite containing 15 wt% SAO almost disappeared, which was related to the strontium aluminate phosphor particles [16]. This means that the addition of SAO particles enhances the elongation at break and decreases the melting point, barrier property, and heat resistance.

3.2. FT-IR Spectra. The FT-IR spectra of pure PLA, 5 wt% SAO/PLA, 10 wt% SAO/PLA, 15 wt% SAO/PLA, and 20 wt% SAO/PLA composites are shown in Figure 2. Two distinct peaks at 2800 cm^{-1} and 1221 cm^{-1} demonstrating the presence of -OH groups indicating that the addition of SAO particles enhances crosslinking between SAO and PLA. The specific FT-IR spectrum diagram is shown in Figure 2. Peaks at 2342 cm^{-2} proved that the SAO is properly copolymerized on PLA. The 1450-1480 cm^{-1} band is weakening vibration of the -CH_3 group, which shows SAO particles transforming into the luminous SAO/PLA particles. At 1109 cm^{-1} in the figure, a new peak can be seen, and the asymmetric stretching vibration of Si-O-Si just corresponds to this peak. This is obvious versus pure PLA and other SAO/PLA composites. All these indicate that the SAO particles have successfully combined with the PLA surface.

3.3. Thermal Properties. Nonisothermal curing behaviors of SAO/PLA composites with different amounts of SAO particles were investigated by DSC. DSC traces of SAO/PLA composites containing different amounts of SAO particles are shown in Figure 3. A glass transition occurs near 63°C, and there is a cold crystallization peak near 75°C. The melting peak occurs near 90°C in all samples [17]. The addition of SAO content leads to a melting peak that shifts to the right as a whole, and the melting temperature increased. The glass transition temperature of those samples shows that the blends of SAO and PLA are compatible, and the compatibility of 5 wt% and 15 wt% is better than all other samples.

To investigate the effect of SAO content, we measured the thermal stability of *as*-prepared SAO/PLA composites (Figure 4). T_g first decreases with increasing SAO loadings. The initial weight loss of neat PLA occurred at around

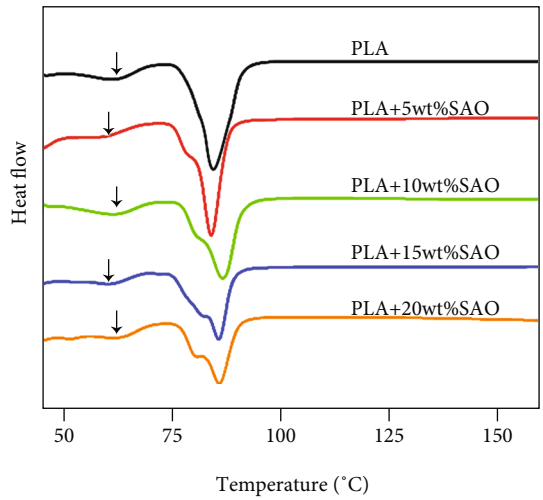

Figure 3: DSC curves of pure PLA, 5 wt% SAO/PLA, 10 wt% SAO/PLA, 15 wt% SAO/PLA, and 20 wt% SAO/PLA.

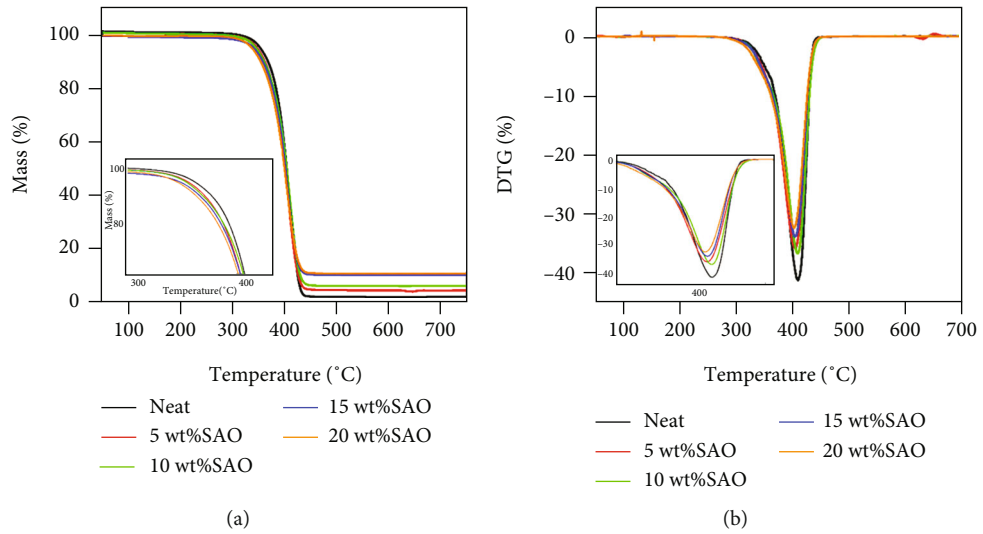

Figure 4: TG (a) and DTG (b) curves of pure PLA, 5 wt% SAO/PLA, 10 wt% SAO/PLA, 15 wt% SAO/PLA, and 20 wt% SAO/PLA.

350°C; the lowest temperature is about 320°C. The addition of SAO decreases the thermal stability of PLA, but the rate of decline is slow. This is because hydrogen bonding between SAO and PLA promotes thermal movement of PLA macromolecules by PLA itself. This reduces the energy required to break the chain among the macromolecules [18]. DTG data are plotted in Figure 5(b). The temperature corresponding to the peak temperature of DTG is the maximum weightlessness rate T_{max}. The T_{max} of neat PLA is 423.36°C . The temperature T_{max} of the maximum weight loss rate of SAO/PLA composite decreases with addition of SAO because SAO inhibits the crystallization of PLA and decreases the thermal stability. There is a hydroxyl effect from the SAO after treatment with the silane coupling agent.

3.4. Mechanical Properties. To investigate the mechanical properties of the *as*-prepared SAO/PLA composites, we measured the tensile strength, fracture elongation, and modulus of elasticity (Table 1, Figure 6). The tensile strength of SAO/PLA composites increases with 5 wt% SAO particles and then decreases at higher contents. This suggests that the tensile strength of the composites is impacted when the crystallinity of the system decreases [19–21]. The fracture elongation decreased when more SAO is added to the composite while the elastic modulus decreases. The toughness and fracture elongation decrease with increasing SAO content. The best overall performance occurs in the SAO/PLA composites containing 5 wt% SAO: 2.7% increase in tensile strength, 29.8% increase in fracture elongation, and 6.3% decrease in fracture elongation. These results indicate that the final mechanical properties of luminescent composite are highly influenced by the addition of SAO [22, 23].

3.5. Micromorphology. Tensile fracture SEM images with different amounts of SAO particles are shown in Figure 5. The fracture surface of pure PLA is shown in Figure 5(a),

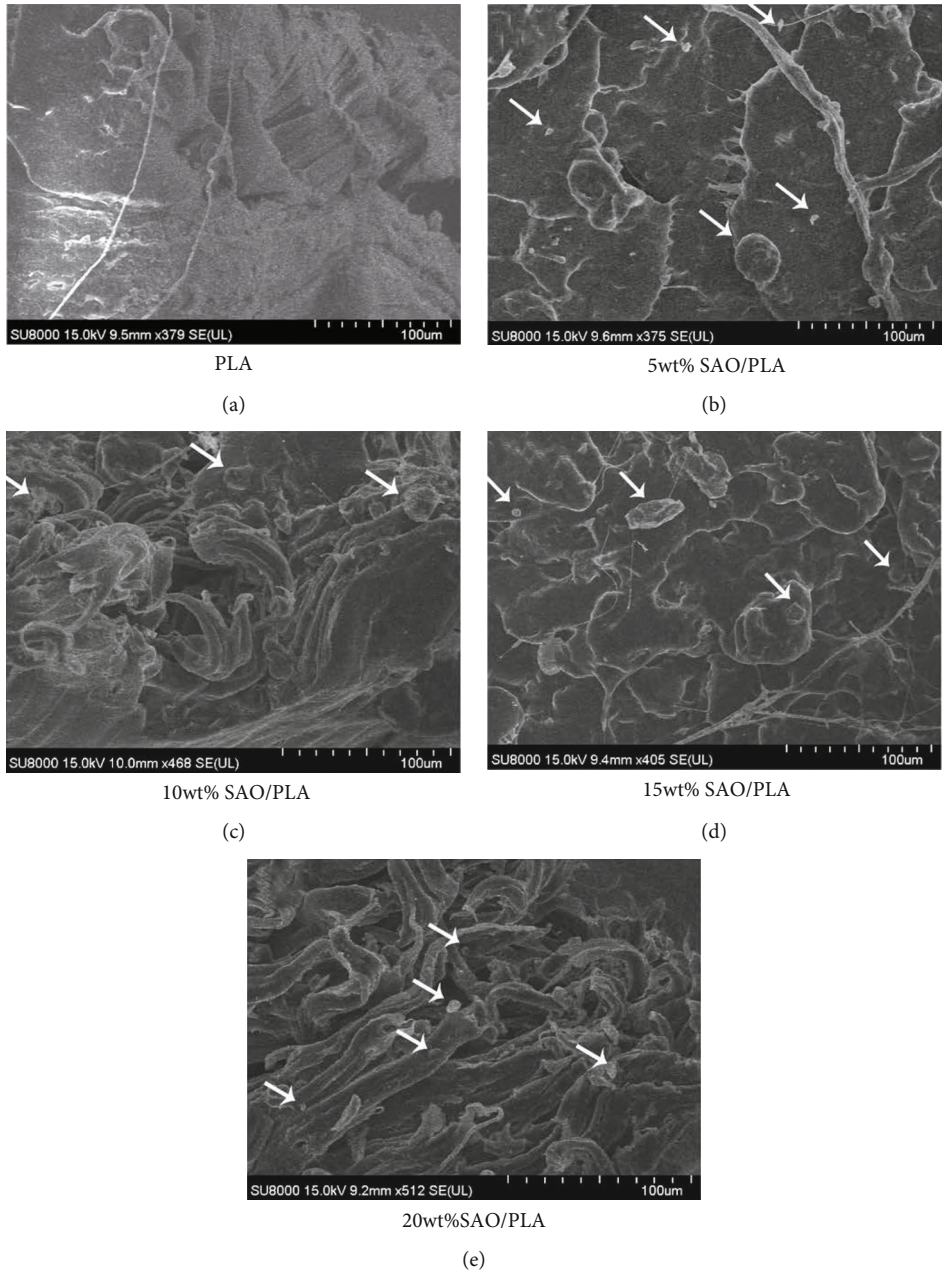

Figure 5: SEM images of fractures for (a) pure PLA, (b) 5 wt% SAO/PLA, (c) 10 wt% SAO/PLA, (d) 15 wt% SAO/PLA, and (e) 20 wt% SAO/PLA.

the fracture is relatively flat, smooth, and arranged regularly, with only some shapes like the lines of rivers, and it can be seen from the above situation that it conforms to the characteristics of brittle failure. The SEM image (Figure 5(b)) shows some tiny SAO particles on the surface of pure PLA, which indicates that SAO particles in the composite agglomerate due to its relatively high surface energy. The SEM images of SAO/PLA (Figures 5(c)–5(e)) show a moderately fair dispersion and uniform distribution of PLA at the micro level; some agglomerations on a pure PLA surface can be observed. However, the filaments may be formed during the preparation of the composites via hydrogen bonding, and the orientation of treated SAO particles is obvious under external force [24]. While SAO particles are uniformly distributed into the PLA matrix, some agglomerations of SAO particles are also present, and this may negatively affect the tensile properties. However, the relatively random distribution of SAO particles is favorable and helps the luminous SAO/PLA composite radiate green light after excitation [25].

3.6. Fluorescence Properties. The fluorescence spectra and phosphorescence spectra of pure SAO are shown in Figure 7 and include 5 wt% SAO/PLA, 10 wt% SAO/PLA, 15 wt% SAO/PLA, and 20 wt% SAO/PLA composites. The above fully shows that it can be excited by the lowest 320 nm and the highest 400 nm broadband, and the highest

Table 1: Tensile properties of tensile strength, elongation at break, and modulus of elasticity.

SAO (wt%)	Tensile strength (MPa)	Fracture elongation (%)	Modulus of elasticity (MPa)
0	14.94 ± 4.06	491.95 ± 284.06	94.78 ± 6.43
5	15.31 ± 5.32	699.61 ± 416.29	88.83 ± 6.96
10	9.74 ± 1.36	478.93 ± 143.38	77.44 ± 15.86
15	9.07 ± 2.22	408.08 ± 82.63	80.53 ± 17.76
20	9.82 ± 2.13	262.87 ± 45.79	98.04 ± 7.46

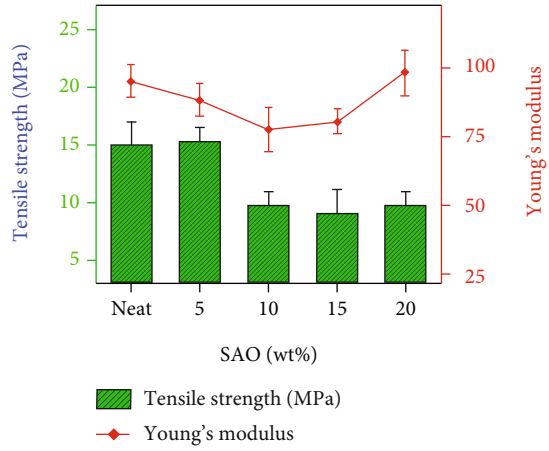

Figure 6: Effect of SAO loading on the tensile properties of PLA.

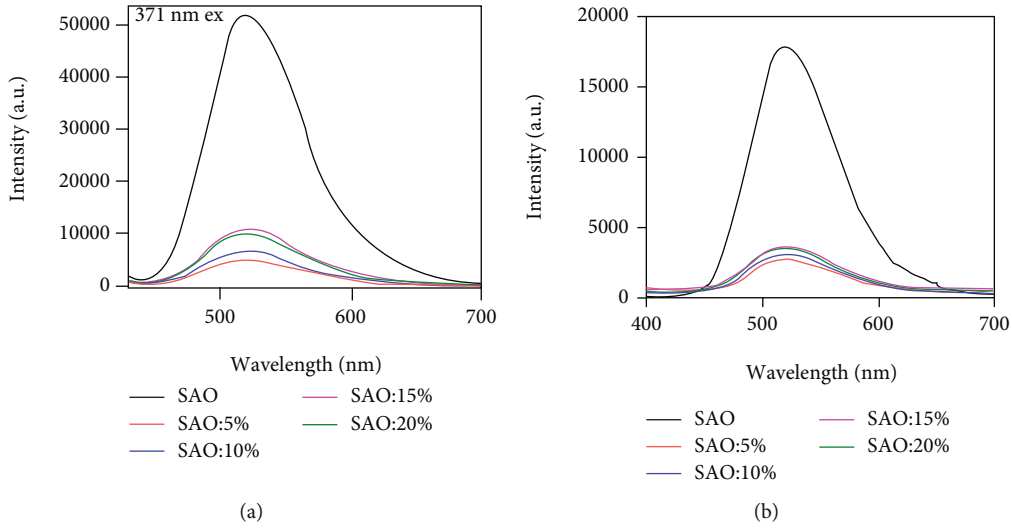

Figure 7: Fluorescence spectra (a) and phosphor spectra (b) of SAO, 5 wt% SAO/PLA, 10 wt% SAO/PLA, 15 wt% SAO/PLA, and 20 wt% SAO/PLA.

excitation intensity is exactly 360 nm in this range. By observing the emission spectra of phosphorescence and fluorescence, it can be found that the SAO particles have a maximum continuous broadband band at 524 nm on both spectra, but it is not difficult to find that the amplitude of fluorescence emission spectrum is significantly higher than that of phosphorescence emission spectrum (Figures 7(a) and 7(b)). Figure 7(a) shows that the fluorescence emission spectra of the composites are similar to those of SAO particles. This indicates that the composite does not change the crystal phase of $SrAl_2O_4:Eu^{2+}$ and Dy^{3+}, which belongs to the energy transition between the $4f^65d^1$ excited state and the $4f^7$ ground state of Eu^{2+} ions [26]. For the same quality samples, the luminescence intensity increased upon addition of SAO content, but the 15 wt% SAO composites have the best luminescence intensity. This indicates that increasing

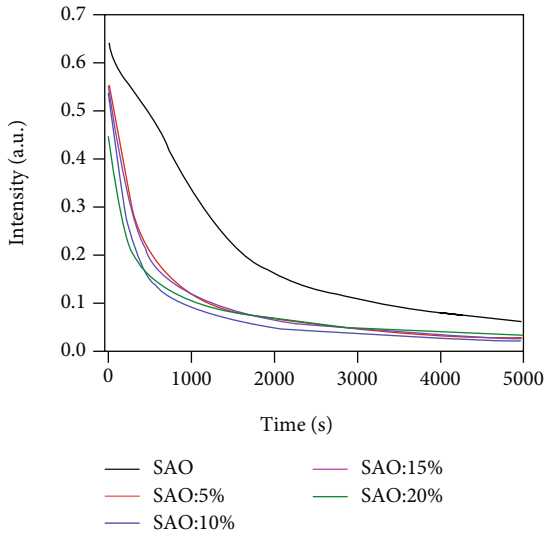

Figure 8: The afterglow decay curve of SAO, 5 wt% SAO/PLA, 10 wt% SAO/PLA, 15 wt% SAO/PLA, and 20 wt% SAO/PLA.

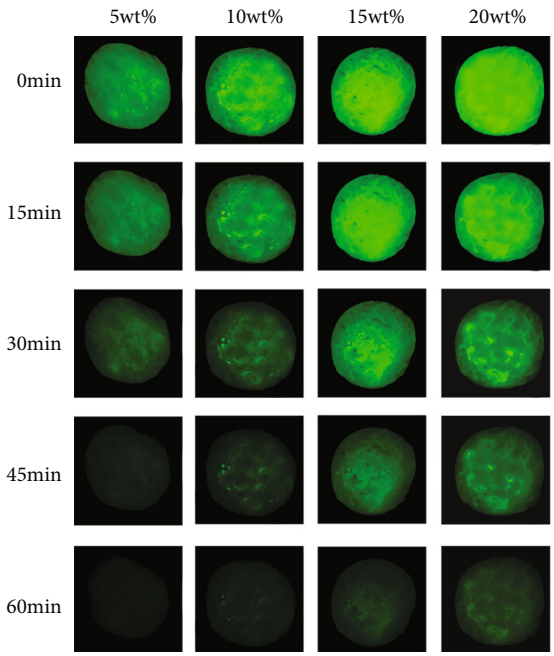

Figure 9: Long afterglow luminescence properties of composites with different SAO contents.

the SAO content does not further increase the luminous intensity. No special emission peak was found for Dy^{3+}, indicating that Dy^{3+} is not the luminescent center, but it does prolong the afterglow time as a trapped energy level [20, 27, 28].

Figure 8 shows the afterglow decay curves of SAO/PLA composites with different amounts of SAO. All samples have the same luminescence decay trend (Figure 8). However, with the gradual increase of the SAO concentration, the initial afterglow intensity will gradually decrease (except of 15 wt%). This is probably because one part of the excitation energy was absorbed and reflected by the PLA crosslinking with the rare-earth-doped particles. However, part of the energy emitted by $SrAl_2O_4:Eu^{2+}$ and Dy^{3+} phosphors was also absorbed and reflected by the PLA. Therefore, when the initial PLA concentration is 15 wt %, the cellulose emits more light energy due to the increase of excitation energy. The afterglow decay curve can be divided into two parts, one is fast decay, and the other is slow decay. After the excitation of the low trap energy level ceases, it begins to release electrons by means of thermal disturbance. The low trap level had a shallow depth, low energy, and small binding effects on the electrons [24]. Therefore, it can be known that the reason for the faster decay of the original brightness is related to the faster escape of electrons from the low trap energy level.

Figure 9 shows the long afterglow luminescence characteristics of composite materials with different SAO contents after sunlight exposure for 2 hours. The luminescence intensity of the composite gradually decreases with time, and it increases with SAO particle content. We concluded that the solvent casting method does not impact the afterglow properties of $SrAl_2O_4:Eu^{2+}$ and Dy^{3+}.

4. Conclusions

The luminous SAO/PLA composites were prepared by a solvent casting method for the first time. The study demonstrated that SAO/PLA composites have the ability to successfully develop materials with fluorescent properties while maintaining good mechanical properties. It only requires SAO particles as a functional agent and PLA as a matrix. All these indicate that the compatibility between SAO and PLA is better improved because of the presence of silane coupling agent. The tenacity, elongation at break, and modulus of the SAO/PLA composites decrease by increasing the SAO content in the composites; 5 wt% SAO composites have the best mechanical properties. The melting and crystallization behavior of the PLA matrix changed upon addition of SAO content. The SAO particles show a moderately fair dispersion and uniform distribution of PLA at the microlevel. The melting and crystallization behavior of the PLA matrix changed after the addition of the SAO particles. Therefore, SAO particles have not been destroyed in the blend with PLA matrix; they retain their luminescent properties. Meanwhile, the decay curves of the composite have a similar behavior to pure particles. By observing the phosphorescence spectra and photoluminescence spectra of the composite SAO particles, we can see that there is a main emission peak at 524 nm of the spectrum, which is consistent with that of pure SAO particles. It can also be seen that the attenuation curve reflected by the composite material is highly similar to that of pure particles. Meanwhile, 5 wt% SAO composite has better fluorescence properties. In conclusion, by controlling the addition of SAO particles, a SAO/PLA composite can be prepared with excellent mechanical properties and useful fluorescence performance. This product may have utility in materials applications. In the future studies, works can be carried out in the following ways: (1) test more different concentration ratios of SAO to find the best one. (2) Better applications should be found for the materials studied in this paper.

Data Availability

The datasets used and/or analyzed during the current study are available from the corresponding author on reasonable request.

Conflicts of Interest

It is declared by the authors that this article is free of conflict of interest.

Acknowledgments

This work was supported by the Planning Project of Zhejiang Provincial Collaborative Innovation Center for Bamboo Resources and High-efficiency Utilization (2017ZZY2-15) and Opening Project of Zhejiang Province Key Laboratory for Digital Design and Intelligent Manufacturing of Characteristics Cultural Creative Products (ZD201803). We thank LetPub (http://www.letpub.com/) for its linguistic assistance during the preparation of this manuscript.

References

[1] Y. Wei, L. Cao, L. Lv et al., "Highly efficient blue emission and superior thermal stability of baAl12O19:Eu2+ phosphors based on highly symmetric crystal structure," *Chemistry of Materials*, vol. 30, no. 7, pp. 2389–2399, 2018.

[2] Y. H. Wang, Y. Gong, X. H. Xu, and Y. Q. Li, "Recent progress in multicolor long persistent phosphors," *Journal of Luminescence*, vol. 133, pp. 25–29, 2013.

[3] K. G. Santosh, A. Maya, P. Z. Jose, A. P. Alexander, and Y. B. Mao, "Samarium-activated La2Hf2O7Nanoparticles as multifunctional phosphors," *ACS Omega*, vol. 4, no. 19, pp. 17956–17966, 2019.

[4] C. Shi, X. Y. Shen, Y. N. Zhu, X. Q. Li, Z. Y. Pang, and M. Q. Ge, "Excitation wavelength dependent dual-mode luminescence emission for dynamic multicolor anticounterfeiting," *ACS Applied Materials & Interfaces*, vol. 11, no. 20, pp. 18548–18554, 2019.

[5] J. Y. Zhong, W. R. Zhao, F. Du et al., "Identifying the emission centers and probing the mechanism for highly efficient and thermally stable luminescence in the La3Si6N11:Ce3+ phosphor," *The Journal of Physical Chemistry C*, vol. 122, no. 14, pp. 7849–7858, 2018.

[6] C. C. Lin, Y. T. Tsai, H. E. Johnston et al., "Enhanced photoluminescence emission and thermal stability from introduced cation disorder in phosphors," *Journal of the American Chemical Society*, vol. 139, no. 34, pp. 11766–11770, 2017.

[7] X. X. Zhang, Z. F. Zhou, F. Ye, X. Liu, and Q. R. Li, "Fabrication and study of properties of the PLA/$Sr_2MgSi_2O_7$:Eu^{2+}, Dy^{3+} long-persistent luminescence composite thin films," *Materials Science in Semiconductor Processing*, vol. 40, pp. 130–135, 2015.

[8] S. Sachhidananda, K. S. Nithin, S. Kumara, K. N. Shilpa, R. B. M. Jagajeevan, and S. Hatna, "Orange-red fluorescent polymer nanocomposite films with large stokes shift: an opto-electronic exercise," *Journal of Luminescence*, vol. 208, pp. 488–494, 2019.

[9] Z. Hosseini, W. K. Huang, C. M. Tsai, T. M. Chen, N. Taghavinia, and E. W. Diau, "Enhanced light harvesting with a reflective luminescent down-shifting layer for dye-sensitized solar cells," *ACS Applied Materials & Interfaces*, vol. 5, no. 12, pp. 5397–5402, 2013.

[10] Z. H. Li, Y. Tao, S. Huang, N. Gao, J. S. Ren, and X. G. Qu, "Lanthanide-based hollow mesoporous nanoparticles: a novel multifunctional platform for simultaneous gene delivery and cell imaging," *Chemical Communications*, vol. 49, pp. 7129–7131, 2013.

[11] W. B. Dai, K. Huang, Y. M. Fan, H. Li, and M. Xu, "Structure, valence change, and optical properties of BaMgSiO4: Eu phosphor," *Journal of Luminescence*, vol. 222, pp. 117–137, 2020.

[12] Y. P. Huang and J. W. Lin, "The trap bag concept of afterglow luminescence," *Scientific Reports*, vol. 7, p. 8475, 2017.

[13] A. Sepahvandi, M. Eskandari, and F. Moztarzadeh, "Fabrication and characterization of $SrAl_2O_4$: Eu^{2+} Dy^{3+}/CS-PCL electrospun nanocomposite scaffold for retinal tissue regeneration," *Materials Science and Engineering: C*, vol. 66, pp. 306–314, 2016.

[14] Z. C. An, S. T. Che, Y. H. Song et al., "Ca (Mg0.8Al0.2) (Si1.8Al0.2) O6: Ce3+, Tb3+ phosphors: structure control, density-functional theory calculation, and luminescence property for pc-wLED application," *Inorganic Chemistry*, vol. 59, no. 7, pp. 4790–4799, 2020.

[15] D. Zhang, X. T. Zhang, Z. C. An et al., "Photoluminescence and color-tunable properties of Na4Ca4Mg21(PO4)18:Eu2+,Tb3+/Mn2+ phosphors for applications in white LEDs," *Inorganic Chemistry*, vol. 59, no. 19, pp. 14193–14206, 2020.

[16] A. Ebrahimzade, M. R. M. Mojtahedi, and R. R. Semnani, "Study on characteristics and afterglow properties of luminous polypropylene/rare earth strontium aluminate fiber," *Journal of Materials Science: Materials in Electronics*, vol. 28, pp. 8167–8176, 2017.

[17] S. Z. Liao, X. Y. Ji, Y. F. Liu, and J. L. Zhang, "Highly efficient and thermally stable blue-green (Ba0.8Eu0.2O)(Al2O3)4.575×(1+x) phosphor through structural modification," *ACS Applied Materials & Interfaces*, vol. 10, no. 45, pp. 39064–39073, 2018.

[18] W. K. Peng, H. F. Xia, Z. H. Zhang et al., "A surface corrosion and expansion mechanism on thermal degradation of SrAl2O4:Eu2+, Dy3+," *Journal of Alloys and Compounds*, vol. 753, pp. 35–40, 2018.

[19] M. L. Wan, X. Jiang, J. L. Nie et al., "Phosphor powders-incorporated polylactic acid polymeric composite used as 3D printing filaments with green luminescence properties," *Applied Polymer*, vol. 137, no. 18, p. 48644, 2020.

[20] C. Shi, X. Hou, and X. Li, "Preparation and characterization of persistent luminescence of regenerated cellulose fiber," *Journal of Materials Science: Materials in Electronics*, vol. 28, pp. 1015–1021, 2017.

[21] M. Tayebi, S. O. Movahed, and A. Ahmadpour, "The effect of the surface coating of a strontium mono-aluminate europium dysprosium-based (SrAl2O4: Eu2+, Dy3+) phosphor by polyethylene (PE), polystyrene (PS) and their dual system on the photoluminescence properties of the pigment," *RSC Advances*, vol. 9, no. 66, pp. 38703–38712, 2019.

[22] A. Erdman, P. Kulpinski, T. Grzyb, and S. Lis, "Preparation of multicolor luminescent cellulose fibers containing lanthanide doped inorganic nanomaterials," *Journal of Luminescence*, vol. 169, pp. 520–527, 2016.

[23] J. Liu, J. Wang, L. Zhu et al., "A high-safety and multifunctional MOFs modified aramid nanofiber separator for

lithium-sulfur batteries," *Chemical Engineering Journal*, vol. 411, p. 128540, 2021.

[24] H. C. Francisco Leonardo, R. P. Moreira, C. F. C. Felinto Maria, V. C. Teixeira, H. F. Brito, and O. L. Malta, "$SrAl_2O_4$: Eu^{2+}, Dy^{3+} persistent luminescent materials functionalized with the Eu^{3+}(TTA)-complex by microwave-assisted method," *Journal of alloys and compounds*, vol. 882, 2021.

[25] Y. N. Zhu, Q. C. Yu, L. B. Zheng, Z. Y. Pang, and M. Q. Ge, "Luminous properties of recycling luminous materials $SrAl_2O_4$: Eu^{2+}, Dy^{3+} based on luminous polyester fabric," *Materials Research Express*, vol. 7, no. 9, 2020.

[26] A. Szczeszak, N. Jurga, and S. Lis, "Effect of the Ce^{3+} ions co-doping on the emission color of the up-converting NaYbF4 doped with Ho3+ ions," *Ceramics International*, vol. 46, no. 16, pp. 26382–26387, 2020.

[27] A. Kumar, G. Kedawat, P. Kumar, J. Dwivedia, and B. P. Gupta, "Sunlight-activated Eu2+/Dy3+doped SrAl2O4water resistant phosphorescent layer for optical displays and defence applications," *New Journal of Chemistry*, vol. 39, no. 5, pp. 3380–3387, 2015.

[28] L. Zhu, J. Wang, J. Liu et al., "Smart formaldehyde detection enabled by metal organic framework-derived doped electrospun hollow nanofibers," *Sensors and Actuators B: Chemical*, vol. 326, article 128819, 2021.

Hindawi
Scanning
Volume 2021, Article ID 1469642, 8 pages
https://doi.org/10.1155/2021/1469642

Research Article

Effect of R Angle of the Outer Extension Tube against the in-Core Flux Thimble in Nuclear Power Plant on Its Wear Behavior

Qiang Chen, Yinhui Che, Jianjun Guan, Yang Li, and Qinhu Wang

Suzhou Nuclear Power Research Institute Co., Ltd., Shenzhen 518120, China

Correspondence should be addressed to Qiang Chen; rcachen@163.com

Received 30 July 2021; Accepted 18 August 2021; Published 23 September 2021

Academic Editor: Jian Chen

Wear failure of the in-core flux thimble is an important problem in the neutron flux measurement system, which threatens the safety of the nuclear power plant. To figure out the wear mechanism of the thimble, a wear tester was designed and manufactured to simulate the wear process of the in-core flux thimble. Outer guide tubes with different R angles were used to abrade the thimbles. The designed tester can well simulate the wear process in the real power plant. R angle of the outer guide tube played important role in the wear behavior of the in-core flux thimbles.

1. Introduction

Nowadays safety of the nuclear power plant becomes more and more important along a big number of nuclear power plants go into operation. The flow around the thimbles of the in core instrumentation induces vibration and shocks against their guides in the vessel, producing wear and even leakage of the thimbles [1]. Almost all nuclear power plants in China were concerned by this problem seriously [2–4].

Although this problem has been noticed to be quite important, no study was focused on it till now. Impact and abrasion between the thimbles and the guide tubes is a very unique wear type, which consists of longitudinal shift and circular movement. No commercial device can be obtained to complete this kind of wear test. In order to characterize the phenomenon and find a way to reduce or suppress wear of the thimbles, a dedicated device have been designed and developed, which can simulate the relative movement between the thimbles and guide tubes.

The most serious wear was found to occur at the end of the outer guide tube with sharp shape. Changing the R angle of this end may help to control the damage of the thimble. So, one end of the outer guide tubes was manufactured as different R angles. These guide tubes were used to contact the thimbles by using the self-made device mentioned above.

2. Experimental

2.1. Test Device. As mentioned above, a dedicated device is needed to simulate the relative movement between the thimbles and guide tubes. The diagram of the device is shown in Figure 1.

The device contains a container for the water which supplies water for the space between the thimble and the guide tube by a water pump. A lever supported by a bearing can make the thimble up and down by a cam with motor I. A funnel is applied for decreasing splash of the water. A slim stick with motor II is used to drive the thimble to move circumferentially. Both motors are controlled by frequency converters which can change their rotational speed.

2.2. Experimental Parameters. The frequency of moving up and down was set as 5 Hz and the driving distance of the level was 5 mm. The rotation frequency of the thimble was set as 10 Hz. The circulating water can fill up the guide tube during the whole test period of 72 hrs. The R angle of the guide tubes were manufactured as R6.3 and R0, respectively.

The thimbles were made of Z5CND17-12. Its nominal chemical composition is shown in Table 1. The guide tubes were made of Z2CN19-10NS, whose nominal chemical composition is shown in Table 2.

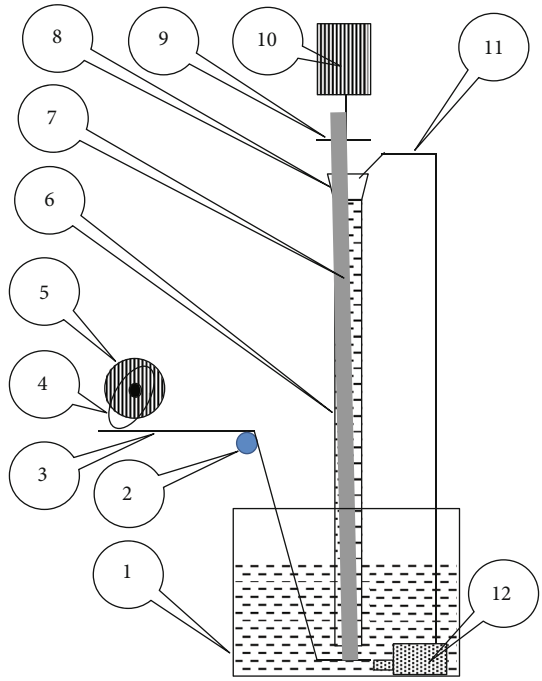

Figure 1: Diagram of the self-made device to simulate the wear of the thimbles. 1. Container; 2. Bearing; 3. Lever; 4. Cam; 5. Motor I; 6. Guide tube; 7. Thimble; 8. Funnel; 9. Stick; 10. Motor II; 11. Water tube; 12. Water pump.

Table 1: Nominal chemical composition of Z5CND17-12.

C	Mn	Si	P	S	Cr	Ni	Mo	Cu	Co	Nb + Ta
≤0.070	≤2.00	≤0.75	≤0.030	≤0.015	16.00-19.00	10.00-14.00	2.00-2.50	≤1.00	≤0.06	≤0.15

2.3. Roughness and Profile Measurement. After the 72-hr test, profiles of the wear scars were measured by a roughness tester (Type 2300A-R, Harbin Measuring & Cutting Tool Group Co. Ltd.) to obtain the roughness and a KEYENCE VR-3200 3D profile tester to obtain depth of the scars.

2.4. SEM and EDS Analysis. The details of the wear scars were analyzed by using an FEI Co. XL30 ESEM FEG scanning electron microscope (SEM) with Energy Dispersive Spectrometer (EDS) to get the morphologies and surface composition of the scars.

2.5. Micro Hardness Measurement. Micro hardness of the original surface and the wear scars were measured by using a HVS-1000 M micro hardness tester produced by Shanghai Microcre Light-Mac. Tech. Co. Ltd. The load was 200 g and the holding pressure time was 10 s.

3. Results and Discussion

3.1. Macro Morphology of the Wear Scars. Figure 2 shows the macro morphologies of the wear scars on the thimble after 72 h of test (Figures 2(a), 2(b)), which are similar to the scars formed in the nuclear power plants (Figures 2(c)). The scars looked shiny like a ring around the thimble. These results confirmed the success of the test device which was designed and manufactured originally. Although the driving distance is the same as 5 mm in the test process, the scar width of the samples against the R6.3 is bigger than that of the R0. This means the guide tube with sharp R angle (0) can hold back the running distance of the sample more than that for the big R angle (6.3). Due to the inertia of the movement, the wear scar is wider than 5 mm.

3.2. Wear Depth and Wear Roughness. Six points near the upper end of the scar to measure the maximum depth based on the profile obtained by using the KEYENCE VR-3200 3D profile tester for each scar. The typical profile of the wear scar is shown in Figure 3 with the measurement of the maximum depth.

The average maximum depth for the sample against R0 is about twice of that for the sample against R6.3 as shown in Figure 4. Enlargement of the R angle for the guide tube can decrease the wear damage caused by the contact and abrasion between the thimble and the guide tube. The sharp angle (R0) of the guide tube can cut the thimble deeply and form sharp overhang in the horizontal direction. At the same time the sharp angle scrapes the thimble in the vertical direction thus remove some of the overhang easily. While the round angle (R6.3) of the guide tube cuts the thimble shallower due to its geometrical

Table 2: Nominal chemical composition of Z2CN19-10NS.

C	Mn	Si	P	S	Cr	Ni	Cu	Co	Nb + Ta
≤0.035	≤2.00	≤1.00	≤0.030	≤0.015	18.50-20.00	9.00-10.00	≤1.00	≤0.06	≤0.15

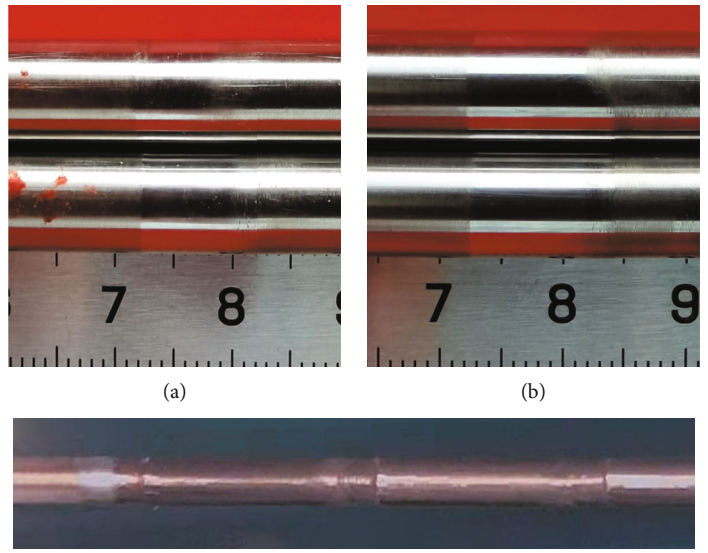

Figure 2: Macro morphology of the wear scars. (a) R0 (b) R6.3 (c) From nuclear power plant.

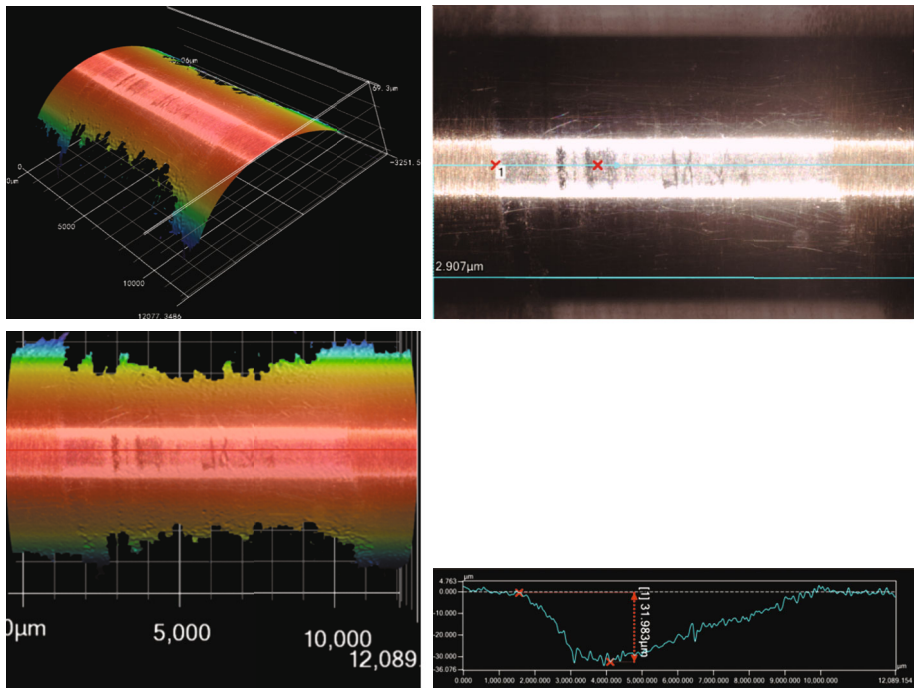

Figure 3: The typical profile of the wear scar and its maximum depth.

shape. In the vertical direction, the round angle squeezes the thimble instead of scraping for the sharp angle thus it is difficult to remove the material from the thimble. So the depth of the scars formed against the round angle was much smaller than that against sharp angle, indicating less material loss of the thimble.

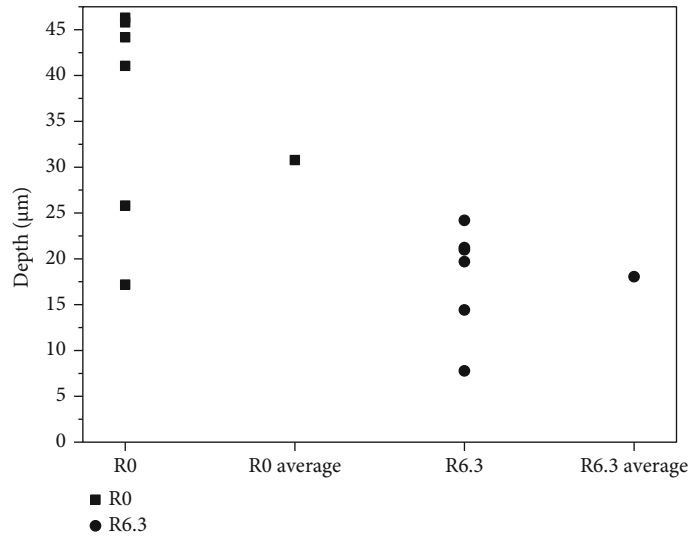

Figure 4: Maximum depth of the scars for the samples.

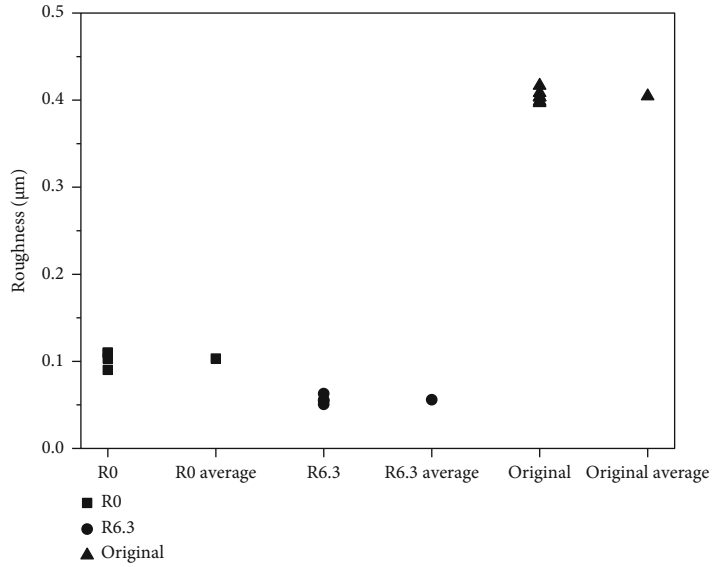

Figure 5: Roughness of the scars and the original surface.

The scar looks shiny and smooth compared to the original surface of the thimble. Roughness of the scars and the original surface was measured for six times and their average value was calculated as shown in Figure 5. Roughness in the scars is much smaller than that for the original surface of the thimble. Roughness for both R angles decreased significantly after the tests. Roughness for the sample against round R angle (6.3 mm) was the smallest which is about 60% of that for sharp R angle (0). When the R angle of the thimble is 0, the sharp angle of the guide tube can cut the thimble deeply in the horizontal direction. At the same time the sharp angle scrapes the thimble in the vertical direction. It is reasonable to say that the round angle (R6.3) of the guide tube cuts the thimble shallower due to its geometrical shape. In the vertical direction, the round angle squeezes the thimble instead of scraping for the sharp angle thus decreases the roughness. That's why the roughness of the scars formed against the round angle was much smaller than that against sharp angle.

Surface roughness always plays important role in the wear process of materials [5–11]. The most common conclusion of these works is that the bigger the roughness is, the more serious the wear damage is. This is an important reason why the wear depth of the thimble for the R0 guide tube is bigger than that for R6.3 (Figure 4). It is reasonable to predict that the thimble for the R0 guide tube will fail first if the test period is long enough.

3.3. SEM Morphology and EDS of the Wear Scars. SEM morphologies of the wear thimble scars of are shown in Figure 6.

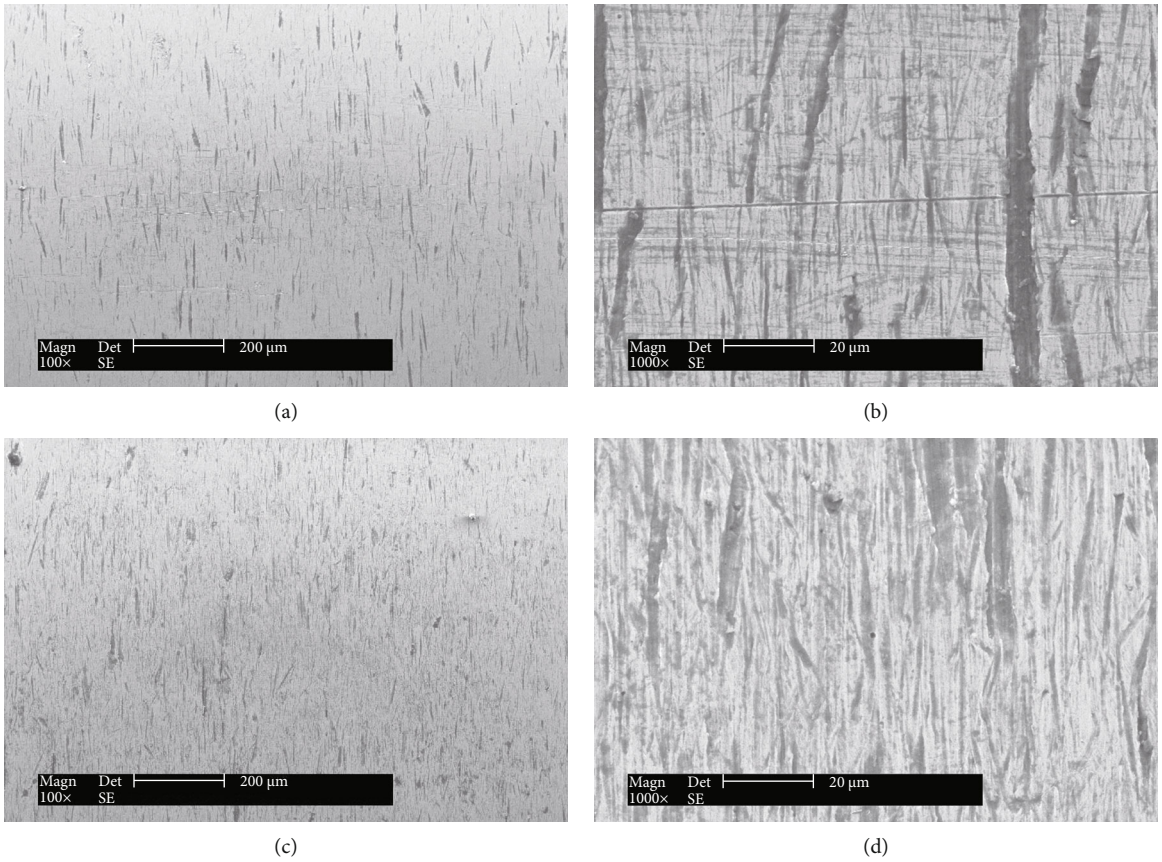

Figure 6: SEM morphologies of the scars against guide tube of R0 (a, b) and R6.3 (c, d).

For both R angles short ploughings can be found around the surface of the thimble in the horizontal direction. Ploughings for the sample against sharp R angle (0) are fewer but deeper compared to that for the samples against round R angle (6.3 mm). With the sharp R angle, the guide tube can cut the thimble to form deep ploughings in the horizontal direction (Figure 6 a, b). With the sharp R angle, the guide tube can seriously cut the protuberance around the plouging and the ploughing itself in the vertical direction of the ploughing thus the old ploughings vanished quickly. While with the round R angle, the guide tube cut the thimble to form relatively shalow ploughings in the horizontal direction (Figure 6 c, d). Although they were shallow, the guide tube with round R angle (R6.3) cannot cut the protuberance around the plouging and the ploughing itself seriously thus the old ploughings vanished slowly. The results are well in accordance with the results of scar depth and scar roughness mentioned above.

For the EDS results (Figure 7), the chemical compositions in the scars were similar to the original alloy (Table 1). No apparent oxidation was found in both wear scars, indicating that the wear was mainly caused by mechanical damage while had nothing to do with chemical reactions.

3.4. Micro Hardness Measurement. Micro hardness of the wear scar formed by the R0 guide tube was almost the same as that of the original surface, while micro hardness of the wear scar formed by the R6.3 guide tube changed a lot (Figure 8). As mentioned above, deformation was found on the wear scar surface for both cases (Figure 6). Crossing slip dislocations formed during plastic deformation can create dipolar and multipolar structures that may contribute to work hardening. Such structures may become plastically relaxed by secondary slip thus the cross-slip of dislocation groups was an important work-hardening mechanism [12]. Z.Q.Wang et al. also found that cross-slip plays a role in the generation and annihilation of dislocations, leading to different dislocation velocities, density evolution and macroscale plastic response, which was related to work-hardening [13]. Although work-hardening occurred during the wear process, the hardness of the scar for the R0 guide tube changed little due to the fast removal of the surface layer.

3.5. Modeling the Impact and Abrasion of the Thimbles. Figure 9 shows a model for the impact and abrading process of the thimbles. When the thimble moves in horizontal direction in the guide tube (Figure 9(a)), it impacts the end of the guide tube and forms ploughings on the thimble surface (Figure 9(b)). When the thimble moves in vertical direction in the guide tube (Figure 9(c)), it is abraded by the end of the guide tube and cuts the ploughings formed on the thimble surface to make it shallow (Figure 9(d)) thus make the surface smoother. In fact, the movements of the thimble

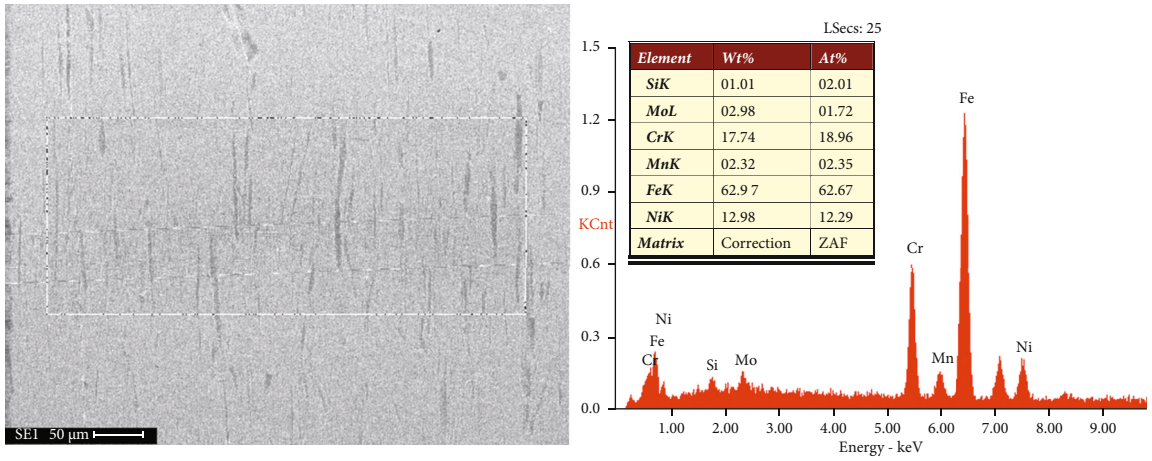

(a)

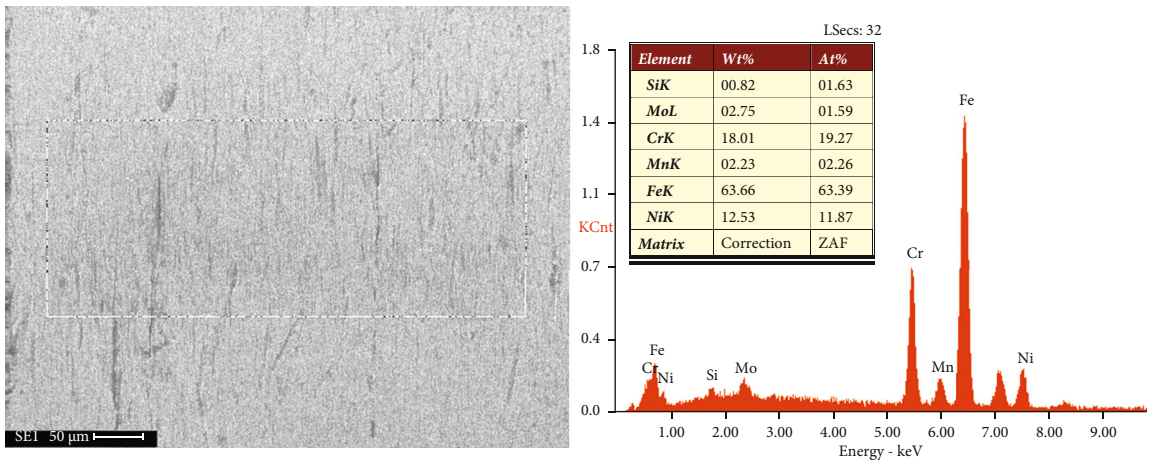

(b)

Figure 7: EDS of the scars against guide tube of R0 (a) and R6.3 (b).

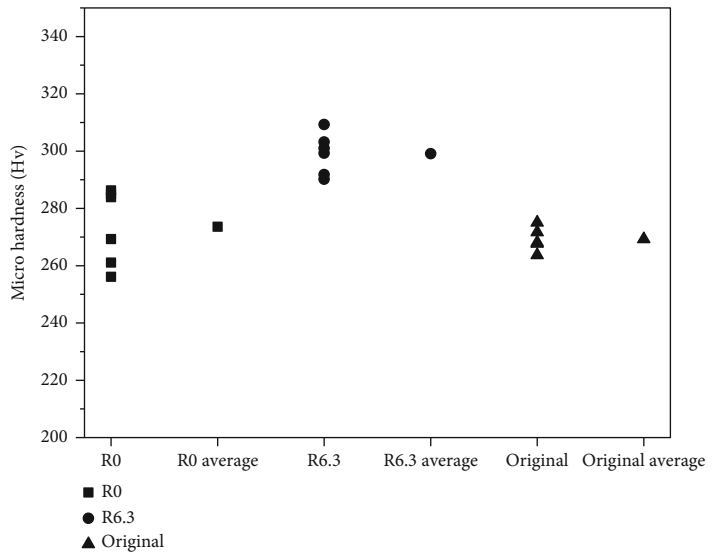

Figure 8: Micro hardness of the wear scars and the original surface.

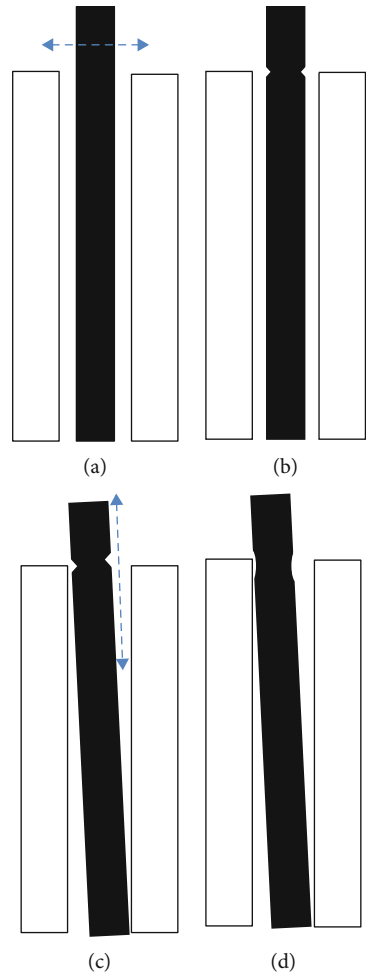

Figure 9: Schematic diagram of the wear process of the thimble against the guide tube.

in horizontal and vertical direction occur simultaneously all the time. The ploughing and the abrasion caused the mass loss of the thimble and make it smoother, showing smaller roughness. The larger the R angle is, the shallower the ploughing is and the weaker the abrasion is, thus the less the mass loss is, showing smaller maximum depth of the wear scar.

4. Conclusion

(1) The self-made device can well simulate the movement between the thimble and the guide tube and the wear process of the thimble in the nuclear power plant

(2) Bigger R angle of the outer guide tube can decrease the roughness and increase the hardness of the wear scar more significantly which is beneficial to reduce wear of the thimble

(3) R angle of the outer guide tube can significantly affect the wear behavior of the thimbles. Bigger R angle is beneficial to extending the service life of the thimbles

Data Availability

All data generated or analyzed during this study are included in this article.

Conflicts of Interest

The author(s) declare(s) that they have no conflicts of interest.

References

[1] A. Trenty, C. Puyal, C. Vincent et al., "Thimble vibration analysis and Monitopring on 1300 and 900 MW reactors using accelerometers and in core neutron noise," *Progress in Nuclear Energy*, vol. 21, pp. 97–106, 1988.

[2] J. R. Hu, T. Luo, J. Jian, C. X. Liu, J. D. Yang, and Z. Li, "Impact analysis of thimble tube of neutron flux measurement system in fang Cheng gang Power Station," *Nuclear Science and Engineering*, vol. 37, pp. 750–755, 2017.

[3] Q. Ma, C. Chen, P. R. Li et al., "Research on impact factors of depth quantification in Eddy current test for thimble tubes Wear of nuclear power plants," *Nucl. Power Eng.*, vol. 41, pp. 150–154, 2020.

[4] L. Zhang, W. J. Liu, S. J. Xie et al., "Swept-frequency ET and innovative feature extraction of abrasion defects for thimble tubes in nuclear power plants," *China Mechanical Engineering*, vol. 32, pp. 18–25, 2021.

[5] H. Christensen, "Stochastic models for hydrodynamic lubrication of rough surfaces," *Proceedings of the Institution of Mechanical Engineers*, vol. 184, no. 1, pp. 1013–1026, 1969.

[6] C. Li, H. H. Wang, X. X. Ren, and M. Liu, "Analysis of elasto-hydrodynamic lubrication of clamping ball screw of all-electric injection," *Appl. Mech. and Mater.*, vol. 644-650, pp. 751–754, 2014.

[7] X. Pang, W. Jiang, and X. W. Jin, "Investigation on Lubrication State of Sliding Bearings in Low-Speed Rotor System Subjected to Torque Load," *International Journal of Rotating Machinery*, vol. 2019, 11 pages, 2019.

[8] C. Qin, Y. Kang, K. Song, H. Zhang, D. Zhen, and Z. Shi, "Effect of surface roughness on static characteristics of floating ring bearing," *Lubrication Engineering*, vol. 5, pp. 66–72, 2017.

[9] J. Y. Shi, "Effect of the roughness on friction and wear of bearing bush," *Internal Combustion Engine & Parts*, vol. 2, pp. 11–18, 1988.

[10] Z. Xie, Z. S. Rao, N. Ta, and L. Liu, "Investigations on transitions of lubrication states for water lubricated bearing. Part II: further insight into the film thickness ratio lambda," *Ind. Lubr. Tribol.*, vol. 68, no. 3, pp. 416–429, 2016.

[11] B. F. Yin, *Lubrication and friction mechanism and application research of laser surface texturing technology on the key friction pairs of internal combustion engine [D].*, Jiangsu University, 2011.

[12] P. J. Jackson, "The role of cross-slip in the plastic deformation of crystals," *Materials Science and Engineering*, vol. 57, no. 1, pp. 39–47, 1983.

[13] Z. Q. Wang, I. J. Beyerlein, and R. LeSar, "The importance of cross-slip in high-rate deformation," *Modelling and Simulation in Materials Science and Engineering*, vol. 15, no. 6, pp. 675–690, 2007.

Hindawi
Scanning
Volume 2021, Article ID 1834556, 5 pages
https://doi.org/10.1155/2021/1834556

Research Article

Relationship between Different Psoriasis Types and Thyroid Dysfunction: A Retrospective Analysis

Juan Du,[1] Chunyue Ma,[2] Runnan Wang,[3] Lanmei Lin,[3] Luhui Gao,[4] Sunyi Chen,[1] and Xiaonian Lu[1]

[1]*Department of Dermatology, Huashan Hospital, Fudan University, Shanghai 200040, China*
[2]*Department of Oral & Maxillofacial-Head & Neck Oncology, 9th People's Hospital, Shanghai Jiao Tong University School of Medicine, National Clinical Center of Oral Diseases, Shanghai Key Laboratory of Stomatology, Shanghai 200011, China*
[3]*Shanghai Medical School, Fudan University, Shanghai 200032, China*
[4]*College of Foreign Languages and Literature, Fudan University, Shanghai 200433, China*

Correspondence should be addressed to Xiaonian Lu; luxiaonian@fudan.edu.cn

Received 2 July 2021; Accepted 30 August 2021; Published 18 September 2021

Academic Editor: Qiao Yanxin

Objective. The aim of this study was to investigate the relationship between different psoriasis types and thyroid dysfunction. *Methods*. The data of patients diagnosed with psoriasis between January 2013 and October 2018 who underwent thyroid function tests were collected. Free triiodothyronine (FT3), free thyroxine (FT4), total triiodothyronine (TT3), total thyroxine (TT4), thyroid-stimulating hormone (TSH), thyroglobulin antibody (TGAb), and thyroid peroxidase antibody (TPOAb) were measured. The thyroid function of patients with psoriasis vulgaris, pustular psoriasis, erythrodermic psoriasis, and psoriatic arthritis was evaluated, and the differences in hormone levels and antibodies in the pituitary-thyroid axis with psoriasis type were analyzed. *Results*. The data of a total of 468 patients were analyzed in this study. The proportion of normal hormone levels was higher among vulgaris patients ($P < 0.001$), while the erythrodermic patients were more likely to have decreased FT3 or FT4 but normal TSH ($P < 0.001$). FT3 levels were lower in pustular patients ($P < 0.05$), FT4 levels were lower in erythrodermic patients ($P < 0.05$), and TSH levels were higher in patients with psoriatic arthritis ($P < 0.05$). TPOAb levels were higher than normal in all patients, but there was no significant difference in the levels of TPOAb and TGAb among 4 types of the patients. *Conclusion*. Psoriasis is related to thyroid dysfunction, especially in patients with atypical psoriasis types. The possibility of complications should be considered in erythrodermic patients.

1. Introduction

Psoriasis is an inflammatory skin disease that is caused by immune dysfunction, determined by the inheritance of multiple genes, and stimulated by many environmental factors. Its prevalence is around 3% worldwide and 0.1–0.5% in China, respectively [1]. This disorder typically affects the skin and joints, but the fingers, toes, and mucous membranes may also be involved. The disease has a chronic and recurrent course. Clinically, psoriasis is broadly divided into 4 types: psoriasis vulgaris, psoriatic arthritis, pustular psoriasis, and erythrodermic psoriasis, of which psoriasis vulgaris is the most common, followed by psoriatic arthritis. The incidence of pustular psoriasis and erythrodermic psoriasis is relatively low, but serious systemic symptoms can occur, affecting the physical and mental health of patients, as well as their quality of life [2].

The precise etiology and pathogenesis of psoriasis have not been fully elucidated. Dysfunction of the innate and acquired immune systems, including activation of the NF-κB signaling pathway for antigen presentation, the dominant response of T helper 1 (Th1) cells, and increased IL-17 response, promoting the development and progression of psoriasis. Thus, patients with psoriasis are at increased risk of other immune system-related diseases, such as rheumatoid arthritis, inflammatory bowel disease, multiple sclerosis, and autoimmune thyroiditis [3, 4]. Hashimoto's thyroiditis, or autoimmune thyroiditis, is a common autoimmune

Table 1: Baseline patient characteristics.

Characteristics	Total patients ($n = 468$)	Psoriasis vulgaris ($n = 300$)	Pustular psoriasis ($n = 60$)	Erythrodermic psoriasis ($n = 54$)	Psoriatic arthritis ($n = 54$)
Mean age ± SD (y)	48.0 ± 15.7	47.8 ± 15.5	46.6 ± 18.6	51.8 ± 15.8	47.4 ± 13.1
Sex (M/F)	318/150	210/90	33/27	44/10	31/23
Duration of disease (y)	5.5 ± 2.9	7.2 ± 4.6	3.8 ± 1.9	4.1 ± 2.3	6.9 ± 3.0
PASI	30.4 ± 11.5	29.53 ± 10.22	33.90 ± 8.32	45.63 ± 12.13	16.10 ± 8.39

M: male; F; female; PASI: psoriasis area and severity index.

disorder [5]. The T cell-mediated inflammatory response in the thyroid is characterized by high serum levels of TPOAb and TGAb. A dominant Th1 cell response is also present in this disorder, suggesting a possible association between psoriasis and Hashimoto's thyroiditis. In psoriasis, especially psoriatic arthritis, the relationship between autoimmune thyroid damage and thyroid dysfunction remains controversial. There may also be differences in the relationship between adult and juvenile patients as well as sex differences. In this study, the characteristics of thyroid dysfunction in patients with the 4 types of psoriasis were analyzed. The characteristics of autoimmune thyroid damage and pituitary-thyroid axis hormones in each type of patient were also assessed.

2. Methods

2.1. Patients. The medical data of patients diagnosed with psoriasis between January 2013 and October 2018 who underwent thyroid function tests during admission were retrospectively analyzed. Cases were classified as psoriasis vulgaris, pustular psoriasis, erythrodermic psoriasis, and psoriatic arthritis based on clinical characteristics and pathological examination [6]. Patients with a history of living for a long time in an iodine-deficient region, past history of thyroid disease, history of thyroid surgery or neck radiation, history of systemic application of drugs that may affect thyroid hormone levels, or history of other autoimmune diseases were excluded. Age- and sex-matched subjects, without psoriasis, served as controls.

2.2. Thyroid Function Tests. Data on the general characteristics and relevant medical history of the patients were collected, as well as the results of thyroid function tests at admission. The Roche electrochemiluminescence analyzer (Elecsys E170, Roche Diagnostics, Tokyo, Japan) and its supporting reagents (Roche Diagnostics) were used for free triiodothyronine (FT3), free thyroxine (FT4), total triiodothyronine (TT3), total thyroxine (TT4), thyroid-stimulating hormone (TSH), thyroglobulin antibody (TGAb), and thyroid peroxidase antibody (TPOAb) measurements. Reference ranges for normal thyroid function are FT3, 3.50-6.50 pmol/L; FT4, 11.50-22.70 pmol/L; TT3, 1.23-3.39 nmol/L; TT4, 54.0-174.0 nmol/L; TSH, 0.550-4.780 mIU/L; TGAb, <60.0 U/mL; and TPOAb, <60.0 U/mL. Clinical hyperthyroidism was defined as elevated FT3 and FT4 with decreased TSH. Subclinical hyperthyroidism was defined as normal FT3 and FT4 with decreased TSH. Clinical hypothyroidism was defined as decreased FT3 and FT4 with elevated TSH. Subclinical hyperthyroidism was defined as normal FT3 and FT4 with elevated TSH (Table 1).

2.3. Ultrasound Tests. Ultrasound examination was carried out using B-mode high-resolution system to measure skin thickness (mm). Normal thickness values were defined as the thickness of the healthy skin surrounding the lesions.

2.4. Statistical Analysis. All data were analyzed using SPSS 19.0 software. Measurement data in test results conforming to the normal distribution were expressed as $\bar{x} \pm SD$. Count data were expressed as n (%). One-way analysis of variance (ANOVA) and the Kruskal-Wallis tests were used to compare multiple groups for data conforming to the normal distribution and not conforming to the normal distribution, respectively. The χ^2 test was used to compare count data between the groups. Differences with $P < 0.05$ were considered statistically significant.

3. Results

3.1. Thyroid Function in Patients with Psoriasis. A total of 468 patients were included in this study, including patients with psoriasis vulgaris ($n = 300$), pustular psoriasis ($n = 60$), erythrodermic psoriasis ($n = 54$), and psoriatic arthritis ($n = 54$). There were 318 male and 150 female patients, and the average age was 48.08 ± 15.76 years. There were no statistically significant differences in age or sex among the patients with each disease type ($P > 0.05$).

No cases of clinical hyperthyroidism were found in the patients; however, 37 (7.91%) of patients had abnormal thyroid function, suggesting a possible correlation between psoriasis and thyroid dysfunction. A condition of subclinical hyperthyroidism was found in 25 patients (25/468, 5.3%), which included 13 cases of vulgaris, 5 pustular, 4 erythrodermic, and 3 arthritis type. There was only one patient of clinical hypothyroidism in each of the erythrodermic group and arthritis group. A condition of subclinical hypothyroidism was found in 12 patients (12/468, 2.56%), including 9 cases of vulgaris, 1 arthritis, and 2 pustular subsets (Table 2).

After laboratory tests for thyroid function, 74.2% (347/468) of patients had normal levels of FT3, FT4, and TSH. The proportion of patients with normal FT3, FT4, and TSH was 80.3% (241), 66.7% (40), 48.2% (26), and 74.1% (40), respectively, in vulgaris, pustular, erythrodermic,

Table 2: Thyroid dysfunction of psoriasis patients.

	Psoriasis vulgaris	Pustular psoriasis	Erythrodermic psoriasis	Psoriatic arthritis	Total
Elevated FT3 or FT4 & decreased TSH (%)	0	0	0	0	0
Normal FT3 and FT4 & decreased TSH (%) (adjusted residuals)	13 (4.33%) (-1.3)	5 (8.33%) (1.1)	4 (7.41%) (0.7)	3 (5.56%) (0.1)	25 (5.34%)
Decreased FT3 or FT4 & elevated TSH (%)	0	0	1 (1.85%)	1 (1.85%)	2 (0.43%)
Normal FT3 and FT4 & elevated TSH (%)	9 (3.00%)	2 (3.33%)	0	1 (1.85%)	12 (2.56%)
Decreased FT3 or FT4 & normal TSH (%) (adjusted residuals)	37 (12.33%) (-3.9)	13 (21.67%) (0.9)	23 (42.59%) (5.2)	9 (16.67%) (-0.2)	82 (17.52%)
Total	300 (64.10%)	60 (12.82%)	54 (11.54%)	54 (11.54%)	468

FT3: free triiodothyronine; FT4: free thyroxine; TSH: thyroid-stimulating hormone; TT3: total triiodothyronine; TT4: total thyroxine.

Table 3: The levels of pituitary-thyroid axis hormones and autoantibodies in the serum of psoriasis patients.

	Psoriasis vulgaris	Pustular psoriasis	Erythrodermic psoriasis	Psoriatic arthritis
FT3 (pmol/L)	4.67 ± 0.60	4.23 ± 0.73	4.57 ± 0.76	4.45 ± 0.71
FT4 (pmol/L)	14.11 ± 2.23	13.68 ± 2.73	12.17 ± 2.57	14.18 ± 2.39
TSH (mIU/L)	1.89 ± 1.44	1.55 ± 1.12	1.63 ± 1.69	3.69 ± 1.48
TT3 (nmol/L)	1.77 ± 0.40	1.57 ± 0.40	1.76 ± 0.59	1.73 ± 0.43
TT4 (nmol/L)	104.05 ± 22.02	96.29 ± 25.67	81.07 ± 24.06	108.49 ± 22.33
TPOAb (U/mL)	75.72 ± 38.47	78.36 ± 43.73	87.23 ± 36.14	85.32 ± 18.18
TGAb (U/mL)	39.99 ± 27.86	46.55 ± 24.46	29.90 ± 23.45	26.97 ± 8.89

FT3: free triiodothyronine; FT4: free thyroxine; TSH: thyroid-stimulating hormone; TT3: total triiodothyronine; TT4: total thyroxine; TPOAb: thyroid peroxidase antibody; TGAb: thyroglobulin antibody.

and arthritis subsets. There was a statistically significant difference among the 4 psoriasis types in the proportion of patients with normal FT3, FT4, and TSH ($\chi^2 = 26.781$, $P < 0.001$). Post hoc analysis between the groups showed a higher proportion of patients with normal hormone levels in the vulgaris group and a higher proportion of patients with abnormal hormone levels in the erythrodermic group. There was a statistically significant difference among the 4 groups in the proportion of patients with decreased FT3 or FT4 but normal TSH ($\chi^2 = 29.816$, $P < 0.001$). Post hoc testing between the groups showed that this abnormality was more likely in the erythrodermic group than in the other 3 groups. Moreover, no statistically significant differences were observed among the 4 groups in the proportion of patients with normal FT3 and FT4 but decreased TSH ($\chi^2 = 2.126$, $P = 0.547$).

3.2. Levels of Pituitary-Thyroid Axis Hormone, TPOAb, and TGAb in Psoriasis Patients. Table 3 shows the FT3, FT4, TSH, TT3, and TT4 levels in patients with the 4 psoriasis types. FT3 levels were lower in pustular psoriasis patients, with a statistically significant difference compared to those in psoriasis vulgaris and erythrodermic psoriasis patients ($P = 0.040$). FT4 levels were lower in erythrodermic psoriasis patients compared to psoriasis vulgaris ($P < 0.001$), pustular psoriasis ($P = 0.019$), and arthritis patients ($P < 0.001$). TSH levels in arthritis patients were higher than those in erythrodermic patients ($P = 0.049$). The average TPOAb level in all groups was higher than normal values (Table 3). There were no significant differences in TPOAb or TGAb levels among the groups ($P > 0.05$).

Table 4: Cases with thyroid dysfunction among study participants.

	Patients ($N = 468$)	Controls ($N = 200$)	P value
Subclinical hyperthyroidism	25 (5.3)	8 (4)	0.043
Ab (+)	12 (2.6)	1 (0.5)	0.024
Ab (-)	13 (2.8)	7 (3.5)	NS
Clinical hypothyroidism	2 (0.4)	2 (1)	NS
Ab (+)	0	0	NS
Ab (-)	2 (0.4)	2 (1)	NS
Subclinical hypothyroidism	12 (2.6)	3 (1.5)	0.037
Ab (+)	7 (1.5)	1 (0.5)	0.03
Ab (-)	5 (1.1)	2 (1)	NS

NS: not significant; Ab (+): positive thyroid autoantiodies; Ab (-): negative thyroid autoantibodies. Numbers in parentheses represent percentages.

3.3. Correlation of Thyroid Dysfunction with Autoantibody Tests between Psoriasis and Controls. To confirm the correlation of thyroid dysfunction with autoantibody tests, we selected 200 age- and sex-matched subjects without psoriasis as controls. Percentage of thyroid dysfunction was similar

Table 5: Ultrasound tests of skin thickness in psoriasis patients.

	Psoriasis vulgaris ($n = 10$)	Erythrodermic psoriasis ($n = 3$)	Psoriatic arthritis ($n = 4$)
Plaque skin thickness	2.1 ± 0.5	1.9 ± 0.7	2.3 ± 0.6
TSH (mIU/L)	1.89 ± 1.44	1.75 ± 1.34	2.57 ± 1.02
TT3 (nmol/L)	1.36 ± 0.22	1.5 ± 0.80	1.2 ± 0.39
TT4 (nmol/L)	107.1 ± 10.6	79.07 ± 12.05	90.33 ± 26.80

between psoriatic patients and controls (Table 4). There were differences between subclinical hyperthyroidism or subclinical hypothyroidism patients and 200 controls in terms of positive autoantibodies.

3.4. Ultrasound Tests of Plaque Skin Thickness in Psoriasis Patients. The patients did not routinely undergo ultrasound tests; therefore, only 17 psoriasis patients (including 10 psoriasis vulgaris, 4 erythrodermic psoriasis, and 3 psoriatic arthritis) had ultrasound tests. We showed the plaque skin thickness by ultrasound in Table 5 and found no correlation of skin thickness with TSH, TT3, and TT4.

4. Discussion

Psoriasis patients are at a higher risk of other autoimmune diseases. In recent years, the relationship between psoriasis and Hashimoto's thyroiditis-related thyroid dysfunction has gained attention [7]. Hashimoto's thyroiditis can present as mild, short-term hyperthyroidism in the early stages but eventually progresses into hypothyroidism. There are many common pathophysiological mechanisms between psoriasis and Hashimoto's thyroiditis. Studies have shown that IFN-γ, Th1 cytokines, CXCL10, IL-23, and Th17 are involved in the pathogenesis of psoriasis. Hashimoto's thyroiditis is a disease also mediated by Th1 cells, in which IFN-γ and its associated chemokines, such as CXCL10, play an important role. IL-23 and Th17 levels are elevated in psoriasis and Hashimoto's thyroiditis, suggesting a relationship between the immunological pathogenesis of these diseases [8].

A recent cross-sectional retrospective study showed that Hashimoto's thyroiditis and psoriasis are highly correlated [9], especially in patients with psoriatic arthritis. Antonelli et al. [10] found an increased prevalence of thyroid autoimmunity in patients with psoriatic arthritis. In psoriatic arthritis patients, the rate of TPOAb positivity was significantly higher and similar to that in rheumatoid arthritis patients, an increase which was more pronounced in female patients [11]. However, the prevalence of subclinical hypothyroidism in the entire psoriatic arthritis group was similar to that in the rheumatoid arthritis and control groups, and only in female patients was the prevalence higher. Psoriatic arthritis patients with subclinical hypothyroidism have a longer course of disease and multiple joint involvement compared to psoriatic arthritis patients with normal thyroid function. In addition, Gul et al. [12] observed elevated FT4 levels in patients with psoriasis. However, another recent study has shown that no correlation exists between psoriasis and thyroid autoimmunity. [13] This study showed that the average level of TPOAb in the 4 groups of patients with different types of psoriasis was higher than the normal value, suggesting the presence of autoimmune damage to the thyroid in patients with psoriasis. Thyroid dysfunction existed to varying degrees among the 468 patients in this study, but thyroid function tended to be closer to normal in the psoriasis vulgaris patients compared to the other 3 groups. We found that FT3 levels were lower in pustular psoriasis patients and FT4 levels were lower in erythrodermic psoriasis patients. Although there was no significant change in FT3 and FT4 levels among the psoriatic arthritis patients, their TSH levels were elevated, which is consistent with the results of Antonelli et al. [10] In a study by Zoabi et al. [14], thyroid function tests were performed on 100 psoriasis patients and 54 healthy controls. There was no significant difference in thyroid function between the 2 groups, but TSH levels and positive autoantibody titers were higher in patients with severe psoriasis than in those with mild psoriasis. The reasons for these inconsistent results may be related to differences in the sample size, ethnicity, dietary habits, and living situations and may also be related to the severity and type of disease [15]. To confirm the correlation of between psoriasis and thyroid dysfunction, we selected age- and sex-matched subjects without psoriasis as controls. We found that there were differences between subclinical hyperthyroidism or subclinical hypothyroidism patients and controls in terms of positive autoantibodies.

The present study also found that FT3 or FT4 was decreased in patients with erythrodermic psoriasis, and the proportion of patients with normal TSH was as high as 42.59% [16]. This may be due to diffuse erythema and repeated shedding of scales in erythrodermic psoriasis patients, resulting in the loss of large amounts of water, protein, and other nutrients, causing water and electrolyte disturbances, metabolic abnormalities such as hypoproteinemia, and severe symptoms of systemic wasting. Therefore, patients may develop euthyroid sick syndrome, which presents as low T3 or low T4 syndrome and can be easily misdiagnosed as hypothyroidism. However, these results are yet to be confirmed by clinical data, and no studies on patients with psoriasis combined with euthyroid sick syndrome have been reported in the literature. It is generally believed that in euthyroid sick syndrome, the body compensates by reducing energy consumption while the patient is in a diseased state, indicating a period of serious illness. At this time, exogenous thyroxine replacement therapy alone may be of no benefit. After the disease improves, changes in thyroid

hormones should be observed and corresponding adjustments made. Therefore, patients with this type of psoriasis should be properly evaluated prior to treatment.

In summary, psoriasis and autoimmune thyroiditis-related thyroid dysfunction may be related to some extent and is associated with the severity and type of psoriasis. The limitations of this study were that this was a retrospective study, and patients do not routinely undergo ultrasound tests so that there were no results of thyroid B-scan ultrasound, pathology, or other diagnostic examinations. Only 17 psoriasis patients (including 10 psoriasis vulgaris, 4 erythrodermic psoriasis, and 3 psoriatic arthritis) had ultrasound tests. We showed the plaque skin thickness by ultrasound and found no correlation of skin thickness with TSH, TT3, and TT4. To elucidate the correlation between various thyroid function test indicators and psoriasis, prospective studies must be conducted in the future for further confirmation. The dominant response of Th1 cells and the high expression of related inflammatory factors appear in both psoriasis and autoimmune thyroiditis. This may be the immune mechanism common to both [14], but a larger sample size, prospective study basis, and more in-depth mechanistic investigation are required. An emphasis on follow-up assessment of thyroid function in psoriasis patients will be beneficial for the proper treatment of those patients with thyroid dysfunction.

Data Availability

The datasets used and/or analyzed during the current study are available from the corresponding author on reasonable request.

Conflicts of Interest

The authors declare no competing interests.

Authors' Contributions

Juan Du and Chunyue Ma contributed equally to this work.

Acknowledgments

This work was supported by the National Nature Science Foundation of China (81673081, 82003382) and Scientific Research Project of Shanghai Science and Technology Commission (Shanghai Natural Science Foundation-19ZR1407600).

References

[1] R. Parisi, D. P. Symmons, C. E. Griffiths, and D. M. Ashcroft, "Global epidemiology of psoriasis: a systematic review of incidence and prevalence," *The Journal of Investigative Dermatology*, vol. 133, no. 2, pp. 377–385, 2013.

[2] B. Szramka-Pawlak, E. Hornowska, H. Walkowiak, and R. Żaba, "Hope as a psychological factor affecting quality of life in patients with psoriasis," *Applied Research in Quality of Life*, vol. 9, no. 2, pp. 273–283, 2014.

[3] J. J. Wu, T. U. Nguyen, K. Y. Poon, and L. J. Herrinton, "The association of psoriasis with autoimmune diseases," *Journal of the American Academy of Dermatology*, vol. 67, no. 5, pp. 924–930, 2012.

[4] F. R. Ali and R. B. Warren, "Psoriasis and susceptibility to other autoimmune diseases: an outline for the clinician," *Expert Review of Clinical Immunology*, vol. 9, no. 2, pp. 99–101, 2013.

[5] P. Caturegli, A. De Remigis, and N. R. Rose, "Hashimoto thyroiditis: clinical and diagnostic criteria," *Autoimmunity Reviews*, vol. 13, no. 4-5, pp. 391–397, 2014.

[6] S. K. Raychaudhuri, E. Maverakis, and S. P. Raychaudhuri, "Diagnosis and classification of psoriasis," *Autoimmunity Reviews*, vol. 13, no. 4-5, pp. 490–495, 2014.

[7] S. R. Khan, A. Bano, M. Wakkee et al., "The association of autoimmune thyroid disease (AITD) with psoriatic disease: a prospective cohort study, systematic review and meta-analysis," *European Journal of Endocrinology*, vol. 177, no. 4, pp. 347–359, 2017.

[8] A. Antonelli, S. M. Ferrari, A. Corrado, A. di Domenicantonio, and P. Fallahi, "Autoimmune thyroid disorders," *Autoimmunity Reviews*, vol. 14, no. 2, pp. 174–180, 2015.

[9] T. Kiguradze, F. M. Bruins, N. Guido et al., "Evidence for the association of Hashimoto's thyroiditis with psoriasis: a cross-sectional retrospective study," *International Journal of Dermatology*, vol. 56, no. 5, pp. 553–556, 2017.

[10] A. Antonelli, A. Delle Sedie, P. Fallahi et al., "High prevalence of thyroid autoimmunity and hypothyroidism in patients with psoriatic arthritis," *The Journal of Rheumatology*, vol. 33, no. 10, pp. 2026–2028, 2006.

[11] Z. Yu and H. Sendong, "Comparative efficacy and safety of high-viscosity versus low-viscosity bone cement in the treatment of osteoporotic vertebral fractures," *Indian Journal of Pharmaceutical Sciences*, vol. 20, no. s2, p. 12, 2020.

[12] U. Gul, M. Gonul, I. Kaya, and E. Aslan, "Autoimmune thyroid disorders in patients with psoriasis," *European Journal of Dermatology*, vol. 19, 2009.

[13] E. Vassilatou, E. Papadavid, P. Papastamatakis et al., "No association of psoriasis with autoimmune thyroiditis," *Journal of the European Academy of Dermatology and Venereology*, vol. 31, no. 1, pp. 102–106, 2017.

[14] A. Zoabi, M. Ziv, D. Rozenman, and R. Lovoshitski, "Prevalence of thyroid abnormalities among psoriatic patients," *Harefuah*, vol. 151, no. 10, 2012.

[15] I. Ruffilli, F. Ragusa, S. Benvenga et al., "Psoriasis, psoriatic arthritis, and thyroid autoimmunity," *Front Endocrinol*, vol. 8, 2017.

[16] B. A. Moharram, A. A. al-Doaiss, H. M. al-Mahbashi et al., "Hepatoprotective, antioxidant and cytotoxic potential of aloe niebuhriana latex extract from Yemen," *Indian Journal of Pharmaceutical Sciences*, vol. 82, no. 3, pp. 514–521, 2020.

Hindawi
Scanning
Volume 2021, Article ID 1167221, 8 pages
https://doi.org/10.1155/2021/1167221

Research Article

Evolution of MSCP-Enabled Healthcare Ecosystem: A Case of China

Yang Liu and Liwei Tian

School of Information Engineering, Shenyang University, Shenyang 110044, China

Correspondence should be addressed to Liwei Tian; tlw@syu.edu.cn

Received 1 July 2021; Accepted 2 August 2021; Published 24 August 2021

Academic Editor: Qiao Yanxin

This paper considers a case that Chinese healthcare organizations in China leverage mobile smart cloud platform (MSCP) to build a self-sustaining healthcare ecosystem, which presents an evolutionary process of three phases. Multiple elements have been involved in the system, which has reinforced one another. Finally, an ecosystem is formed, which is economically sustainable and scalable nationwide. The study adds to the understanding of the ecosystem-based approach to address complex problems. It offers important implications for designing healthcare MSCPs which may help transform the healthcare industry.

1. Introduction

As is well known, China is the most populous country in the world as well as one of the fastest-growing markets in the world. At present, China's healthcare industry is facing many problems that other developed countries faced in the past or are even facing to this day. In terms of China's social environment, the issue of an aging population is worsening (China is the only country with more than 100 million elderly persons and the largest aging population in the world), the number of people with chronic diseases continues to increase, and people's health management awareness has been increasing as well. In the industrial environment, the high concentration of high-quality medical resources is concentrated in few big cities. The whole country faces the challenges of unbalanced structure of healthcare service system, inefficient implementation of graded medical services, shortage of healthcare workers, increasing medical costs, and inefficient risks of implementing national medical insurance system which have exacerbated the existing crisis in China's healthcare service industry. There are information and communication technologies (ICTs) and Internet-enabled solutions to these issues. As an example, the mobile smart cloud platform (MSCP) has been used to improve healthcare services, including, e.g., in professional online healthcare treatment, health counseling, and telemedicine services for outpatients.

In the 1980s, countries like the UK started to promote the use of Internet-based technologies in healthcare. As an example, a doctor can track and provide consultation to his patients equipped with intelligent wearable devices when locating at home or in public places [1]. In October 2014, China's first online hospital was born in Guangdong Province. Since then, the Internet healthcare entrepreneurs have mushroomed. In just one year until the end of 2016, more than 10 online hospitals have emerged, some with different labels like cloud hospitals and Internet hospitals. The fast growth of Internet healthcare industry in China is based on a supportive policy and technology environment; Internet healthcare services have been included in the "13th Five-Year Plan" as an industrial organization; "smart healthcare" is the use of digital, visual mode, vital sign collection, and health monitoring to achieve the sharing and rational distribution of healthcare resources. The information and communication technologies (ICTs) and Internet technologies including sensor technology, wearable smart devices like mobile phones, mobile and WiFi technologies, deep learning technologies, big data, and cloud computing enable quick access to a broader range of information and services.

Table 1: Interview arrangements.

Interviewees	Interview topics
10 patients	Patient satisfaction as a measure of whether a mobile health ecosystem is a net-positive system
6 healthcare service providers	Relevant technologies for each mode of healthcare service delivery and their relationship with other actors within the platform
4 developers of the SMCP	Key inflection points in the strategy, and each supporting technology and the stage of the activity
2 managers of health insurance agency	The positive elements for cooperating with the healthcare service platform
6 government officers	Their motivation and demand for setting up the healthcare service platform

This paper focuses on MSCP in healthcare from the ecosystem perspective. The ecosystem concept was initially used to analyze the applications of ICTs, which involved the collaboration of a broad range of actors [2]. In recent years, the term of service ecosystem is introduced, academics insist on service-led (SD) logic, placing services at the core of ecosystems, which is composed of social actors and their respective resources, linked together by value propositions across a network of relationships [3, 4]. Within this system, stakeholders form a unitary, interrelated, collaborative, and competitive community which promotes the added value of products and services. Healthcare represents a service ecosystem which included multiple social actors and is more complex than a simplistic consideration of the doctor-patient model. The healthcare service ecosystem is composed of heterogeneous and complementary entities such as patients, doctors, equipment suppliers, pharmaceutical companies, insurance companies, and public health authorities [5, 6]. They form an interconnected and interdependent organism. Each actor in the ecosystem exerts its core strengths and works together with others to sustain the system. The system is dynamic. It evolves by phases and finally achieves sustainability. A broader perspective is also necessary to understand how ecosystems evolve, which takes into account all the roles and interrelationships involved in the infrastructure, policies, and regulations required, promotion mechanisms and sustainability approaches, cultural values, interconnections with external factors, and so on.

This article focuses on MSCP-enabled ecosystem in healthcare, a kind of service ecosystem, which takes the healthcare cloud service as the core asset, connects the stakeholder of healthcare through internet technology, forms a virtual organism that interacts with each other and promotes each other, the social actors that depended on each other, seeks the dynamic balance of the system in the competition, and finally realized the value increment of the whole system. Through a case study, we will address such a research question: at the macro-, meso-, or microlevels, how do relevant societal actors collaborate to use MSCP to form a healthcare ecosystem?

2. Research Methods

To understand the evolution of healthcare service ecosystems, we consider a pioneering case of MSCP based healthcare project in China. A case study design is proper for addressing how to type research question.

The research originated from the author's participation in the healthcare project, which was initiated by the healthcare authority of A City, and entrusted B Company and P University to develop a mobile smart cloud platform (MSCP) in the way of school-enterprise cooperation. Company B is willing to share the relevant information of the smart healthcare project. City A is a second-tier city located in the south-central region. The rural population is mostly, and the city's information base is weaker than that of developed cities along the eastern coast. In order to test the MSCP platform, the government healthcare administrations in City A established 24 small-scale healthcare clinics and identified 6 medium-scale basic hospitals and 1 large-scale and high-level hospital as pilot healthcare institutions. Through the analysis of the case, we can explore the use of a mobile intelligent cloud platform to build a self-sustaining healthcare ecosystem for similar cities in China. In order to solve the problems of reducing healthcare costs, making up for healthcare shortcomings, adjusting the structural distribution of healthcare resources, etc., the first experience and revelation are provided. To collect data, we carried semistructured interviews with sponsors and leaders of the project to develop a preliminary understanding of the various stages through which MSCP has progressed. The interviews help us to understand the key actors in the healthcare ecosystem, including patients, healthcare service providers, health insurance agencies, and government healthcare administrations. Among them, the healthcare service providers include the local doctor in the small-scale healthcare clinics, online doctors in the medium-scale basic hospitals, the specialist doctors in the large-scale and high-level hospitals, pharmaceutical companies, healthcare equipment companies, and third-party developers. Before each interview, the researcher would carefully design an outline according to relevant research questions and who the interviewee was. After the outline was laid out, the interview was recorded for future analysis. After the interview was conducted, the recorded file would be transcribed into a text summary and issued an identification number. The field interview process began in January 2017 and concluded in December 2017, covering 28 interviewees. The interview arrangements are illustrated in Table 1. In the process of data analysis, we kept contact with interviewees and would consult them when any concerns emerged.

Except for interviews, there are mainly two data sources: internal documents including the project implementation plan and project process documentation; data from online channels such as the government authorities' websites and news media. In order to improve the reliability and validity

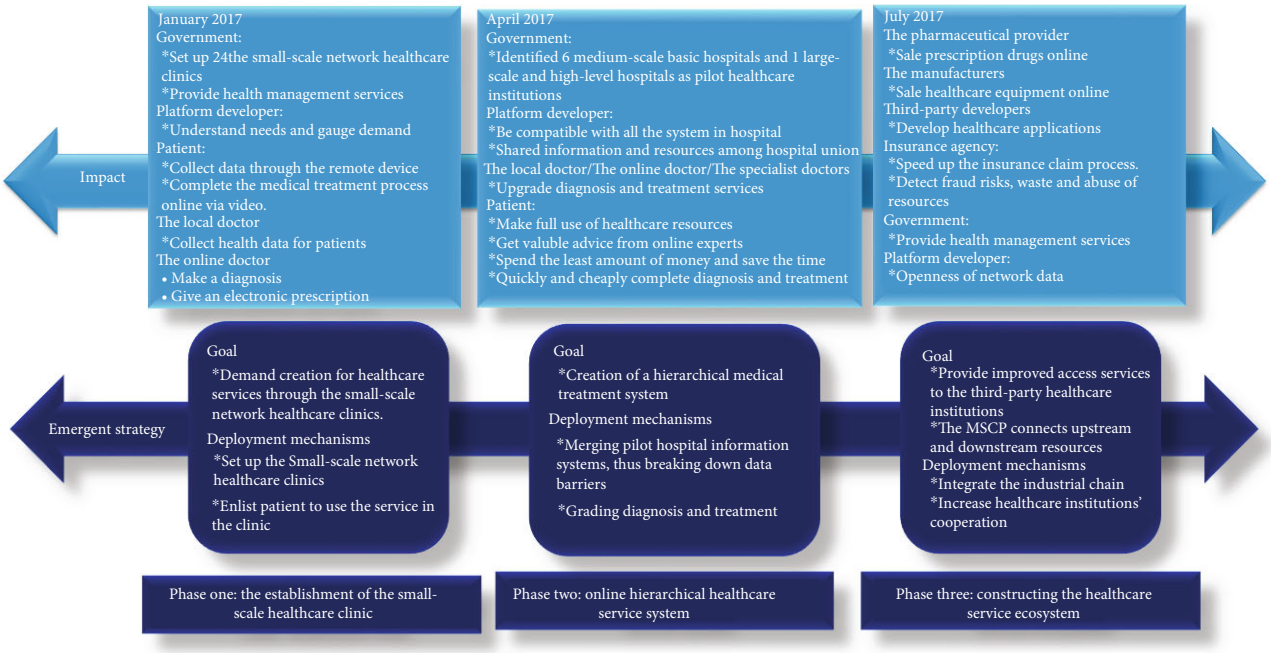

Figure 1: Evolution of MSCP-enabled ecosystem.

of the research results [7], researchers implemented a triangulation approach to cross-validate key information from multiple sources.

3. The Emergence of an MSCP-Enabled Healthcare Ecosystem

The case study results are summarized in Figure 1. The healthcare service ecosystem supported by MSCP has progressed through three significant phases since its inception. In the first stage, it assessed the existing demand for technology-enabled services to establish MSCP, and the small-scale network healthcare clinics are being built to complete the information collection and transformation for MSCP. The second phase expanded the service coverage to a larger area through integrating the small-scale network healthcare clinics, the medium-scale basic hospitals, and the large-scale and high-level hospitals, which established a hierarchical healthcare treatment pattern by MSCP. In the third phase, participants from diverse and complementary sectors in the healthcare field were also integrated into the platform ecosystem to develop collaboratively.

3.1. The First Stage: The Establishment of the Small-Scale Healthcare Clinics. In January 2017, MSCP engaged with the doctor in the medium-scale basic hospitals and all the patients to understand their needs and gauge demand for the platform. In this stage, the doctors in 6 medium-scale basic hospitals can diagnose online by the MSCP platform, and 24 small-scale healthcare clinics were established in urban residential communities and rural areas according to the geographical division. The telemedicine equipment was set up, with the help of the local doctor in the small-scale healthcare clinics, patients used telemedicine equipment to collect health data and complete the process of seeking healthcare treatment directly with online doctors in the medium-scale basic hospitals by video. This new healthcare pattern diagnosed diseases through remote consultation, remote ECG, remote imaging, and remote inspection and gives an electronic prescription online; at the same time, a personal electronic health archive was established. Services provided by small-scale healthcare clinics to patients through the platform include generation and cancellation of appointments online, telemedicine, home health monitoring, self-care, health training, health management, first aid nursing, and public health information. Patients can receive health check-ups via the small-scale healthcare clinics as well. In the same time, the MSCP's extended functions include treatment through prevention and rehabilitation of chronic diseases including providing health assessments, health interventions, and health promotion services. Customer-downloaded apps may be used to guide patients with reasonable exercise, diets, accommodations, and so on.

Technically, the small-scale healthcare clinics are characterized by the large number and wide geographic distribution. Due to the small flow of patients and the small amount of data in a single small-scale healthcare clinic, the SSL VPN is the simplest and safest solution to the remote user access data. The medium-scale basic hospitals are characterized by the small number and a larger flow of patients. Due to a large amount of data, the connection stability requirements, the IPSec VPN is the main mode of connection, which is a relatively complete system of VPN technology and provides a series of protocol standards.

In the first stage, MSCP provides technology to extend the healthcare service of the medium-scale basic hospitals to the small-scale healthcare clinics through MSCP. The government healthcare administrations in City A established 24

small-scale healthcare clinics. Patients can be treated directly by the doctor online via video. The local doctors in the small-scale network healthcare clinics help patients collect and monitor all kinds of health indicators through physical examinations and offer daily health management services, general health management, and disease prevention for a subhealth population. The online doctors in the medium-scale basic hospitals undertake outpatient clinical services online, make a diagnosis, and give an electronic prescription according to the patient's own description of the illness, the test results collected by telemedicine equipment. Patients and doctors establish cooperative relationships to cope with the disease and complete the online diagnosis and treatment process.

As a result, the treatment of common diseases, frequently occurring diseases, and chronic diseases can be achieved online at local small-scale healthcare clinics. 80-90% of patients with diseases can be treated remotely online via the platform, without going to the large-scale and high-level hospitals.

In village clinics, I can communicate with a doctor from the network hospital conveniently. I do not need to worry about to travel to a faraway big hospital for a small health problem. (Patient)

The patients can be diagnosed and treated in their own community hospital and directly take needed medicine or injections, they can skip going to a big hospital to wait in line and conduct various tests, which saves the time and energy. (Online doctor)

The patients suffering from chronic diseases such as diabetes mellitus and hypertension can conduct real-time examinations directly from community hospitals and collect health indicators to complete the referral rehabilitation without traveling to a large hospital far away. (Online doctor)

3.2. The Second Stage: The Establishment of Online Hierarchical Healthcare Service System. In April 2017, the large-scale and high-level hospitals were connected to the MSCP in this stage. The online hierarchical healthcare service system was established based on MSCP, which consisted of with the small-scale network healthcare clinics, the medium-scale basic hospitals, and the large-scale and high-level hospitals, which established the division and cooperative relations, and healthcare resources could be reasonably distributed. Patients can be registered into the system, and prediagnosis will be based on the patient's conditions when finding a suitable healthcare service provider. After the patient's initial visit, they will receive diagnostic results back online and complete their referral remotely. The hospital decentralization has been promoted, and the patient resources of big hospitals have been diverted according to the graded diagnosis and treatment system. Only patients with critical illness need to be hospitalized at the large-scale and high-level hospitals, thereby relieving workloads in the large-scale and high-level hospitals, which can concentrate on research and healthcare services for difficult diseases. The MSCP can provide data sharing and assist hospitals at all levels to implement linkages throughout the network, including remote consultation and healthcare service/supply exchanges. In-person healthcare services would be extended to all levels of health institutions' network via the Internet and a proprietary app.

Technically, the healthcare information system of every given pilot hospital will be transformed to accommodate the MSCP. One common information standard should be constructed to merge pilot hospital information systems and break down data barriers. Existing healthcare information systems were independently constructed by major hospitals. They need to conform to a new standard so that data would be transferable throughout the new system. Process management through business process reengineering and optimization is conducted. Issues arising from discrepancies in personnel, assets, business management, patient service, and online interaction with healthcare insurance agencies between each location have been addressed. Utilizing data exchange technology, the original HIS, LIS, PACAS, and EHR systems of the pilot hospitals were connected to the MSCP. Based on unified data standards, the data could be merged successfully. Information and resources may be effectively shared among all-level hospitals. The large-scale and high-level hospitals are also characterized by a relatively small number and a larger flow of patients. Due to a large amount of data, taking into account the demand for image data sharing, the flow is 5 to 10 times of the general small-scale healthcare clinics and the medium-scale basic hospitals; the connection mode is dominated by MPLS VPN. MPLS VPN refers to the use of MPLS technology to build enterprise IP network to achieve cross-regional, security, high-speed, reliable multiservice high-quality communication methods.

In the second stage, the government healthcare administrations in City A identified 6 medium-scale basic hospitals and 1 large-scale and high-level hospital as pilot healthcare institutions. MSCP provides technology to be compatible with all the systems in all-level hospitals and establishes the online hierarchical healthcare service system. For rare cases of illness, the specialist doctors in the large-scale and high-level hospitals would be responsible for the diagnosis and treatment of critically ill patients and the guidance of basic hospitals and the patients can get valuable advice from well-known experts in the large-scale and high-level hospitals. The patients could spend the least amount of money and time to make full use of healthcare resources of the online hierarchical healthcare service system. The doctors in all levels of hospitals aim to achieve up and down linkages and upgrade diagnosis and treatment services for the patients.

The patients can make full use of the large-scale and high-level hospitals and expert medical staff throughout the network to share healthcare resources. (Local doctor)

For rare cases of illness, the patients can get valuable advice from well-known experts in the large-scale and high-level hospitals. (Online doctor)

I can quickly and cheaply choose the best diagnosis and treatment using the online system. (Patient)

Technically, the healthcare information system of every given pilot hospital will be transformed to a given hospital's healthcare information system which is usually built internally by the hospital, causing such systems to be incompatible with one another. A comprehensive system would

improve the overall work efficiency of healthcare staff and managers. (Developer of the SMCP)

The establishment of unified data standards is conducive to the sharing of information and resources of the online hierarchical healthcare service system. (Developer of the SMCP)

3.3. The Third Stage: Constructing the Healthcare Service Ecosystem. In July 2017, the MSCP provided improved access services, software services, hardware services, and platform services to the third-party healthcare institutions, integrates the hospital resources, and gradually opens up the upstream and downstream resources such as pharmaceutical provider, manufacturers of the healthcare equipment, third-party developers of healthcare cloud services, healthcare insurance agencies, and government health administrations. The functions of MSCP transformed traditional professional solutions to the healthcare service ecosystem step by step. The industrial chain is integrated into the system to improve the wealth of wisdom within the healthcare service platform's service portfolio and increase healthcare institutions' cooperation in the field of development.

The drug and the equipment decentralization have been pushed forward; the process of medicine, healthcare equipment, and diagnostics are separated. MSCP also provides medical big data for government healthcare administrations and healthcare insurance agencies. The medical big data obtained through personal electronic health archive include drug data, clinical medical data, healthcare expenses and healthcare insurance fund data, and personal health management data. Applications developed by third-party developers based on market demand can be directly released to users on the cloud service platform, or services to support the background of the cloud service platform management system.

In the third stage, the pharmaceutical provider is allowed to sell prescription drugs to patients online. The manufacturers of the healthcare equipment could sell healthcare equipment online to patients and all-level hospitals. MSCP provides the openness of technological interfaces and freely accessible data on cloud service platforms to all actors in the healthcare service ecosystem. Third-party developers develop healthcare applications which meet market demand, in turn, improve the quality of services provided on the platform. The government healthcare administrations will provide policy support, strengthening healthcare quality management, healthcare procedure assessment, and healthcare outcome assessment going forward using MSCP in building a self-sustaining online ecosystem. The government health administrations at all levels of cities, districts, and county administration can provide health management services through dynamic collection, analysis, and evaluation of residents' daily health data, control the spread of epidemics more quickly by monitoring infectious diseases early on, at the same time, scientifically assess healthcare expenses, quality measures, control healthcare facility costs, and ensure healthcare service quality. The healthcare insurance agencies may formulate the reimbursement policy for drugs on the market based on the outcome of treatment and its corresponding social and economic benefits, detect fraud risks, waste, and abuse of resources, and help speed up the healthcare insurance claim process. The patients could get more convenient and efficient service from other actors in the healthcare service ecosystem.

MSCP will eventually form a self-evolving and self-enriching healthcare service ecosystem of its own, leading to new wisdom in the realm of healthcare applications and business models. The establishment of the healthcare service ecosystem can free up precious healthcare resources and push efficiency to a greater extent, helping to solve problems within healthcare equality applications and business models. The establishment of the healthcare service ecosystem can free up precious healthcare resources and push efficiency to a greater extent, helping to solve problems within healthcare equality.

After the patient completes the online diagnosis and treatment process, purchases the medicine directly online according to the electronic prescription, it is very convenient. (Pharmaceutical provider)

SMCP have opened to healthcare equipment suppliers, including sensor technology manufacturers and health measurement equipment manufacturers to provide more accurate and higher-quality services for hospitals at all levels. (Manufacturers of the healthcare equipment)

Relying on the open interface of the healthcare service platform, openness of network data, and so on, healthcare applications with nuanced functions may be developed in line with demand. These applications can be released directly to members of the service platform or simply utilize the service platform as back-end infrastructure. (Third-party developers)

The current direction of development of healthcare services should be from high-quality healthcare resources concentrated in the large-scale and high-level hospitals to the medium-scale basic hospitals, ending at the small-scale network healthcare clinics. (Government Officers)

The healthcare service industry has gradually changed its direction from government control to the market. (Government Officers)

Collaboration between doctors and hospitals is seen as a means of improving the quality and efficiency of care, which can create a personalized experience for patients. (Government Officers)

The process of providing healthcare services starts with traditional treatment as the core, and then, it gradually develops to include the entire industrial healthcare chain such as prevention and rehabilitation. (Government Officers)

We can obtain medical data from the MSCP and develop the new insurance products and find new customers. (Manager of the healthcare insurance agencies)

The medical data can help us promptly detect fraud risks, waste, and abuse of resources and speed up the healthcare insurance claim process. (Manager of the healthcare insurance agencies)

The cost of health management services will be paid by all levels of government, along with a gradual increase in the number of the small-scale network healthcare clinic associated with telemedicine technology, which is expected to account for 65% of the total healthcare costs. (Government Officers)

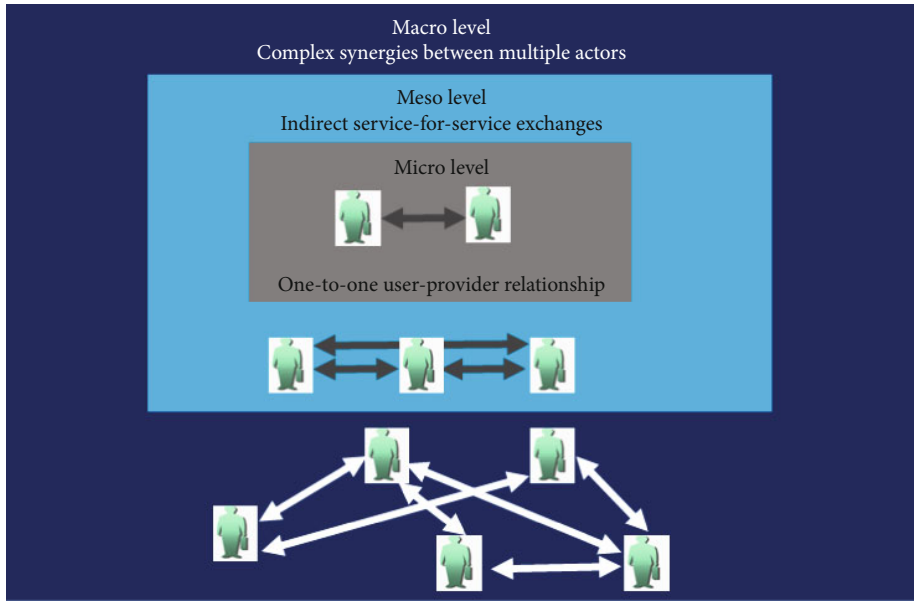

Figure 2: The service ecosystem levels.

4. Discussion: The Collaboration between the Relevant Actors to Enable a Healthcare Service Ecosystem

The study discusses below how the relevant actors of the ecosystem address complex issues in healthcare in a coordinated manner. It offers important implications for designing healthcare MSCPs which may help transform the healthcare industry by suggesting a blueprint for the implementation of a sustainable healthcare service ecosystem.

The service ecosystem is proposed to consider as the micro-, meso-, and macrolevels which are shown in Figure 2, in which the interacting actors share and exchange their resources to adapt to the environment and coevolve [8]. The structure of the service ecosystem was constantly changed and adapted to achieve a long-lasting well-being. At the microlevel, interactions mainly involve the one-to-one user-provider relationship, which may be understood as a direct service-for-service exchange. At the mesolevel, indirect service-for-service exchanges occur, which are realized through triadic relationships between dyads of actors [9–11]. Synergies between multiple actors may occur in the macrolevel, and all actors comply with specific norms and rules to establish a cooperative environment [12].

In the studied case, this paper has documented the emergence and evolution of the MSCP-enabled healthcare service ecosystem, which evolved in three phases and integrated relevant actors in complementary fields, including patients, healthcare service providers, health insurance agencies, and government health administrations [13]. Among them, the healthcare service providers include online doctors, local doctors, pharmaceutical provider, and manufacturers of the healthcare equipment and third-party developers of healthcare cloud services. All actors in the MSCP-enabled healthcare service ecosystem in China have impacting factors at three levels.

At the microlevel, the actors include patients, local doctors, and online doctors. According to Akaka and Chandler [14], interactions mainly involve the one-to-one user-provider relationship. Patients (aka the "user") are the heart of the healthcare service ecosystem, who utilize the applications provided by the platform to establish effective relationships such as the communication and exchange mechanism with the doctor online. Healthcare service providers ("Provider," in this stage) include online doctors and local doctors. Understanding the roles and responsibilities of resource-sharing actors is important in appreciating current and potential relationships within the ecosystem. From an ecosystem perspective, there is a certain degree of interdependence between service providers and users; in this case, the local doctors and the online doctors are responsible for providing patients with various healthcare services by MSCP's application, simplify the diagnosis and treatment process, relieve the doctor's work pressure, and address a critical need of the patients; a cooperative relationship can be established to cope with illness, thus participating in the design and delivery of care for future iterations [15]. At the same time, the patients' satisfaction is regarded as a measure of whether MSPC is a net-positive system. The MSCP-enabled healthcare ecosystem is sustainable when it is designed at the microlevel.

At the mesolevel, drawing on the conceptual framework proposed by Tsiotsou [11], indirect service-for-service exchange is concerned. The actors include pharmaceutical provider, manufacturers of the healthcare equipment, and third-party developers of healthcare cloud services, who are responsible for providing patients with various healthcare service applications directly and have close interactions with patients. With the reduction of intermediate links, more benefits are obtained, the demand of the actors at mesolevel is met through the MSCP, the viability of the business model received further pragmatic validation, and MSCP is proved to be more sustainable.

At the macrolevel, the multiple participants may be expanded to involve government health administrations, and health insurance agencies [16]. They determine funding allocation and healthcare policy formulation, which can impact the operations of healthcare organizations. The main purpose of these actors is to increase the friendliness of the healthcare service ecosystem and make the effective and rational use of healthcare resources by patients. These actors directly influence the behaviors of patients and healthcare service providers at both the micro- and mesolevels. If the effects are positive, it will stimulate these agencies to adhere to an ecosystem perspective at the strategic and operational level, smoothing the transition going forward [17]. As the scale of the healthcare service ecosystem continues to grow, each actor in the ecosystem has gained more value, further enhancing its sustainability.

Practice actors at three levels interact to build the MSCP-enabled healthcare service ecosystem. In each level, the number and types of actors engaged in healthcare services, as well as the breadth of services provided, differ. Multiple elements of the ecosystem have progressively evolved and reinforced one another to create a dynamic system. The case MSCP ecosystem in China is economically sustainable and scalable and can accelerate transformation.

5. Conclusion

The case study suggests that the mobile smart healthcare cloud platform could enable the development of an ecosystem capable of unleashing multipronged, integrated improvements to address complex problems, which would help address the increasingly serious service crisis and promote the evolution and restructuring of the healthcare industry in developing countries. The case study offers insights into the evolution of the MSCP, enabling a healthcare service ecosystem of key actors and their impact. This paper offers an empirical inquiry into the process of healthcare ecosystem evolution and its consequences in an effort to uncover the value added by technologically enhanced healthcare services, which is based on Internet ICTs, at the same time, which has conducted the healthcare service ecosystem to direct the future medical model and shift focus towards development. In future research, we should focus on the formation of such an ecosystem, which requires efforts from multiple actors (e.g., patients, doctors, healthcare providers, insurance companies, and government healthcare administrations); actors who operate within the healthcare system create value at different ecosystem levels; they strengthen each other through their cooperation, each leveraging its core competencies, but doing so in collaboration with others for self-sustaining, maximum impact.

Data Availability

The datasets used and/or analyzed during the current study are available from the corresponding author on reasonable request.

Conflicts of Interest

It is declared by the authors that this article is free of conflict of interest.

Acknowledgments

This work was supported by the Scientific Research Project of Liaoning Province under Grants No. 2017104005 and Liaoning Province Innovative Talent Support Program No. LR201861.

References

[1] Y. Hui, "BT: building an ecosystem and promoting medical informatization," *Telecom World*, vol. 8, pp. 61–61, 2012.

[2] A. Tiwana, B. Konsynski, and A. A. Bush, "Research commentary—platform evolution: coevolution of platform architecture, governance, and environmental dynamics," *Information Systems Research*, vol. 21, no. 4, pp. 675–687, 2010.

[3] P. Frow, J. R. McColl-Kennedy, T. Hilton, A. Davidson, A. Payne, and D. Brozovic, "Value propositions," *Marketing Theory*, vol. 14, no. 3, pp. 327–351, 2014.

[4] S. L. Vargo and R. F. Lusch, "Institutions and axioms: an extension and update of service-dominant logic," *Journal of the Academy of Marketing Science*, vol. 44, no. 1, pp. 5–23, 2016.

[5] S. L. Vargo and R. F. Lusch, "It's all B2B…and beyond: Toward a systems perspective of the market," *Industrial Marketing Management*, vol. 40, no. 2, pp. 181–187, 2011.

[6] J. R. McColl-Kennedy, S. L. Vargo, T. S. Dagger, J. C. Sweeney, and Y. Van Kasteren, "Health care customer value cocreation practice styles," *Journal of Service Research*, vol. 15, no. 4, pp. 370–389, 2012.

[7] T. Tamm, P. Seddon, and G. Shanks, "Pathways to Value from Business Analytics," in *Thirty Fourth International Conference Information Systems*, Milan, 2013.

[8] M. A. Akaka and S. L. Vargo, "Extending the context of service: from encounters to ecosystems," *Journal of Services Marketing*, vol. 29, no. 6/7, pp. 453–462, 2015.

[9] L. Chen and X. Xu, "Effect evaluation of the long-term care insurance (LTCI) system on the health care of the elderly: a review," *Journal of Multidisciplinary Healthcare*, vol. Volume 13, pp. 863–875, 2020.

[10] X. Wang, P. Gao, Y. Liu, H. Li, and F. Lu, "Predicting thermophilic proteins by machine learning," *Current Bioinformatics*, vol. 15, no. 5, pp. 493–502, 2020.

[11] R. H. Tsiotsou, "A service ecosystem experience-based framework for sport marketing," *The Service Industries Journal*, vol. 36, no. 11-12, pp. 478–509, 2016.

[12] S. Rozenes and Y. Cohen, *Handbook of Research on Strategic Alliances and Value Co-Creation in the Service Industry*, IGI Global, Hershey, PA, 2017.

[13] Y. Liu, A. Li, G. Xie, G. Liu, and X. Hei, "Computational methods and online resources for identification of piRNA-related molecules," *Interdisciplinary sciences: computational life sciences*, vol. 13, no. 2, pp. 176–191, 2021.

[14] M. Archpru Akaka and J. D. Chandler, "Roles as resources: a social roles perspective of change in value networks," *Marketing Theory*, vol. 11, no. 3, pp. 243–260, 2011.

[15] J. E. Epping-Jordan, S. D. Pruitt, R. Bengoa, and E. H. Wagner, "Improving the quality of health care for chronic conditions," *Quality and Safety in Healthcare*, vol. 13, no. 4, pp. 299–305, 2004.

[16] P. Frow, J. R. McColl-Kennedy, and A. Payne, "Co-creation practices: their role in shaping a health care ecosystem," *Industrial Marketing Management*, vol. 56, pp. 24–39, 2016.

[17] R. Adner, "Ecosystem as structure," *Journal of Management*, vol. 43, no. 1, pp. 39–58, 2017.

Hindawi
Scanning
Volume 2021, Article ID 8231559, 10 pages
https://doi.org/10.1155/2021/8231559

Research Article

Cholecystokinin Expression in the Development of Myocardial Hypertrophy

Zhongshu Han,[1] Sheng Bi,[2] Yongsheng Xu,[3] Xiaoying Dong,[1] Lixia Mei,[4] Hailong Lin,[5] and Xueqi Li[1]

[1]*Department of Cardiology, Harbin Medical University Fourth Hospital, Harbin 150086, China*
[2]*Department of Critical Care Medicine, Affiliated Qiqihar Hospital, Southern Medical University (The First Hospital of Qiqihar), Qiqihar 161005, China*
[3]*Department of Anesthesiology, Affiliated Hospital of Qingdao University, Qingdao 266000, China*
[4]*Department of Ultrasonic Medicine, Affiliated Qiqihar Hospital, Southern Medical University (The First Hospital of Qiqihar), Qiqihar 161005, China*
[5]*Department of Cardiology, Central Hospital of Dalian, Dalian 116003, China*

Correspondence should be addressed to Xueqi Li; john.christian@bellevuecollege.edu

Received 10 June 2021; Accepted 6 August 2021; Published 23 August 2021

Academic Editor: Qiao Yanxin

Background. Expression of cholecystokinin is found in myocardial tissues as a gastrointestinal hormone and may be involved in cardiovascular regulation. However, it is unclear whether there is an increase in cholecystokinin expression in myocardial hypertrophy progression induced by abdominal aortic constriction. The study is aimed at exploring the relationship between cholecystokinin expression and myocardial hypertrophy. *Methods*. We randomly divided the 70 Sprague-Dawley rats into two groups: the sham operation group and the abdominal aortic constriction group. The hearts of rats were measured by echocardiography, and myocardial tissues and blood were collected at 4 weeks, 8 weeks, and 12 weeks after surgery. Morphological changes were assessed by microscopy. The cholecystokinin expression was evaluated by immunochemistry, Western blotting, quantitative real-time polymerase chain reaction, and enzyme-linked immunosorbent assay. *Results*. The relative protein levels of cholecystokinin were significantly increased in the abdominal aortic constriction groups compared with the corresponding sham operation groups at 8 weeks and 12 weeks. The cholecystokinin mRNA in the abdominal aortic constriction groups was significantly higher than the time-matched sham operation groups. Changes in the left ventricular wall thickness were positively correlated with the relative protein levels of cholecystokinin and the mRNA of cholecystokinin. *Conclusions*. The development of myocardial hypertrophy can affect the cholecystokinin expression of myocardial tissues.

1. Introduction

The heart is not only a contractile organ but also an endocrine organ. There is evidence that the cardiomyocytes produce a variety of peptide hormones, such as the natriuretic peptides [1], parathyroid hormone-like protein [2], endothelin [3], and relaxin [4]. These hormones affect the function of the cardiovascular system. A recent study has found that gastrointestinal hormones are associated with the change of the heart's structure and function [5], and CCK is one of these gastrointestinal hormones. It is made up of 33 amino acids, and all biological activity is present in the C-terminal octapeptide fragment. It initially extracts from the upper segment of the intestine of the gut [6]. The study showed that cardiomyocytes could produce the classic intestinal hormone cholecystokinin (CCK) in amounts comparable to natriuretic prohormones, and CCK was found in the lung, kidney, gastrointestinal tract, and brain later [7].

The abnormal cardiomyocytes can induce the expression of CCK. The study found that CCK expression in the postinfarction heart failure (HF) group was higher than that in the sham group. So, HF can induce the expression of CCK [8]. Whether hypoxia caused by myocardial infarction can affect the expression of CCK? The study reported that acute

myocardial hypoxia increases the BNP mRNA contents in porcine heart muscle [9]. However, using the myocardial hypoxia model, there was no significant different in the expression of pro-CCK between the myocardial hypoxia groups and the control groups, so myocardial hypoxia does not affect the expression of CCK in myocardial tissues [10]. From the above description, we know that HF can lead to high CCK expression, the feature is similar to an increase in the BNP caused by HF. The part of HF develops from myocardial hypertrophy (MH) caused by the high-pressure load of the heart. The expression of CCK in MH tissue is not clear.

In this study, we applied a rat model of (4-12 weeks) abdominal aortic constriction- (AAC-) related cardiac pressure overload with morphological changes of MH, to systematically investigate CCK expression in the MH tissue.

2. Methods

The study was performed in accordance with the Guide for the Care and Use of Laboratory Animals published by the US National Institutes of Health (NIH Publication No. 85-23, revised 19-96). The experiment protocols were approved by the Research Ethics Committee of Harbin Medical University Fourth Hospital.

2.1. Rat Model of MH. 70 male Sprague-Dawley rats (weighing 310-330 g, 11-13 weeks of age) were purchased from the Animal Experimental Center of the Second Affiliated Hospital of Harbin Medical University; the number of rats was determined by preliminary experiment. Rats were free to eat and drink. 4 rats were put in a cage with the room temperature at 22°C and room humidity 50 ± 5%, maintained on 12 hours light/dark cycles for 7 days before surgery.

We made a rat model of MH by abdominal aortic constriction operation as described previously [11] with a few modifications. The animals were randomly divided into two groups: (1) the sham operation (sham) group ($n = 30$), in which the surgical procedure of AAC was performed in the same way except for ligation of the abdominal aorta, and (2) the AAC group ($n = 40$), in which the surgical procedure of AAC was performed by ligation of the abdominal aorta 5 mm above the branching of the right renal artery to induce pressure overload of the heart. The rats were well anesthetized with 4% pentobarbital sodium (40 mg/kg, intraperitoneal injection) and placed on the operating table. Skin preparation and iodine disinfection were carried out on the abdomen of the rats. An incision of about 2.0 cm was made on midline's left side, and the abdominal cavity was opened layer by layer. The intestines were pushed to the right side of the abdominal cavity, while the stomach was pushed upwards to expose the abdominal aorta (5 mm above the right renal artery branches). A needle (0.7 mm in diameter) was laid alongside the abdominal aorta, and they were bundled together with a surgical suture (0.3 mm in diameter); the needle was taken out. Internal organs were restored, and penicillin (200,000 U) was infused into the abdominal cavity. The abdominal wall was sutured layer by layer. The rats were kept warm until they were awake. During the next 7 days, the rats were given penicillin (200,000 U/day) by intraperitoneal injection. All surgeries were performed using sterile techniques. For the sham group, in addition to the abdominal aorta was not bundled, other steps are the same. 12 rats died of surgery. Surviving rats of the sham group were randomly assigned into 4 weeks sham group (9 rats), 8 weeks sham group (9 rats), and 12 weeks sham group (10 rats); surviving rats of the AAC group were randomly assigned into 4 weeks AAC group (10 rats), 8 weeks AAC group (10 rats), and 12 weeks AAC group (10 rats).

2.2. Echocardiography. The rats were anesthetized and prepared skin and applied an ultrasonic coupling agent to the abdomen. The systolic cardiac function and the dimension of heart's left ventricular were measured 4 weeks, 8 weeks, and 12 weeks after surgery by two-dimensional echocardiography (SONOS 7500, Philips) fitted with a 12-MHz transducer. The operator of an ultrasonic machine was blinded to the sham and ACC groups. Data were recorded as the mean of at least three consecutive cardiac cycles. The parameters recorded included left atrial diameter (LA), interventricular septal thickness at end-diastole (IVSd), left ventricular end-diastolic posterior wall thickness (LVPWd), left ventricular end-systolic diameter (LVDs), left ventricular end-diastolic diameter (LVDd), left ventricular fractional shortening (LVFS), and the left ventricular ejection fraction (LVEF).

2.3. The Blood Sample Collection. The blood samples of rats from each group were obtained from the carotid artery on the operating table after rats were well anesthetized with 4% pentobarbital sodium (40 mg/kg, intraperitoneal injection). Blood samples were centrifuged at 3000 x g for 15 min, and then, the plasma was collected for measurement and stored at -20°C.

2.4. Procedure of Euthanasia. After euthanasia using an overdose of pentobarbital, the breathing and heartbeat of the rats stopped, and the pupils dilated.

2.5. The Myocardial Tissue Sample Collection. The hearts from rats of sham groups and ACC groups were excised and irrigated with cold saline solution after rats were euthanized. Each heart weight (HW) was obtained by high-accuracy electronic scale. Subsequently, the ratio of heart weight to body weight (HW/BW) was calculated. A portion of the myocardial tissues was fixed in 4% paraformaldehyde for histological analysis, another portion was stored in liquid nitrogen for Western blotting (WB), and the remaining myocardial samples were saturated in RNA later Stabilization Solution (Thermo Fisher Scientific, Massachusetts, USA) and stored at -80°C.

2.6. Morphological Changes in the Myocardium. Myocardial tissue samples were fixed in formaldehyde and embedded in paraffin. After that, they were cut into 5 μm thick sections and stained with hematoxylin and eosin (H&E) to analyze myocardial morphology and Masson's trichrome to evaluate the severity of myocardial fibrosis. Their pathological slides were randomly selected from three rats in each group for myocardial morphological analysis.

Table 1: Sequences of primers used for qPCR.

CCK-F	5′-GTG CTG AGG ACT ACG AAT ACC-3′
CCK-R	5′-GAA ACA TTG CCT TCC CAC-3′
CCKAR-F	5′-CTG GGA TTG TGA TGG TGG TG-3′
CCKAR-R	5′-GCA AGT AAC AGC CAT CAC TAT CC-3′
CCKBR-F	5′-TAA GAA GCG GGT GGT GCG AATG-3′
CCKBR-R	5′-ACA AGC AGA GAC GTA GCT CAG CAAG-3′
GAPDH-F	5′-ATG CCG CCT GGA GAA ACC-3′
GAPDH-R	5′-GCA TCA AAG GTG GAA GAA TGG-3′

F: forward; R: reverse.

2.7. Quantitative Real-Time PCR for CCK Expression Measurements. CCK mRNA expression levels in the left ventricle myocardial tissue were detected by quantitative real-time polymerase chain reaction (qPCR). RNA was extracted from myocardial tissues using a high pure RNA isolation kit (Roche, Basel, Switzerland) according to manufacturer's protocol. Transcriptor Reverse Transcriptase (Roche, Basel, Switzerland) and Protector RNase Inhibitor were used to synthesize cDNA. Fast Start Universal SYBR Green Master (Roche, Basel, Switzerland), cDNA templates, and specific primers were mixed, and amplification was performed using Step One Plus™ PCR system (Applied Biosystems, Foster, CA, USA). The sequences of the primer were listed in Table 1. GAPDH was used as an internal standard. The program was comprised of 95°C for 10 min, followed by 40 cycles at 95°C for 15 s, and 60°C for 1 min. The relative expression levels of CCK were determined using the $2^{-\triangle\triangle Ct}$ method.

2.8. Immunohistochemistry (IHC) for CCK Expression Measurements. The myocardial tissue samples were fixed with 4% paraformaldehyde, embedded in paraffin, and then, sectioned at a thickness of 4 μm. The sections were subsequently deparaffinized and rehydrated, after that they were incubated with a rabbit anti-rat polyclonal antibody against CCK (EterLife, Birmingham, UK) diluted 1 : 100 overnight at 4°C. The sections were then counterstained with hematoxylin and observed under the microscope (Leica DM4B, Germany).

2.9. WB for CCK Expression Measurements. To measure endogenous CCK expression levels, myocardial tissues were ground and homogenized with a protein lysis solution (Sclarbio, China). Briefly, the frozen myocardium stored in liquid nitrogen was homogenized in RIPA lysis buffer (RIPA) with a protease inhibitor cocktail (Roche, South San Francisco, CA, USA) using a tissue grinder. The mixture was centrifuged at 12,000 rpm for 15 min at 4°C. Supernatants were obtained and assayed for total protein using the BCA method (Beyotime biotechnology, China). Equivalent amounts of protein were resolved on 15% Trisglycine sodium dodecyl sulphate (SDS) polyacrylamide gels and transferred to nitrocellulose membranes. After blocking in 5% dried milk in Tris-buffered saline containing Tween-20 for 1 h at room temperature, membranes were incubated for 24 h at 4°C with one of the following antibodies: anti-CCK polyclonal antibody (Santa Cruz Biotechnology, USA) and anti-GAPDH (ZSGB-BIO, China) to obtain the proteins levels. Membranes were incubated with horseradish peroxidase-conjugated donkey anti-rabbit or anti-mouse immunoglobulin (1 : 5,000; ZSGB-BIO, China) for 1 h at room temperature. All images were captured using the enhanced chemiluminescence Western blotting detection system (ChemiDoc XRS+, Bio-Rad, USA) and analyzed by densitometry. The optical density values were normalized to that of GAPDH.

2.10. Enzyme-Linked Immunosorbent Assay (ELISA) for CCK Expression Measurements. Plasma CCK levels were obtained by using enzyme-linked immunoassay kits (#JL11700, Jianglai Biological, China), according to manufacturer's protocol. The lower limit of detection for CCK was 1.0 pg/ml.

2.11. Statistical Analysis. Statistical analysis software was IBM SPSS 23 Statistics (IBM, Armonk, New York, USA). Data were assessed for normality using the Kolmogorov-Smirnov test. The results are presented as mean values ± standard deviation (SD). Statistical analysis of sham groups and AAC groups were performed using independent samples t-tests or Mann-Whitney test. Statistical analysis of three different groups at three-time points in AAC groups was performed using ANOVA or the Kruskal-Wallish; multiple comparison tests were performed using Mann-Whitney U or SNK-q ($a = 0.05$). Spearman's correlation coefficient was applied to study the associations between CCK expression and left ventricular wall thickness. All tests were two-sided, and the statistical significance was defined as $P < 0.05$.

3. Results

3.1. Body Weight and Cardiac Structural Parameters. From the postoperation of AAC to the end of the experiment, there were 6 rats without MH, including 2 rats in the 4 weeks AAC group, 3 rats in the 8 weeks AAC group and 1 rat in the 12 weeks AAC group, 6 rats died, including 1 rat in the 4 weeks AAC group, 1 rat in the 8 weeks AAC group, 2 rats in the 12 weeks sham group, and 3 rats in the 12 weeks AAC group; they were excluded from the study. The remaining 45 rats completed the whole experiment, including 9 rats in the 4 weeks sham group, 7 rats in the 4 weeks AAC group, 9 rats in the 8 weeks sham group and 6 rats in the 8 weeks AAC group and 8 rats in the 12 weeks sham group, and 6 rats in the 12 weeks AAC group. To observe the progression of MH, the hearts of rats were measured by echocardiography. The photo of the M-mode echo-cardiogram indicated (Figure 1) that significant MH was present in the AAC groups of 4 weeks, 8 weeks, and 12 weeks, but the sham group has not changed. The results of the cardiac parameters (Table 2) showed that BW in the AAC group was lower than that in the time-matched group at 4 weeks ($P < 0.05$), 8 weeks ($P < 0.01$), and 12 weeks ($P < 0.01$); HW/BW, LVDs, and LVDd of AAC groups were significantly higher compared with time-matched sham groups ($P < 0.01$, 0.05, 0.05, respectively) at 4 weeks. The HW/BW, IVSd, and LVPWd were significantly higher compared with the time-matched sham groups ($P < 0.01$, $P < 0.01$, and $P < 0.01$, respectively) at 8

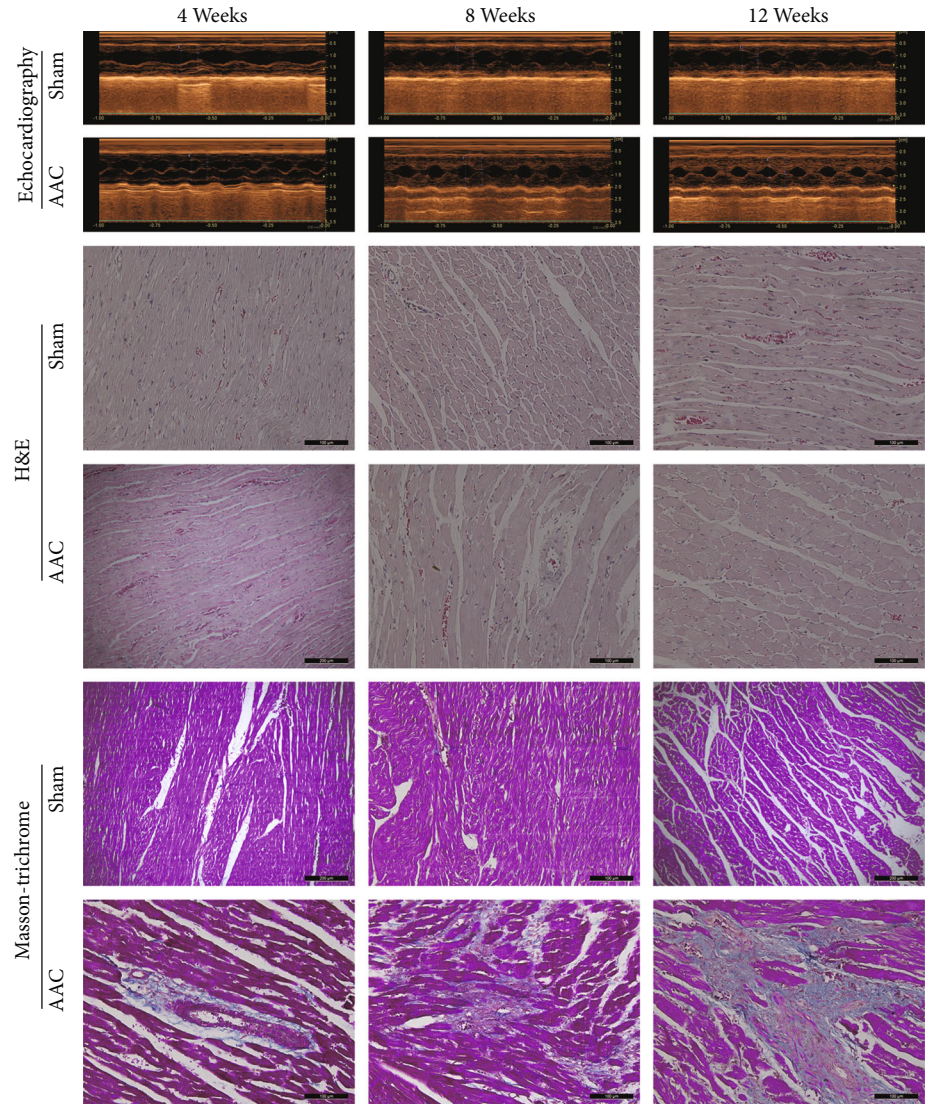

Figure 1: Echocardiography and pathological examination of rat heart. Echocardiography (first and second panels), H&E (third and fourth panels), and Masson's trichrome (fifth and sixth panels) staining of myocardial tissues at 4, 8, and 12 weeks after surgery. Sham: sham operation group; AAC: abdominal aortic constriction; H&E: haematoxylin and eosin. Pathological images were photographed at ×200 magnification.

weeks and 12 weeks. LVDd in 12 weeks AAC group was higher than that in 12 weeks sham group ($P < 0.05$). No significant differences in LA (4, 8, and 12 weeks), IVSd (4 weeks), LVDs (8, 12 weeks), LVDd (8 weeks), LVPW (4 weeks), LVEF (4, 8, and 12 weeks), and LVFS (4, 8, and 12 weeks) were observed between sham group and AAC group.

3.2. Pathological Changes of Myocardial Tissue. H&E and Masson's trichrome staining showed (Figure 1) that significantly increased myocyte size and myocardial interstitial fibrosis was present in the AAC groups at three different time points. Moreover, the MH and myocardial interstitial fibrosis in 8 weeks and 12 weeks AAC groups were severer than in the 4 weeks AAC group. Sham groups had not changed.

3.3. Detection of CCK Expression by Immunohistochemical Staining in Myocardial Tissue. CCK was detected by immune-histochemical staining. CCK antibody used in the experiment was polyclonal antibody. Its method was similar to the previous study about CCK expression in the development of postinfarction heart failure [5]. Expression of CCK was observed in myocardial myofilaments and the nucleus. The expression of CCK was obviously enhanced on the myocardial horizontal stripes, and the expression of CCK was distributed as a "finger pattern" in myocardial tissue under the microscope. The expression of CCK in the nucleus edge was stronger than that in other parts of the nucleus. Staining for CCK was significantly higher in 4 weeks, 8 weeks, and 12 weeks ACC groups compared with those in the corresponding sham groups (Figure 2).

3.4. Expression of CCK and CCK mRNA in Myocardial Tissue. The relative protein level was measured by WB. CCK antibody used in the experiment was polyclonal

Table 2: Body weight and echocardiographic evaluation of heart at 4 weeks, 8 weeks, and 12weeks after surgery.

	4 weeks Sham	ACC	8 weeks Sham	ACC	12 weeks Sham	ACC
BW (g)	438.11 ± 15.94	418.00 ± 19.21*	551.00 ± 35.04	494.33 ± 23.63**	607.00 ± 25.85	512 ± 15.59**
HW/BW (mg/g)	3.31 ± 0.05	3.77 ± 0.31**	3.95 ± 0.27	4.84 ± 0.52**	3.80 ± 0.21	4.54 ± 0.58**
LA (mm)	3.48 ± 0.50	3.79 ± 0.59	3.62 ± 0.81	4.13 ± 0.60	4.56 ± 0.80	4.82 ± 0.55
IVSd (mm)	1.88 ± 0.58	2.32 ± 0.26	2.19 ± 0.60	3.10 ± 0.35**	2.32 ± 0.34	3.32 ± 0.25**
LVDs (mm)	2.16 ± 0.24	2.48 ± 0.25*	2.15 ± 0.40	2.14 ± 0.78	2.37 ± 0.29	2.37 ± 0.47
LVDd (mm)	4.89 ± 0.62	5.52 ± 0.49 ∗	5.48 ± 0.72	5.54 ± 0.47	6.05 ± 0.38	6.31 ± 0.72*
LVPWd (mm)	2.44 ± 0.84	3.23 ± 0.60	2.31 ± 0.47	3.63 ± 0.57**	2.78 ± 0.42	3.97 ± 0.44**
LVEF (%)	90.45 ± 1.74	90.14 ± 1.95	93.22 ± 2.59	93.50 ± 5.17	93.63 ± 1.60	93.83 ± 3.31
LVFS (%)	54.89 ± 2.57	54.86 ± 3.93	60.56 ± 6.42	64.67 ± 9.75	60.75 ± 4.77	61.83 ± 8.89

Data was presented as the mean ± standard deviation (SD). Sham: sham operation group; AAC: aortic artery constriction; BW: body weight; HW: heart weight; LA: left atrial diameter; IVSd: end-diastolic interventricular septal thickness; LVDd: left ventricular end-diastolic diameter; LVDs: left ventricular end-systolic diameter; LVPWd: left ventricular end-diastolic posterior wall thickness; LVEF: left ventricular ejection fraction; LVFS: left ventricular short-axis f-ractional shortening. $^{*}P < 0.05$, $^{**}P < 0.01$, compared with the time-matched sham groups.

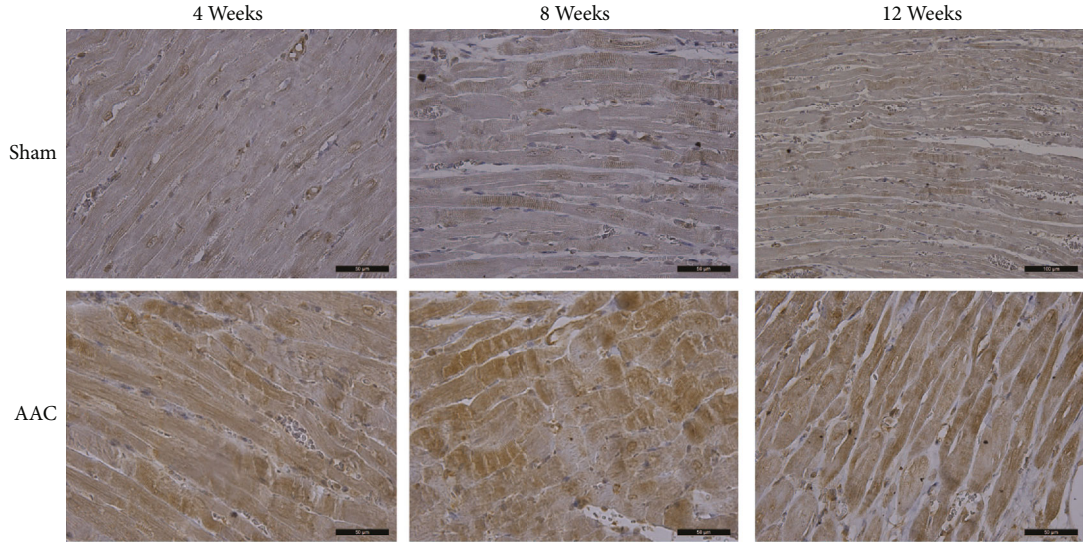

Figure 2: CCK expression levels were detected by immunohistochemical staining (×400 magnification). Sham: sham operation group; AAC: abdominal aortic constriction.

antibody. The relative protein level of CCK was significantly higher in 8 weeks and 12 weeks AAC groups than that in the corresponding sham groups ($P < 0.01$ and $P < 0.05$, respectively). Nevertheless, there was not difference between sham and AAC group at 4 weeks. The relative protein level of CCK in the 4 weeks AAC group was less than that in 8 weeks and 12 weeks AAC groups ($P < 0.05$). Quantitative analysis of CCK mRNA showed that CCK mRNA was significantly higher in 4 weeks, 8 weeks, and 12 weeks AAC groups than that in the corresponding sham groups ($P < 0.01$, $P < 0.01$, and $P < 0.01$, respectively). CCK mRNA levels were significantly different from each other in 4 weeks, 8 weeks, and 12 weeks AAC groups ($P < 0.05$) and showed a gradually increasing trend with time (Figure 3).

3.5. Measurement of Plasma CCK Levels. Plasma CCK levels were measured by ELISA (Figure 3), which showed that plasma CCK levels were not different between the sham and AAC group at 4, 8, and 12 weeks.

3.6. Associations between the Expression of CCK and Left Ventricular Wall Thickness. The left ventricular wall thickness was represented by IVSd and LVPWd measured by echocardiography. The correlation between CCK levels and left ventricular wall thickness was showed in the indicated figure (Figures 4 and 5). IVSd was positively correlated with the CCK mRNA levels ($P < 0.001$) and the relative protein level of CCK ($P < 0.001$) (Figure 4). LVPWd was positively correlated with the CCK mRNA levels ($P < 0.001$) and the relative protein level of CCK ($P < 0.001$) (Figure 5).

4. Discussion

Myocardial hypertrophy is induced by heart overload and characterized by increased myocyte size and the incrassate

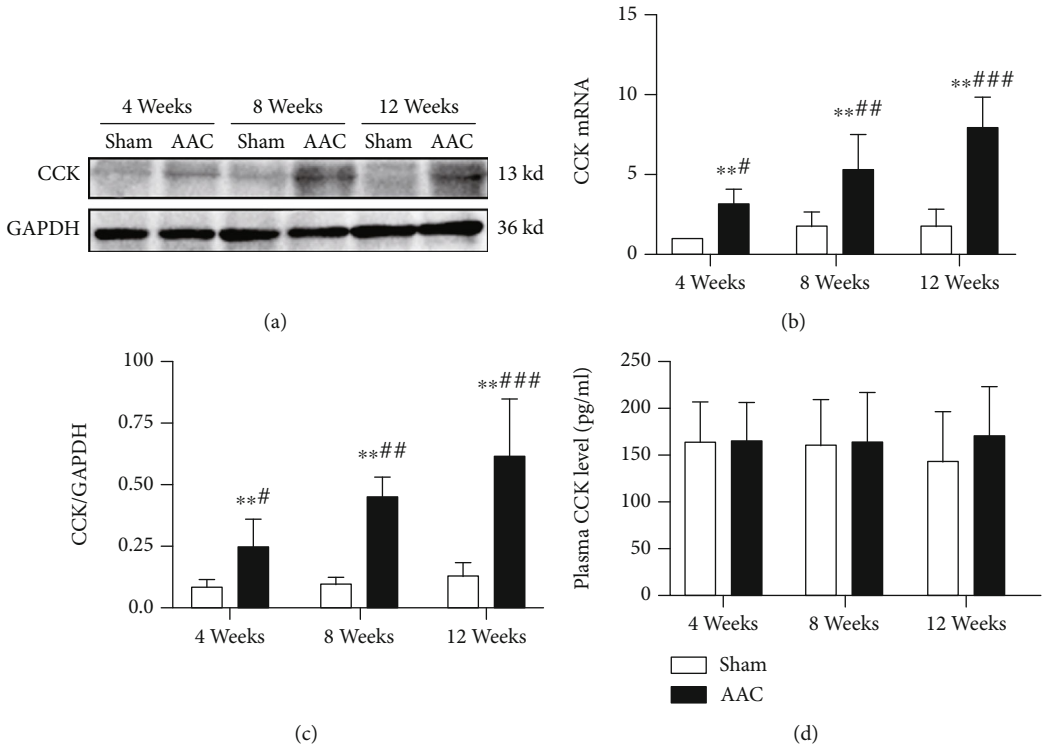

Figure 3: The myocardial tissues of the left ventricular were collected and analyzed by RT-PCR and Western blotting; the plasma samples were collected at the end of experiment and analyzed by ELISA. (a) Analysis of CCK and GAPDH protein expression from myocardial tissues of the left ventricular by Western blotting. (b) Bar graph shows levels of CCK mRNA in myocardial tissue. (c) Bar graph shows relative intensity of CCK to GAPDH in myocardial tissue. (d) The bars indicate the plasma CCK levels. CCK: cholecystokinin; GAPDH: glyceraldehyde-3-phosphate dehydrogenase; ELISA: enzyme-linked immunosorbent assay; sham: sham operation group; AAC: abdominal aortic constriction. $^{*}P < 0.05$, $^{**}P < 0.01$, compared with sham groups at the same time point; $^{\#}P < 0.01$, versus the 8 weeks and 12 weeks. AAC groups; $^{\#\#}P < 0.01$, versus the 4 weeks and 12 weeks AAC groups; $^{\#\#\#}P < 0.01$, versus the 4 weeks and 8 weeks AAC groups; $^{\&}P < 0.01$, versus the 8 weeks and 12 weeks AAC groups.

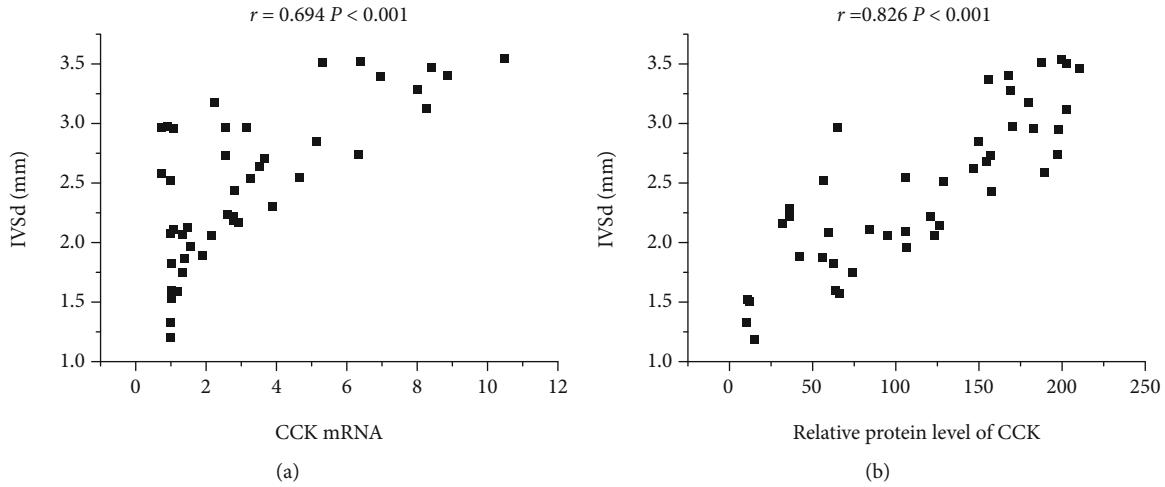

Figure 4: Associations between expression of IVSd and C-CK in model rat. (a) Correlation between IVSd and CCK mRNA ($r = 0.694$, $P < 0.001$); (b) correlation between IVSd and relative protein level of CCK ($r = 0.826$, $P < 0.001$). CCK: cholecystokinin; IVSd: end-diastolic interventricular septal thickness.

cardiac wall and thought to be an adaptive response to cardiac wall stress resulting from the cardiac pressure afterload and volume overload, including hypertension [12], aortic constriction [13, 14], and valve regurgitation [15, 16]. MH is first described by Cotton in 1914 [17]. With the increasing understanding of MH, we find that if the underlying causes of MH are not removed. It can eventually develop into HF, leading to death from HF. The clinical study also reported MH is

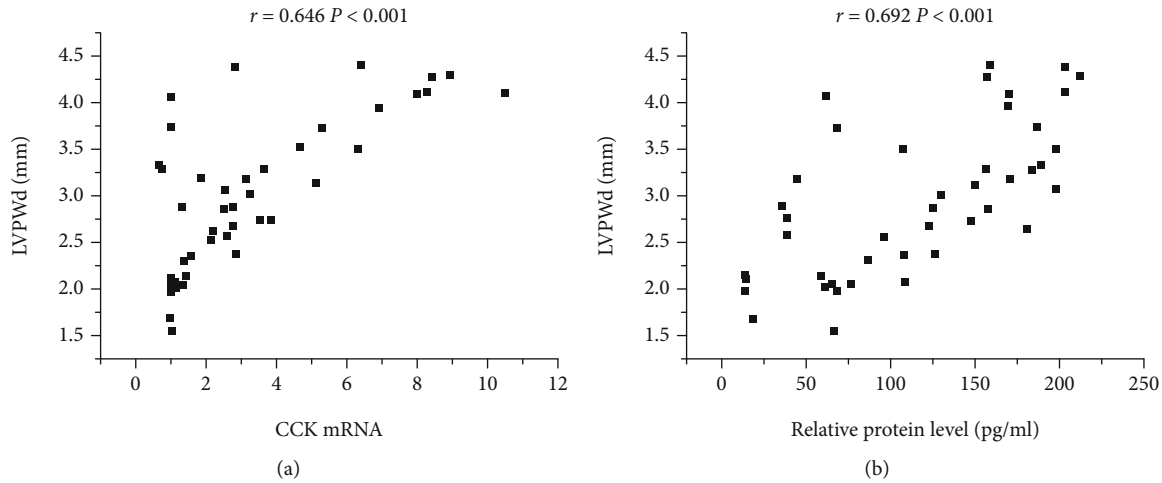

Figure 5: Associations between expression of LVPWd and CCK in model rat. (a) Correlation between LVPWd and CCK mRNA ($r = 0.646$, $P < 0.001$); (b) Correlation between LVPWd and relative protein level of CCK ($r = 0.692$, $P < 0.001$). CCK: cholecystokinin; LVPWd: left ventricular end-diastolic posterior wall thickness.

associated with morbidity and mortality of patients [18]. As research has progressed, we have found that many factors are related to MH and affect the process of MH, such as sex difference [19], fat diet [20], testosterone [21], angiotensin II [22], isoproterenol [23], and leptin [24].

CCK has various chemical structures, such as CCK-58, CCK-33, CCK-22, CCK-8, and CCK-4, and they work by stimulating the corresponding receptors for CCK [25]. CCK has many biological functions, mainly stimulating the secretion and synthesis of pancreatic enzymes, enhancing the secretion of pancreatic bicarbonate, stimulating gallbladder's contraction and odil sphincter relaxation and the secretion of liver bile, and regulating the movement of the small intestine and colon.

CCK appears to have several effects on the cardiovascular system, although the mechanisms underlying these effects remain unknown [26]. Some studies have shown that CCK is involved in regulating blood pressure and improving heart function [27–29]. In 1998, Zou et al. inserted an end hole PE-50 catheter into heart's left ventricle through the left jugular artery. Left ventricular wall motion modes were recorded during the intravenous administration of CCK-8. The results show the intravenous CCK-8 affected cardiac function [30], and the pretreatment with proglmide (nonselective CCK antagonist; 30 mg/kg; i.p.) causes a further decrease of blood pressure in endotoxic shock, most likely through the CCK AR/BR, which is expressed on cardiac myocytes [31, 32]. Therefore, the relationship between CCK and heart is worthy of further study.

In this study, we produced an MH model of a rat by AAC. The hearts of rats were measured by echocardiography 4, 8, and 12weeks after an operation. We found that IVSd and LVPWd were significantly higher compared with the time-matched sham groups ($P < 0.01$, $P < 0.01$, $P < 0.01$, respectively) at 8 weeks and 12 weeks, but no significant differences in IVSd and LVPW between sham group and AAC group 4 weeks after the operation. The rat hearts were obtained 4, 8, and 12 weeks after the operation and be sliced for H&E and Masson's trichrome staining. H&E and Masson's results showed that significantly increased myocyte size and myocardial interstitial fibrosis were present in the AAC groups at three different time points. Moreover, the MH and myocardial interstitial fibrosis in 8 weeks and 12 weeks AAC groups were severer than in the 4 weeks AAC group; however, sham groups had not changed. Although no difference in ventricular wall thickness (IVSd and LVPWd) was found by echocardiography between AAC and sham 4 weeks after the operation, the size of myocytes of AAC was more than that of sham, and myocardial tissues had obvious fibrosis 4, 8, and 12 weeks after the operation. So, the heart had become hypertrophy 4 weeks after the operation.

CCK in myocardial tissue was detected by IHC. We found that CCK expression in AAC was higher than that in sham 4, 8, and 12 weeks after the operation, and CCK expression was higher in AAC groups compared with sham groups and showed a gradual increase following the change of time in AAC groups. The expression of CCK detected by IHC was consistent with that by WB, but CCK expression detected by WB is not different between the AAC group and sham group at 4 weeks; it may be related to insufficient samples. These results show that MH can affect the expression of CCK.

The known hormonal CCK peptides in the brain and intestine, i.e., α-amidated and tyrosyl-sulfated CCK-58, CCK-33, CCK-22, and CCK-8, were detected only in negligible trace amounts, indicating that only little pro-CCK in the normal heart is processed to α-amidated CCK peptides, which regulate gallbladder emptying, and pancreatic enzyme secretion, and which act as potent neurotransmitters in the central and peripheral nervous systems [33]. On the contrary, we found a considerable amount of CCK expression from the heart in this study. The reason may be related to the antibody used. The antibodies used in IHC and WB were polyclonal antibodies with poor specificity. So, CCK detected by IHC and WB could be pro-CCK. Quantitative analysis of CCK mRNA showed that CCK mRNA was significantly

higher in 4 weeks, 8 weeks, and 12 weeks AAC groups than in the corresponding sham groups. CCK mRNA levels were significantly different in 4 weeks, 8 weeks, and 12 weeks AAC groups and showed a gradually increasing trend with time. It indicated that MH could induce the transcription and synthesis of CCK mRNA.

CCK can express in myocardial tissue, but the cause of CCK expression is not clear. A previous report demonstrated that cardiac CCK gene expression in vitro and in vivo is stimulated by isoprenaline [34], which has a strong excitatory effect on β-adrenoceptors, and leads to cardiac contraction, an increase in heart rate, and sympathetic excitation; this report reflected that expression of CCK is associated with sympathetic activity. Jens P. Goetze's study found the duodenal.

CCK mRNA did not change 5 h after the rats were injected intraperitoneally with isoprenaline. In contrast, the cardiac CCK mRNA increased by 5-fold [10, 35]. Therefore, isoproterenol can induce high expression of cholecystokinin in myocardial tissues by stimulating β-adrenergic receptors. Liu et al.'s study found that the serum norepinephrine level in rats with myocardial hypertrophy was higher than those in control groups 2, 3, and 4 weeks after AAC operation, and it may be related to autonomic excitation induced by AAC operation and pressure overload of the heart [36]. So, MH induced the secretion of catecholamine, which lead to the expression of CCK and transcription of CCK mRNA. However, it was possible that there were other undiscovered causes involved in CCK expression in myocardial tissue.

The clinical study showed the plasma CCK levels were associated with cardiovascular mortality in elderly female patients [8, 37]. Recent animal studies have shown that high expression of CCK can be seen in HF rat myocardial tissue, and the concentration of CCK in plasma of heart failure model rats is higher than that of the non-HF group [5, 22]. In this study, the plasma CCK detected by ELISA is derived from the gastrointestinal tract and the heart. We found that the plasma CCK level was not different between the sham and AAC group at 4, 8, and 12 weeks. The results indicated that little amount of CCK synthesized by the heart could not affect the plasma CCK level during MH. So, the plasma CCK cannot be used as a biomarker for MH.

The correlation analysis indicated that the IVSd and LVPWd were a high-positive correlation with relative protein expression of CCK and CCK mRNA levels in AAC groups. These results suggested that MH can affect the expression of CCK in myocardial tissues, but the mechanism is unclear.

Results from rats with MH provided the basic experimental data and evidence for further studies of CCK in myocardial tissue. The mechanism is not clear, so it deserves further investigation.

5. Limitations of the Study

Firstly, we were unable to distinguish CCK from pro-CCK. Secondly, we did not investigate whether CCK was involved in the development of MH. In addition, it had not been identified which subtype of CCK was associated with MH. Further investigations are required to elucidate the specific mechanism of MH affecting CCK expression.

6. Conclusion

In conclusion, our study finds that the development of MH induced by AAC can affect the CCK expression of myocardial tissues.

Abbreviations

CCK: Cholecystokinin
ACC: Abdominal aortic constriction
MH: Myocardial hypertrophy
HF: Heart failure
HW: Heart weight
IVSd: Interventricular septal thickness at end-diastole
LVDd: Left ventricular end-diastolic dimension
LVDs: Left ventricular end-systolic dimension
LVPWd: Left ventricular posterior wall thickness at end-diastole
LVEF: Left ventricular ejection fraction
LVFS: Left ventricular factional shorting
IHC: Immunohistochemistry
WB: Western blotting
qPCR: Quantitative real-time polymerase chain reaction.

Data Availability

The datasets used and/or analyzed during the current study are available from the corresponding author on reasonable request.

Ethical Approval

The experiment protocols were approved ahead of a performance by the Committee on Ethics of Animal Experiments of Harbin Medical University.

Conflicts of Interest

The authors declare that they have no competing interests.

Authors' Contributions

ZH, XL, SB, BC, and XD are responsible for the conception and design; ZH, YS, and SB for raising animal and animal models of cardiac pressure overload; ZH, BC, and XD for the echocardiographic examination; ZH and SB for blood sampling and measurements of plasma CCK; ZH, SB, and YS for determining the ratio of heart to body weight; ZH, BC, and XD for the quantitative real-time PCR; ZH, SB, and BC for Western blot analyses; ZH, SB, BC, and XD for statistical analyses; and ZH, XL, SB, BC, and HL draft the manuscript. All authors read and approved the final manuscript.

Acknowledgments

The authors thank Hongyan Zou for kindly assisting with the Western blotting and qPCR studies.

References

[1] J. P. Goetze, "B-Type natriuretic peptide: from posttranslational processing to clinical measurement," *Clinical Chemistry*, vol. 58, no. 1, pp. 83–91, 2012.

[2] L. J. Deftos, D. W. Burton, and D. W. Brandt, "Parathyroid hormone-like protein is a secretory product of atrial myocytes," *The Journal of Clinical Investigation*, vol. 92, no. 2, pp. 727–735, 1993.

[3] H. Ito, Y. Hirata, S. Adachi et al., "Endothelin-1 is an autocrine/paracrine factor in the mechanism of angiotensin II-induced hypertrophy in cultured rat cardiomyocytes," *The Journal of Clinical Investigation*, vol. 92, no. 1, pp. 398–403, 1993.

[4] T. Dschietzig, C. Richter, C. Bartsch et al., "The pregnancy hormone relaxin is a player in human heart failure," *The FASEB Journal*, vol. 15, no. 12, pp. 2187–2195, 2001.

[5] C. Wang, X. Y. Dong, L. M. Wei et al., "The relationship of Appetite-Regulating hormones in the development of cardiac cachexia," *International Heart Journal*, vol. 60, no. 2, pp. 384–391, 2019.

[6] H. Doubilet, "Separation and assay of secretin and cholecystokinin," *Gastroenterology*, vol. 7, pp. 108–117, 1946.

[7] A. Funakoshi, A. Tanaka, T. Kawanami, K. Tateishi, K. Miyasaka, and A. Kono, "Expression of the cholecystokinin precursor gene in rat tissues," *Journal of Gastroenterology*, vol. 29, no. 2, pp. 125–128, 1994.

[8] X. Y. Dong, C. Wang, J. Q. Zhang et al., "Cholecystokinin expression in the development of postinfarction heart failure," *Cellular Physiology and Biochemistry*, vol. 43, no. 6, pp. 2479–2488, 2017.

[9] J. P. Goetze, A. Gore, C. H. Møller, D. A. Steinbrüchel, J. F. Rehfeld, and L. B. Nielsen, "Acute myocardial hypoxia increases BNP gene expression," *The FASEB Journal*, vol. 18, no. 15, pp. 1928–1930, 2004.

[10] J. P. Goetze, A. H. Johnsen, C. Kistorp, F. Gustafsson, C. B. Johnbeck, and J. F. Rehfeld, "Cardiomyocyte Expression and Cell-specific Processing of Procholecystokinin," *Journal of Biological Chemistry*, vol. 290, no. 11, pp. 6837–6843, 2015.

[11] M. Luo, P. P. Chen, L. Yang et al., "Sodium ferulate inhibits myocardial hypertrophy induced by abdominal coarctation in rats: involvement of cardiac PKC and MAPK signaling pathways," *Biomedicine & Pharmacotherapy*, vol. 112, p. 108735, 2019.

[12] E. Agabiti-Rosei and M. L. Muiesan, "Cardiac hypertrophy and hypertension," *Current Opinion in Nephrology and Hypertension*, vol. 7, no. 2, pp. 211–216, 1998.

[13] J. Y. Wu, C. Zhang, C. J. Liu et al., "Aortic constriction induces hypertension and cardiac hypertrophy via (pro)renin receptor activation and the PLC-β3 signaling pathway," *Molecular Medicine Reports*, vol. 19, no. 1, pp. 573–580, 2019.

[14] X. J. Bai, J. T. Hao, J. Wang et al., "Curcumin inhibits cardiac hypertrophy and improves cardiovascular function via enhanced Na^+/Ca^{2+} exchanger expression after transverse abdominal aortic constriction in rats," *Pharmacological Reports*, vol. 70, no. 1, pp. 60–68, 2018.

[15] M. Sandrock, A. Schmidt-Trucksäß, D. Schmitz, A. Niess, and H. H. Dickhuth, "Influence of physiologic cardiac hypertrophy on the prevalence of heart valve regurgitation," *Journal of Ultrasound in Medicine*, vol. 27, no. 1, pp. 85–93, 2008.

[16] T. Murakami, D. Kikugawa, K. Endou et al., "Changes in patterns of left ventricular hypertrophy after aortic valve replacement for aortic stenosis and regurgitation with St. Jude Medical cardiac valves," *Artificial Organs*, vol. 24, no. 12, pp. 953–958, 2000.

[17] T. F. Cotton and H. Cardiac, "Cardiac hypertrophy," *Canadian Medical Association Journal*, vol. 4, no. 8, pp. 709–714, 1914.

[18] A. Y. Wang, M. Wang, J. Woo et al., "Inflammation, residual kidney function, and cardiac hypertrophy are interrelated and combine adversely to enhance mortality and cardiovascular death risk of peritoneal dialysis patients," *Journal of the American Society of Nephrology*, vol. 15, no. 8, pp. 2186–2194, 2004.

[19] A. Oláh, C. Mátyás, D. Kellermayer et al., "Sex differences in morphological and functional aspects of exercise-induced cardiac hypertrophy in a rat model," *Frontiers in Physiology*, vol. 10, p. 889, 2019.

[20] I. C. Okere, D. J. Chess, T. A. McElfresh et al., "High-fat diet prevents cardiac hypertrophy and improves contractile function in the hypertensive dahl salt-sensitive rat," *Clinical and Experimental Pharmacology & Physiology*, vol. 32, no. 10, pp. 825–831, 2005.

[21] C. Beaumont, E. Walsh-Wilkinson, M. Drolet et al., "Testosterone deficiency reduces cardiac hypertrophy in a rat model of severe volume overload," *Physiological Reports*, vol. 7, no. 9, article e14088, 2019.

[22] Y. Liu, H. J. Shen, X. Q. Wang, H. Q. Liu, L. Y. Zheng, and J. D. Luo, "EndophilinA2 protects against angiotensin II-induced cardiac hypertrophy by inhibiting angiotensin II type 1 receptor trafficking in neonatal rat cardiomyocytes," *Journal of Cellular Biochemistry*, vol. 119, no. 10, pp. 8290–8303, 2018.

[23] N. Nalban, R. Sangaraju, S. Alavala, S. M. Mir, M. K. Jerald, and R. Sistla, "Arbutin attenuates Isoproterenol-Induced cardiac hypertrophy by inhibiting TLR-4/NF-κB pathway in mice," *Cardiovascular Toxicology*, vol. 20, no. 3, pp. 235–248, 2020.

[24] M. E. Hall, R. Harmancey, and D. E. Stec, "Lean heart: role of leptin in cardiac hypertrophy and metabolism," *World Journal of Cardiology*, vol. 7, no. 9, pp. 511–524, 2015.

[25] G. J. Dockray, "Cholecystokinin," *Current Opinion in Endocrinology, Diabetes, and Obesity*, vol. 19, no. 1, pp. 8–12, 2012.

[26] J. P. Goetze and J. F. Rehfeld, "Procholecystokinin expression and processing in cardiac myocytes," *Peptides*, vol. 111, pp. 71–76, 2019.

[27] R. J. Wisniewska, "Effects of cholecystokinin, caerulein and pentagastrin on arterial blood pressure and plasma renin activity in rats," *Polish Journal of Pharmacology*, vol. 49, no. 6, pp. 419–423, 1997.

[28] R. Wisniewska and K. Wisniewski, "The effect of pentagastrin, cholecystokinin and their analogues on rat arterial blood pressure and isolated heart," *Roczniki Akademii Medycznej w Białymstoku*, vol. 41, no. 2, pp. 183–190, 1996.

[29] S. Koyama, T. Fujita, T. Shibamoto, Y. Matsuda, H. Uematsu, and R. O. Jones, "Contribution of baroreceptor reflexes to blood pressure and sympathetic responses to cholecystokinin and vasoactive intestinal peptide in anesthetized dogs,"

European Journal of Pharmacology, vol. 175, no. 3, pp. 245–251, 1990.

[30] S. Zou, J. Zhang, and F. Qiu, "Influence of octapeptide of cholecystokinin, vasoactive intestinal peptide and substance P on dynamics of biliary system and cardiovascular system," *Chinese Medical Journal*, vol. 111, no. 12, pp. 1071–1074, 1998.

[31] P. Wu, W. Gao, M. Su et al., "Adaptive mechanisms of tumor therapy resistance driven by tumor microenvironment," *Frontiers in Cell and Developmental Biology*, vol. 9, article 641469, 2021.

[32] X. Y. Zhao, Y. L. Ling, Y. G. Li, A. H. Meng, and H. Y. Xing, "Cholecystokinin octapeptide improves cardiac function by activating cholecystokinin octapeptide receptor in endotoxic shock rats," *World Journal of Gastroenterology*, vol. 11, no. 22, pp. 3405–3410, 2005.

[33] C. Christoffersen, E. Bollano, M. L. S. Lindegaard et al., "Cardiac lipid accumulation associated with diastolic dysfunction in obese mice," *Endocrinology*, vol. 144, no. 8, pp. 3483–3490, 2003.

[34] J. P. Goetze, I. Hunter, N. E. Zois et al., "Cardiac procholecystokinin expression during haemodynamic changes in the mammalian heart," *Peptides*, vol. 108, pp. 7–13, 2018.

[35] S. Wang, Y. Zhao, J. Li et al., "Neurostructural correlates of hope: dispositional hope mediates the impact of the SMA gray matter volume on subjective well-being in late adolescence," *Social Cognitive and Affective Neuroscience*, vol. 15, no. 4, pp. 395–404, 2020.

[36] W. Liu, X. Wang, Z. Mei et al., "Chronic stress promotes the progression of pressure overload-induced cardiac dysfunction through inducing more apoptosis and fibrosis," *Physiological Research*, vol. 64, no. 3, pp. 325–334, 2015.

[37] J. P. Goetze, J. F. Rehfeld, and U. Alehagen, "Cholecystokinin in plasma predicts cardiovascular mortality in elderly females," *International Journal of Cardiology*, vol. 209, pp. 37–41, 2016.